X-RAY CRYSTAL STRUCTURES OF

Xe(II)–N AND Xe(II)–O BONDED COMPOUNDS,

AND THE SYNTHESES OF $OTeF_5$ DERIVATIVES OF

As(III) AND Sb(III)

X-RAY CRYSTAL STRUCTURES OF Xe(II)–N AND Xe(II)–O BONDED COMPOUNDS, AND THE SYNTHESES OF $OTeF_5$ DERIVATIVES OF As(III) AND Sb(III)

By

BARBARA ANNE FIR, B.Sc.

A Thesis

Submitted to the School of Graduate Studies

In Partial Fulfilment of the Requirements

for the Degree

Master of Science

McMaster University

September 1999

MASTER OF SCIENCE (1999) **McMASTER UNIVERSITY**

(Chemistry) Hamilton, Ontario

TITLE: X-ray Crystal Structures of Xe(II)–N and Xe(II)–O Bonded Compounds, and the Syntheses of $OTeF_5$ Derivatives of As(III) and Sb(III)

AUTHOR: Barbara Anne Fir, B.Sc.

SUPERVISORS: Professor G.J. Schrobilgen

Dr. H.P.A. Mercier

NUMBER OF PAGES: xxiii, 352

ABSTRACT

The chemistry of xenon(II) has been extended by the low-temperature X-ray structure determinations of the Xe–N bonded adduct salts, $HC{\equiv}N{-}XeF^+AsF_6^-$, $CH_3C{\equiv}N{-}XeF^+AsF_6^-{\cdot}HF$, $(CH_3)_3CC{\equiv}N{-}XeF^+AsF_6^-$, $s\text{-}C_3F_3N_2N{-}XeF^+AsF_6^-{\cdot}2.5BrF_5$, $C_5F_5N{-}XeF^+AsF_6^-{\cdot}2.5BrF_5$, and $F_5TeN(H)Xe^+AsF_6^-$, and the Xe–O bonded compounds, $F_5ChOXe^+AsF_6^-$ and $Xe(OChF_5)_2$ (Ch = Te, Se).

The thermally unstable Xe–N bonded salts represent classes of compounds in which xenon(II) is directly bonded to formally sp-, sp^2-, or sp^3-hybridized nitrogen atoms. The $R{-}C{\equiv}N{-}XeF^+AsF_6^-$ (R = H, CH_3, $(CH_3)_3C$) salts were synthesized by the low-temperature reaction of the nitrogen base with $XeF^+AsF_6^-$ in HF. The $C_5F_5N{-}XeF^+AsF_6^-{\cdot}2.5BrF_5$ and $F_5TeN(H)Xe^+AsF_6^-$ compounds were prepared by the reaction of the N-protonated bases with XeF_2 in BrF_5 and with $XeF^+AsF_6^-$ in HF, respectively. The $s\text{-}C_3F_3N_2N{-}XeF^+AsF_6^-{\cdot}2.5BrF_5$ salt was prepared by the direct interaction of $s\text{-}C_3F_3N_3$ with $XeF^+AsF_6^-$ at room temperature and subsequent recrystallization from BrF_5. The covalent nature of the Xe–N bonds was observed to increase in the order: $s\text{-}C_3F_3N_2N{-}XeF^+AsF_6^-{\cdot}2.5BrF_5$ (2.316(6) Å) < $C_5F_5N{-}XeF^+AsF_6^-{\cdot}2.5BrF_5$ (2.287(7) Å) < $HC{\equiv}N{-}XeF^+AsF_6^-$ (2.235(3) Å) < $(CH_3)_3CC{\equiv}N{-}XeF^+AsF_6^-$ (2.212(4) Å) < $CH_3C{\equiv}N{-}XeF^+AsF_6^-{\cdot}HF$ (2.179(7) Å) <

$F_5TeN(H)Xe^+AsF_6^-$ (2.044(4) Å), indicating that *s*-$C_3F_3N_2N$–$XeF^+AsF_6^-\cdot 2.5BrF_5$ contains the most ionic Xe–N bond in this series. It was also observed that as the covalent nature of the Xe–N bond increases, the Xe–F bond becomes more ionic. The X-ray crystal structures of $HCNH^+AsF_6^-$, $F_5TeNH_3^+AsF_6^-$, and F_5TeNH_2 were also determined and provided comparisons with those of HC≡N–$XeF^+AsF_6^-$ and $F_5TeN(H)Xe^+AsF_6^-$, respectively.

The X-ray crystal structures of the $XeOChF_5^+AsF_6^-$ salts have been determined and are isostructural and disordered. The structure of $Xe(OSeF_5)_2$ is in agreement with a previous structure report, but is now assigned to the correct space group. The single-crystal X-ray structure of $Xe(OTeF_5)_2$ was determined for the first time and contradicts an earlier published cell determination of this compound. The structures of $XeOChF_5^+AsF_6^-$ and $Xe(OChF_5)_2$, which are analogs of XeF^+ and XeF_2, respectively, confirm that the $OChF_5$ groups have lower electronegativities than F. When compared with the structure of $F_5TeN(H)Xe^+AsF_6^-$, which is isolobal with $XeOChF_5^+AsF_6^-$, it was determined that the relative electronegativities of these groups, and subsequent Lewis acidities of the cations, $F_5TeN(H)Xe^+$, $XeOChF_5^+$, and XeF^+, increase in the order: $F_5TeN(H) > OSeF_5 > OTeF_5 > F$.

Local density functional theory (LDFT/DZVP) calculations which were done for $F_5TeN(H)Xe^+AsF_6^-$, $F_5TeNH_3^+AsF_6^-$, F_5TeNH_2, and $XeOChF_5^+AsF_6^-$, reproduce the structures and have been used to assign their vibrational spectra. Only the calculated vibrational spectra for $XeOChF_5^+AsF_6^-$ are discussed in this Thesis.

The $OTeF_5$ chemistry of As and Sb has also been extended by the syntheses and detailed structural characterizations by ^{19}F and ^{125}Te NMR spectroscopy and by Raman spectroscopy of the new pnicogen anions, $Pn(OTeF_5)_4^-$ (Pn = Sb, As), as their $N(CH_3)_4^+$ and $N(CH_2CH_3)_4^+$ salts. The $As(OTeF_5)_4^-$ anion was found to be thermally less stable in CH_3CN and SO_2ClF solvents when compared to the analogous antimony anion. Both anions have trigonal-bipyramidal AX_5E VSEPR geometries with two equatorial and two axial $OTeF_5$ ligands that undergo intermolecular exchange in solution by Berry pseudorotation. However, the exchange could not be slowed down sufficiently on the NMR time scale to observe separate environments due to the freezing points of the solvents used. An equilibrium was also observed to occur between $Sb(OTeF_5)_4^-$, $Sb(OTeF_5)_3$, and $OTeF_5^-$ in CH_3CH_2CN solvent. All attempts to crystallize $Sb(OTeF_5)_4^-$ were unsuccessful and produced the less soluble, but novel, $Sb(OTeF_5)_5^{2-}$ anion instead, whose preliminary disordered X-ray crystal structure is reported in this Thesis.

ACKNOWLEDGEMENTS

I wish to thank Dr. Gary J. Schrobilgen for his immense guidance and support throughout this work.

I would especially like to thank Dr. Hélène P.A. Mercier for all her assistance, particularly with the X-ray crystal structures, and for her constant advice and encouragement.

I gratefully acknowledge Dr. Jim Britten for his patience and for operating the X-ray instrument for my needs at all hours of the day and night. I would also like to thank Dr. David A. Dixon for the density functional theory calculations, Dr. Alex Bain for his assistance with the MEXICO program, and Dr. David Santry for the calculated NMR spectra.

I am also grateful to the many people who have offered their friendship, support, and assistance throughout my stay at McMaster. In particular, I wish to thank Michael Gerken for spending a great deal of time assisting me with the NMR instrument and with X-ray techniques. My thanks, also, to Bernie Pointner, John Lehmann, Dr. Nicolas LeBlond, and Tom Bajorek.

Special thanks to my parents and sister, Julie, for their love and continuous support.

I especially thank my fiancé, Paul, for his emotional support, love, and encouragement during all my years at McMaster.

LIST OF ABBREVIATIONS AND SYMBOLS

FEP	perfluoroethylene / perfluoropropylene copolymer
Kel-F	chlorotrifluoroethylene polymer
Teflon (PTFE)	tetrafluoroethylene polymer
i.d.	inner diameter
o.d.	outer diameter
SAE	Society of Automotive Engineers
FID	free-induction decay
NMR	nuclear magnetic resonance
ppm	parts per million
eV	electron volt (1 eV/molecule = 23.061 kcal/mol)
IP	ionization potential
Me	methyl group (CH_3)
DME	1,2-dimethoxyethane ($CH_3O(CH_2)_2OCH_3$)
thf	tetrahydrofuran (C_4H_8O)
dppm	$Ph_2PCH_2PPh_2$
δ	chemical shift in ppm from a reference compound
K	reduced coupling constant in T^2J^{-1}
γ	gyromagnetic ratio of a nucleus in $rad \cdot s^{-1}T^{-1}$
I	nuclear spin quantum number
J	scalar coupling constant in hertz (Hz)

TABLE OF CONTENTS

LIST OF TABLES

LIST OF FIGURES

CHAPTER 1

INTRODUCTION

SECTION A:

GENERAL BACKGROUND OF Xe(II) CHEMISTRY

No attempt is made here to review noble-gas chemistry as there are several comprehensive reviews available detailing developments in the field.[1-13] Xenon compounds, particularly those involving xenon in the +2 oxidation state, are the most readily prepared and the most intensively studied compounds in the field of noble-gas chemical behavior. The present work further details the structures and properties of several Xe(II) compounds using mainly X-ray crystallography, as well as vibrational and multi-nuclear magnetic resonance (NMR) spectroscopy.

Among the driving forces behind the syntheses of new noble-gas species are the desire to extend the known chemistry to other noble gases such as argon, for which no compounds are yet known, to define the limits and criteria for reactivity with elements other than fluorine, and to confirm their predicted geometries based on known isoelectronic species and the valence-shell electron pair repulsion (VSEPR) rules.[13] Structural characterizations have been obtained for noble-gas compounds by infrared, Raman, and multi-NMR spectroscopy. However, the most definitive method of characterization is X-ray crystallography, although the thermal instability and/or air-

sensitivity of noble-gas compounds often present a formidable barrier to achieving the structural data by this means.

The single most important criterion for the syntheses of noble-gas species is that the reacting species have sufficiently high electronegativity to withstand the high electron affinities of the noble gases in their positive oxidation states.[14] The ability of electronegative elements to form bonds to xenon is now well-established for fluorine, oxygen, nitrogen, and, to some extent, for carbon and chlorine. Given the high electronegativity of fluorine, it is no surprise that XeF_2 was one of the first noble-gas compounds prepared [eq (1.1)].[15]

$$Xe_{(g)} + F_{2(g)} \xrightarrow{h\nu \text{ or } \Delta} F\text{–}Xe\text{–}F \qquad (1.1)$$

Xenon difluoride readily undergoes a variety of ligand substitution reactions and, as such, is always the ultimate starting material in the syntheses of other xenon(II) compounds. The thermodynamic stability of XeF_2 is derived from the high electron affinity (-333 ± 0.4 kJ/mol)[16] and small size of the fluorine atom. Consequently, ligands (L) capable of replacing fluorine in XeF_2 to give FXeL or LXeL derivatives, must have a high electronegativity.[1,14,18] One common synthetic strategy leading to the formation of new xenon(II) compounds is the reaction of XeF_2 with suitably strong fluoride ion acceptors, such as AsF_5 and SbF_5, to form the XeF^+ and $Xe_2F_3^+$ cations.[11,17,19-23] The X-ray crystal structures of these cations have been obtained and those of XeF^+ demonstrate a significant bridging interaction between xenon and a fluorine atom of the counteranion (see Figure 1.1).

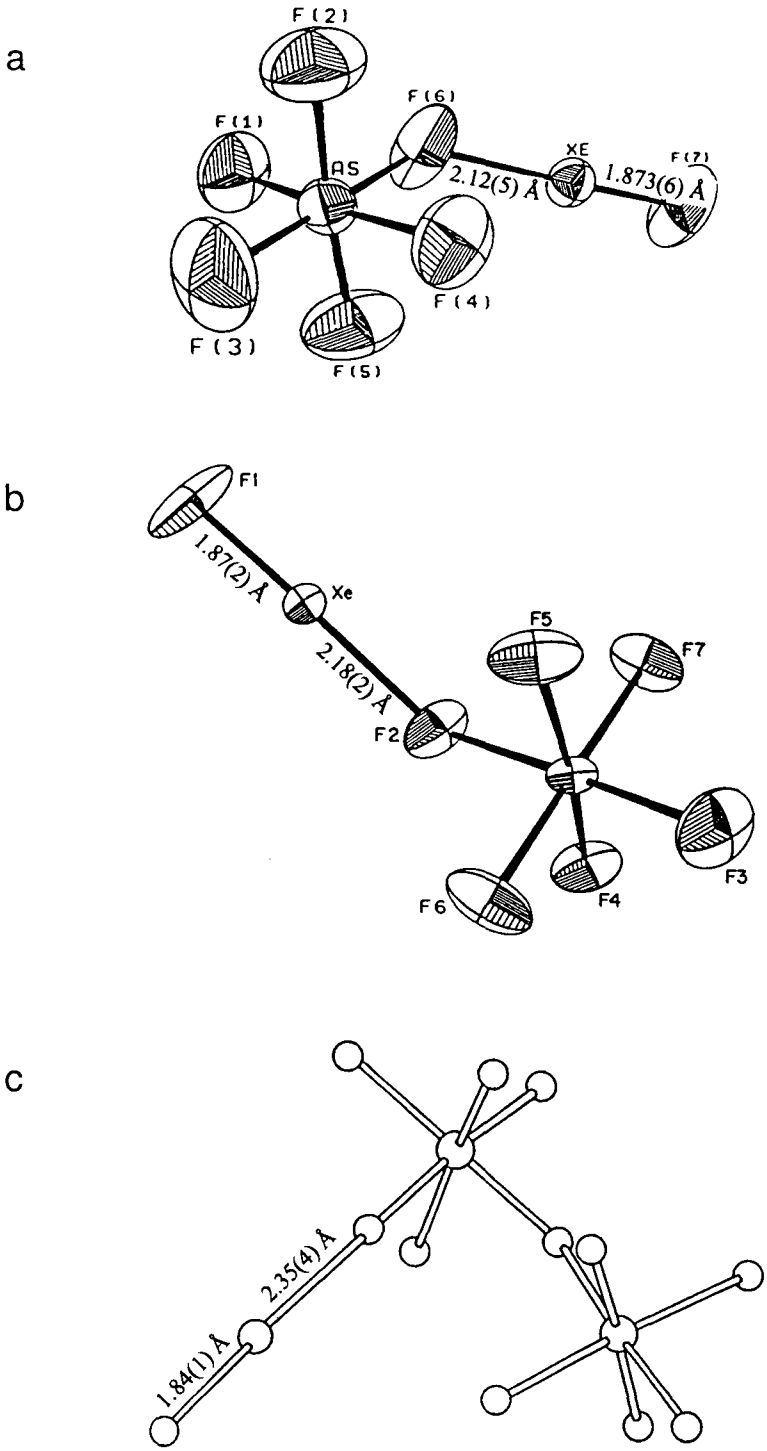

Figure 1.1 X-ray crystal structures of (a) $XeF^+AsF_6^-$,[19] (b) $XeF^+RuF_6^-$,[22] and (c) $XeF^+Sb_2F_{11}^-$.[23]

The valence bond[24] and molecular orbital[25] descriptions of XeF_2 indicate a high degree of ionic character in the Xe–F bonds with considerable negative charge on the fluorine atoms, such that the charge distribution may be described as $F^{-½}Xe^{+1}F^{-½}$.[13,26] The valence bond description of XeF_2 incorporates Xe–F bond polarity according to the resonance structures I and II.[9] The Xe–F bond polarity in XeF_2 contributes to its fluoride

$$F–Xe^{+}\ F^{-} \quad \leftrightarrow \quad F^{-}\ {}^{+}Xe–F$$

I II

ion donor behavior towards many strong Lewis acids (MF_5; M = As, Sb) yielding the xenon difluoride-metal pentafluoride adducts $XeF_2{\cdot}MF_5$, $XeF_2{\cdot}2MF_5$, and $2XeF_2{\cdot}MF_5$.[10] Despite these adducts displaying a considerable amount of covalent bridging interaction between xenon and a fluorine atom of the anion, they have also been formulated as $XeF^{+}MF_6^{-}$, $XeF^{+}M_2F_{11}^{-}$, and $Xe_2F_3^{+}MF_6^{-}$.[27-29] Consequently, a certain amount of caution is required when defining these systems without accurate geometrical data from single crystal X-ray diffraction. For instance, XeF_2 adducts with the weak fluoride ion acceptors MOF_4 (M = Xe, Mo, W) were shown to possess the stoichiometries $XeF_2{\cdot}MOF_4$ (M = Xe, Mo, W) and $XeF_2{\cdot}2MOF_4$ (M = Mo, W), and have single, Xe–F–M bridge interactions with the Xe–F bridging bond lengths, *i.e.*, $XeF_2{\cdot}WOF_4$, (2.04(3) Å),[30] approaching values reported for Xe–F bonds in XeF_2 (2.010(6) Å).[31] On the other hand, the bridging Xe···F bond in the $XeF^{+}AsF_6^{-}$ salt is considerably more ionic (2.12(5) Å).[19] Single crystal X-ray diffraction studies of these systems reveal that the degree of ionicity in the adducts is largely dependent on the Lewis acid character of the

pentafluoride.[9,32,33] That is, as the fluoride ion acceptor ability of the MF_5 molecule increases, the bridging Xe···F bond becomes more ionic and the terminal Xe–F bonds become more covalent. For instance, due to the stronger basic character of the $Sb_2F_{11}^-$ anion as compared to AsF_5 and RuF_5, the terminal Xe–F bond length in the $XeF^+Sb_2F_{11}^-$ salt (1.84(1) Å)[11,20] is significantly shorter than those in $XeF^+AsF_6^-$ (1.873(6) Å)[19] and $XeF^+RuF_6^-$ (1.87(2) Å).[34,35] Accordingly, the bridging Xe···F bond length in $XeF^+Sb_2F_{11}^-$ (2.35(4) Å)[11,20] is more ionic than those in $XeF^+AsF_6^-$ (2.12(5) Å)[19] and $XeF^+RuF_6^-$ (2.18(2) Å),[34,35] but is still shorter than the sum of the fluorine and xenon van der Waals radii (Xe, 2.20 Å; F, 1.50-1.60 Å).[36-38]

The propensity of the XeF^+ cation to form strong fluorine bridges with weak fluorobasic anions, such as AsF_6^-, SbF_6^-, and $Sb_2F_{11}^-$, in the solid state reflects its substantial Lewis acid character.[1] Early work by Bartlett and Sladky[39] showed that the oxidizing ability of XeF^+ greatly surpassed that of XeF_2 by the redox reaction of XeF_2, I_2, and trace amounts of the Lewis acids SO_2, HF, or BF_3, forming IF_5 and xenon gas. The observation of xenon gas was consistent with the formation of XeF^+ from the interaction of the Lewis acid (A) with XeF_2 according to equation (1.2). The electron affinity of

$$A + XeF_2 \rightleftharpoons AF^- + XeF^+ \qquad (1.2)$$

XeF^+ has been estimated to be 10.9 eV using a modified form of the Born-Haber cycle (Figure 1.2). The XeF^+ cation has been used extensively as a chemical reagent to oxidatively fluorinate other species, and its utility is the subject of this Thesis and will be discussed further in the subsequent sections.

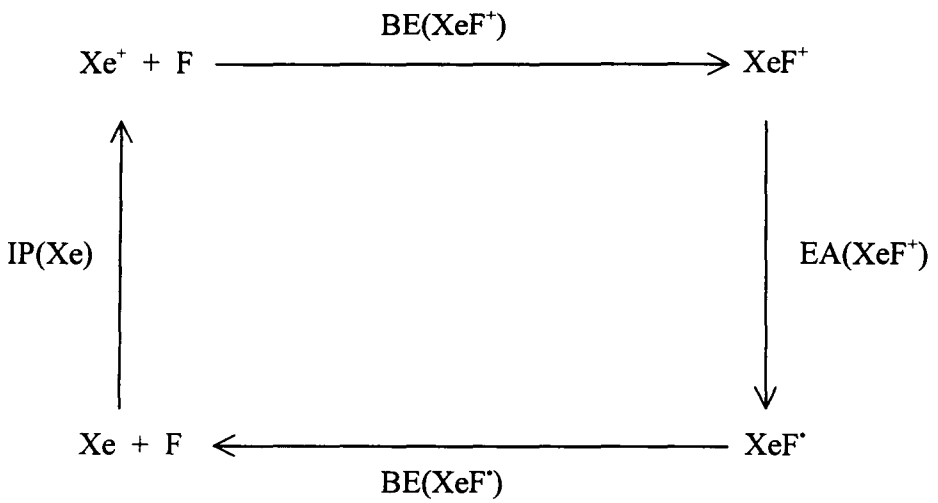

$EA(XeF^+) = IP(Xe) + BE(XeF^\bullet) - BE(XeF^+)$

$IP(Xe)^{13} = 12.10$ eV

$BE(XeF^+)^{13} \approx 2.10$ eV $= 2.03$ eV (gas phase)

$BE(XeF^\bullet)^{13} \approx 0.86$ eV

$EA(XeF^+) \approx 10.90$ eV

Figure 1.2 Estimation of the electron affinity of XeF^+.

GENERAL CRITERIA FOR Xe(II)–L (L = LIGAND) BOND FORMATION

There are two general classes of ligands which are suitable for stabilizing xenon in its +2 oxidation state; those derived from protic acids, which also exist as stable anions, and neutral Lewis base species. Ligands derived from protic acids must possess properties that render them resistant to redox degradation if they are to withstand the high electron affinity associated with the xenon(II) atom. Consequently, ligands of this class:[14]

1. must have high effective group electronegativities,
2. usually exist as moderate to strong monoprotic acids,
3. should exist as stable anions in alkali metal salts,
4. should have the least electronegative element of the ligand in its highest oxidation state (*i.e.*, Te(VI) of the $OTeF_5$ group).

On the other hand, neutral Lewis base ligands must meet the following criteria in order to form xenon(II) derivatives:[14]

1. the base should possess a first adiabatic ionization potential greater than the estimated electron affinity of the strongly oxidizing xenon(II) cation (XeF^+, 10.9 eV),
2. the ligand must be basic enough to donate a lone pair of electrons to the xenon(II) cation.

Xe(II)–O BONDED COMPOUNDS

There are several monoprotic oxoacids (HOL) that are capable of replacing F^- in XeF_2 by HF elimination reactions to form xenon-oxygen bonds, namely, $HOSO_2F$, $HOTeF_5$, $HOSeF_5$, HNO_3, $HOClO_3$, HSO_3CF_3, and $HOC(O)CF_3$, according to equations (1.3) and (1.4).[1,40,41] Similar to XeF_2, these xenon(II) derivatives contain linear F–Xe–O

$$XeF_2 + HOL \longrightarrow F\text{–}Xe\text{–}OL + HF \qquad (1.3)$$

$$XeF_2 + 2HOL \longrightarrow LO\text{–}Xe\text{–}OL + 2HF \qquad (1.4)$$

and O–Xe–O arrangements. The strong oxo-acid, $HOIOF_4$,[42] may also be used to prepare mono- and disubstituted xenon(II) derivatives according to equations (1.5) and (1.6),

$$IO_2F_3 + XeF_2 \xrightarrow{SO_2ClF} FXeOIOF_4 \qquad (1.5)$$

$$2HOIOF_4 + Xe(OTeF_5)_2 \xrightarrow{0\,^\circ C} Xe(OIOF_4)_2 + 2HOTeF_5 \qquad (1.6)$$

respectively. Likewise, substitution reactions of fluorine in $Xe_2F_3^+$ have provided a means of isolating xenon(II) derivatives. For example, the $Xe_2F_3^+$ cation, which has two terminal and one bridging fluorine as determined by X-ray crystallography, readily undergoes solvolysis in HSO_3F solvent to give the $(FXe)_2SO_3F^+$ cation [eq (1.7)], which

$$Xe_2F_3^+ + HSO_3F \longrightarrow (FXe)_2SO_3F^+ + HF \qquad (1.7)$$

has been shown by X-ray crystallography to contain the fluorosulfate group in the bridging position.[43]

The thermal stabilities of some of the oxygen-containing ligands (OL) known to form covalent bonds to xenon(II) increase in the order: $OC(O)CF_3 < OClO_3 < OSO_2F <$

$OSeF_5 < OTeF_5$.[41,44] Consequently, the mono- and disubstituted xenon(II) derivatives of the ligands $OSeF_5$ and $OTeF_5$ have been studied extensively. However, the stability of these compounds is still considerably less than XeF_2, because the electron-withdrawing effect by the five fluorine atoms stabilizes both the xenon compound and the peroxides of the decomposition reactions given by equations (1.8) and (1.9) (cf. decomposition of XeF_2 into Xe and F_2 at temperatures above 500 °C).[41]

$$Xe(OL)_2 \longrightarrow Xe + L\text{–}O\text{–}O\text{–}L \qquad (1.8)$$

$$F\text{–}Xe\text{–}OL \longrightarrow XeF_2 + Xe + L\text{–}O\text{–}O\text{–}L \qquad (1.9)$$

The relative electronegativity of the $OTeF_5$ ligand compared to that of F had been controversial for some time. Initially, it was argued that the $OTeF_5$ group possessed a higher electronegativity than fluorine, on the basis of the square-pyramidal structure of $FI(OTeF_5)_4$, in which the fluorine occupies the axial position; a position reserved for the least electronegative ligand according to VSEPR rules.[41] However, related Mössbauer experiments in which ^{129}Xe quadrupole splittings were correlated with electronegativities,[45] and experiments correlating the ^1H chemical shift differences between the methyl and methylene protons in CH_3CH_2X with the electronegativity of X (X = F, Cl, Br, I),[46] gave values of 3.88 and 3.98 on the Pauling scale for $OTeF_5$ [45,47] and F,[48] respectively. These results were also confirmed by differences in the ^{129}Xe chemical shifts for F and $OTeF_5$ analogues, which consistently showed that the $OTeF_5$ group was significantly more shielding towards the central xenon nucleus than F. Furthermore, it was determined that $FI(OTeF_5)_4$ was actually based on a trigonal bipyramidal structure,

and not square-pyramidal as previously reported. The high effective group electronegativity of $OTeF_5$ stems from the inductive effect of the five fluorines on tellurium. Although the effective electronegativity of $OSeF_5$ has not been determined, it should be slightly less than that of $OTeF_5$ based on Mössbauer data and ^{125}Te and ^{129}Xe NMR spectroscopic measurements.[41,45]

The stable disubstituted $OChF_5$ (Ch = Te, Se) analogs of XeF_2 can be synthesized in several ways [eqs (1.10), (1.11), (1.12)].[49-52] However, the synthesis of $Xe(OSeF_5)_2$ according to equation (1.12) is preferred, since the difficult preparation of $HOSeF_5$ can be

$$XeF_2 + HOChF_5 \longrightarrow Xe(OChF_5)_2 + 2HF \quad (1.10)$$

$$3XeF_2 + 2B(OTeF_5)_3 \longrightarrow 3Xe(OTeF_5)_2 + 2BF_3 \quad (1.11)$$

$$2SeO_2F_2 + 3XeF_2 \longrightarrow Xe(OSeF_5)_2 + 2Xe + O_2 \quad (1.12)$$

avoided. The susceptibility of the $Xe(OChF_5)_2$ compounds to vacuum sublimation has enabled their X-ray crystal structures to be determined. The reported geometry for $Xe(OSeF_5)_2$ is disordered, enhanced by the spherical shape of the ligands (Figure 1.3).[50]

The mono-substituted derivatives are formed in an equilibrium reaction of $Xe(OChF_5)_2$ with XeF_2 [eq (1.13)].[49,53,54] Additionally, the analogs of XeF^+, namely the

$$Xe(OChF_5)_2 + XeF_2 \longrightarrow 2FXeOChF_5 \quad (1.13)$$

salts of $XeOChF_5^+$ (Ch = Te, Se) with AsF_6^- and of $XeOTeF_5^+$ with $Sb_2F_{11}^-$ have also been isolated.[53,55,56] The $XeOChF_5^+AsF_6^-$ salts have been prepared by fluoride abstraction from $FXeOChF_5$ using the strong Lewis fluoroacid, AsF_5 [eq (1.14)]. The

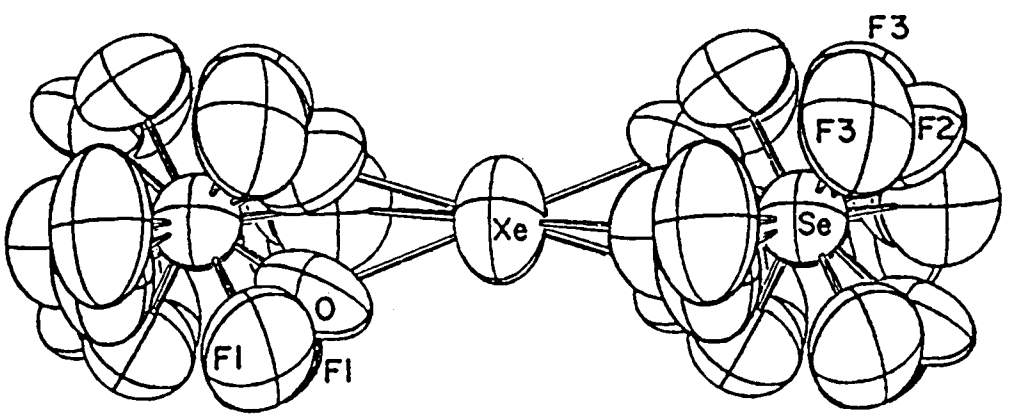

Figure 1.3 X-ray crystal structure of $Xe(OSeF_5)_2$ (disordered model).[50]

$$FXeOChF_5 + AsF_5 \longrightarrow XeOChF_5^+AsF_6^- \quad (1.14)$$

$XeOTeF_5^+Sb_2F_{11}^-$ salt has also been prepared by displacement of AsF_6^- upon solvolysis of $XeOTeF_5^+AsF_6^-$ in SbF_5, followed by removal of AsF_5 under vacuum [eq (1.15)].[56]

$$XeOTeF_5^+AsF_6^- + 2SbF_5 \longrightarrow XeOTeF_5^+Sb_2F_{11}^- + AsF_5 \quad (1.15)$$

Raman and NMR spectroscopic parameters of these salts have implied a significant Xe···F bridging interaction between xenon in $XeOChF_5^+$ and a fluorine atom of the anion.

The bonding in xenon(II) compounds has been studied extensively by ^{129}Xe NMR spectroscopy. Typically, the $\delta(^{129}Xe)$ values increase in the order: $XeL_2 < FXeL < (LXe)_2F^+ < XeL^+$, where L = F, $OTeF_5$, $OSeF_5$, OSO_3F, $OIOF_4$.[12] In compounds of the form F–Xe–L and F–Xe–L^+ (L = terminal or bridging F, oxygen-containing ligand), the ^{129}Xe and ^{19}F chemical shifts and $^1J(^{129}Xe\text{-}^{19}F)$ coupling constants can also be used to assess the ionic character of the Xe–L bond.[12] It has been established that as the ionic character of the Xe–F bond increases, the covalent nature of the Xe–L bond also increases, and the ^{129}Xe nucleus becomes more deshielded. The ^{129}Xe chemical shift values for $XeOTeF_5^+$ (-1481.9 ppm, -56 °C)[57] and $XeOSeF_5^+$ (-1438 ppm, 5 °C)[14] in BrF_5 and SbF_5 solvents, respectively, are larger than those observed for XeF_2 in BrF_5 (-1708 ppm, -40 °C),[59] $Xe(OTeF_5)_2$ in $CFCl_3$ (-2423 ppm, 5 °C),[42] and $Xe(OSeF_5)_2$ in $CFCl_3$ (-2200, 30 °C),[60] but are smaller than those observed for the weakly fluorine-bridged adducts $XeF_2{\cdot}WOF_4$ (-1331, -66 °C)[61] and $XeF_2{\cdot}MoOF_4$ (-1381 ppm, -80 °C),[61] and $FXeF{\cdots}BrOF_2^+$ (-1359 ppm, -59 °C)[56] in BrF_5 solvent. Accordingly, the bridging Xe···F interactions observed in the $XeOChF_5^+AsF_6^-$ (Ch = Te, Se) salts are expected to be

considerably covalent. Owing to the high electronegativities of the $OTeF_5$ and $OSeF_5$ groups, which approach that of fluorine, the Lewis acidities of the $Xe–L^+$ cations (L = $OTeF_5$, $OSeF_5$) should also approach that of the XeF^+ analogue.

Xe(II)–N BONDED COMPOUNDS

While many examples of xenon bonded to oxygen or fluorine and of xenon bonded to other highly electronegative ligands through oxygen were synthesized immediately following the discovery of noble-gas reactivity, it is only more recently that the first xenon-nitrogen bonded compound, $FXeN(SO_2F)_2$, was prepared [eq (1.16)] and

$$XeF_2 + HN(SO_2F)_2 \xrightarrow{CF_2Cl_2,\ 0\ °C} FXeN(SO_2F)_2 + HF \qquad (1.16)$$

characterized by X-ray crystallography (Figure 1.4), Raman spectroscopy, and multi-NMR spectroscopy.[62] The $FXeN(SO_2F)_2$ compound possesses both the longest terminal Xe–F bond (1.967(3) Å) and the lowest Xe–F stretching frequency (506 cm^{-1}) observed to date for an F–Xe–L (L = oxygen or nitrogen-containing ligand) type compound (cf. $FXeOTeF_5$, 516 cm^{-1}; $FXeOIOF_4$, 527 cm^{-1}; $FXeOSO_2F$, 528 cm^{-1}, 1.940(8) Å; $(FXeO)_2SOF^+$, 568 cm^{-1}, 1.86(3) Å).[17,34,52] Since the Xe–F bond length, stretching frequency, and bond order (0.59) for $FXeN(SO_2F)_2$ are closer to the corresponding values observed for XeF_2 (2.010(6) Å, 497 cm^{-1}, 0.50),[31] it was concluded that this bond was the most XeF_2-like bond encountered thus far.

Following the isolation of $FXeN(SO_2F)_2$, other imidodisulfurylfluoride xenon-nitrogen bonded species were characterized using primarily NMR spectroscopy, namely

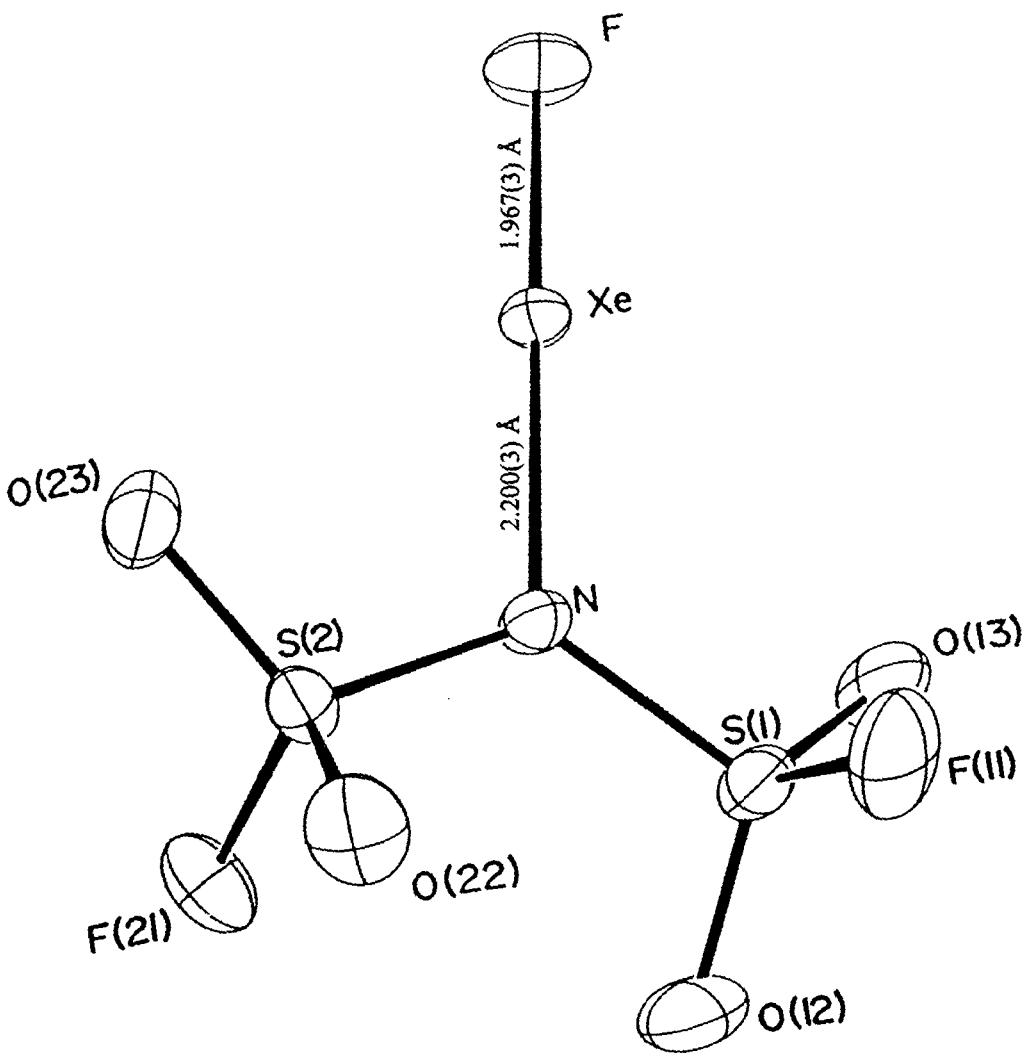

Figure 1.4 X-ray crystal structure of $FXeN(SO_2F)_2$.[62]

$Xe[N(SO_2F)_2]_2$,[63,64] $F[XeN(SO_2F)_2]_2^+AsF_6^-$,[20,63,64] $XeN(SO_2F)_2^+AsF_6^-$,[20] and $XeN(SO_2)_2^+Sb_3F_{16}^-$,[20] although $XeN(SO_2)_2^+Sb_3F_{16}^-$ was also characterized by X-ray crystallography (Figure 1.5). The $XeN(SO_2F)_2^+$ cation was prepared by the reaction of $FXeN(SO_2F)_2$ with the Lewis acid, AsF_5, at low temperatures [eq (1.17)].[20] However,

$$FXeN(SO_2F)_2 + AsF_5 \xrightarrow{78\ ^\circ C} XeN(SO_2F)_2^+AsF_6^- \quad (1.17)$$

$XeN(SO_2F)_2^+AsF_6^-$ decomposes under dynamic vacuum at 22 °C to give $F[XeN(SO_2F)_2]_2^+AsF_6^-$, which contains a fluorine bridge like the $Xe_2F_3^+$ cation [eq (1.18)]. Solvolysis of $F[XeN(SO_2F)_2]_2^+AsF_6^-$ in SbF_5 displaces the weaker fluoride ion

$$2XeN(SO_2F)_2^+AsF_6^- \xrightarrow{23\ ^\circ C} F[XeN(SO_2F)_2]_2^+AsF_6^- + AsF_5 \quad (1.18)$$

acceptor, AsF_5, yielding $XeN(SO_2F)_2^+Sb_3F_{16}^-$, which crystallizes from SbF_5 [eq (1.19)].[20]

$$F[XeN(SO_2F)_2]_2^+AsF_6^- + 6SbF_5 \xrightarrow{SbF_5\ /\ 0\ ^\circ C} 2XeN(SO_2F)_2^+Sb_3F_{16}^- + AsF_5 \quad (1.19)$$

The X-ray crystal structure of the $XeN(SO_2)_2^+$ cation is structurally similar to the neutral $FXeN(SO_2F)_2$ compound and shows a weakly covalent Xe···F (2.457(8) Å) bridge bond between xenon and a fluorine atom of the $Sb_3F_{16}^-$ anion.[20] The increase of the Xe···F bond length in the cation results in a decrease in the Xe–N bond length of 2.02(1) Å, compared to 2.200(3) Å in $FXeN(SO_2F)_2$.

The neutral $Xe[N(SO_2F)_2]_2$ compound was formed by the HF elimination reaction of $HN(SO_2F)_2$ with XeF_2 according to equation (1.20).[63,64] Additionally, the ligand

$$XeF_2 + 2HN(SO_2F)_2 \xrightarrow{CF_2Cl_2\ /\ 0\ ^\circ C} Xe[N(SO_2F)_2]_2 + 2HF \quad (1.20)$$

transfer reagent, $(CH_3)_3SiN(SO_2CF_3)_2$, prepared as in equation (1.21), was used to

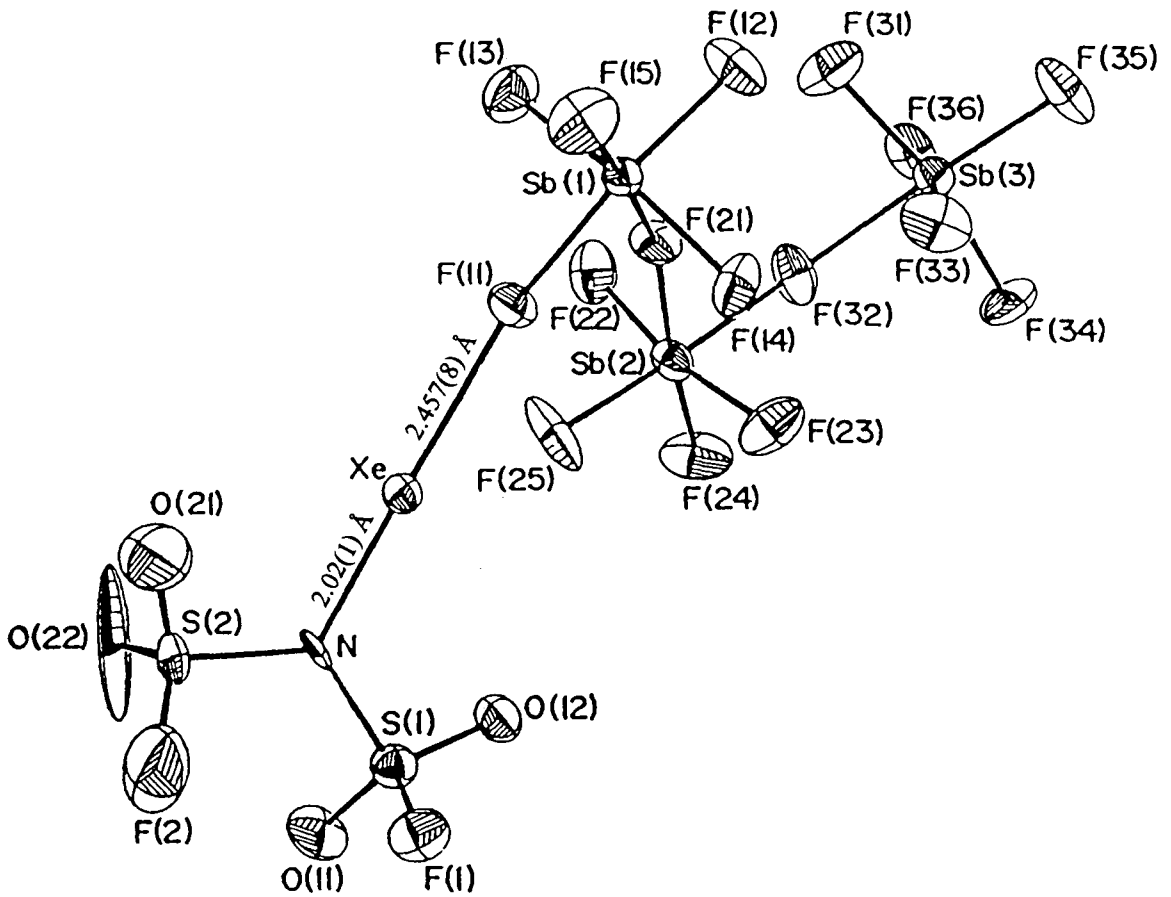

Figure 1.5 X-ray crystal structure of $XeN(SO_2)_2^+Sb_3F_{16}^-$.[20]

$$(CH_3)_3SiH + (CF_3SO_2)_2NH \longrightarrow (CH_3)_3SiN(SO_2CF_3)_2 + H_2 \quad (1.21)$$

prepare $Xe[N(SO_2CF_3)_2]_2$ in a $(CH_3)_3SiF$ elimination reaction with XeF_2, avoiding the formation of HF [eq (1.22)].[65] The $Xe[N(SO_2CF_3)_2]_2$ compound is the most thermally

$$2(CH_3)_3SiN(SO_2CF_3)_2 + XeF_2 \xrightarrow{CF_2Cl_2} Xe[N(SO_2CF_3)_2]_2 + 2(CH_3)_3SiF \quad (1.22)$$

stable of the imido derivatives of xenon. The ability of the $N(SO_2F)_2$ and $N(SO_2CF_3)_2$ ligands to form stable bonds to xenon arises from the highly electron withdrawing groups bonded to the nitrogen atoms, resulting in ligands which are resistant to oxidative fluorination.

Two C–Xe–N bonded systems, namely $CH_3CN\cdots Xe–C_6F_5^+$ (Figure 1.6)[66] and 2,6-$C_5H_3F_2N\cdots Xe–C_6F_5^+$ (Figure 1.7),[67] have been isolated and characterized by single crystal X-ray diffraction by Frohn *et al.* The 2,6-$C_5H_3F_2N\cdots Xe–C_6F_5^+$ cation has been prepared by coordination of the strongly basic pyridine, 2,6-$C_5H_3F_2N$, with the $C_6F_5Xe^+AsF_6^-$ salt according to equation (1.23).[67] The $CH_3CN\cdots Xe–C_6F_5^+$ cation was

$$C_6F_5Xe^+AsF_6^- + 2,6\text{-}C_5H_3F_2N \longrightarrow 2,6\text{-}C_5H_3F_2N\cdots Xe–C_6F_5^+AsF_6^- \quad (1.23)$$

prepared by the reaction of CH_3CN with the ligand transfer reagent, $C_6F_5Xe^+(C_5F_5)_2BF_2^-$ [eqs (1.24) and (1.25)].[66] The Xe–N bond lengths observed in the $CH_3CN\cdots Xe–C_6F_5^+$

$$B(C_6F_5)_3 + XeF_2 \xrightarrow{CH_2Cl_2} C_6F_5Xe^+(C_5F_5)_2BF_2^- \quad (1.24)$$

$$C_6F_5Xe^+(C_5F_5)_2BF_2^- + CH_3CN \longrightarrow CH_3CN\cdots Xe–C_6F_5^+ + (C_6F_5)_2BF_2^- \quad (1.25)$$

(2.681(8) Å) and 2,6-$C_5H_3F_2N\cdots Xe–C_6F_5^+$ (2.694(5) Å) cations are significantly longer than those observed in $FXeN(SO_2F)_2$ and $XeN(SO_2)_2^+$ (*vide infra*).

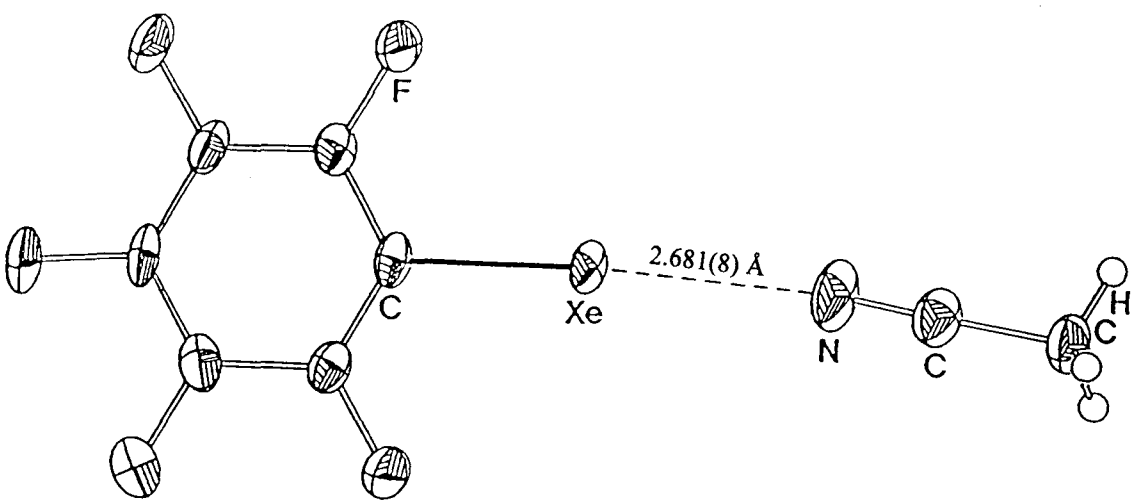

Figure 1.6 X-ray crystal structure of $CH_3CN\cdots Xe–C_6F_5^+$.[66]

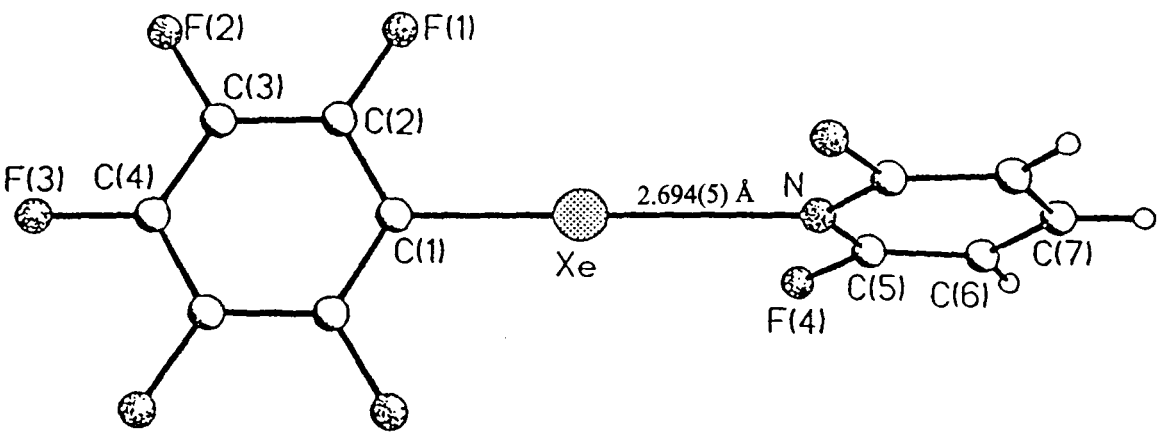

Figure 1.7 X-ray crystal structure of 2,6-$C_5H_3F_2N\cdots Xe–C_6F_5^+$.[67]

Recently, the Lewis acidity of the XeF^+ cation has been exploited to synthesize the novel adduct salts, $D–XeF^+AsF_6^-$, containing Xe–N bonds by reacting $XeF^+AsF_6^-$ (or $Xe_2F_3^+AsF_6^-$) with several classes of oxidatively resistant Lewis nitrogen bases (D) in HF [eq (1.26)].[68,69] An alternative approach to the synthesis of XeF^+ adducts involves

$$D + XeF^+AsF_6^- (Xe_2F_3^+AsF_6^-) \xrightarrow{HF} D–XeF^+AsF_6^- (+ XeF_2) \qquad (1.26)$$

protonation of the nitrogen base in anhydrous HF solvent in the presence of the Lewis acid, AsF_5 [eq (1.27)], followed by its reaction with XeF_2 in the strongly oxidizing aprotic solvent, BrF_5 according to equation (1.28).[70] In this case, an equilibrium occurs,

$$D + HF + AsF_5 \longrightarrow DH^+AsF_6^- \qquad (1.27)$$

$$DH^+AsF_6^- + XeF_2 \overset{BrF_5}{\rightleftharpoons} D–XeF^+AsF_6^- + HF \qquad (1.28)$$

from which the xenon adduct can be isolated by pumping off the HF product and the BrF_5 solvent at low temperatures. In the acid-base reactions, XeF^+ functions as an electron-pair acceptor for the lone pair on the nitrogen base of specific ligands, providing the ligand can withstand oxidation by XeF^+. Given the oxidizing strength of XeF^+, appropriate nitrogen bases that are resistant to oxidation may be selected according to their first adiabatic ionization potentials (Table 1.1), which should be close to or exceed the estimated electron affinity of XeF^+ (EA $\approx$ 10.9 eV; *vide supra*).[71] Those $D–XeF^+AsF_6^-$ salts which have been isolated at low temperatures by the reaction of equimolar amounts of XeF^+ with neutral bases in HF [see eq (1.26)] include the nitriles, $R–C\equiv N–XeF^+AsF_6^-$ (R = H, CH_3, $(CH_3)_3C$, CH_2F, C_2H_5),[68-70] and the

Table 1.1 First Adiabatic Ionization Potentials (IP_1) of Some Nitrogen Bases.

Nitrogen Base	IP_1 (eV)	Reference
CF_3CN	13.90	73
HCN	13.59	74
CH_2FCN	13.00 ± 0.1	75
NSF_3	12.50	76
CH_2ClCN	12.2 ± 0.1	75
CHF_2CN	12.40	75
CH_3CN	12.194 ± 0.005	77
C_2H_5CN	11.85	78
s-$C_3F_3N_3$	11.50	79
$(CH_3)_2CHCN$	11.49	80
$(CH_3)_3CCN$	11.11	80
2,4,5,6-$C_4F_4N_2$	10.75	81
3,4,5,6-$C_4F_4N_2$	10.70	81
2,3,5,6-$C_4F_4N_2$	10.34	81
NH_3	10.34 ± 0.07	82
C_5F_5N	10.08 ± 0.05	79
s-$C_3H_3N_3$	10.07 ± 0.05	83
2,4,5,6-$C_4H_4N_2$	9.73	81
2,3,5,6-$C_4H_4N_2$	9.63	81
3,4,5,6-$C_4H_4N_2$	9.31	81

perfluoroalkanenitriles, $R_FC{\equiv}N{-}XeF^+AsF_6^-$ (R_F = CF_3, C_2F_5, C_2F_7, C_6F_5, *n*-C_3F_7).[69,72] These adducts provide examples of xenon bonded to an sp-hybridized nitrogen atom and have been characterized solely in solution by low-temperature multi-NMR spectroscopy (^{129}Xe, ^{19}F, ^{14}N, ^{15}N, ^{13}C, ^{1}H) and in the solid state by Raman spectroscopy.

Adducts of XeF^+ with the perfluoropyridines, *n*-$CF_3C_5F_4N{-}XeF^+AsF_6^-$ (*n* = 2, 3, 4)[70,72] and $C_5F_5N{-}XeF^+AsF_6^-$,[70] the tetrafluorodiazines,[84] 3,4,5,6-$C_4F_4NN{-}XeF^+AsF_6^-$, 2,4,5,6-$C_4F_4NN{-}XeF^+AsF_6^-$, and 2,3,5,6-$C_4F_4NN{-}XeF^+AsF_6^-$, and *s*-trifluorotriazine, *s*-$C_3F_3N_2N{-}XeF^+AsF_6^-$ [72] have also been obtained from HF solution and by the reaction of XeF_2 with the protonated base in BrF_5 [see eqs (1.27) and (1.28)], and are stable only to -25 °C. The *s*-trifluorotriazine adduct, *s*-$C_3F_3N_2N{-}XeF^+AsF_6^-$,[72] has also been prepared by the neat reaction of *s*-$C_3F_3N_3$ with $XeF^+AsF_6^-$ for several hours at room temperature, followed by removal of excess *s*-$C_3F_3N_3$ under vacuum, and represents the only salt of the series which is stable indefinitely at room temperature. Low-temperature Raman and ^{129}Xe, ^{19}F, and ^{14}N NMR spectroscopic results for the perfluoropyridines, tetrafluorotriazines, and *s*-trifluorotriazine are consistent with planar aromatic cations in which the xenon atom is weakly coordinated to the aromatic ring through a formally sp^2-hybridized nitrogen atom. These cations were the first examples of a noble-gas bonded to aromatic rings.

Because of the thermal instability and air-sensitivity of crystals of nitrogen base adducts of XeF^+, accurate geometrical information from X-ray crystallography has not yet been obtained. However, along with vibrational data from low-temperature Raman

spectroscopy, the ^{129}Xe chemical shifts have served as a particularly sensitive probes in assessing the nature of the xenon-nitrogen bonds in this class of Xe(II) species, which exhibit trends similar to those observed for compounds of the form F–Xe–L and F–Xe–L^+ (L = terminal or bridging F, oxygen-containing ligand) (*vide infra*). That is, as the base strength of the nitrogen ligand groups increase, the effective electronegativity of the nitrogen atoms also decrease, resulting in a more covalent Xe–N bond, a more ionic Xe–F bond, and a more shielded ^{129}Xe nucleus.[12] These trends predict that the bonds between xenon and the formally sp^2-hybridized nitrogen atoms in the perfluoropyridines, tetrafluorotriazines, and s-trifluorotriazine adducts should be considerably more ionic than those observed in the nitriles and perfluoroalkanenitriles having formally sp-hybridized nitrogen atoms.

More recently, xenon-nitrogen bonded adduct cations have been prepared from the reaction of the XeF^+ cation with the inorganic bases, $N{\equiv}SF_3$ and F_5TeNH_2.[26,123] The ligand, $N{\equiv}SF_3$ (IP_1, 12.50 eV), was allowed to react with $XeF^+AsF_6^-$ in BrF_5 solvent at -60 °C giving $F_3S{\equiv}N{-}XeF^+AsF_6^-$, which has been fully characterized by ^{129}Xe, ^{14}N, and ^{19}F NMR spectroscopy [eq (1.29)].[14] Redissolving $F_3S{\equiv}N{-}XeF^+AsF_6^-$ in anhydrous HF

$$N{\equiv}SF_3 + XeF^+AsF_6^- \longrightarrow F_3S{\equiv}N{-}XeF^+AsF_6^- \qquad (1.29)$$

at -20 °C results in the addition of one molecule of HF across the S≡N bond to give $F_4S{=}N(H)XeF^+AsF_6^-$, followed by HF elimination to give the imide salt, $F_4S{=}NXe^+AsF_6^-$ [eq (1.30)].[14] A second solvolysis corresponding to the addition of HF

$$F_3S{\equiv}N{-}XeF^+AsF_6^- + HF \longrightarrow F_4S{=}N(H)XeF^+AsF_6^- \xrightarrow{-HF} F_4S{=}NXe^+AsF_6^- \quad (1.30)$$

across the S=N bond of $F_4S{=}NXe^+AsF_6^-$ gives $F_5SN(H)Xe^+AsF_6^-$ [eq (1.31)].[14] The

$$F_4S{=}NXe^+AsF_6^- + HF \longrightarrow F_5SN(H)Xe^+AsF_6^- \quad (1.31)$$

increase in shielding at the ^{129}Xe nucleus in this series of closely related cations parallels the decrease in electronegativity anticipated when the nitrogen lone pair hybridization changes from sp to sp^2 to sp^3 along the series $F_3S{\equiv}N{-}XeF^+$ (-1653 ppm), $F_4S{=}N{-}Xe^+$ (-2672 ppm), $F_5SN(H)Xe^+$ (-2886 ppm).

The tellurium analog of $F_5SN(H)Xe^+$, namely $F_5TeN(H)Xe^+AsF_6^-$, was prepared in HF and BrF_5 solvents at -45 and -50 °C, respectively [eq (1.32)], following protonation of the F_5TeNH_2 base in HF acidified with the Lewis fluoroacid, XeF^+ [eqs (1.33) and (1.34)].[26]

$$XeF^+AsF_6^- + HF \rightleftharpoons XeF_2 + H_2F^+AsF_6^- \quad (1.32)$$

$$F_5TeNH_2 + H_2F^+AsF_6^- \rightleftharpoons F_5TeNH_3^+AsF_6^- + HF \quad (1.33)$$

$$F_5TeNH_3^+AsF_6^- + XeF_2 \rightleftharpoons F_5TeN(H)Xe^+AsF_6^- + 2HF \quad (1.34)$$

The $F_5SN(H)Xe^+$ and $F_5TeN(H)Xe^+$ cations represent the first examples where xenon is bonded to formally sp^3-hybridized nitrogen, and are isolobal with the F_5ChOXe^+ cations (Ch = Se, Te). Both cations contain highly shielded ^{129}Xe environments ($F_5TeN(H)Xe^+$, -2841 ppm; $F_5SN(H)Xe^+$, -2886 pm) and are expected to contain among the most covalent Xe–N bonds.

In addition to nitrogen base (D) adducts of XeF^+, adducts of $XeOChF_5^+$ (Ch = Se,

Te), have also been prepared [eq (1.35)] and characterized by multi-NMR spectroscopy.

$$XeOChF_5^+AsF_6^- + D \longrightarrow D\text{–}XeOChF_5^+AsF_6^- \quad (1.35)$$

They include CH_3CN–$XeOTeF_5^+$, C_5F_5N–$XeOTeF_5^+$, *s*-$C_3F_3N_2N$–$XeOTeF_5^+$, and $F_3S{\equiv}N$–$XeOSeF_5^+$, and comprise the first examples of N–Xe–O linkages.[1] The *s*-$C_3F_3N_2N$–$XeOTeF_5^+AsF_6^-$ salt is the only example that has been prepared near room temperature by reaction of the neat compounds. The $XeOChF_5^+$ cation vigorously oxidizes the other nitrogen bases in the absence of a solvent.

The large number of successful syntheses and characterizations of novel Xe–N bonded XeF^+ adducts has recently prompted the preparation of adducts of the strong oxidant cation, KrF^+, the most powerful chemical oxidant known. However, the choice of nitrogen bases that are stable with respect to oxidation by KrF^+ is much more limited than for XeF^+, since the KrF^+ cation has an estimated electron affinity of 13.2 eV.[71] Consequently, KrF^+ adducts with nitrogen bases that are analogous to those of XeF^+ were prepared using the weaker oxidizer, KrF_2. The series of Kr–N bonded adducts that have been prepared include $HC{\equiv}N$–$KrF^+AsF_6^-$, by the reaction of $HC{\equiv}NH^+AsF_6^-$ with KrF_2 in BrF_5 or HF at -60 °C [eq (1.36)],[85] and $RC{\equiv}N$–$KrF^+AsF_6^-$ (R = H, CF_3, C_2F_5, *n*-C_3F_7),[72]

$$KrF_2 + HC{\equiv}NH^+AsF_6^- \xrightarrow{BrF_5 / HF} HC{\equiv}N\text{–}KrF^+AsF_6^- + HF \quad (1.36)$$

by the reaction of the adducts $R_FC{\equiv}NAsF_5$ (R_F = CF_3, C_2F_5, n-C_3F_7) with KrF_2 in BrF_5 solvent at *ca.* -60 °C [eq (1.37)]. These cations provide the first examples of Kr–N bonds

$$R_FC{\equiv}NAsF_5 + KrF_2 \xrightarrow{BrF_5} R_FC{\equiv}N\text{–}KrF^+AsF_6^- \quad (1.37)$$

and the first examples of krypton bonded to an element other than fluorine. The nitrile and perfluoroalkylnitrile adducts with KrF^+ have been characterized by low-temperature Raman and multi-NMR spectroscopy.[72,85] The salts are thermally less stable with respect to redox decomposition than the xenon(II) analogs, and those of $R_FC{\equiv}N{-}KrF^+AsF_6^-$ are thermally less stable than $HC{\equiv}N{-}KrF^+AsF_6^-$, preventing their isolation and characterization in the solid state. Since the ^{19}F NMR resonances for the $D{-}KrF^+$ adducts (91.1 – 99.4 ppm)[72,85] occur at higher frequencies than for KrF_2 (55.6 – 77.7 ppm),[86] which is in marked contrast with those of $D{-}XeF^+$ (-213.2 – -182.8 ppm),[68-70] which occur at lower frequencies than XeF_2 (-199.6 – -181.8 ppm),[31,59] it has been suggested that the Kr–N bonds are more covalent when compared with their Xe(II) analogs.

The nature of the Ng–N bonds (Ng = Xe, Kr) in $HC{\equiv}N{-}NgF^+AsF_6^-$ has been examined by several theoretical calculations at the SCF level using the theory of atoms in molecules.[88-95] The calculations, which complement the syntheses and spectroscopic measurements, showed that the ability of the NgF^+ cations (Ng = Xe, Kr) to act as Lewis acids and function as an electron-pair acceptors for the lone pair on a nitrogen base was shown by theory at the SCF level to be related to the presence of holes in the valence shell concentration of the Ng(II) atom which expose its core.[88] The mechanism of the formation of Ng–N bonds were described as similar to the formation of a hydrogen bond, in which mutual penetration of outer diffuse nonbonded densities of the Xe and N atoms is facilitated by their dipolar and quadrupolar polarizations. As a consequence, density is removed along the axis of approach yielding a final density in the interatomic surface that

is only slightly greater than the sum of the unperturbed densities. The calculated results are consistent with an ionic and a covalent component in the bonding of the NgF^+ cations with HCN. The Ng–N (Ng–F) bond lengths were calculated[88] to be 2.421 (1.904) Å and 2.307 (1.748) Å for Ng = Xe and Kr, respectively (cf. sum of van der Waals radii: Xe···N = 3.75 Å; Kr···N = 3.40 Å).[41,56,96] Additionally, the molecular structure and force field of $HC{\equiv}N{-}KrF^+AsF_6^-$, which was calculated at higher levels of theory, predicts that the cation will be linear.

SECTION B:

$OTeF_5$ DERIVATIVES OF THE PNICOGENS

A significant number of main-group derivatives of the pentafluorooxotellurate(VI), $OTeF_5$, group have been synthesized and structurally characterized since $HOTeF_5$ was first reported in 1964 by Engelbrecht and Sladky.[101] The $OTeF_5$ group is bulky, oxidatively resistant, very weakly basic, and highly electronegative. The usefulness of the $OTeF_5$ group stems from its ability to stabilize the same oxidation states as fluorine. Consequently, nearly all of the chemistry of the $OTeF_5$ compounds has been developed by analogy with the existing fluorides. However, unlike the fluorides, $OTeF_5$ derivatives virtually never participate in fluorine bridge formation and are stable with respect to fluoride abstraction. Additionally, because of their spherical form and very weak intermolecular forces, compounds with several $OTeF_5$ groups have a pronounced tendency to sublime.[41] The structure of the free $OTeF_5$ anion

is a distorted octahedron, with Te–O and average Te–F bond distances of 1.786(3) Å and 1.853(3) Å, respectively, and an average O–Te–F_{eq} bond angle of 95.2(2)°.[97]

There are several excellent reviews available which cover most of the developments in the field of $OTeF_5$ chemistry.[41,98-100] Due to the large number of $OTeF_5$ derivatives that have been isolated, only those related to the present work will be reviewed, namely $OTeF_5$ derivatives of the pnicogens (As, Sb, Bi) and Te.

The precursor for the synthesis of all $OTeF_5$ derivatives, $HOTeF_5$, is prepared by the reaction of $Te(OH)_6$ with a stoichiometric amount of HSO_3F according to equation (1.38), followed by separation from H_2SO_4 by fractional distillation.[101] The

$$Te(OH)_6 + 5HSO_3F \longrightarrow HOTeF_5 + 5H_2SO_4 \qquad (1.38)$$

pentafluoroorthotelluric acid, $HOTeF_5$, is a moderately strong monoprotic acid (pKa = 9.2)[102] and only decomposes above 310 °C to give HF and a number of Te(IV) and Te(VI) species, including $(TeOF_4)_n$, TeF_6, and TeF_4.

A common route to the preparation of $OTeF_5$ derivatives involves displacement of a hydrogen halide, as illustrated by equations (1.39) – (1.41) using BCl_3, XeF_2, and

$$3HOTeF_5 + BCl_3 \longrightarrow 3HCl + B(OTeF_5)_3 \qquad (1.39)$$

$$XeF_2 + HOTeF_5 \rightleftharpoons FXeOTeF_5 + HF \qquad (1.40)$$

$$FXeOTeF_5 + HOTeF_5 \rightleftharpoons Xe(OTeF_5)_2 + HF \qquad (1.41)$$

$FXeOTeF_5$, respectively.[49,54,103,104] The strong Lewis acid and inert solvent, $B(OTeF_5)_3$, prepared in reaction (1.39) is itself a useful $OTeF_5$ ligand transfer reagent and is employed in metathetical reactions with fluorides, leading to BF_3 elimination and

element-oxygen bond formation. Equations (1.42) – (1.45) illustrate this general

$$B(OTeF_5)_3 + AsF_3 \longrightarrow BF_3 + As(OTeF_5)_3 \quad (1.42)$$

$$4B(OTeF_5)_3 + 3XeF_4 \longrightarrow 4BF_3 + 3Xe(OTeF_5)_4 \quad (1.43)$$

$$3XeO_2F_2 + 2B(OTeF_5)_3 \longrightarrow 3O_2Xe(OTeF_5)_2 + 2BF_3 \quad (1.44)$$

$$3XeF_2 + 2B(OTeF_5)_3 \longrightarrow 3Xe(OTeF_5)_2 + 2BF_3 \quad (1.45)$$

preparative method using AsF_3, XeF_4, XeO_2F_2, and XeF_2, respectively, as examples.[41,105,106] The advantage of this method is that highly volatile BF_3 can be easily removed under vacuum from the reaction mixture. This method has also allowed the isolation of the $OTeF_5$ analogues of PnF_5 (Pn = As, Bi) by the reaction of PnF_5 with stoichiometric amounts of $B(OTeF_5)_3$ [eq (1.46)].[107] The synthesis of $As(OTeF_5)_5$ is

$$3PnF_5 + 5B(OTeF_5)_3 \longrightarrow 3Pn(OTeF_5)_5 + 5BF_3 \quad (1.46)$$

carried out at room temperature in anhydrous liquid SO_2, whereas $Bi(OTeF_5)_5$ has been synthesized in Freon-114 at 0 °C. Although both $As(OTeF_5)_5$ and $Bi(OTeF_5)_5$ are stable indefinitely at room temperature, all attempts to prepare pure $Sb(OTeF_5)_5$ have been unsuccessful and indicate that the compound is unstable above 0 °C.

The replacement of fluorine atoms with $OTeF_5$ groups generally leads to the stabilization of higher oxidation states and the stabilization is further enhanced when the high-valent oxide fluoride occurs as an anion. Recently, the high effective group electronegativity of the $OTeF_5$ group was demonstrated by the preparations of the weakly coordinating $B(OTeF_5)_4^-$,[108] $Pd(OTeF_5)_4^{2-}$,[109] $Ti(OTeF_5)_6^{2-}$,[110] $I(OTeF_5)_4^-$,[111] $Te(OTeF_5)_5^-$,[112] $Pn(OTeF_5)_6^-$ (Pn = As, Sb, Nb, Bi),[107,110] and *cis*-$ReO_2(OTeF_5)_4^-$ [102]

anions. The pnicogen anions, $Pn(OTeF_5)_6^-$ (Pn = As, Sb, Bi), which are of interest in this work, have been synthesized as their $N(CH_3)_4^+$ salts and structurally characterized by X-ray crystallography (Figure 1.8), ^{19}F, ^{125}Te, ^{75}As, $^{121,123}Sb$, and ^{209}Bi NMR spectroscopy, and Raman spectroscopy, and are non-labile on the NMR time scale in SO_2ClF and CH_3CN solvents.[107] Their formal (-1) charges are dispersed over 30 fluorines compared to six in their MF_6^- analogs, making them weakly coordinating. The syntheses of the $N(CH_3)_4^+As(OTeF_5)_6^-$ and $N(CH_3)_4^+Bi(OTeF_5)_6^-$ salts were accomplished by the direct interaction of $N(CH_3)_4^+OTeF_5^-$ with $Pn(OTeF_5)_5$ (Pn = As, Bi) according to equation (1.47).[107] The instability of $Sb(OTeF_5)_5$ makes it inconvenient to use this compound for

$$Pn(OTeF_5)_5 + N(CH_3)_4^+OTeF_5^- \longrightarrow N(CH_3)_4^+Pn(OTeF_5)_6^- \qquad (1.47)$$

the syntheses of $Sb(OTeF_5)_6^-$ salts. Rather, the method of choice for the synthesis of this anion involves the reaction of $NR_4^+OTeF_5^-$ (R = CH_3, CH_2CH_3) with $Sb(OTeF_5)_3$ to give $NR_4^+Sb(OTeF_5)_4^-$ [eq (1.48)], which is then oxidized to $NR_4^+Sb(OTeF_5)_6^-$ using an equimolar amount of $Xe(OTeF_5)_2$ [eq (1.49)].[107,110]

$$NR_4^+OTeF_5^- + Sb(OTeF_5)_3 \longrightarrow NR_4^+Sb(OTeF_5)_4^- \qquad (1.48)$$

$$NR_4^+Sb(OTeF_5)_4^- + Xe(OTeF_5)_2 \longrightarrow NR_4^+Sb(OTeF_5)_6^- + Xe \qquad (1.49)$$

By virtue of the weakly coordinating nature of the $Pn(OTeF_5)_6^-$ anions, they have contributed to the preparation and stabilization of novel and unusual species. Recently, the $Sb(OTeF_5)_6^-$ and $As(OTeF_5)_6^-$ anions have been used to stabilize the previously unreported SbX_4^+ (X = Br, Cl)[114] and $BiCl_4^+$ cations, respectively [eqs (1.50) and (1.51)].

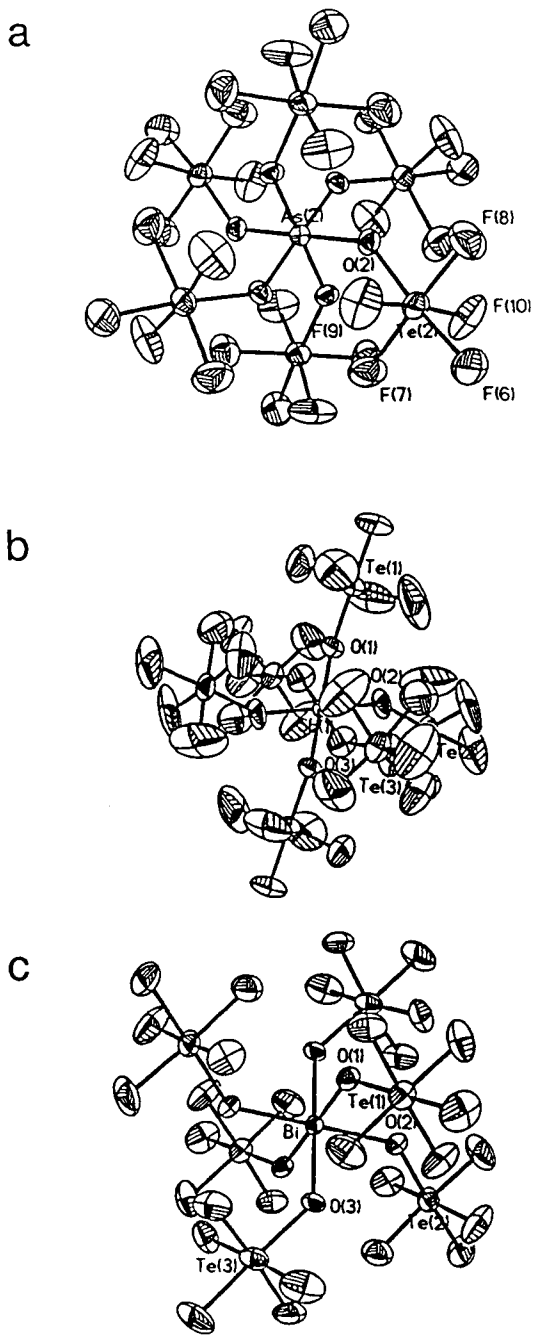

Figure 1.8 X-ray crystal structures of (a) $N(CH_3)_4^+As(OTeF_5)_6^-$, (b) $N(CH_3)_4^+Sb(OTeF_5)_6^-$, and (c) $N(CH_3)_4^+Bi(OTeF_5)_6^-$.[107] For clarity, the $N(CH_3)_4^+$ cations are not shown.

$$2Sb(OTeF_5)_3 + 2X_2 \longrightarrow SbX_4^+Sb(OTeF_5)_6^- \quad (1.50)$$

$$BiCl_3 + ClOTeF_5 + As(OTeF_5)_5 \longrightarrow BiCl_4^+As(OTeF_5)_6^- \quad (1.51)$$

Owing to the weakly coordinating nature of the $Sb(OTeF_5)_6^-$ anion, the salts of SbX_4^+ are very soluble in SO_2ClF and their X-ray crystal structures exhibit very weak anion-cation interactions that are significantly weaker than in their PnF_6^- analogs.

Recently, tetrakis- and pentakis-$OTeF_5$ derivatives of TeF_4 and TeF_5^-, respectively, were synthesized and characterized by X-ray crystallography (Figure 1.9), Raman spectroscopy, and by ^{19}F and ^{125}Te NMR spectroscopy.[112,115] The $Te(OTeF_5)_5^-$ anion was prepared by the interaction of $N(CH_3)_4^+OTeF_5^-$ with $Te(OTeF_5)_4$ at ambient temperature in SO_2ClF according to equation (1.52).[112] The X-ray crystal structure of the

$$Te(OTeF_5)_4 + N(CH_3)_4^+OTeF_5^- \xrightarrow{SO_2ClF\,/\,25\,^\circ C} N(CH_3)_4^+Te(OTeF_5)_5^- \quad (1.52)$$

$Te(OTeF_5)_5^-$ anion consists of the central Te^{IV} atom bonded to five $OTeF_5$ groups, such that the geometry may be described as pseudo-octahedral. The structure of $Te(OTeF_5)_4$ has been shown by X-ray crystallography to be a disphenoid with an AX_4E VSEPR geometry in which a lone electron pair and two $OTeF_5$ groups occupy the equatorial plane and two $OTeF_5$ groups occupy the axial positions of a trigonal bipyramid.[112] The structure provides one of the few known examples of an $OTeF_5$ group that bridges through its fluorines. That is, two secondary $Te^{IV}\cdots F$ contacts exist with two nearest neighbor $Te(OTeF_5)_4$ molecules giving rise to a chain structure. The $Te(OTeF_5)_4$ molecule was shown to be fluxional on the NMR time scale. The exchange observed was consistent with the axial and equatorial $OTeF_5$ groups undergoing rapid intramolecular

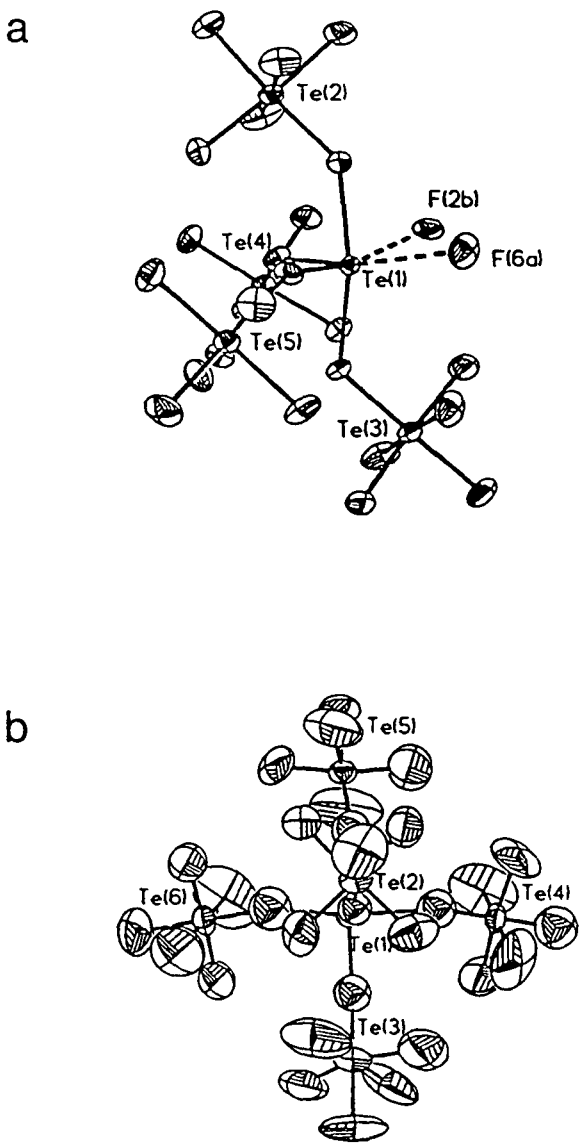

Figure 1.9 X-ray crystal structures of (a) $Te(OTeF_5)_5^-$ and (b) $Te(OTeF_5)_4$.[112]

rearrangement by means of a Berry pseudorotation. For pentacoordinate AX_4E and AX_5 systems, these type of rearrangements are common and have been observed in the fluoride species, PF_4^-,[116] SF_4,[117-119] PF_5,[120] and PF_3X_2 (X = Br, Cl).[121] The barrier for the two-site intramolecular exchange in these complexes were sufficiently high to reduce the exchange to a frequency that was low on the NMR time scale at low temperatures to observe separate axial and equatorial environments. The activation energy barriers ($\Delta G^{\ddagger}$) to intramolecular exchange in these compounds have been derived from variable-temperature NMR spectroscopy. Until recently, however, the only known pseudo-trigonal bipyramidal main-group $OTeF_5$ derivative whose intramolecular exchange barrier has been determined is $Te(OTeF_5)_4$ (29.6 $kJmol^{-1}$).[115]

SECTION C:

PURPOSE AND GENERAL SYNTHETIC STRATEGIES UNDERPINNING THE PRESENT WORK

The overall purpose of the present work was to extend the chemistry of Xe(II), Sb(III), and As(III), and, more specifically, to use X-ray crystallography to provide a description of the structures of XeF^+ adducts with nitrogen bases, to use both X-ray crystallography and Raman spectroscopy to characterize some potentially useful compounds containing Xe–O bonds, and to use X-ray crystallography, Raman and multi-NMR spectroscopy to characterize novel $OTeF_5$ derivatives of As(III) and Sb(III). Structural information obtained from X-ray crystallography of some Xe–N and Xe–O

bonded species were compared with previously acquired NMR and Raman spectroscopic data and with local density functional theory (LDFT/DZVP) calculations.

The synthetic route to the Xe–N bonded systems in the present work was through the interaction of $XeF^+AsF_6^-$ with selected nitrogen bases in anhydrous HF, or reaction of the protonated base with XeF_2 in BrF_5 solvent (*vide supra*). In view of the powerful oxidizing strength of XeF^+, a series of organic, perfluoro-organic, and inorganic nitrogen bases were selected having varying first adiabatic ionization potentials (IP_1) that were greater than or equal to the estimated electron affinity of XeF^+ (10.9 eV). Only those AsF_6^- salts of cations containing Xe–N bonds that had already been successfully isolated and characterized by Raman and NMR spectroscopy were undertaken in this work.

The thermal instability and air-sensitivity of Xe–N bonded adduct cations of XeF^+ have, until now, limited the use of X-ray crystallography for the structural characterization of these compounds. Prior to this work, it has only been possible to hypothesize about the bonding in these compounds based on Raman and multi-NMR spectroscopic data. Recent developments in this laboratory in the low-temperature growing, mounting, and structural data acquisition has now allowed the structures of these compounds to be well-characterized. A systematic comparison of the structures with the spectroscopic data provided significant information relating to the ligand base strengths, electronegativities, and %s characters of the valence hybrid orbitals required to stabilize the compounds.

Accurate bond lengths and angles obtained from X-ray crystal structures of the

well-known $OChF_5$ (Ch = Te, Se) derivatives of the XeF_2 and XeF^+ analogs are important as they serve as comparisons with other $OTeF_5$ derivatives and aid in evaluating the relative electronegativities of F, $OTeF_5$, and $OSeF_5$; a subject that had been controversial for some time. Although the $Xe(OTeF_5)_2$ and $Xe(OSeF_5)_2$ structures have previously been reported, no structural details were given for $Xe(OTeF_5)_2$ [50] and those reported for $Xe(OSeF_5)_2$ [51] are clearly affected by a three-fold orientational disorder of O and F atoms.

The purpose of the present work has also been to extend the known chemistry of main-group $OTeF_5$ derivatives by the syntheses and detailed structural characterizations by ^{19}F and ^{125}Te NMR spectroscopy and by Raman spectroscopy of the novel pnicogen anions, $Pn(OTeF_5)_4^-$ (Pn = Sb, As), as their $N(CH_3)_4^+$ and $N(CH_2CH_3)_4^+$ salts. These anions, which contain fewer $OTeF_5$ groups than the previously characterized weakly coordinating $Pn(OTeF_5)_6^-$ anions,[101] are expected to have pseudo-trigonal bipyramidal AX_4E VSEPR geometries with two equatorial and two axial $OTeF_5$ ligands that exchange in solution. Sufficient lability of the anions on the NMR time scale would allow activation energy barriers ($\Delta G^{\ddagger}$) to intramolecular exchange to be derived from variable-temperature NMR spectroscopy and compared with that obtained for the isoelectronic $Te(OTeF_5)_4$ molecule (29.6 $kJmol^{-1}$).[115]

CHAPTER 2

EXPERIMENTAL SECTION

SYNTHETIC TECHNIQUES

Vacuum and Inert Atmosphere Systems

Because the compounds synthesized and described in the present work are air-sensitive, all preparative work was carried out under rigorously anhydrous conditions by manipulation of materials in a drybox, on a glass vacuum line system, or in a dry nitrogen filled glove bag. The two-station nitrogen atmosphere drybox (Vacuum Atmospheres Model DLX) used to handle non-volatile materials had moisture and oxygen levels less than 0.1 ppm. Apparatus and materials were evacuated in the drybox port three times prior to entry into the drybox, with each evacuation cycle lasting at least 20 min. In order to dissipate electrostatic charges arising from the dry environment of the drybox, samples were handled, when necessary, in the vicinity of an α-source consisting of a silver strip impregnated with $^{241}Am_2O_3$ (Amersham) having an activity of 2.4 mCi = 88.8 MBq. Compounds were weighed inside the drybox in close proximity to the α-source on a Mettler AE 163 electronic balance equipped with a printer external to the drybox. Preparative work requiring low temperatures was carried out either in a glass cryowell mounted on the bottom of the drybox or in a Dewar filled with 4.5-mm copper plated steel spheres (air rifle BB's) which had been previously cooled in the cryowell for several

hours. The temperature was monitored by placing a thermocouple wire in the Dewar containing the cooled metal spheres and reading the temperature on a Fluke 52 K/J readout outside the drybox.

Volatile materials that were non-corrosive to glass in the absence of water (*i.e.*, CH_3CN, $(CH_3)_3CC{\equiv}N$, SO_2ClF) were handled on a grease-free Pyrex glass vacuum line equipped with 6-mm J. Young Teflon/glass stopcocks and glass liquid nitrogen traps (Figure 2.1). Pressures inside the glass manifold were monitored using a mercury manometer. When not in use, the vacuum line was maintained under dynamic vacuum with the mercury manometer isolated from the dynamic vacuum of the manifold.

Volatile materials which attack glass (*i.e.*, HF and BrF_5) were handled on a metal vacuum line constructed from nickel and 316 stainless steel valves and fittings (Autoclave Engineers, Inc.; Figure 2.2). Pressures were measured at ambient temperatures on the metal vacuum line using an MKS Model PDR-5B power supply and digital readout in conjunction with pressure transducers (effective ranges, 0 – 1000 Torr and 0 – 1 Torr) having inert wetted surfaces constructed of Inconel. The pressures were accurate to ± 0.5% of scale.

Vacuum on the glass (*ca.* 10^{-4} to 10^{-5} Torr) and metal lines (*ca.* 10^{-3} to 10^{-4} Torr) was attained by using Edwards two stage E2M8 direct drive vacuum pumps. Two vacuum pumps were used on the metal vacuum line; one, a roughing pump, was connected to a volatile fluoride trap consisting of a copper tube (*ca.* 60-cm length, 15-cm diameter) packed with soda lime absorbent (Fisher Scientific, 4-8 mesh). Removal and

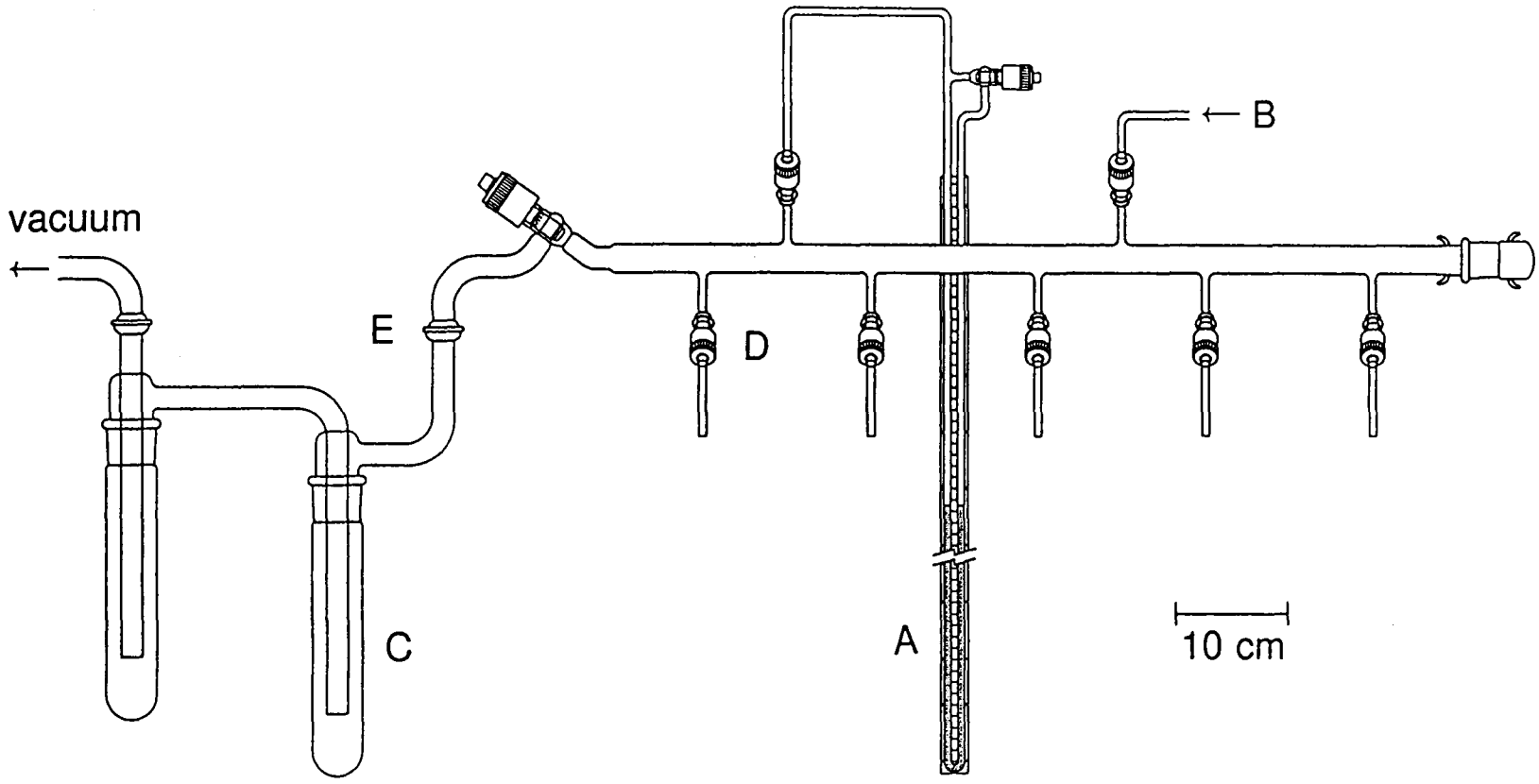

Figure 2.1 Glass vacuum line system; (A) mercury manometer, (B) dry nitrogen inlet, (C) liquid nitrogen trap, (D) 6-mm J. Young PTFE/glass stopcock, (E) ball and socket joint.

Figure 2.2 Metal vacuum line system; (A) outlet to liquid nitrogen and charcoal traps followed by a two stage direct drive rotary vacuum pump (Edwards, E2M8) - hard vacuum, (B) outlet to soda lime and liquid nitrogen traps followed by a two stage direct drive rotary vacuum pump (Edwards, E2M8) - rough vacuum, (C) dry nitrogen inlet, (D) fluorine inlet, (E) MKS Model PDR-5B pressure transducers (0 – 1000 Torr), (F) MKS Model PDR-5B pressure transducer (0 – 1 Torr), (G) pressure gauge (0 – 1500 Torr), (H) $^{3}/_{8}$-in. 316 stainless steel high pressure valve (Autoclave Engineers, 30BM6071), (I) 316 stainless steel cross, (J) 316 stainless steel T-piece, (K) 316 stainless steel L-piece, (L) nickel connectors, (M) ¼-in. o.d., $^{1}/_{8}$-in. i.d. nickel tube.

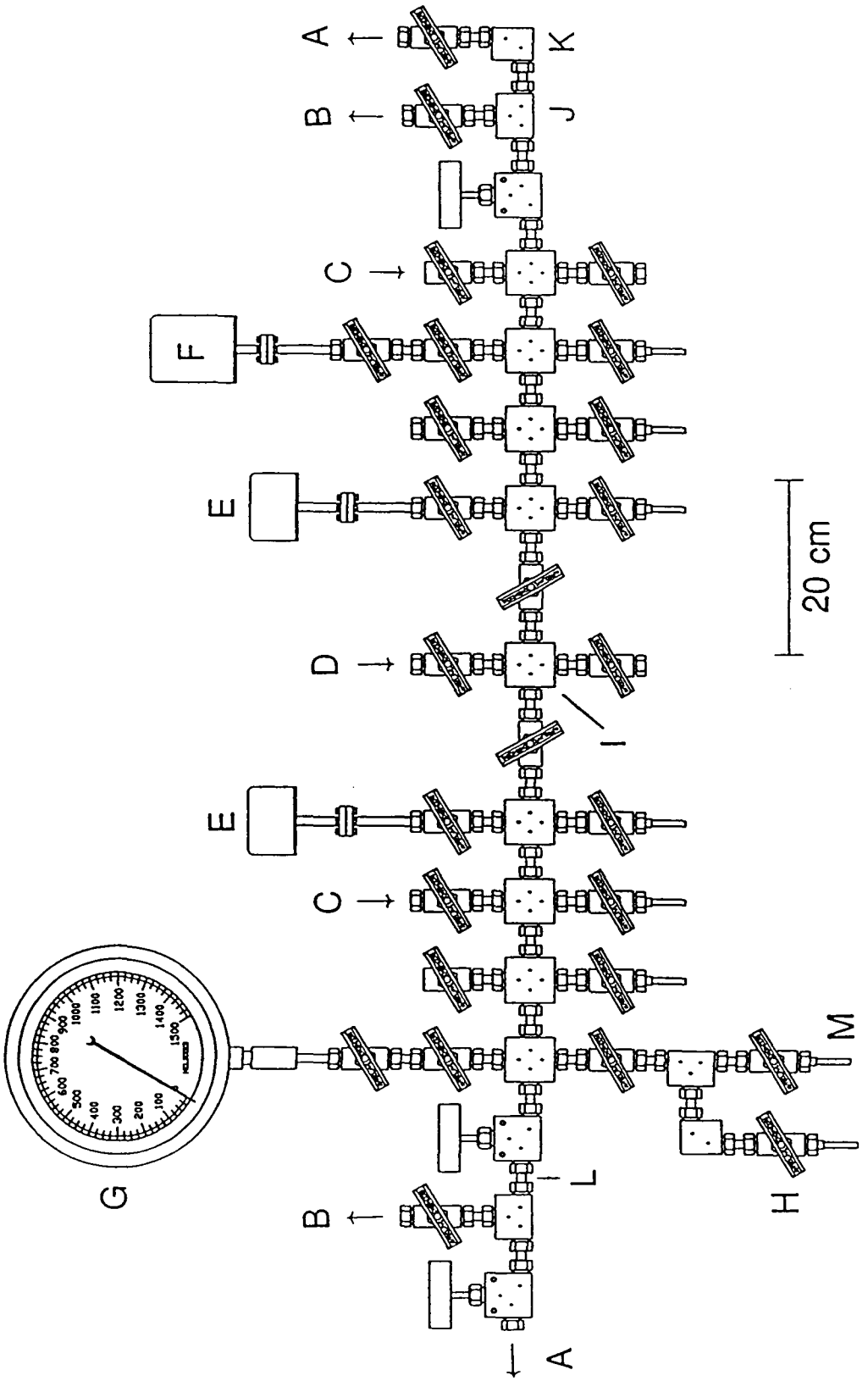
A
B
C
D
E
F
G
H
I
J
K
L
M
20 cm

disposal of volatile reactive fluorinated compounds was accomplished by pumping through and entrapment on the bed of soda lime followed by trapping of the displaced volatiles, CO_2 and H_2O, in a glass liquid nitrogen trap. The second vacuum pump provided the high vacuum source for the manifold and was trapped in a glass liquid nitrogen trap.

Preparative Apparatus and Spectroscopic Sample Vessels

All synthetic procedures were performed in apparatus constructed from nickel, glass, Kel-F, or FEP. Glass reaction vessels were joined to Young valves through ¼-in. o.d. lengths of glass tubing fused to the valve which, in turn, was joined to the reaction vessel using ¼-in. stainless steel Cajon Ultra-Torr unions fitted with Viton O-rings. All reaction vessels were dried under dynamic vacuum for a minimum of 10 h prior to use. Sample preparations involving materials which attack glass were carried out in reactors constructed of ¼-in. or ½-in. o.d. FEP tubing (Furon) which were heat-sealed at one end and heat-flared (45° SAE) at the other. The tubes were then attached to Kel-F valves encased in aluminum housings by means of brass flare nuts (Figure 2.3). All vessels built in this manner were dried by initially pumping on a glass vacuum line for at least 10 h followed by passivation on a metal vacuum line with *ca.* 1000 Torr of fluorine for *ca.* 8 h. Volatiles were then removed under vacuum and vessels were pressurized with 900 - 1000 Torr of dry nitrogen gas.

Nuclear magnetic resonance (NMR) spectra were recorded on samples prepared in 5-mm o.d. medium-wall precision glass NMR tubes (Wilmad) fused to ¼-in.

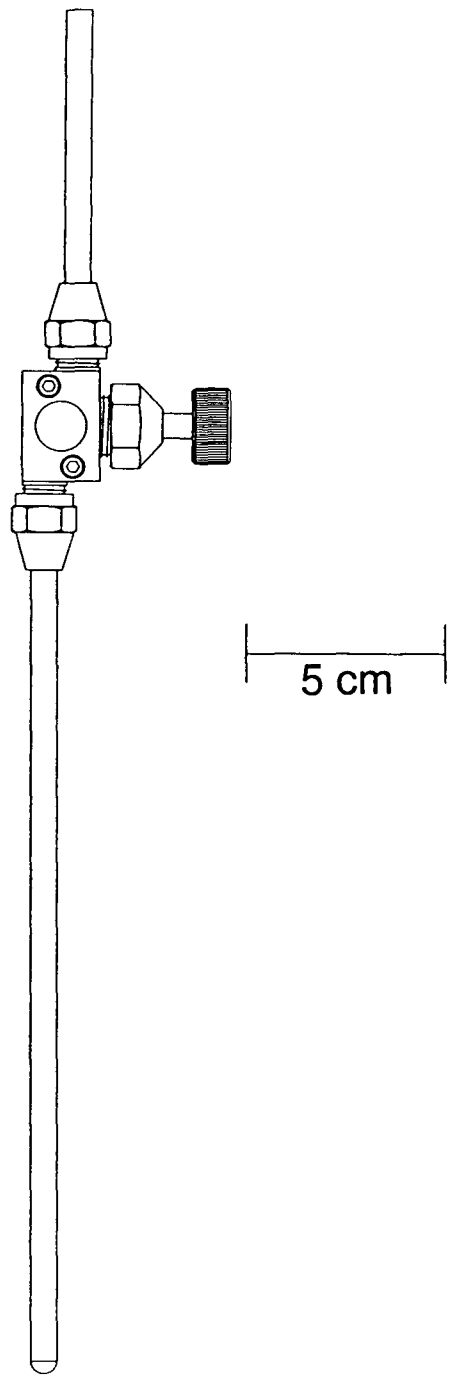

Figure 2.3 FEP reaction tube (¼-in. o.d.) equipped with a Kel-F valve.

o.d. glass tubing. The ¼-in. o.d. end of the glass tube was attached to a 4-mm J. Young glass valve equipped with a PTFE barrel and dried overnight under dynamic vacuum. After the appropriate materials were loaded into each tube in a drybox, the tubes were flame sealed below the valve with an oxygen-natural gas torch.

Raman spectra of solids were recorded on samples in Pyrex melting point capillaries. Prior to use, the melting point capillaries were heated under dynamic vacuum for 24 h at 200 °C and then stored in a drybox where they were loaded with the appropriate materials. The ends of the loaded melting point capillaries were temporarily plugged with Kel-F grease before removal from the drybox. The capillaries were then permanently sealed with a miniature oxygen-natural gas torch. Raman spectra of liquids were recorded on samples in 5-mm o.d. medium-walled glass NMR tubes fused to ¼-in. o.d. glass tubing and connected to a 4-mm J. Young glass valve equipped with a PTFE barrel. After the tubes were dried under dynamic vacuum overnight, the solid samples were loaded into the dry tubes in the drybox. The appropriate solvents were condensed onto the solids and the tubes were flame-sealed below the valve.

Low-Temperature Crystal Growth for X-ray Crystallography

Crystals were grown slowly in ¼-in. o.d. FEP h- or T-shaped reactors (Figure 2.4) with arm A or C, respectively, containing the dissolved compound, inserted into the open end of a horizontally mounted unsilvered glass Dewar jacket (Figures 2.5). The Dewar was maintained at the appropriate temperature by flowing cold, dry nitrogen gas along the outside of the FEP tube. The cold N_2 flow was derived by submersion of a nichrome

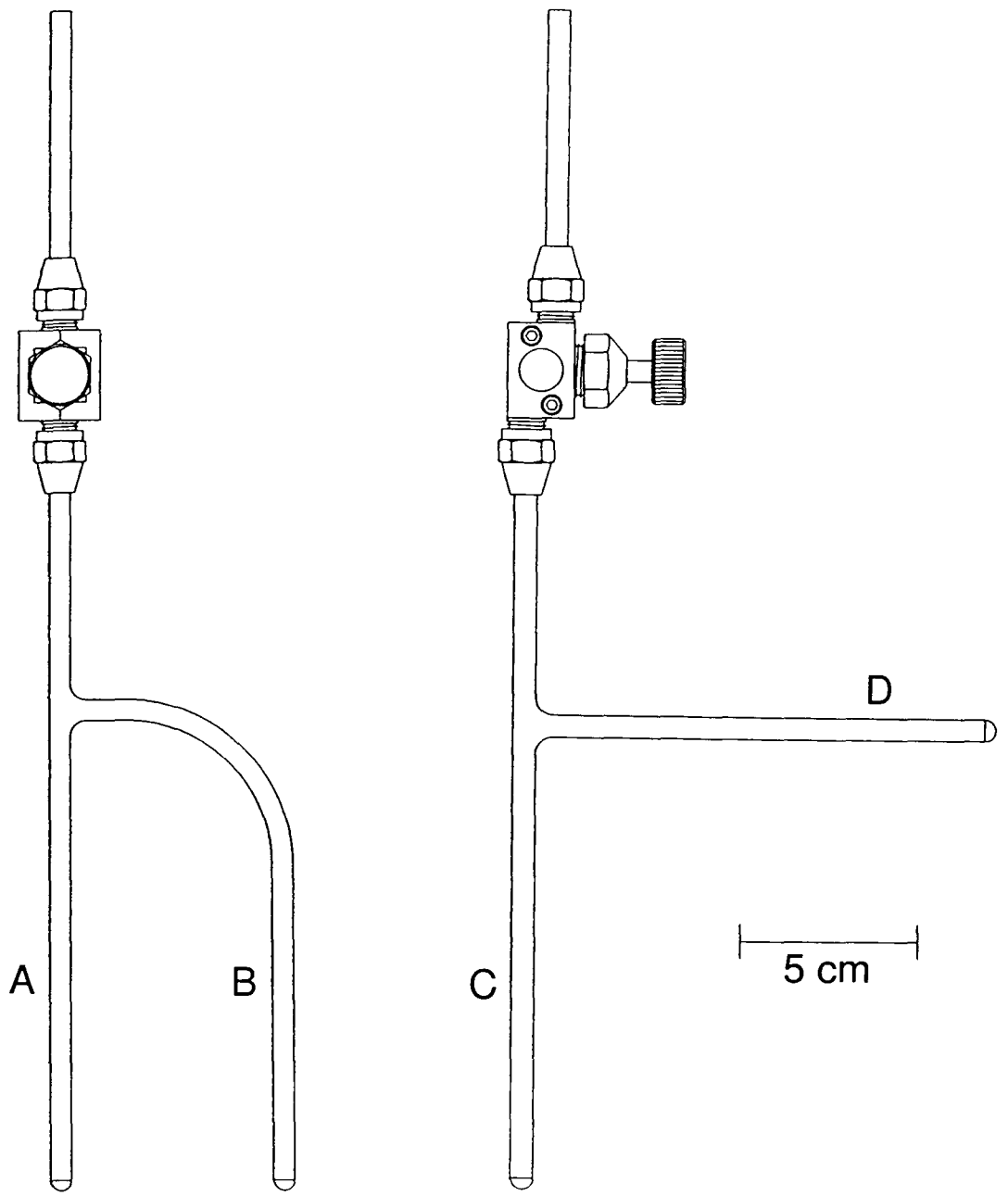

Figure 2.4 FEP h-shaped and T-shaped reactors (¼-in. o.d.) equipped with Kel-F valves; (A) arm A, (B) arm B, (C) arm C, (D) arm D.

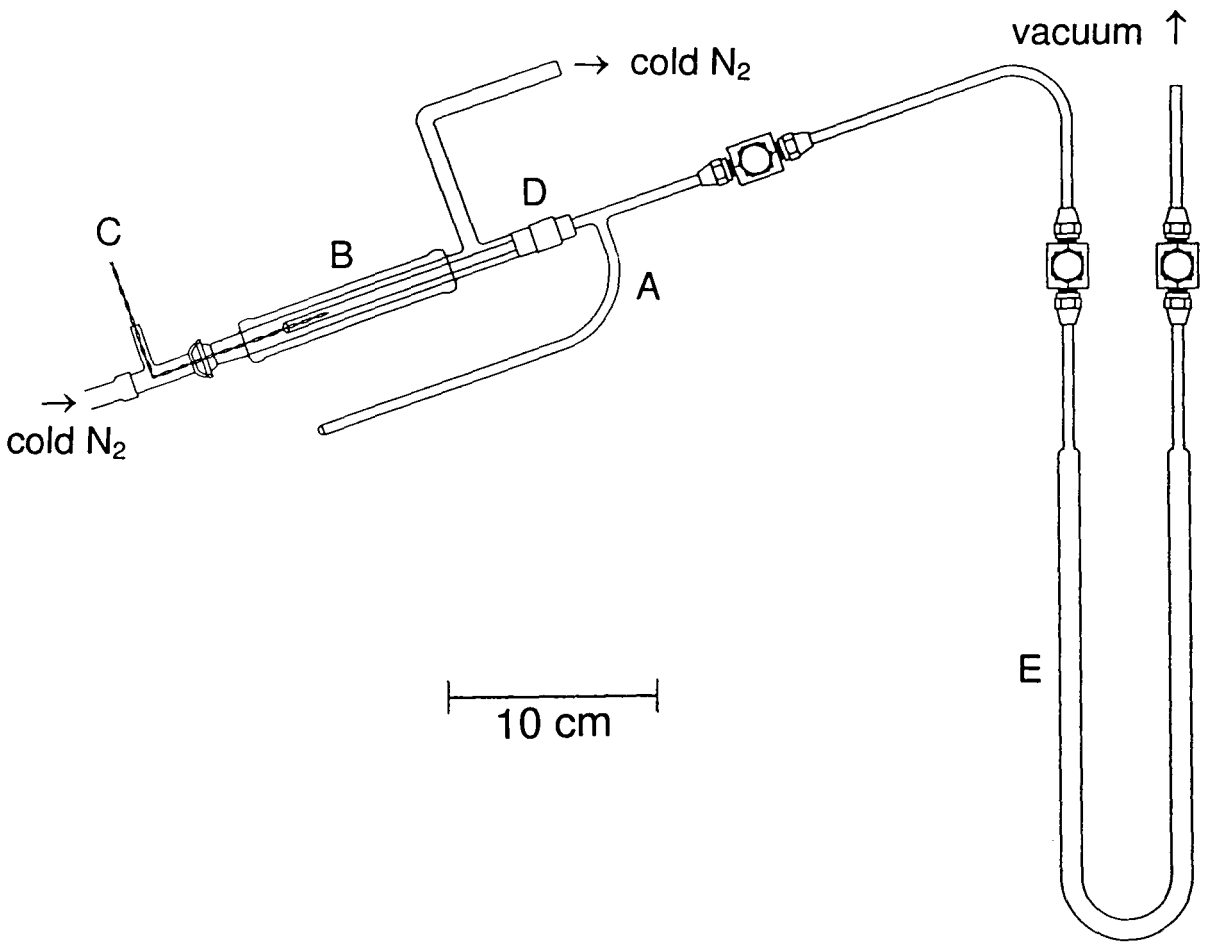

Figure 2.5 Low-temperature crystal growing apparatus; (A) ¼-in. o.d. FEP h-shaped reactor equipped with a Kel-F valve, (B) unsilvered glass Dewar jacket, (C) copper-constantan thermocouple, (D) rubber neoprene adapter, (E) ¾-in. o.d. FEP U-trap equipped with Kel-F valves and cooled to -196 °C.

resistor in a 50-L Dewar of liquid N_2. The flow was directed to the crystal growing Dewar through insulated rubber tubing and regulated by means of a Variac. The temperature near the FEP tube was measured with a copper-constantan thermocouple (error ± 0.8 °C). The solvent and temperature used for the crystal growth of each compound are given in Table 2.1. Once the crystals were grown, the supernatant was decanted into side-arm B (h-reactor) or D (T-reactor) which was then heat-sealed using a small diameter nichrome wire resistance furnace. The remaining arm, A or C, containing the crystals was pumped under high vacuum using a glass vacuum line equipped through an intermediate ¾-in. o.d. FEP U-trap cooled to -196 °C to remove any remaining supernatant. The reactor was pressurized to *ca.* 1 atm with dry nitrogen and maintained at *ca.* -78 °C (0 °C for $Xe(OSeF_5)_2$) until the crystals could be mounted on the X-ray diffractometer.

Low-Temperature Mounting of Single Crystals for X-ray Crystallography

A low-temperature crystal mounting technique was utilized for thermally unstable and/or moisture-sensitive crystals. Each FEP reactor containing crystals was cut open below the Kel-F valve at *ca.* -78 °C under a flow of dry nitrogen. The crystals were then quickly trasferred from the chilled tube onto an aluminum trough cooled by passing a flow of dry nitrogen through a 5-L Dewar of liquid nitrogen (Figure 2.6). The temperature of the trough, given in Table 2.1 for each compound, had been previously measured with a copper-constantan thermocouple inserted midway into the steam *ca.* 2-mm above the trough. Each crystal was selected under a stereomicroscope and mounted

Table 2.1 Conditions for Low-Temperature Crystal Growing and Crystal Mounting onto the X-Ray Diffractometer.

Compound [a]	Temp. for Crystal Growth (°C)	Solvent	Mounting Temp. (°C) [b]	Oil Used to Mount Crystal	Temp. of Data Acquisition (°C)
$HC{\equiv}N{-}XeF^{+}AsF_6^{-}$	-15 – (-35)	HF	-115	Fomblin Z-25	-122
$HC{\equiv}NH^{+}AsF_6^{-}$	-8 – (-20)	HF	-120	Fomblin Z-15	-122
$CH_3C{\equiv}N{-}XeF^{+}AsF_6^{-}$ (A)	-43 – (-78)	HF	-120	—	—
(B)	-40 – (-68)	HF	-120	Fomblin Z-25	-125
$(CH_3)_3CC{\equiv}N{-}XeF^{+}AsF_6^{-}{\cdot}HF$	-46 – (-55)	HF	-115	Fomblin Z-25	-127
$Xe_2F_3^{+}AsF_6^{-}$	-23 – (-45)	HF	-115	Fomblin Z-25	-127
$s\text{-}C_3F_3N_2N{-}XeF^{+}AsF_6^{-}{\cdot}2.5BrF_5$	-40 – (-50)	BrF_5	-120	Fomblin Z-15	-122
$C_5F_5N{-}XeF^{+}AsF_6^{-}{\cdot}2.5BrF_5$	-54 – (-57)	BrF_5	-122	Fomblin Z-15	-122
$F_5TeNH_3^{+}AsF_6^{-}$	-40 – (-48)	HF	-109	Fomblin Z-15	-128
$F_5TeN(H)Xe^{+}AsF_6^{-}$	-53 – (-55)	HF	-109	Fomblin Z-15	-128
F_5TeNH_2 (B)	*ca.* 30	—	-128	Fomblin Z-15	—
(D)	*ca.* -70	SO_2	-120	Fomblin Z-25	-113
$XeOSeF_5^{+}AsF_6^{-}$ (C)	*ca.* 30	—	-120	Fomblin Z-15	-113

Table 2.1 (continued)

$Xe(OTeF_5)_2$ (B)	*ca.* -30	Freon-114	-120	Fomblin Z-25	-127
$Xe(OSeF_5)_2$ (B)	*ca.* –10	Freon-114	-43	Fomblin YR-1500	-45

[a] Crystals were grown as described in the section **Preparation and Crystal Growth of Xe–N and Xe–O Bonded Compounds**.
[b] The temperature of the trough was measured at the midpoint and *ca.* 2-mm above the trough floor.

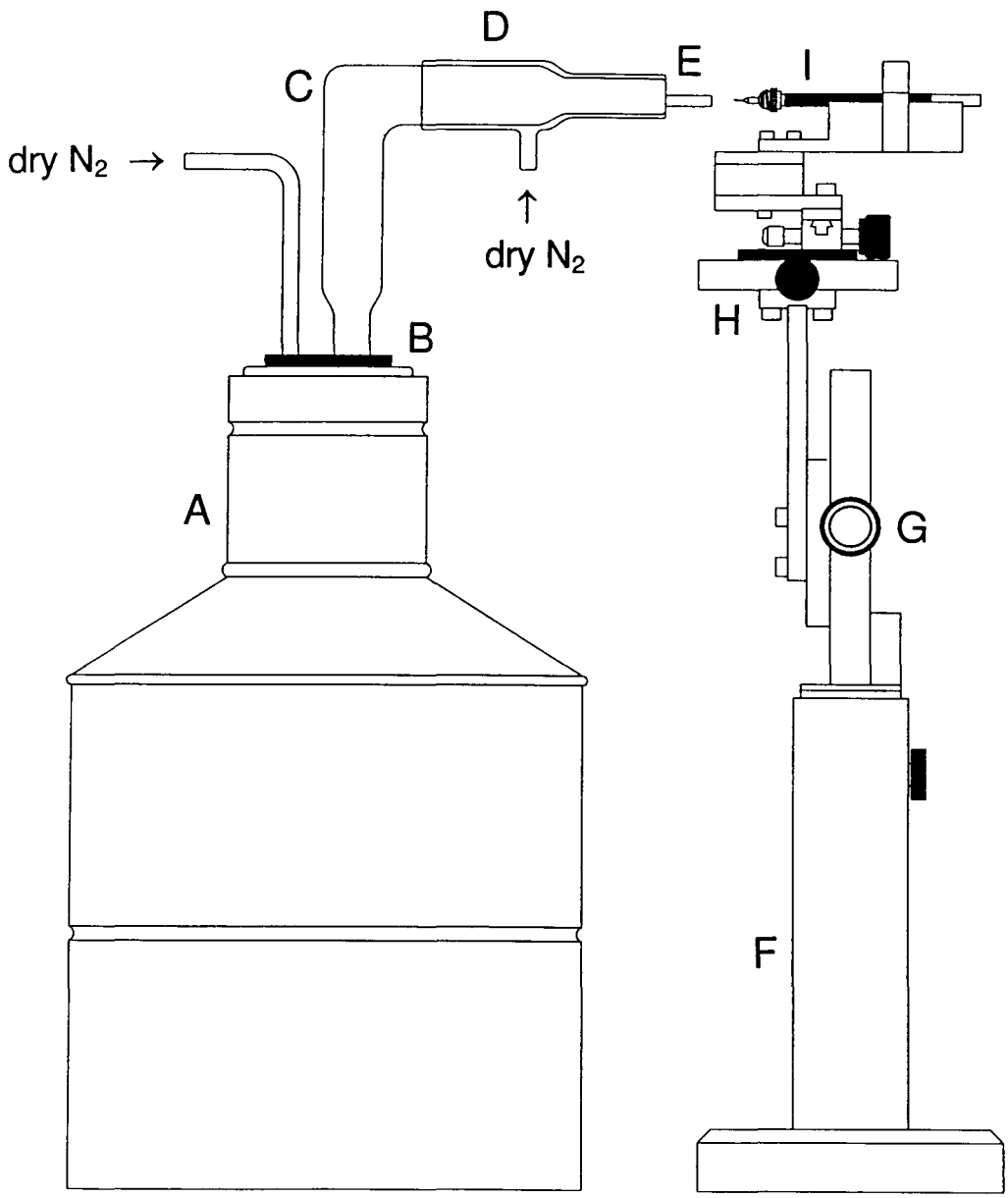

Figure 2.6 Low-temperature crystal mounting apparatus; (A) 5-L silvered glass Dewar enclosed containing liquid N_2 and enclosed in a metal container, (B) two-hole rubber stopper, (C) silvered glass Dewar, (D) glass jacket, (E) metal trough chilled by cold N_2 flow, (F) metal stand, (G) z-adjustable dial, (H) xy-adjustable dial, (I) glass fibre attached to metallic pin on a wand.

on a glass fibre using an inert perfluorinated polyether. The glass fibre had previously been attached using epoxy to a metallic pin that was, in turn, magnetically mounted on a wand. The perfluorinated polyethers used to attach crystals to the glass fibres were chosen based on their pour points and the trough temperature (Table 2.2). The polyethers selected for crystal mounting were sufficiently viscous to adhere to the crystal, engulf it, and freeze quickly thereafter. The attached crystal was quickly (*ca.* < 30 s) transferred to the goniometer head of the X-ray instrument using a cryotong, which had been chilled by liquid nitrogen for *ca.* 5 min prior to use, and attached by means of a magnetic interface. Nitrile gloves and a respirator were worn as precautions during crystal mounting of $HC{\equiv}N{-}XeF^{+}AsF_6^{-}$ and $HCNH^{+}AsF_6^{-}$ to avoid accidental exposure/inhalation of HCN that would result should the crystals be accidentally hydrolyzed in the atmosphere. The antidote, amylnitrite, was close at hand in the event of an incident.

PREPARATION AND PURIFICATION OF STARTING MATERIALS

The physical properties of the solvents commonly used in this work are listed in Table 2.3.

Fluorine

Fluorine, 98% containing *ca.* 0.2% HF, (Air Products and Chemicals, Inc.) was used extensively during the course of this work for the drying and seasoning of fluoro-plastic apparatus. None of the contaminants interfere with the chemistry described in this work. Consequently, fluorine was used without further purification.

Table 2.2 Physical Properties of Oils for Low-Temperature Crystal Mounting.

Oil	Pour Point (°C)	Approx. Freezing Point (°C)	Best Mounting Temp. (°C)
Fomblin YR-1800	-20	-38	-32
Fomblin Y-1500	-25	-42	-38 – (42)
Fomblin Y-45	-30	-50	*ca.* -45
Fomblin M-100	*ca.* -35		-80
Fomblin Z-60	-60		> -110
Fomblin Z-25	-66	-110	*ca.* -90 – (-100)
Fomblin Z-15	-80		*ca.* -110

Table 2.3 Some Physical Properties of the Solvents Used

Solvent	Melting Point (°C)	Boiling Point (°C)	Vapour Pressure at 25 °C (Torr)	Dielectric Constant (ε_r)
CF_2ClCF_2Cl	-94.0	3.8	218	2.5
CH_2Cl_2	-95.1	40.0	58.2	51.0
HCN	-13.4	26.0	98.8	
CH_3CN	-43.8	81.6	11.9	36.6
CH_3CH_2CN	-92.8	97.1	6.14	29.7
$(CH_3)_3CC{\equiv}N$	15.0	106.1	14.8	21.1
s-$C_3F_3N_3$	-38.0	-72.0		
SO_2ClF	-124.7	7.1		
SO_2	-72.7	-10	359	16.3
HF	-83.4	19.5	123	83.6
BrF_5	-61.3	40.5		99.6

HF, BrF_5, SO_2, and SO_2ClF Solvents

Anhydrous hydrogen fluoride, HF, (Harshaw Chemical Co., 47%) was purified by treatment with 5 atm of F_2 gas in a nickel can for a period of 1 month, converting residual water to HF and O_2 gas. The anhydrous HF was then vacuum distilled into a dry Kel-F storage vessel equipped with a Kel-F valve and stored at room temperature until used. Hydrogen fluoride was transferred into reaction vessels by vacuum distillation on a metal vacuum line through connections constructed of PTFE, Kel-F, and FEP as shown in Figure 2.7.

Bromine pentafluoride, BrF_5, (Ozark-Mahoning Co.) was purified as described earlier,[108] and stored over dry KF in a ¾-in. FEP storage tube equipped with a Kel-F valve. Bromine pentafluoride solvent was stored under 500 Torr F_2 and ½-atm dry N_2 in solid dry ice. Transfer into reaction vessels was achieved by vacuum distillation on a metal vacuum line through connections constructed of PTFE, Kel-F, and FEP similar to that shown in Figure 2.7.

Sulfurylchlorofluoride, SO_2ClF, (Aldrich) and sulfur dioxide, SO_2, (Aldrich) were stored over KF and P_4O_{10}, respectively, in glass vessels equipped with 6-mm J. Young glass valves equipped with glass barrels. Transfers of SO_2ClF and SO_2 solvents were performed under vacuum using a vacuum line and side manifolds constructed of glass (see Figure 2.8).

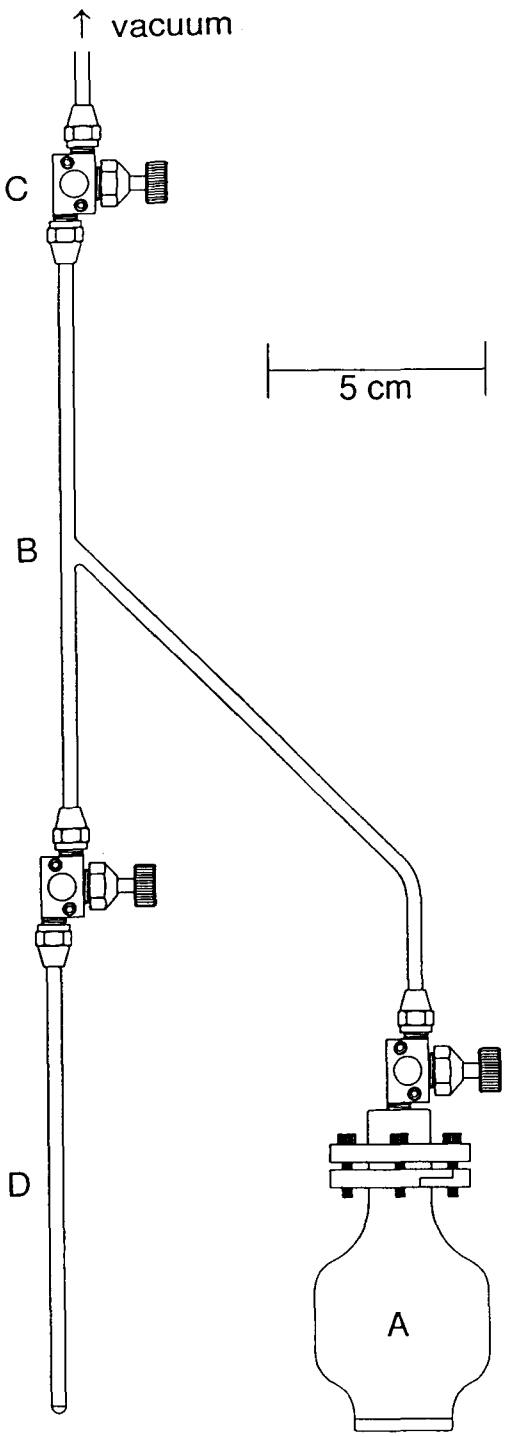

Figure 2.7 Apparatus used for the vacuum transfer of anhydrous HF solvent; (A) 250-mL Kel-F HF container equipped with a Kel-F valve, (B) FEP connector, (C) Kel-F valve, (D) FEP reaction vessel fitted with a Kel-F valve.

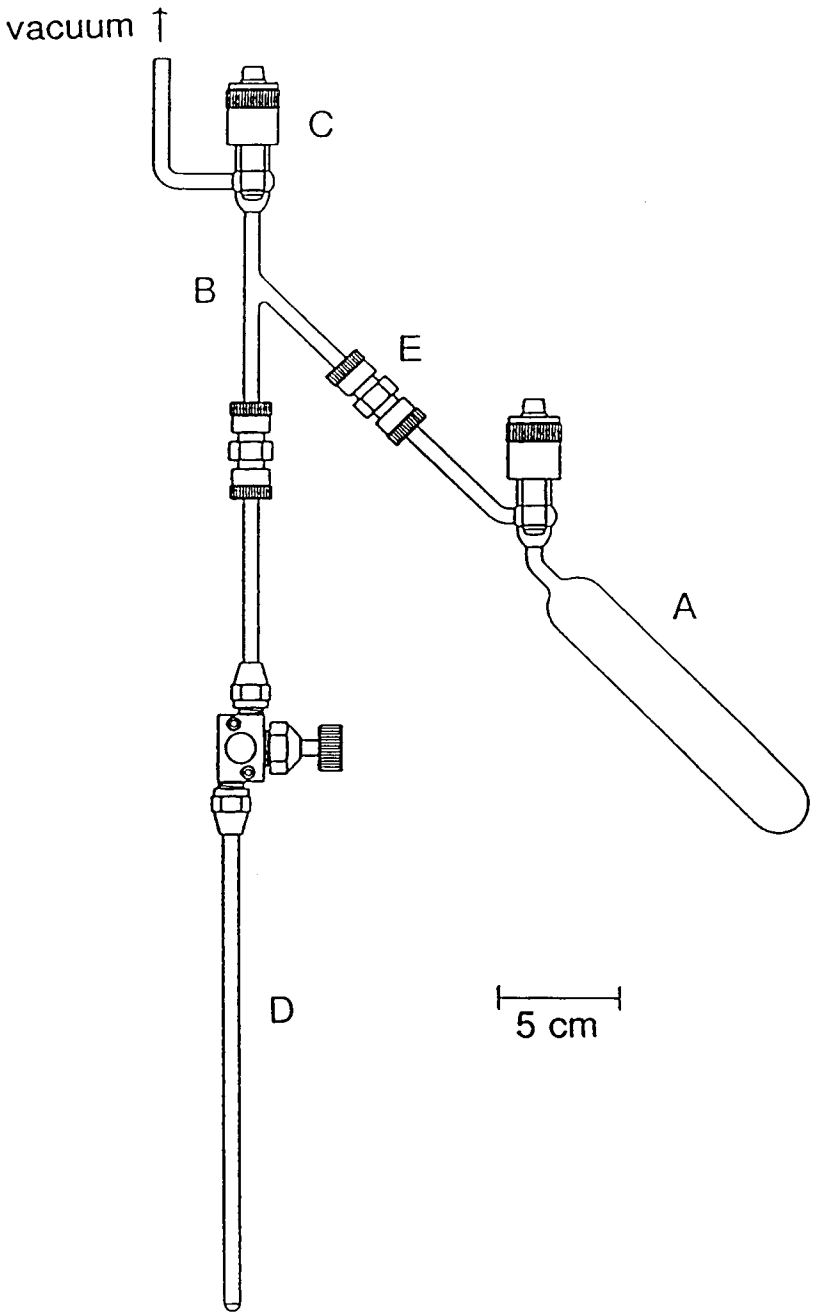

Figure 2.8 Apparatus used for the vacuum transfer of CH_3CN solvent; (A) 25-mL glass vessel equipped with a 4-mm J. Young PTFE/glass valve containing CH_3CN over CaH_2, (B) glass Y-connector, (C) 6-mm J. Young PTFE/glass valve, (D) FEP reaction vessel fitted with a Kel-F valve, (E) stainless steel Cajon connector.

CF_2ClCF_2Cl and CH_2Cl_2 Solvents

Freon-114, CF_2ClCF_2Cl, (Aldrich) was dried over P_4O_{10}, and vacuum distilled into a dry Pyrex storage vessel just prior to use.

Dichloromethane, CH_2Cl_2, (Caledon Reagent Grade) was dried as previously described[26,107] by refluxing over CaH_2 for 1 h, distilling onto Davison Type 4A molecular sieves (Fisher Scientific) for 24 h, and then distilling *in vacuo* into a dry Pyrex storage vessel prior to use. Dry CH_2Cl_2 and CF_2ClCF_2Cl were transferred under vacuum using all glass apparatus with ¼-in. connections and ¼-in. stainless steel Cajon unions similar to that shown in Figure 2.8.

Preparation of XeF_2 and $XeF^+AsF_6^-$

Xenon difluoride, XeF_2, was prepared from elemental xenon and fluorine by the thermal method described in the literature.[122] The $XeF^+AsF_6^-$ salt was prepared in anhydrous HF solvent according to the method of Gillespie and Landa [eq (2.1)].[34] Both

$$XeF_2 + AsF_5 \xrightarrow{HF} XeF^+AsF_6^- \qquad (2.1)$$

reagents were stored in ¾-in. o.d. Kel-F tubes in the drybox. All transfers of the solids to reaction vessels were made from their Kel-F or FEP storage vessels inside the drybox.

Preparation and Purification of Nitriles and Perfluoropyridines

Potassium cyanide, KCN, (Aldrich) was dried under static vacuum for several days in a ¼-in. o.d. glass tube equipped with a 4-mm J. Young glass valve and a PTFE barrel.

Acetonitrile, CH_3CN, (Caledon, HPLC Grade) was purified according to the literature procedure[116] and was stored in a 50-mL glass vessel equipped with a 4-mm J. Young glass valve and PTFE barrel. Vacuum transfers of the solvents were done on the glass vacuum line into FEP reactors as shown in Figure 2.8.

Commercially available CH_3CH_2CN (Aldrich, HPLC Grade), $(CH_3)_3CC{\equiv}N$ (Aldrich), $C_3F_3N_3$ (Armagedon Chemicals), and C_5F_5N (Aldrich) solvents were dried by periodic shaking with anhydrous CaH_2 over a period of several days prior to use and were stored over anhydrous CaH_2 (British Drug Houses) in 10-mL glass storage bulbs equipped with grease-free 4-mm J. Young glass valves and PTFE barrels. Contamination of samples with CaH_2 was avoided by vacuum distilling small amounts of the solvents into intermediate, previously vacuum-dried, glass bulbs just prior to use (Figure 2.9). Accurate amounts of each solvent vacuum distilled to the reaction vessel were obtained by weight difference of the preweighed evacuated glass bulb containing the solvent.

Preparation and Purification of F_5TeNH_2

The amine, F_5TeNH_2, was prepared according to the method of Seppelt *et al.*[123,124] [eqs (2.2) and (2.3)] and stored in a ½-in. o.d. FEP vessel equipped with a Kel-F valve in the drybox. It is a volatile colorless solid at room temperature, subliming easily under

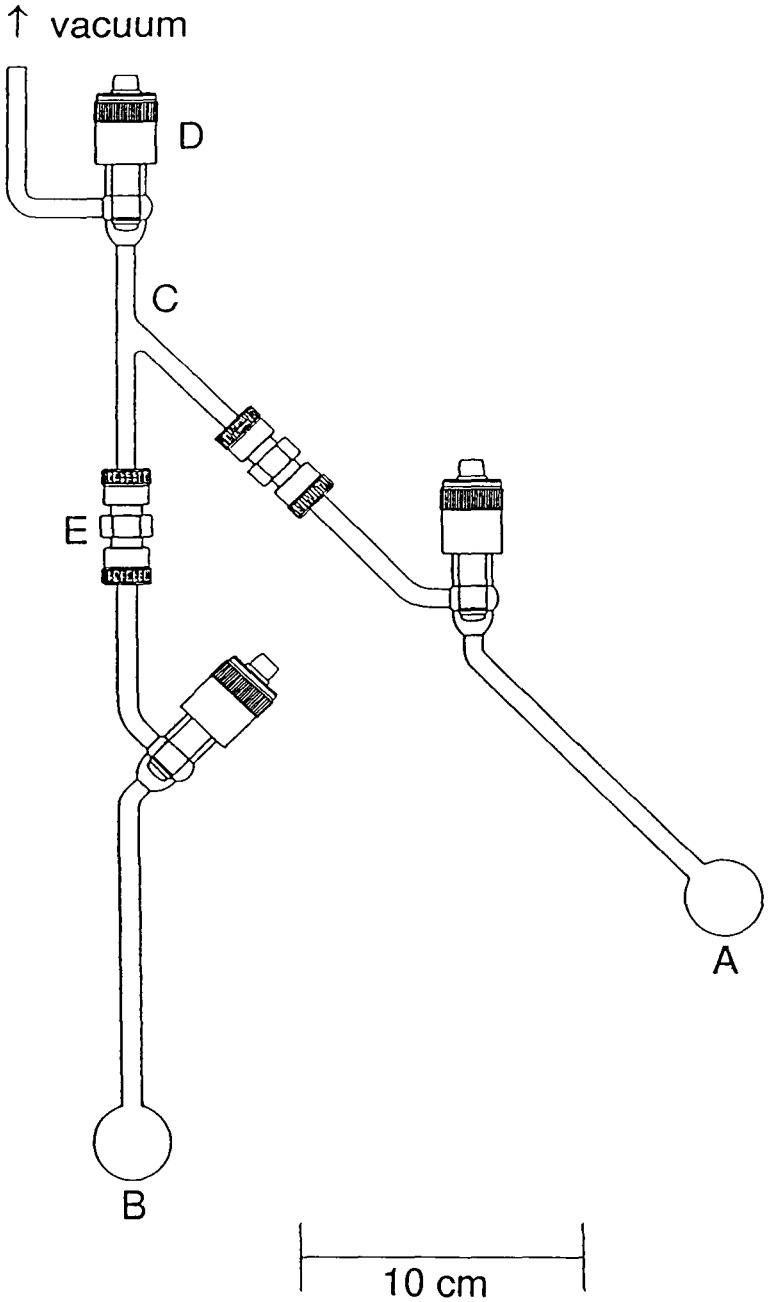

Figure 2.9 Apparatus used for the vacuum transfer of nitrile and perfluoropyridine solvents; (A) 10-mL glass bulb equipped with a 4-mm J. Young PTFE/glass valve containing nitrile or perfluoropyridine solvent over CaH_2, (B) 10-mL empty glass bulb equipped with a 4-mm J. Young PTFE/glass valve, (C) glass Y-connector, (D) 6-mm J. Young PTFE/glass valve, (E) stainless steel Cajon connector.Figure 2.10

vacuum. The amine was purified by sublimation under dynamic vacuum at -196 °C into an intermediate ½-in. o.d. FEP tube on a glass vacuum line. All transfers of the amine into reactors were performed in the drybox.

$$TeF_6 + (CH_3)_3SiNHSi(CH_3)_3 \longrightarrow F_5TeNHSi(CH_3)_3 + (CH_3)_3SiF \quad (2.2)$$

$$F_5TeNHSi(CH_3)_3 + HF \longrightarrow F_5TeNH_2 + (CH_3)_3SiF \quad (2.3)$$

Preparation and Purification of SbF_3, AsF_5, and $Pn(OTeF_5)_3$ (Pn = B, Sb, As)

Antimony trifluoride, SbF_3, (Aldrich) was purified by sublimation under dynamic vacuum and transferred into the drybox prior to use.

Arsenic pentafluoride, AsF_5, was prepared according to the literature method[122] by the fluorination of AsF_3 [125] in a nickel can. The AsF_5 was used directly from the reactor without further purification. Transfers were carried out through the calibrated volume of the manifold of the metal vacuum line and pressures were measured using a pressure transducer (see Figure 2.2).

The compounds, $B(OTeF_5)_3$ [103] and $As(OTeF_5)_3$,[126] were prepared and purified according to the literature procedures and stored in ½-in. o.d. FEP tubes equipped with FEP plugs inside the drybox. Transfers of the solids into reaction vessels were done in the inert nitrogen atmosphere of the drybox.

The $Sb(OTeF_5)_3$ reagent was prepared from SbF_3 (2.0102 g, 11.2462 mmol) and $B(OTeF_5)_3$ (8.2017 g, 11.2880 mmol) by the literature method [eq (2.4)].[127] The sample was stored under an atmosphere of dry nitrogen in the drybox in a ½-in. o.d. FEP tube

fused to a ¼-in. o.d. FEP tube fitted with a Kel-F valve. The purity of the $Sb(OTeF_5)_3$ and $As(OTeF_5)_3$ compounds were confirmed by ^{19}F NMR spectroscopy (*vide infra*).

$$SbF_3 + B(OTeF_5)_3 \longrightarrow Sb(OTeF_5)_3 \quad (2.4)$$

Preparation of $Xe(OChF_5)_2$ (Ch = Te, Se)

The $Xe(OChF_5)_2$ (Ch = Te, Se) compounds were prepared as described in the literature[50,107] [eqs (2.5) and (2.6)] and stored at *ca.* -78 °C in ½-in. o.d. FEP vessels equipped with Kel-F valves under *ca.* 1 atm of dry nitrogen gas. All transfers of the solids into reaction vessels were made from their storage vessels inside the drybox.

$$3XeF_2 + 2B(OTeF_5)_3 \longrightarrow 3Xe(OTeF_5)_2 + 2BF_3 \quad (2.5)$$

$$3XeF_2 + 2SeO_2F_2 \longrightarrow Xe(OSeF_5)_2 + 2Xe + O_2 \quad (2.6)$$

Preparation of $XeOChF_5^+AsF_6^-$ (Ch = Te, Se)

The $XeOChF_5^+AsF_6^-$ (Ch = Te, Se) salts were prepared as described in the literature[53,55,128] [eqs (2.7) and (2.8)]. The solids were stored in ½-in. o.d. FEP vessels equipped with Kel-F valves in the inert nitrogen atmosphere of the drybox, and transfers of the salts were done in the drybox.

$$Xe(OChF_5)_2 + XeF_2 \longrightarrow 2FXeOChF_5 \quad (2.7)$$

$$FXeOChF_5 + AsF_5 \longrightarrow XeOChF_5^+AsF_6^- \quad (2.8)$$

Preparation of $N(CH_3)_4^+OTeF_5^-$ and $N(CH_2CH_3)_4^+OTeF_5^-$

The $N(CH_3)_4^+OTeF_5^-$ and $N(CH_2CH_3)_4^+OTeF_5^-$ salts were prepared as described in the literature[107] and stored in Kel-F containers in the drybox. All transfers of the solids into reactors were done in the drybox.

PREPARATION AND CRYSTAL GROWTH OF Xe(II)–N AND Xe(II)–O BONDED COMPOUNDS, AND $OTeF_5$ DERIVATIVES OF ANTIMONY(III) AND ARSENIC(III)

A summary of the low-temperature crystal growing and mounting conditions for each compound is given in Table 2.1.

Synthesis and Crystal Growth of $HC{\equiv}N{-}XeF^+AsF_6^-$

In the drybox, KCN (0.0297 g, 0.4560 mmol) was added to arm A of a ¼-in. o.d. FEP h-shaped reactor and $XeF^+AsF_6^-$ (0.1532 g, 0.4518 mmol) was added to arm C of a ¼-in. o.d. FEP T-shaped reactor. The reactors were assembled on the metal vacuum line as illustrated in Figure 2.10. Anhydrous HF solvent (*ca.* 2-mL) was condensed onto KCN and the mixture was allowed to react at room temperature. The resulting HCN product was distilled into the empty side-arm B of the reactor and arm A containing the residual solid was heat-sealed off under dynamic vacuum at -196 °C. The HCN solvent was condensed onto $XeF^+AsF_6^-$ in arm C of the adjacent reactor at -196 °C. The mixture was warmed to *ca.* -15 °C forming a clear, colorless solution. The reactor was pressurized at -78 °C with *ca.* 1 atm of dry nitrogen and arm C, containing the solution mixture, was placed inside the glass Dewar of the crystal growing apparatus (see **Low-**

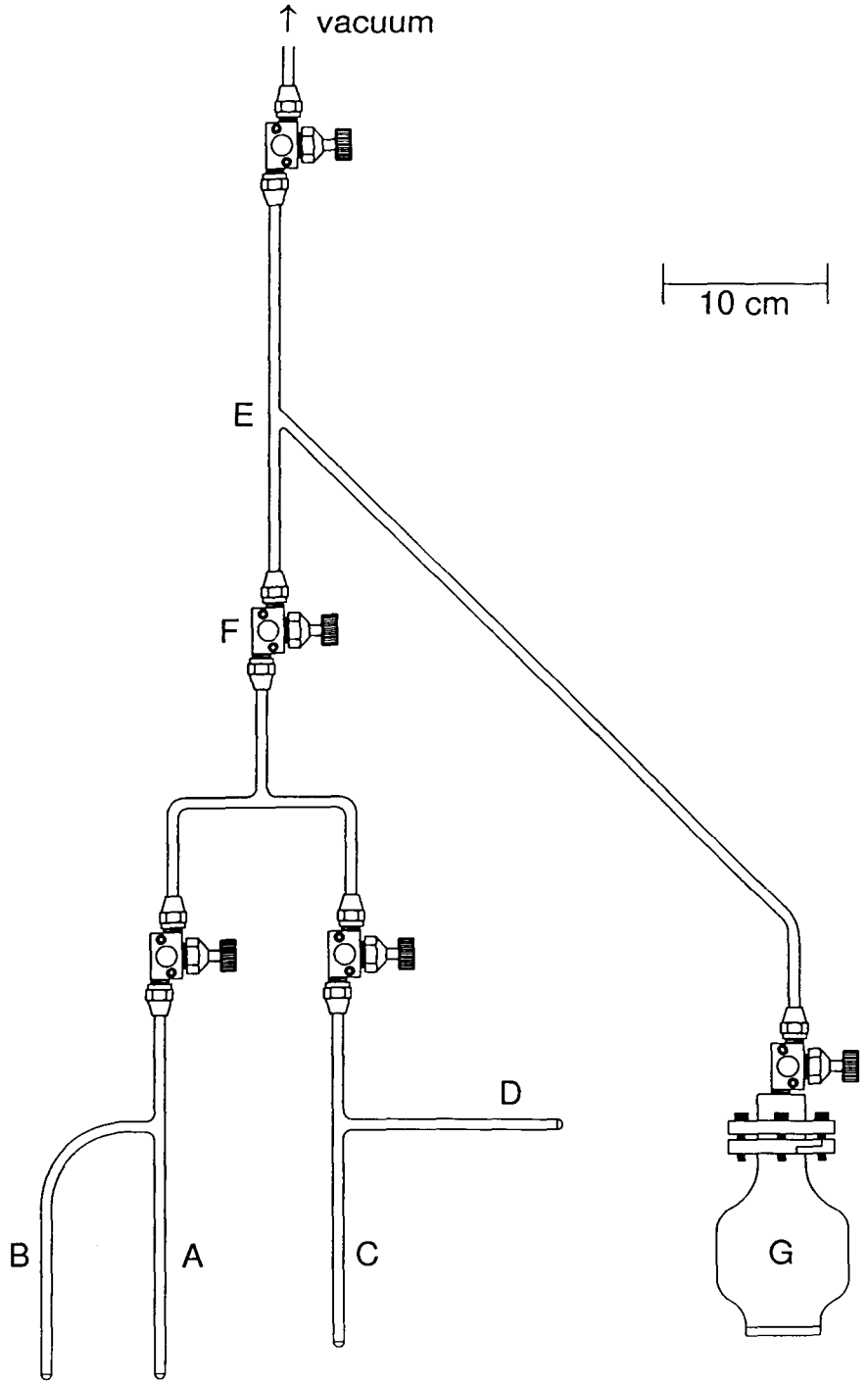

Figure 2.10 Apparatus used for the preparation of $HC{\equiv}N{-}XeF^{+}AsF_6^{-}$; (A) arm A of an FEP h-shaped reactor, (B) arm B of an FEP h-shaped reactor, (C) arm C of an FEP T-shaped reactor, (D) arm D of an FEP T-shaped reactor, (E) FEP connector, (F) Kel-F valve, (G) 250-mL Kel-F HF container equipped with a Kel-F valve.

Temperature Crystal Growth for X-ray Crystallography) set at an initial temperature of -15 °C. Over a period of *ca.* 10 h, large, clear, colorless crystalline plates developed throughout the reactor as the temperature of the Dewar was slowly decreased to -35 °C. The crystals were isolated and a single crystal was mounted at low-temperature on the X-ray diffractometer as previously described (see **Low-Temperature Mounting of Single Crystals for X-ray Crystallography**). The crystal used for the X-ray structure determination had the dimensions 0.34 × 0.20 × 0.05 mm^3. Crystals were disposed of in commercially available bleach. All vessels used during the synthesis, crystal growth, and mounting of $HC{\equiv}N{-}XeF^+AsF_6^-$, as well as the nitrile gloves used in handling the vessels, were carefully rinsed with bleach.

Synthesis and Crystal Growth of $HC{\equiv}NH^+AsF_6^-$

In the drybox, KCN (0.09107 g, 1.3986 mmol) was transferred into arm A of a ¼-in. o.d. FEP h-shaped reactor. The reactor was connected to the metal vacuum line as illustrated in Figure 2.10 and HF (*ca.* 3-mL) was condensed onto KCN at -196 °C. The mixture was slowly warmed to room temperature whereupon KCN rapidly dissolved. The resulting HCN solution was immediately distilled into arm B. Arm A containing the residual solid, $KHF_2{\cdot}x$HF, was heat-sealed off under dynamic vacuum while the HCN solvent in arm B was frozen at -196 °C. The contents of B were warmed to room temperature and condensed into arm C of a second ¼-in. o.d. FEP T-reactor at -196 °C. A stoichiometric excess of AsF_5 (1750 Torr, 1.797 mmol) was condensed onto the HCN

solvent at -196 °C. The mixture was briefly warmed to *ca.* -15 °C to effect complete reaction, and then the HF solvent along with excess AsF_5 was removed at *ca.* -78 °C. Anhydrous HF solvent was distilled back into the reactor on top of the frozen mixture at -78 °C. The reactor was pressurized with *ca.* 1 atm of dry nitrogen at -78 °C and arm C containing the mixture was placed inside the glass Dewar of the low-temperature crystal growing apparatus (see **Low-Temperature Crystal Growth for X-ray Diffraction**) set at an initial temperature of 0 °C. As the temperature of the Dewar was decreased to -20 °C over *ca.* 5 h, clear, colorless, needle-shaped crystals developed throughout the solution. The crystals were isolated and a single crystal was mounted at low-temperature on the X-ray diffractometer as previously described (see **Low-Temperature Mounting of Single Crystals for X-ray Crystallography**). The crystal used for the data acquisition had the dimensions 0.15 × 0.12 × 0.08 mm^3. All vessels used during the synthesis, crystal growth, and mounting of $HC{\equiv}NH^+AsF_6^-$, as well as the nitrile gloves used in handling the vessels, were carefully rinsed with bleach.

Synthesis and Crystal Growth of $CH_3C{\equiv}N{-}XeF^+AsF_6^-$

(A) Under static vacuum at -196 °C, 0.0108 g (0.2631 mmol) of $CH_3C{\equiv}N$ was condensed into arm C of a ¼-in. o.d. FEP T-shaped reactor fitted with a Kel-F valve. On the metal vacuum line, anhydrous HF solvent (*ca.* 3-mL) was condensed onto $CH_3C{\equiv}N$ at -196 °C, and then the reactor was transferred into the drybox through the glass cryowell maintained at -196 °C. Arm C was placed inside a steel Dewar containing BB's which

had been cooled in the cryowell, and a stoichiometric amount of $XeF^+AsF_6^-$ (0.0867 g, 0.2557 mmol) was added on top of the chilled mixture. The mixture was slowly warmed to -20 °C with agitation, forming a clear, colorless solution. When cooled to -78 °C, the mixture salted out forming two distinct liquid phases. Additional HF was condensed onto the mixture at -196 °C, which only slightly diminished the denser phase. Arm C containing the mixture was placed inside the low-temperature crystal growing apparatus as previously described (see **Low-Temperature Crystal Growth for X-ray Crystallography**) set at an initial temperature of -20 °C. The Dewar was slowly cooled over a period of 3 h to -43 °C, whereupon a large amount of microcrystalline material formed along the walls of the reactor initiated in the denser phase. The Dewar was then cooled to -78 °C over 5 h and shiny clear, colorless plates formed. The crystals were isolated and attempts were made to mount single crystals at low-temperature on the X-ray diffractometer as previously described (see **Low-Temperature Mounting of Single Crystals for X-ray Crystallography**), however, the crystals were too small, difficult to see due to their clarity, and brittle to mount.

(B) The $CH_3C{\equiv}N{-}XeF^+AsF_6^-$ salt was prepared as in Trial A using the following quantities of reagents: $XeF^+AsF_6^-$ (0.18218 g, 0.5371 mmol) and a stoichiometric excess of CH_3CN (0.0304 g, 0.7405 mmol). The low-temperature crystal growing technique was used as in Trial A, however, when a small amount of a yellow viscous liquid appeared and colorless microcrystalline material deposited at -40 °C, the reactor was removed from the Dewar and the solid material was shaken to the bottom of the reactor. The reactor was placed back in the Dewar at -40 °C and the temperature was slowly

decreased to -60 °C, whereupon very thin, clear, and colorless plates formed throughout the tube. The crystals were isolated and a single crystal was mounted at low-temperature on the X-ray diffractometer as previously described (see **Low-Temperature Mounting of Single Crystals for X-ray Crystallography**). The crystal used for the data acquisition had the dimensions 0.15 × 0.12 × 0.08 mm^3.

Synthesis and Crystal Growth of (A) $Xe_2F_3^+AsF_6^-$ and (B) $(CH_3)_3CC{\equiv}N{-}XeF^+AsF_6^-$

(A) Under static vacuum at *ca.* -196 °C, 0.0139 g (0.1672 mmol) of $(CH_3)_3CC{\equiv}N$ was condensed into arm C of a ¼-in. o.d. FEP T-shaped reactor fitted with a Kel-F valve. On the metal vacuum line, anhydrous HF solvent (*ca.* 3-mL) was condensed onto $(CH_3)_3CC{\equiv}N$ at -196 °C. The reactor was transferred into the drybox through the glass cryowell maintained at -196 °C. Arm C was placed inside a steel Dewar containing BB's which had been cooled in the cryowell, and an excess of $XeF^+AsF_6^-$ (0.07106 g, 0.2095 mmol) was added on top of the chilled solvent mixture. The mixture was slowly warmed to *ca.* -20 °C, whereupon a clear, colorless solution formed. Arm C containing the solvent mixture was placed inside the glass Dewar of the low-temperature crystal growing apparatus (see **Low-Temperature Crystal Growth for X-ray Crystallography**) set at an initial temperature of -18 °C. Over a period of 6 h, clear, colorless, crystalline plates developed along the walls of the tube as the temperature was decreased to -45 °C. The crystals were isolated and a single crystal was mounted at low-temperature on the X-ray diffractometer as previously described (see **Low-Temperature Mounting of Single Crystals for X-ray Crystallography**). The crystal used for the data

acquisition had the dimensions 0.2 × 0.2 × 0.2 mm^3, and was later shown by X-ray crystallography to be $Xe_2F_3^+AsF_6^-$.

(B) The $(CH_3)_3CC{\equiv}N{-}XeF^+AsF_6^-$ salt was synthesized again according to Trial A above using the following quantities of reagents: $(CH_3)_3CC{\equiv}N$ (0.3170 g, 0.3813 mmol) and a stoichiometric amount of $XeF^+AsF_6^-$ (0.1276 g, 0.3762 mmol). Low-temperature crystal growing and mounting techniques were used as in Trial A. The clear, colorless, needle-shaped crystal used for the data acquisition had the dimensions 0.22 × 0.05 × 0.04 mm^3, and was later shown by X-ray crystallography to be $(CH_3)_3CC{\equiv}N{-}XeF^+AsF_6^-$.

Synthesis and Crystal Growth of *s*-$C_3F_3N_2N{-}XeF^+AsF_6^-$

In the drybox, 0.10442 g (0.3078 mmol) of $XeF^+AsF_6^-$ was loaded into arm C of a ¼-in. o.d. FEP T-shaped reactor fitted with a Kel-F valve. An excess of anhydrous $C_3F_3N_3$ (*ca.* 1-mL) was condensed under static vacuum at -196 °C on top of the solid. The reactor was pressurized with *ca.* 1 atm of dry nitrogen at -78 °C and then the mixture was continuously agitated for 3 h at room temperature. Removal of excess $C_3F_3N_3$ *in vacuo* at room temperature resulted in a white powder that was stable indefinitely at room temperature. On the metal vacuum line, BrF_5 solvent was condensed onto the solid in arm C at -196 °C giving a yellow solution when agitated at *ca.* -40 °C. The reactor was pressurized with *ca.* 1 atm of dry nitrogen at -78 °C and arm C was placed inside the glass Dewar of the low-temperature crystal growing apparatus (see **Low-Temperature**

Crystal Growth for X-ray Crystallography) set at an initial temperature of -30 °C. As the temperature of the Dewar was decreased to *ca.* -40 °C over 4 h, clear, yellow, needle-shaped crystals developed throughout the tube. The crystals were isolated and a single crystal was mounted at low-temperature on the X-ray diffractometer as previously described (see **Low-Temperature Mounting of Single Crystals for X-ray Crystallography**). The crystal used for the data acquisition had the dimensions 0.21 × 0.07 × 0.03 mm^3.

Synthesis and Crystal Growth of C_5F_5N–$XeF^+AsF_6^-$

Under static vacuum at -196 °C, C_5F_5N (0.0336 g, 0.1988 mmol) was condensed into arm C of a ¼-in. o.d. FEP T-shaped reactor fitted with a Kel-F valve. On the metal vacuum line at -196 °C, anhydrous HF solvent (*ca.* 3 mL) was first condensed onto the liquid C_5F_5N, followed by a stoichiometric amount of AsF_5 (330 Torr, 0.339 mmol). The reaction mixture was agitated at or below -40 °C to effect dissolution, and then excess HF and AsF_5 were removed under vacuum at *ca.* -50 °C yielding a colorless solid. The reactor was pressurized with *ca.* 1 atm of dry nitrogen at -78 °C and transferred into the drybox at room temperature. In the drybox, arm C of the reactor was placed inside a steel Dewar containing BB's that had been cooled at -196 °C in the glass cryowell and an excess of XeF_2 (0.03710 g, 0.21916 mmol) was added to the cold solid. The sample was maintained cold during removal from the drybox and BrF_5 solvent was condensed onto the mixture at -196 °C. The reactants dissolved readily at -40 °C forming a clear, yellow solution. The reactor was pressurized at -78 °C with *ca.* 1 atm with dry nitrogen and arm

C, containing the mixture, was placed inside the glass Dewar of the low-temperature crystal growing apparatus (see **Low-Temperature Crystal Growth for X-ray Crystallography**) set at an initial temperature of -50 °C. Crystals were not observed as the temperature of the Dewar was decreased to -60 °C. However, as the BrF_5 solvent was slowly pumped off under dynamic vacuum at -56 °C for *ca.* 5 h on the glass vacuum line equipped with an intermediate ¾-in. o.d. FEP U-trap cooled to -196 °C. Colorless, needle-shaped crystals deposited on the walls of the tube. The crystals were isolated and a single crystal was mounted at low-temperature on the X-ray diffractometer as previously described (see **Low-Temperature Mounting of Single Crystals for X-ray Crystallography**). The crystal used for X-ray structure determination had the dimensions 0.2 × 0.06 × 0.06 mm^3.

Syntheses and Crystal Growth of $F_5TeNH_3^+AsF_6^-$ and $F_5TeN(H)Xe^+AsF_6^-$

In the drybox, F_5TeNH_2 (0.1837 g, 0.770 mmol) and $XeF^+AsF_6^-$ (0.2657 g, 0.783 mmol) were loaded into arm A of a ¼-in. o.d. FEP h-shaped reactor fitted with a Kel-F valve. The reactor was maintained at *ca.* -160 °C to prevent reaction of the solids. Upon removal of the cold sample from the drybox, anhydrous HF (*ca.* 2-mL) was condensed onto the solids at -196 °C. At -48 °C, a pale yellow solution was observed from which a colorless, microcrystalline solid precipitated after *ca.* 1 min. The colorless crystals were attributed to the formation of $F_5TeNH_3^+AsF_6^-$. Upon agitation at *ca.* -30 °C, the colorless crystals dissolved. The reactor was pressurized to *ca.* 1 atm with dry nitrogen and arm A containing the solution mixture was placed inside the glass Dewar of the low-temperature

crystal growing apparatus (see **Low-Temperature Crystal Growth for X-ray Crystallography**) set at an initial temperature of -40 °C. After 10 min, the solution exhibited a more intense yellow coloration, while colorless crystals of $F_5TeNH_3^+AsF_6^-$ began to appear on the walls of the reactor. The reactor was then slowly cooled over a period of 1 h to -53 °C. Lustrous, yellow needle-shaped crystals of $F_5TeN(H)Xe^+AsF_6^-$ formed throughout the solution which had become almost colorless. The reactor was maintained at -55 °C for two additional hours to allow complete deposition of the yellow crystals. The crystals were isolated and mounted at low-temperature on the X-ray diffractometer as previously described (see **Low-Temperature Mounting of Single Crystals for X-ray Crystallography**). Care was taken to prevent warming of the yellow crystals above -40 °C, where slow decomposition begins to occur. The colorless $F_5TeNH_3^+AsF_6^-$ and two yellow $F_5TeN(H)Xe^+AsF_6^-$ crystals used for X-ray structure determinations had the dimensions 0.4 × 0.15 × 0.1, 0.8 × 0.16 × 0.15, and 0.22 × 0.08 × 0.07 mm^3, respectively.

F_5TeNH_2 Crystal Growth

(A) In the drybox, F_5TeNH_2 (*ca.* 50-mg) was loaded into a previously vacuum dried and flamed 40-cm long, 10-mm o.d. standard-wall glass tube joined to a metal valve by means of a graded glass seal to Kovar. The glass vessel was then flame-sealed with an oxygen-natural gas torch below the valve under dynamic vacuum at -196 °C and mounted horizontally in the fumehood. Clear, colorless crystals sublimed throughout the vessel over several days. The crystals could not be immobilized since small fluctuations

in the temperature of the vessel caused the crystals to resublime to other points in the vessel.

(B) In the drybox, F_5TeNH_2 (*ca.* 50-mg) was loaded into a ¼-in. o.d. FEP tube fitted with a Kel-F valve. The tube was evacuated at -78 °C on a glass vacuum line and then warmed to room temperature. Clear, colorless crystals formed on the walls of the tube over a period of several days and were detached by cooling and flexing the tube. The vessel was pressurized to *ca.* 1 atm with dry nitrogen at -78 °C. Several crystals were mounted at low-temperature on the X-ray diffractometer as previously described (see **Low-Temperature Mounting of Single Crystals for X-ray Crystallography**), however X-ray data could not be collected on any of the crystals examined since they were polycrystallites and/or powdered.

(C) In the drybox, F_5TeNH_2 (*ca.* 50-mg) was loaded into a dry glass vessel equipped with a cold finger and four capillaries drawn from 5-mm thin-wall NMR tubes (Figure 2.11). The vessel was mounted on the glass vacuum line with the capillaries oriented in a horizontal position. Under static vacuum, F_5TeNH_2 was condensed into the cold finger at -78 °C. The cold finger was then warmed to room temperature and over several days small, clear, and colorless crystals sublimed into the capillaries and throughout the glass vessel. The vessel was pressurized to *ca.* 70 Torr with dry nitrogen and then mounted horizontally inside of a box, to exclude drafts, for several days. The capillaries were flame-sealed with a miniature oxygen-natural gas torch and mounted using epoxy onto brass pins. At room temperature crystals of F_5TeNH_2 diffracted well. However, when the temperature of the crystals was lowered to -14 (± 2) °C a phase

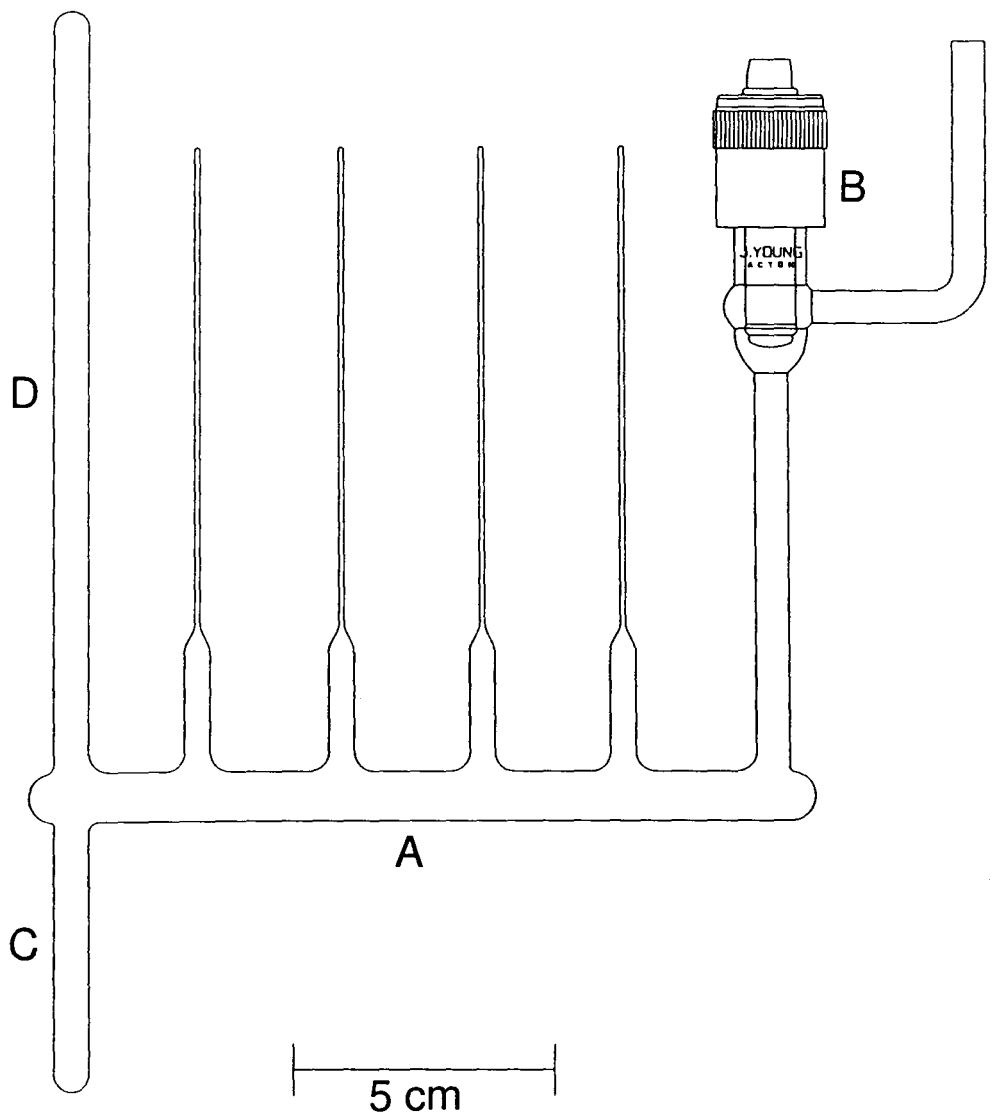

Figure 2.11 Apparatus used for the crystallization of F_5TeNH_2; (A) ½-in. o.d. glass vessel equipped with 4 capillaries drawn from 5-mm thin-wall NMR tubes, (B) 4-mm J. Young glass valve equipped with PTFE barrel, (C) ½-in. o.d. hollow, glass cold finger, (D) ½-in. o.d. solid glass rod.

transition occurred whereupon the crystals powdered. Examination of the crystals in the drybox revealed that they were very "plastic". Another crystal was used for the data acquisition at -5 °C which had the dimensions 0.35 × 0.26 × 0.12 mm^3.

(D) In order to obtain the X-ray crystal structure of the low-temperature phase of F_5TeNH_2, crystals of the compound were grown and maintained at low temperature. In the drybox, F_5TeNH_2 (*ca.* 50-mg) was loaded into arm C of a dry 7-mm o.d. glass T-shaped reactor equipped with a 4-mm J. Young glass valve and a PTFE barrel. Anhydrous SO_2 (*ca.* 5-mL) was condensed onto F_5TeNH_2 at -78 °C on a glass vacuum line and then the reactor was pressurized to *ca.* 1 atm with dry nitrogen. Arm C containing the solution mixture was placed inside the glass Dewar of the low-temperature crystal growing apparatus (see **Low-Temperature Crystal Growth for X-ray Crystallography**) set at room temperature. The temperature inside the Dewar was decreased to -50 °C at a rate of 2 °C/minute. The Dewar was then cooled more slowly over 2 h to -70 °C. At -70 °C, clear, colorless, needle-shaped crystals of F_5TeNH_2 formed throughout the solution. The vessel was maintained at -70 °C for two additional hours to allow for more complete deposition of the crystals. The colorless supernatant was decanted into the empty side-arm (D) of the reactor, and then arm D was flame-sealed off from the reactor. Residual SO_2 in the reactor was pumped off under dynamic vacuum at -75 °C. The vessel containing the crystals was pressurized to *ca.* 1 atm with dry nitrogen and maintained at -78 °C until the crystals could be mounted on the X-ray diffractometer. The low-temperature crystal mounting apparatus was utilized as previously described (see **Low-Temperature Mounting of Single Crystals for X-ray Crystallography**).

Since the crystals were too large for X-ray data collection, several were cut into smaller fragments. The crystal fragment used for the data acquisition had the dimensions 0.15 × 0.08 × 0.02 mm^3.

$XeOTeF_5^+AsF_6^-$ Crystal Growth

Thin, yellow, and extremely brittle crystalline plates of $XeOTeF_5^+AsF_6^-$ had grown over a period of six years by sublimation at room temperature onto the walls of a ¾-in. o.d. FEP storage tube pressurized to *ca.* 1 atm with dry nitrogen inside the drybox. Suitable crystals of $XeOTeF_5^+AsF_6^-$ were removed inside the drybox equipped with a microscope by prying them off the storage tube walls with a steel needle and mounting each inside 0.2- and 0.3-mm i.d. Lindemann glass capillaries followed by flame-sealing. The crystal which was used for X-ray structure determination had the dimensions 0.6 × 0.3 × 0.02 mm^3.

$XeOSeF_5^+AsF_6^-$ Crystal Growth

(A) Over a period of several years, pale yellow crystals of $XeOSeF_5^+AsF_6^-$ had sublimed onto the walls of a ½-in. o.d. FEP storage tube inside the drybox. Suitable crystals of $XeOSeF_5^+AsF_6^-$ were removed from the tube in the drybox by prying them off the walls with a steel needle and mounting them inside 0.1-mm i.d. Lindemann glass capillaries under a stereomicroscope, followed by flame-sealing. The mounting procedure was complicated by the tendency of the crystals to readily sublime. A single crystal could not be observed by X-ray diffraction.

(B) In the drybox, $XeOSeF_5^+AsF_6^-$ was loaded into three dry, thin-walled glass capillaries fused to ¼-in. o.d. glass tubing connected to 4-mm J. Young glass valves equipped with PTFE barrels. The capillaries were flame-sealed with a miniature oxygen-natural gas torch under dynamic vacuum on a glass vacuum line and vertically mounted on a wooden platform. Pale yellow crystals of $XeOSeF_5^+AsF_6^-$ sublimed inside the capillaries at room temperature over several days. X-ray data acquired on a crystal at -60 °C showed that the crystal was not single.

(C) In the drybox, $XeOSeF_5^+AsF_6^-$ was loaded into a dry, 40-cm long, 10-mm o.d. standard-wall glass tube joined to a metal valve by means of a graded glass seal to Kovar. The glass vessel was connected to a glass vacuum line, pressurized to 10 Torr with dry nitrogen, flamed-sealed while cooling the sample at -196 °C, and then mounted at a 45° angle in the fumehood. Clear, yellow crystals sublimed slowly on the walls of the glass vessel over a period of 1 year. The low-temperature crystal mounting apparatus was utilized as previously described to mount the crystals on the X-ray diffractometer (see **Low-Temperature Mounting of Single Crystals for X-ray Crystallography**). The crystals were deposited onto the aluminum trough of the crystal mounting apparatus set at -113 °C by cutting open the glass vessel with a steel file under a flow of dry nitrogen and scrapping them off of the walls of the vessel with a steel spatula. The crystal used for the data acquisition had the dimensions $0.15 \times 0.08 \times 0.02$ mm^3.

$Xe(OTeF_5)_2$ Crystal Growth

(A) In the drybox, $Xe(OTeF_5)_2$ (*ca.* 0.1 g) was loaded into a dry, 40-cm long, 10-mm o.d. standard-wall glass tube joined to a metal valve by means of a graded glass seal to Kovar. The glass vessel was connected to a glass vacuum line, pressurized to 400 Torr with dry nitrogen, flamed-sealed with an oxygen-natural gas torch while cooling the sample at -196 °C, and then mounted at a 45° angle in the fumehood. Clear, colorless crystals sublimed slowly onto the walls of the glass vessel over several days. Suitable crystals were removed from the tube in the drybox by prying them off the walls with a steel needle. The crystals were mounted in 0.1- and 0.2-mm i.d. Lindemann glass capillaries under a stereomicroscope and were temporarily plugged with Kel-F grease until they were taken out of the drybox, where they were permanently flame-sealed with a miniature oxygen-natural gas torch. X-ray diffraction of the crystals showed that they were polycrystalline.

(B) In the drybox, $Xe(OTeF_5)_2$ (*ca.* 0.1 g) was loaded into arm C of a T-shaped FEP reactor constructed from ¼-in. o.d. FEP tubing and fitted with a Kel-F valve. Freon-114 (*ca.* 3-mL) was condensed onto the solid at -196 °C, which dissolved completely at room temperature. Arm C containing the solution mixture was placed inside the glass Dewar of the low-temperature crystal growing apparatus (see **Low-Temperature Crystal Growth for X-ray Crystallography**) set at an initial temperature of -18 °C. The Dewar was then slowly cooled down over a period of 4 h to -30 °C. At -30 °C, clear, colorless crystalline plates formed throughout the solution and along the walls of the tube. The tube was maintained at -30 °C for an additional hour to allow complete

deposition of the crystals. The supernatant solution was decanted into the empty side-arm D of the reactor, and then arm D was heat-sealed off from the apparatus. The tube containing the crystals was pressurized to *ca.* 1 atm with dry nitrogen and maintained at -78 °C until the crystals could be mounted. The dry crystals were detached from the walls of the tube by flexing the tube. The low-temperature crystal mounting technique was utilized as previously described to mount the crystals on the X-ray diffractometer (see **Low-Temperature Mounting of Single Crystals for X-ray Crystallography**). The crystal used for X-ray structure determination had the dimensions 0.25 × 0.20 × 0.06 mm^3.

$Xe(OSeF_5)_2$ Crystal Growth

(A) In the drybox, $Xe(OSeF_5)_2$ (*ca.* 0.1 g) was loaded into a dry, 40-cm long, 10-mm o.d. standard-wall glass tube joined to a metal valve by means of a graded glass seal to Kovar. The glass vessel was connected to a glass vacuum line, pressurized to *ca.* 1 atm with dry nitrogen, flamed-sealed with an oxygen-natural gas torch, and then mounted at a 45° angle in the fumehood. Clear, colorless crystalline plates sublimed slowly onto the walls of the glass vessel over several days. Suitable crystals of $Xe(OSeF_5)_2$ were removed from the tube in the drybox by prying them off the walls with a steel needle and then mounted under a stereomicroscope and flame-sealed with a miniature oxygen-natural gas torch inside 0.1- and 0.2-mm i.d. Lindemann glass capillaries. The X-ray diffraction data acquired on a crystal at -50 °C showed that the crystal was twinned.

(B) In the drybox, $Xe(OSeF_5)_2$ (*ca.* 0.1 g) was loaded into arm C of a T-shaped FEP reactor constructed from ¼-in. o.d. FEP tubing and fitted with a Kel-F valve. Freon-114 (*ca.* 3-mL) was condensed onto $Xe(OSeF_5)_2$ at -196 °C and then the reactor was pressurized to *ca.* 1 atm with dry nitrogen at -78 °C. The mixture was allowed to dissolve at room temperature and then arm C containing the solution mixture was placed inside the glass Dewar of the low-temperature crystal growing apparatus (see **Low-Temperature Crystal Growth for X-ray Crystallography**) set at room temperature. The Dewar was then cooled down slowly over a period of 3 h to -10 °C. At *ca.* -10 °C clear, colorless crystalline plates grew throughout the solution and along the walls of the tube. The tube was maintained at -10 °C for an additional hour to allow for more complete deposition of the crystals. The supernatant solution was decanted into the empty side-arm D of the reactor, and then arm D was heat-sealed off from the apparatus. The tube containing the crystals was pressurized to 1 atm with dry nitrogen and maintained at 0 °C until the crystals could be mounted. The low-temperature crystal mounting technique was utilized as previously described to mount the crystals on the X-ray diffractometer (see **Low-Temperature Mounting of Single Crystals for X-ray Crystallography**). The crystal used for X-ray structure determination at -45 °C had the dimensions $0.30 \times 0.25 \times 0.20$ mm^3.

The X-ray diffraction pattern of the crystal was examined as a function of decreasing temperature after the data collection at -45 °C. For a given frame, as the temperature of the crystal was decreased from -45 °C to -79 (± 2) °C a greater number of diffraction spots became visible. As the temperature was further decreased to

-129 (± 2) °C all original diffraction spots seen at -45 °C split indicating that the crystal cracked into multiple fragments. The crystal also appeared to be more opaque under the microscope.

Synthesis and Crystal Growth of $N(CH_3)_4^+Sb(OTeF_5)_4^-$

In the drybox, $Sb(OTeF_5)_3$ (1.5450 g, 1.845 mmol) was loaded into a dry ½-in. o.d. FEP tube fused to a ¼-in. o.d. FEP tube equipped with Kel-F valve. The reactor was placed in a steel Dewar containing BB's inside the drybox which had been cooled in the glass cryowell at -196 °C. A stoichiometric amount of $N(CH_3)_4^+OTeF_5^-$ (0.5748 g, 1.838 mmol) was added onto the chilled $Sb(OTeF_5)_3$. The reactor was attached to a glass vacuum line and SO_2ClF (*ca.* 3-mL) was condensed onto the mixture at -78 °C. After the mixture was warmed to room temperature and agitated vigorously to effect complete reaction, the SO_2ClF solvent was pumped off under dynamic vacuum at room temperature resulting in a colorless solid. The tube was pressurized to *ca.* 1 atm with dry nitrogen at -78 °C, transferred into the drybox, the valve was removed, and the tube was weighed. The mass of the product was 2.1119 g (theor. 2.1141 g, 99.9 % yield).

(A) In the drybox, $N(CH_3)_4^+Sb(OTeF_5)_4^-$ (*ca.* 50-mg) was loaded into arm A of a two-arm Pyrex vessel equipped with one J. Young stopcock (Figure 2.12). Approximately 4-mL of SO_2ClF was condensed onto the solid, which did not dissolve entirely upon warming the solution to room temperature. After some of the solvent mixture was decanted into the empty side-arm B, the reactor was immersed in a water bath set at 40 °C. Clear, colorless crystalline plates grew on the walls of the reactor over

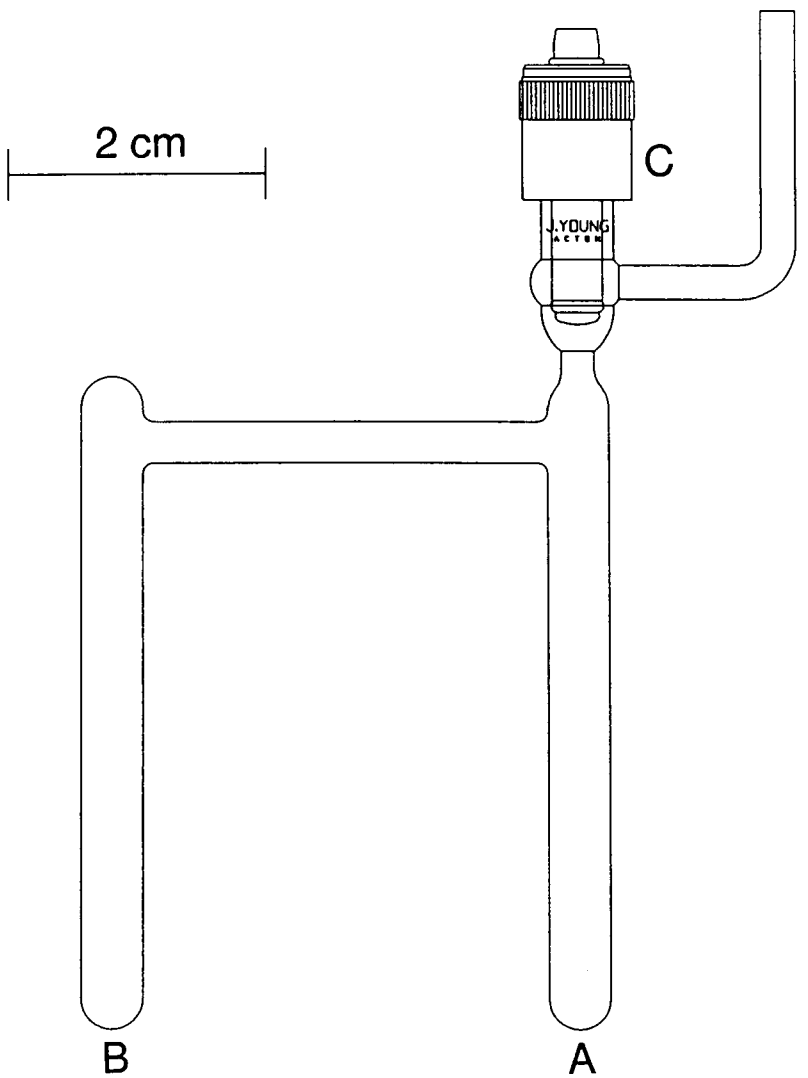

Figure 2.12 Glass reaction vessel used for the crystallization of $N(CH_3)_4^+Sb(OTeF_5)_4^-$; (A) Pyrex glass reaction vessel (arm A), (B) Pyrex glass reaction vessel (arm B), (C) 4-mm J. Young Teflon/glass stopcock.

several weeks. The crystals were pumped dry under dynamic vacuum and the reactor was pressurized to *ca.* 1 atm with dry nitrogen before it was transferred into the drybox equipped with a microscope. The glass vessel was cut open with a steel file and six crystals were pried off the walls with a steel needle. The crystals were mounted inside 0.1-mm i.d. Lindemann glass capillaries which were temporarily plugged with Kel-F grease until they were taken out of the drybox. The capillaries were permanently flame-sealed with a miniature oxygen-natural gas torch. A structural solution could not be obtained from X-ray diffraction data acquired on a crystal at -120 °C due to complicated disordering and possible twinning of the model having the *C2/c* space group ($a = c =$ 18.4808(3) Å, b = 11.4187(1) Å, β = 102.864(1)°, V = 3799.803(61) Å^3). A partial structural solution for a model having a different space group (*I4*) was obtained from X-ray diffraction data acquired on a second crystal at -45 °C having the dimensions 0.18 × 0.18 × 0.12 mm^3.

(B) Crystal growth of $N(CH_3)_4^+Sb(OTeF_5)_4^-$ was carried out in a two-arm Pyrex vessel equipped with J. Young stopcocks. The two arms were connected together by means of a second J. Young stopcock (Figure 2.13). The $N(CH_3)_4^+Sb(OTeF_5)_4^-$ salt (*ca.* 0.2 g, 0.174 mmol) was loaded into arm A of the reaction vessel in the drybox. The vessel was attached to a glass vacuum line, and anhydrous CH_3CN (*ca.* 3-mL) was condensed at -196 °C into the empty arm B of the vessel while the stopcock between the two arms was kept closed. Approximately 4-mL of SO_2ClF was condensed onto the salt, which dissolved entirely upon warming the solution to room temperature. The stopcock

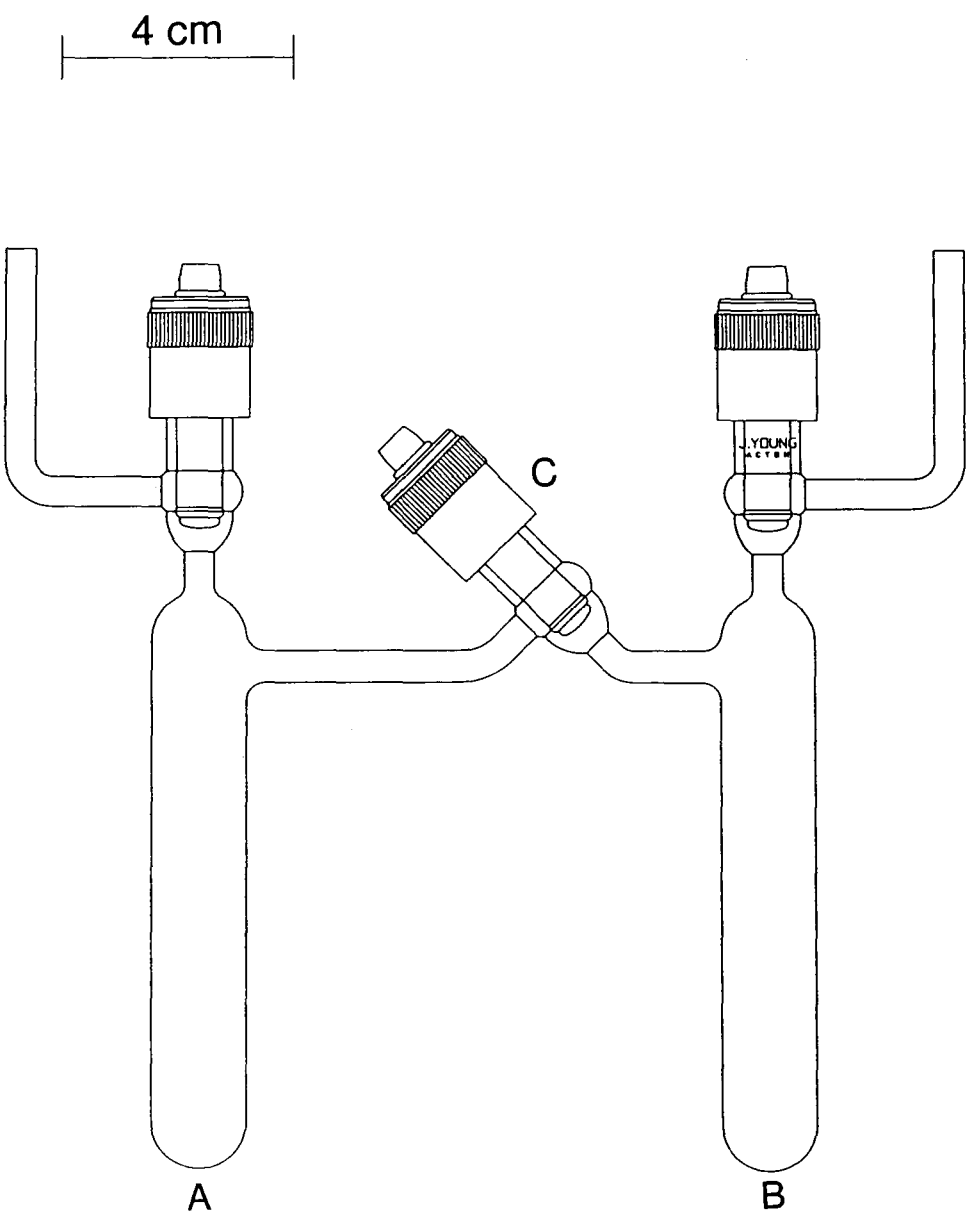

Figure 2.13 Glass reaction vessel used for the crystallization of $N(CH_3)_4^+Sb(OTeF_5)_4^-$; (A) Pyrex glass reaction vessel (arm A), (B) Pyrex glass reaction vessel (arm B), (C) 4-mm J. Young Teflon/glass stopcock.

separating the two arms was opened, allowing CH_3CN to diffuse into the SO_2ClF solution under static vacuum. The vessel was mounted in a fume hood at a 45° angle. There was no indication of crystal growth after several days. The solutions were allowed to mix, and again the vessel was left to stand. Clusters of clear, colorless crystalline plates formed over several days. The supernatant was decanted from the crystals into arm B, and the stopcock separating the two arms was closed. After the crystals were pumped dry under dynamic vacuum and arm A was pressurized with dry nitrogen at -78 °C, the vessel was transferred into the drybox, and arm A was cut open with a steel file. Using a microscope, four crystals were mounted and flame-sealed with a miniature oxygen-natural gas torch inside 0.1- and 0.2-mm i.d. Lindemann glass capillaries which were stored at 5 °C prior to mounting on the X-ray diffractometer. A structural solution could not be obtained from X-ray diffraction data acquired on a crystal at -120 °C due to disorder and possible twinning of the model having the *P6* space group ($a = b = 22.352$ Å, $c = 27.463$ Å, $\gamma = 120°$, $V = 11882.3$ Å^3).

(C) In the drybox, $N(CH_3)_4^+Sb(OTeF_5)_4^-$ (*ca.* 0.2 g, 0.174 mmol) was loaded into arm A of a two-arm Pyrex vessel equipped with one J. Young stopcock (see Figure 2.12). Approximately 5 mL of anhydrous CH_3CN was condensed onto the solid at -196 °C, which dissolved upon warming the solution to room temperature. The reactor was clamped in a vertical position with the solvent mixture in an ice/water bath and the empty side-arm B immersed in a dry ice/acetone bath. The CH_3CN slowly condensed into the cooler part of the reactor over several days, concentrating the solution until clear, colorless plates formed. The solution was then decanted off the crystals, the reactor was

connected to a vacuum line, and the residual CH_3CN was pumped off under dynamic vacuum. In the drybox equipped with a microscope, the crystals were removed by cutting open the reactor with a steel file and prying them off the walls with a steel needle. The crystals were mounted and flame-sealed with a miniature oxygen-natural gas torch inside 0.1-mm i.d. Lindemann glass capillaries. A structural solution could not be obtained from X-ray diffraction data acquired on a crystal at -120 °C due to disorder and/or twinning of the model having the *P4/m* space group ($a = b = c = 23.8367$ Å, V = 13543.690 Å^3).

Synthesis and Crystal Growth of $N(CH_2CH_3)_4^+Sb(OTeF_5)_4^-$

The $N(CH_2CH_3)_4^+Sb(OTeF_5)_4^-$ salt was prepared analogous to $N(CH_3)_4^+Sb(OTeF_5)_4^-$ using the following quantities of reagents: $Sb(OTeF_5)_3$ (1.5781 g, 1.884 mmol) and $N(CH_2CH_3)_4^+OTeF_5^-$ (0.6946 g, 1.883 mmol). After completion of the reaction, the SO_2ClF solvent was pumped off resulting in a colorless solid (2.2687 g, theor. 2.2718 g, 99.86% yield).

(A) The $N(CH_2CH_3)_4^+Sb(OTeF_5)_4^-$ salt (*ca.* 0.1 g) was dissolved in SO_2ClF (*ca.* 4-mL) in arm A of a two-arm Pyrex vessel equipped with J. Young stopcocks, and joined together by a J. Young stopcock (see Figure 2.13). Freon-114 (*ca.* 4-mL) was condensed into the empty side-arm B. The vessel was clamped at a 45° angle with arm A containing the $N(CH_2CH_3)_4^+Sb(OTeF_5)_4^-/SO_2ClF$ mixture in a water bath maintained at 20 °C. The Freon-114 solvent slowly condensed into the mixture over a period of 3 days, forming two distinct liquid layers and colorless crystals at the interphase of these layers. The

solution was then decanted off and the crystals were pumped dry under dynamic vacuum before being transferred into the drybox. Inside the drybox equipped with a microscope, the crystals were removed by cutting open the reactor with a steel file and flame-sealed with a miniature oxygen-natural gas torch inside 0.1-, 0.2-, and 0.3-mm i.d. Lindemann glass capillaries. X-ray diffraction showed that the material was polycrystalline.

(B) Crystal growth of $N(CH_2CH_3)_4^+Sb(OTeF_5)_4^-$ was attempted again according to the procedure applied in (A) with anhydrous CH_2Cl_2 instead of SO_2ClF. Crystals did not form from this mixture.

Synthesis of $N(CH_3)_4^+As(OTeF_5)_4^-$

In the drybox, $As(OTeF_5)_3$ (1.2551 g, 1.587 mmol) was loaded into a dry 10-mm o.d. FEP reaction vessel fused to a ¼-in. o.d. FEP tube and equipped with a Kel-F valve. The reactor was placed in a steel Dewar containing BB's cooled in the glass cryowell of the drybox at -196 °C, and a stoichiometric amount of $N(CH_3)_4^+OTeF_5^-$ (0.4973 g, 1.590 mmol) was added to the vessel. The cold tube was removed from the drybox and attached to a glass vacuum line where SO_2ClF solvent (*ca.* 3-mL) was condensed onto the solids at -196 °C. The mixture was warmed to room temperature and agitated vigorously to effect complete reaction before pumping off the solvent at 0 °C. The tube was then pressurized to *ca.* 1 atm with dry nitrogen at -78 °C and transferred into the drybox. The mass of the colorless product was 1.6603 g (theor. 1.7515 g, 94.8% yield).

Synthesis of $N(CH_2CH_3)_4^+As(OTeF_5)_4^-$

The $N(CH_2CH_3)_4^+As(OTeF_5)_4^-$ salt was prepared in a manner analogous to that of $N(CH_3)_4^+As(OTeF_5)_4^-$ using the following quantities of reagents: $As(OTeF_5)_3$ (1.2639 g, 1.598 mmol) and $N(CH_2CH_3)_4^+OTeF_5^-$ (0.5886 g, 1.596 mmol). After completion of the reaction, the SO_2ClF solvent was pumped off at 0 °C for *ca.* 3 h resulting in a colorless solid. The tube was pressurized to *ca.* 1 atm with dry nitrogen and transferred into the drybox where it was weighed. The mass of the product was 1.8189 g (theor. 1.8504 g, 98.3% yield).

X-RAY CRYSTALLOGRAPHY

Collection and Reduction of X-ray Data

The parameters used for the collection and reduction of X-ray diffraction data are summarized in Appendix A. The crystals were centered on a P4 Siemens diffractometer, equipped with a Siemens SMART 1K charge-coupled device (CCD) area detector (using the program SMART) and a rotating anode using graphite-monochromated Mo-Kα radiation (λ = 0.71073 Å). The diffraction data collection consisted of a full ψ rotation at $\chi = 0^\circ$ using (1200 + 50) 0.3° frames, followed by a series of short (100 frames) ω scans at various ψ and χ settings to fill the gaps. The crystal-to-detector distance was 5.000 cm, and the data collection was carried out in a 512 × 512 pixel mode using 2 × 2 pixel binning. Processing was carried out by using the program SAINT, which applied Lorentz and polarization corrections to three-dimensionally integrated diffraction spots. The

program SADABS was used for the scaling of diffraction data, the application of a decay correction, and an empirical absorption correction based on redundant reflections. The data set used in the solution of $F_5TeN(H)Xe^+AsF_6^-$ was obtained by an isotopic combination of two data sets obtained from two individual crystals using the program XPREP. A total of 2202 unique reflections remained after combination of unique reflections from the two $F_5TeN(H)Xe^+AsF_6^-$ crystals.

Solution and Refinement of the Structures

The final refinement results for each compound are listed in Appendix A and are summarized in the individual chapters. The XPREP program was used to confirm the unit cell dimensions and the crystal lattice. The final refinement for most of the structures was obtained by introducing anisotropic parameters for all the atoms, except the hydrogen atoms, an extinction parameter, and the recommended weight factor. For $XeOSeF_5^+AsF_6^-$, only the heavy atoms are anisotropic. For the partial solution of $[N(CH_3)_4^+]_2[Sb(OTeF_5)_5^{2-}]$ all atoms remain isotropic. The maximum electron densities in the final difference Fourier maps were located around the heavy atoms.

All calculations were performed on a Silicon Graphics Model 4600PC workstation with the SHELXL package for structure determination, refinement, and molecular graphics.

(A) $HC{\equiv}N{-}XeF^+AsF_6^-$, $HC{\equiv}NH^+AsF_6^-$, $CH_3C{\equiv}N{-}XeF^+AsF_6^-{\cdot}HF$, $Xe_2F_3^+AsF_6^-$, $(CH_3)_3CC{\equiv}N{-}XeF^+AsF_6^-$, *s*-$C_3F_3N_2N{-}XeF^+AsF_6^-{\cdot}2.5BrF_5$, and $C_5F_5N{-}$

$XeF^+AsF_6^-\cdot 2.5BrF_5$. A solution was obtained for $HC{\equiv}N{-}XeF^+AsF_6^-$ by using a Patterson function which located the general positions of the Xe and As atoms. Successive difference Fourier syntheses revealed the positions of the fluorine, nitrogen, and carbon atoms. The hydrogen atom was located after introducing anisotropic parameters for all other atoms.

A solution for $HC{\equiv}NH^+AsF_6^-$ was obtained by direct methods which initially located the positions of As and two F atoms. Successive difference Fourier syntheses revealed the positions of the other F atoms, as well as the N and C atoms on general positions. The location of the cation on the general position implied a positional disorder for the C and N atoms. Both C and N atoms were refined on the same position and with a site occupancy factor of 0.5. The spherical shape of the N/C ellipsoids showed that the two atoms indeed occupied almost identical sites. Consequently, the N–C bond length may be considered accurate. The positions of the H atoms were found from the Fourier difference map, and used in the final refinement of the structure. Due to the disorder, the N/C–H bond length is not accurate.

A solution was obtained for $CH_3C{\equiv}N{-}XeF^+AsF_6^-$ by using a Patterson function which located the positions of As, Xe, and two F atoms on As. Successive difference Fourier syntheses revealed the positions of all other atoms, except the hydrogen atoms. The positions of the methyl protons were calculated [d(C–H) $\approx$ 0.980 Å; U(H) fixed to -1.5 U(N)]. An HF molecule was also found after several successive Fourier syntheses.

The hydrogen coordinate of the HF molecule was constrained to "ride" with the fluorine coordinate [U(H) fixed to -1.5 U(N)].

Solutions were obtained for $Xe_2F_3^+AsF_6^-$ and $(CH_3)_3CC{\equiv}N{-}XeF^+AsF_6^-$ by direct methods which located the Xe and As atoms on general positions, except for one As and one F atom in $Xe_2F_3^+AsF_6^-$ which were located on special positions. Successive difference Fourier syntheses revealed the positions of all other atoms.

Direct methods were used to obtain solutions for s-$C_3F_3N_2N{-}XeF^+AsF_6^-\cdot 2.5BrF_5$ and $C_5F_5N{-}XeF^+AsF_6^- \cdot 2.5BrF_5$ which located all the atoms and positional disorder for 0.5 BrF_5 molecules after successive difference Fourier syntheses.

(B) $F_5TeNH_3^+AsF_6^-$, $F_5TeN(H)Xe^+AsF_6^-$, and F_5TeNH_2. A solution was obtained for $F_5TeNH_3^+AsF_6^-$ by direct methods which located a Te atom on a general position, and one Te and three As atoms on special positions. Successive difference Fourier syntheses revealed the positions of all the fluorine and nitrogen atoms. Nitrogen and fluorine atoms were assigned on the basis of their bond lengths with tellurium. The positions of the hydrogen atoms were calculated [d(N–H) ≈ 0.82 Å; U(H) fixed to -1.5 U(N)]. A solution was obtained for $F_5TeN(H)Xe^+AsF_6^-$ by using a Patterson function which located the general positions of the Te, As, and Xe atoms. Successive difference Fourier syntheses revealed the general positions of the N, H, and F atoms. A solution was obtained for the low-temperature (-113 °C) phase of F_5TeNH_2 by direct methods. Successive difference Fourier syntheses revealed the positions of the nitrogen and fluorine atoms which were assigned on the basis of their bond lengths with tellurium.

The hydrogen atoms were calculated to be disordered about three positions [d(N-H) ≈ 0.9 Å; U(H) fixed to -1.5 U(N), site occupancy fixed to 0.667]. Direct methods was also used to obtain a solution involving a sixth-fold disorder for the high-temperature (-5 °C) phase of F_5TeNH_2 [site occupancy fixed to 0.20833 for F/N and 0.04167 for N/F].

(C) $XeOTeF_5^+AsF_6^-$, $XeOSeF_5^+AsF_6^-$, $Xe(OTeF_5)_2$, and $Xe(OSeF_5)_2$. Direct methods were used to obtain solutions involving a four-fold disorder for $XeOTeF_5^+AsF_6^-$ and $XeOSeF_5^+AsF_6^-$ in which the xenon, tellurium or selenium, and arsenic atoms are on special positions. Successive difference Fourier syntheses revealed the general positions of all the oxygen and fluorine atoms. Solutions were obtained for $Xe(OTeF_5)_2$ and $Xe(OSeF_5)_2$ by direct methods and by using a Patterson function, respectively. The solution obtained for $Xe(OSeF_5)_2$ involved a three-fold positional disorder of fluorine and oxygen positions, as well as a disorder placed by symmetry.

(D) $[N(CH_3)_4^+]_2[Sb(OTeF_5)_5^{2-}]$. Initially, an attempt was made to solve the structure assuming the presence of the $N(CH_3)_4^+Sb(OTeF_5)_4^-$ salt. However, the calculated density was found to be equal to 3.936 $g\cdot cm^{-3}$ which seemed to be too high compared to that reported for $N(CH_3)_4^+Sb(OTeF_5)_6^-$ (3.135 $g\cdot cm^{-3}$).[107] A solution was obtained using direct methods and revealed that the anion was not $Sb(OTeF_5)_4^-$, but $Sb(OTeF_5)_5^{2-}$. Another attempt was made to solve the structure now assumed to be $[N(CH_3)_4^+]_2[Sb(OTeF_5)_5^{2-}]$ (ρ = 2.503 $g\cdot cm^{-3}$). Of the five suggested space groups, two were rejected ($I\bar{4}$ and $I\bar{4}2m$) since the symmetry obtained was unrealistic (*i.e.*, the four equatorial oxygen atoms were not coplanar). The structure was solved in *I4/m*, *I4*, and

I4/mmm. In all three space groups the $OTeF_5$ groups of the anion were found to be highly positionally disordered and, moreover, the axial $OTeF_5$ group and one of the $N(CH_3)_4^+$ cation were also found to be positionally disordered, alternating along the axial axis. The best preliminary solution was obtained in the *I4* space group.

NUCLEAR MAGNETIC RESONANCE SPECTROSCOPY

Instrumentation

Nuclear magnetic resonance spectra were recorded unlocked (field drift < 0.1 Hz h^{-1}) on a Bruker DRX-500 spectrometer equipped with an 11.744 T cryomagnet and a Silicon Graphics INDY workstation. For low temperature work, the NMR probe was cooled using a nitrogen flow and variable temperature controller (BV-T 2000). The ^{19}F NMR spectra were obtained using a 5-mm broad-band inverse probe operating at 470.599 MHz. The spectra were recorded in 32 K memories. A spectral width setting of 30 or 50 kHz was employed, yielding data point resolutions of 0.763 and 0.458 Hz/data point and acquisition times of 0.66 and 1.09 s, respectively. No relaxation delays were applied. Typically, 350-2000 transients were accumulated. The pulse width corresponding to a bulk magnetization tip angle, θ, of approximately 30° was 2.5 μs. No line-broadening was used in the exponential multiplication of the free induction decays prior to Fourier transformation.

The ^{125}Te NMR spectra were obtained using a 5-mm broad-band inverse probe which was tuned to 157.794 MHz to observe ^{125}Te. Free induction decays for ^{125}Te were accumulated in 32 K memories with a spectral width setting of 50 kHz, yielding an

acquisition time of 0.33 s and a data point resolution of 1.53 Hz/data point. No relaxation delays were applied. Typically, 10,000 - 95,000 transients were accumulated for the ^{125}Te NMR spectra. The pulse width corresponding to a bulk magnetization tip angle, θ, of approximately 90° was 11 μs. A line-broadening parameter used in the exponential multiplication of the free induction decays was 20 Hz.

The ^{19}F and ^{125}Te NMR spectra were referenced externally at 30 °C to samples of neat $CFCl_3$ and $Te(CH_3)_2$, respectively. The chemical shift convention used is that a positive (negative) sign indicates a chemical shift to high (low) frequency of the reference compound.

The ^{19}F and ^{125}Te NMR samples were prepared in 5-mm o.d. medium wall precision glass NMR tubes (Wilmad) fused to ¼-in. o.d. glass tubing which were attached to 4-mm J. Young glass valves equipped with PTFE barrels. Solids were weighed into the previously dried NMR tubes in the drybox and transferred to a glass vacuum line, where SO_2ClF, CH_3CN, or CH_3CH_2CN solvent was distilled *in vacuo* onto the solid at -78 °C. The tubes were flame-sealed under dynamic vacuum at -196 °C.

Spectral Simulations

The ^{19}F and ^{125}Te NMR spectral simulations of $N(CH_2CH_3)_4^+As(OTeF_5)_4^-$ in SO_2ClF and of $N(CH_3)_4^+Sb(OTeF_5)_4^-$ in CH_3CH_2CN, along with their impurities, were carried out using an Isotopomer NMR program on a Pentium 486 computer. Chemical

shifts and coupling constants were introduced and perturbed one at a time until visual agreement between the simulated and experimental spectra were obtained.

The ^{19}F and ^{125}Te NMR spectral simulations of $N(CH_3)_4^+Sb(OTeF_5)_4^-$ in CH_3CH_2CN at various temperatures were carried out using the lineshape analysis program MEXICO[129] in conjunction with Bruker's XWINNMR program on a Silicon Graphics INDY Workstation. Chemical shifts, coupling constants, and a rate were introduced for what appeared to be two exchanging sites and perturbed one at a time until visual agreement between the simulated and experimental lineshapes were obtained. The estimated error for the measurements of exchange rates derived from the simulations is $\pm$ 200 s^{-1}. The calculated exchange rates were used to determine the thermodynamic activation parameters, E_a, $\Delta H^{\ddagger}$, $\Delta S^{\ddagger}$, and $\Delta G^{\ddagger}$, for the exchange process.

RAMAN SPECTROSCOPY

Instrumentation

Summaries of the Raman spectrometer conditions for low-temperature Raman spectroscopic characterization of each compound are detailed in Table 2.4. Raman spectra were recorded on a Bruker RFS 100 FT Raman spectrometer which employed a quartz beamsplitter and a liquid nitrogen-cooled Ge diode detector. The backscattered (180 $^{\circ}C$) radiation was sampled and spectra were corrected for instrument response. Rayleigh filters consisting of a series of transmission and reflection filters were used. The scanner velocity was 5 kHz and the wavelength range for acquisition was 5500 –

Table 2.4 Conditions for Acquisition of the Raman Spectra.[a]

Sample	Laser Power (mW)	Spectral Resolution (cm^{-1})	Number of Scans	Temperature (°C)
$XeOTeF_5^+AsF_6^-$	200	2	500	-145
$XeOSeF_5^+AsF_6^-$	178	2	200	-145
$N(CH_3)_4^+Sb(OTeF_5)_4^-$ [b]	75 (165) [50]	2 (4) [2]	100 (200) [100]	-140 (30) [-140]
$N(CH_2CH_3)_4^+Sb(OTeF_5)_4^-$ [c]	[200]	[2]	[100]	[-140]
$N(CH_3)_4^+As(OTeF_5)_4^-$	100	2	150	-140
$N(CH_2CH_3)_4^+As(OTeF_5)_4^-$ [c]	[250]	[2]	[1000]	[-166]

[a] Unless otherwise indicated, the spectra were recorded on powdered microcrystalline samples which were sealed under *ca.* 1 atm of dry nitrogen in Pyrex capillaries.

[b] Values in parentheses denote the conditions in which spectra were recorded on samples in CH_3CN solution in 5-mm o.d. medium-wall glass NMR tubes, which were flame-sealed.

[c] Values in square brackets denote the conditions in which spectra were recorded on powdered microcrystalline samples in 5-mm o.d. medium-wall glass NMR tubes, which were flame-sealed.

10500 cm^{-1} when shifted relative to the laser line at 9394 cm^{-1}, giving a spectral range of 3895 to -1105 cm^{-1}. The usable Stokes range was approximately 50 – 3500 cm^{-1}. The Fourier transformations were carried out by using a Blackman Harris 3-term apodization and a zero-filling factor of 4. The 1064-nm line of a Nd YAG laser (350 mW maximum output) was used for excitation of the samples with a laser spot of *ca.* 0.2-mm.

THEORETICAL CALCULATIONS

Theoretical calculations were performed by Dr. David A. Dixon of the William R. Wiley Environmental Molecular Sciences Laboratory, Pacific Northwest Laboratory, 906 Batelle Blvd., P.O. Box 999, KI-83 Richland, Washington 99352. All calculations were done with the density functional theory program Dgauss on SGI computers. The basis set for the nitrogen, oxygen, and fluorine atoms is of the form (621/41/1) (DZVP) with a (7/3/3) fitting set. For selenium, tellurium, and xenon, the basis set has the form (633321/53211/531) with a fitting basis set of the form (10/5/5). For hydrogen, the basis set has the form (4/1) and a fitting basis set of the form (4). This basis set is denoted as DZVP. The calculations were done at the local level with the potential fit of Vosko, Wilk, and Nusair. The geometries were optimized by using analytic gradient methods, and second derivatives were also calculated analytically.

CHAPTER 3

STRUCTURAL CHARACTERIZATIONS OF XENON(II)–NITROGEN BONDED ADDUCT CATIONS

INTRODUCTION

While several X-ray crystal structures of compounds containing xenon-oxygen or xenon-fluorine bonds, and of xenon bonded to other highly electronegative ligands through oxygen have been reported, few examples of xenon-nitrogen bonded species have been definitively characterized by single-crystal X-ray diffraction.[17] They include the neutral compound $FXeN(SO_2F)_2$[62] and the $[MeC{\equiv}N{\cdots}Xe{-}C_6F_5]^+$,[66] 2,6-$C_5H_3F_2N{\cdots}Xe{-}C_6F_5^+$,[67] and $XeN(SO_2F)_2^+$ [20] cations, where $XeN(SO_2F)_2^+$ has the most covalent Xe–N bond (2.02(1) Å).

The XeF^+ cation has long been known to exhibit Lewis acid character in its salts with weakly fluorobasic anions such as AsF_6^-, SbF_6^-, and $Sb_2F_{11}^-$. The XeF^+ cation is not a naked cation, but interacts with the fluoroanion in the solid state by means of a weak covalent Xe···F contact to form $F{-}Xe^+{\cdots}F{-}MF_5^-$ or $F{-}Xe^+{\cdots}F{-}M_2F_{10}^-$ fluorine bridges. Recently, it has been shown by Raman and NMR spectroscopy that several classes of oxidatively resistant organic and perfluoro-organic nitrogen bases, D, can interact with the Lewis acid, XeF^+, in HF to form xenon-nitrogen bonded adduct cations, $D{-}XeF^+$, according to equation (3.1). Given the oxidizing strength of XeF^+, appropriate

$$D + XeF^+AsF_6^- \xrightarrow{HF} D\text{–}XeF^+AsF_6^- \quad (3.1)$$

nitrogen bases that are resistant to oxidation may be selected according to their first adiabatic ionization potentials, which should be close to or exceed the estimated electron affinity of XeF^+ (EA ≈ 10.9 eV).[71] Those $D\text{–}XeF^+AsF_6^-$ salts which have been isolated at low temperatures by the reaction of equimolar amounts of XeF^+ with neutral bases in HF or by the reaction of XeF_2 with the protonated base in BrF_5 [eq (3.2)] include

$$DH^+AsF_6^- + XeF_2 \xrightarrow{BrF_5} D\text{–}XeF^+AsF_6^- + HF \quad (3.2)$$

$R\text{–}C{\equiv}N\text{–}XeF^+AsF_6^-$ (R = H, alkyl, fluoroalkyl, C_6F_5),[68,69] *s*-$C_3F_3N_2N\text{–}XeF^+AsF_6^-$,[72] $C_5F_5N\text{–}XeF^+AsF_6^-$,[70] and *n*-$CF_3C_5F_4N\text{–}XeF^+AsF_6^-$ (*n* = 2, 3, 4).[70,72]

In the present work, a significant extension of noble-gas chemistry has been achieved by determining the low-temperature X-ray crystal structures of $HC{\equiv}N\text{–}XeF^+AsF_6^-$, $CH_3C{\equiv}N\text{–}XeF^+AsF_6^-\cdot HF$, $(CH_3)_3CC{\equiv}N\text{–}XeF^+AsF_6^-$, *s*-$C_3F_3N_2N\text{–}XeF^+AsF_6^-\cdot 2.5BrF_5$, and $C_5F_5N\text{–}XeF^+AsF_6^-\cdot 2.5BrF_5$ which provide the detailed structures of the cations which had been previously characterized by multi-NMR and Raman spectroscopy. The adduct salts were prepared as previously reported according to equation (3.1) or (3.2) with alkyl and (fluoro)aryl nitrogen bases having first adiabatic ionization potentials of 13.80 eV, 12.194 eV, 11.11 eV, 11.50 eV, and 10.08 eV for HCN,[68,69] $CH_3C{\equiv}N$,[17] $(CH_3)_3CC{\equiv}N$,[17,44] *s*-$C_3F_3N_3$,[72] and C_5F_5N,[70] respectively. The complete characterization of these salts by single-crystal X-ray diffraction has been made possible by recent developments in this laboratory that have led to a reliable and routine

method for the low-temperature growing, mounting, and data collection of thermally unstable crystals (see **Experimental Section**).

Since HCN is among the most oxidatively resistant ligands investigated thus far, the X-ray crystal structure of $HC{\equiv}NH^+AsF_6^-$ was also determined in order to better understand the nature of the bonding in $HC{\equiv}N{-}XeF^+AsF_6^-$, as well as to complement recent theoretical investigations of the $HC{\equiv}N{-}NgF^+$ (Ng = Xe, Kr) cations at the SCF level.[88-95]

A systematic comparison of the bonding in the title compounds based on ligand electronegativities will be dealt with in this Chapter and compared with conclusions drawn from NMR and Raman spectroscopy,[68-70,72] as well as theoretical investigations of $HC{\equiv}N{-}XeF^+$.[88-95]

RESULTS AND DISCUSSION

Preparation of $HC{\equiv}N{-}XeF^+AsF_6^-$ and $HC{\equiv}NH^+AsF_6^-$

Hydrogen cyanide, HCN, was prepared as a solution in HF by the reaction of KCN in HF solvent according to equation (3.3). The thermally unstable

$$KCN + (x{+}1)HF \longrightarrow KHF_2 \cdot xHF + HCN \qquad (3.3)$$

$HC{\equiv}N{-}XeF^+AsF_6^-$ salt was prepared by vacuum distillation of an HF solution of HCN onto a stoichiometric amount of $XeF^+AsF_6^-$ according to the method of Schrobilgen and Emara [eq (3.4)],[68,69] followed by warming to -10 °C to effect reaction and dissolution.

$$HCN + XeF^+AsF_6^- \xrightarrow{HF} HC{\equiv}N{-}XeF^+AsF_6^- \qquad (3.4)$$

Colorless, needle-shaped crystals of $HC{\equiv}N{-}XeF^+AsF_6^-$ were grown from HF at -15 °C.

Hydrogen cyanide was protonated in HF solvent containing AsF_5 forming $HC{\equiv}NH^+AsF_6^-$ [eq (3.5)]. Colorless, crystals of $HC{\equiv}NH^+AsF_6^-$ were slowly grown from

$$HCN + AsF_5 \xrightarrow{HF} HC{\equiv}NH^+AsF_6^- \quad (3.5)$$

HF over the temperature range -8 to -20 °C.

Preparation of $R{-}C{\equiv}N{-}XeF^+AsF_6^-$ ($R = CH_3$, $(CH_3)_3C$) and $Xe_2F_3^+AsF_6^-$

Equimolar amounts of $XeF^+AsF_6^-$ and $R{-}C{\equiv}N$ react in anhydrous HF solvent forming $R{-}C{\equiv}N{-}XeF^+AsF_6^-$ according to the method of Schrobilgen and Emara [eq (3.6)].[44,69] Colorless, needle-shaped crystals of $(CH_3)_3CC{\equiv}N{-}XeF^+AsF_6^-$ and crystalline

$$XeF^+AsF_6^- + R{-}C{\equiv}N \xrightarrow[ca.\ -20\ °C]{HF} R{-}C{\equiv}N{-}XeF^+AsF_6^- \quad (3.6)$$

plates of $CH_3C{\equiv}N{-}XeF^+AsF_6^-$ were grown from HF at -46 and -60 °C.

The addition of an excess of $XeF^+AsF_6^-$ with respect to $(CH_3)_3CC{\equiv}N$ results in a shift in equilibrium between the $(CH_3)_3CC{\equiv}N{-}XeF^+$ and $(CH_3)_3CC{\equiv}NH^+$ cations according to equations (3.7) – (3.11), favoring the formation of $Xe_2F_3^+AsF_6^-$ and its crystallization from HF solvent.[44]

$$XeF^+AsF_6^- + 2HF \rightleftharpoons XeF_2 + H_2F^+AsF_6^- \quad (3.7)$$

$$(CH_3)_3CC{\equiv}N + (x+1)HF \rightleftharpoons (CH_3)_3CC{\equiv}NH^+F(HF)_x^- \quad (3.8)$$

$$(CH_3)_3CC{\equiv}NH^+F(HF)_x^- + XeF_2 \rightleftharpoons (CH_3)_3CC{\equiv}N{-}XeF^+F(HF)_x^- \quad (3.9)$$

$$(CH_3)_3CC{\equiv}N{-}XeF^+F(HF)_x^- + H^+AsF_6^- \rightleftharpoons (CH_3)_3CC{\equiv}N{-}XeF^+AsF_6^- + (1+x)HF \quad (3.10)$$

$$XeF^+AsF_6^- + XeF_2 \rightleftharpoons Xe_2F_3^+AsF_6^- \quad (3.11)$$

Preparation of *s*-$C_3F_3N_2N$–$XeF^+AsF_6^-$ · 2.5BrF_5 and C_5F_5N–$XeF^+AsF_6^-$ · 2.5BrF_5.

The *s*-$C_3F_3N_2N$–$XeF^+AsF_6^-$ salt was prepared by the reaction of neat liquid *s*-$C_3F_3N_3$ with $XeF^+AsF_6^-$ at room temperature followed by removal of excess *s*-$C_3F_3N_3$ *in vacuo* at ambient temperature according to the method of Schrobilgen and Paprica [eq (3.12)].[72,130] The resulting white powder is stable indefinitely at room temperature. Pale

$$XeF^+AsF_6^- + s\text{-}C_3F_3N_3 \longrightarrow s\text{-}C_3F_3N_2N\text{–}XeF^+AsF_6^- \quad (3.12)$$

yellow crystals of *s*-$C_3F_3N_2N$–$XeF^+AsF_6^-$ · 2.5BrF_5 were grown from BrF_5 at *ca.* -40 °C.

Equimolar amounts of C_5F_5N and AsF_5 react in anhydrous HF to form $C_5F_5NH^+AsF_6^-$ according to equation (3.13). Removal of the HF solvent followed by the addition of a stoichiometric amount of XeF_2 and reaction in BrF_5 solvent form C_5F_5N–$XeF^+AsF_6^-$ according to the method of Schrobilgen and Emara [eq (3.14)].[70] Pale

$$C_5F_5N + AsF_5 \xrightarrow{HF} C_5F_5NH^+AsF_6^- \quad (3.13)$$

$$C_5F_5NH^+AsF_6^- + XeF_2 \xrightarrow{BrF_5} C_5F_5N\text{–}XeF^+AsF_6^- + HF \quad (3.14)$$

yellow crystals of C_5F_5N–$XeF^+AsF_6^-$ were grown from BrF_5 as the solvent was slowly pumped off under dynamic vacuum at -56 °C.

X-Ray Crystal Structures of R–C≡N–$XeF^+AsF_6^-$ (R = H, $(CH_3)_3C$), CH_3C≡N–$XeF^+AsF_6^-$·HF, D–$XeF^+AsF_6^-$ (D = *s*-$C_3F_3N_2N$, C_5F_5N), HC≡$NH^+AsF_6^-$, and $Xe_2F_3^+AsF_6^-$

A summary of the refinement results and other crystallographic information are given in Table 3.1. The final atomic coordinates and equivalent isotropic thermal

Table 3.1 Summary of Crystal Data and Refinement Results for $HC{\equiv}N{-}XeF^+AsF_6^-$, $HC{\equiv}NH^+AsF_6^-$, $CH_3C{\equiv}N{-}XeF^+AsF_6^-{\cdot}HF$, $(CH_3)_3CC{\equiv}N{-}XeF^+AsF_6^-$, *s*-$C_3F_3N_2N{-}XeF^+AsF_6^-\cdot 2.5BrF_5$, $C_5F_5N{-}XeF^+AsF_6^-\cdot 2.5BrF_5$, and $Xe_2F_3^+AsF_6^-$.

	$HC{\equiv}N{-}XeF^+AsF_6^-$	$HC{\equiv}NH^+AsF_6^-$	$CH_3C{\equiv}N{-}XeF^+AsF_6^-{\cdot}HF$	$(CH_3)_3CC{\equiv}N{-}XeF^+AsF_6^-$
empirical formula	$AsCF_7HNXe$	$AsCF_6H_2N$	$AsC_4F_7H_9NXe$	$AsC_5F_7H_9NXe$
space group (No.)	*Pbca* (61)	$P\bar{1}$ (2)	$P\bar{1}$ (2)	$Pca2_1$ (29)
a (Å)	9.8025(8)	5.051(2)	7.8397(8)	17.9177(8)
b (Å)	10.5354(8)	5.088(2)	7.9901(8)	6.0500(2)
c (Å)	14.5381(11)	5.359(2)	8.5539(9)	10.9365(4)
α (deg.)	90	98.983(6)	94.873(2)	90
β (deg.)	90	98.96(2)	114.9090(10)	90
γ (deg.)	90	95.146(4)	94.045(3)	90
V ($Å^3$)	1501.4(2)	133.48(10)	480.85(9)	1185.54(8)
molecules/unit cell	8	1	2	4
mol. wt. (g mol^{-1})	366.25	216.96	400.28	422.35
calcd. density (g cm^{-3})	3.241	2.699	2.765	2.366
T (°C)	-122	-122	-125	-127
μ (mm^{-1})	9.033	6.414	7.078	5.737
λ(Å) used for data collection	0.71073	0.71073	0.71073	0.71073
final agreement factors[a]	$R_1 = 0.0210$	$R_1 = 0.0431$	$R_1 = 0.0530$	$R_1 = 0.0257$
	$wR_2 = 0.0560$	$wR_2 = 0.1191$	$wR_2 = 0.1357$	$wR_2 = 0.0443$

[a] R_1 is defined as $\Sigma||F_o| - |F_c||/\Sigma|F_o|$ for $I > 2\sigma(I)$; wR_2 is defined as $[\Sigma[w(F_o^2 - F_c^2)^2]/\Sigma w(F_o^2)^2]^{1/2}$ for $I > 2\sigma(I)$.

Table 3.1 (continued)

	***s*-$C_3F_3N_2N$–$XeF^+AsF_6^-$·2.5BrF_5**	**C_5F_5N–$XeF^+AsF_6^-$·2.5BrF_5**	**$Xe_2F_3^+AsF_6^-$**
empirical formula	$AsC_3F_{22.5}N_3XeBr_{2.5}$	$AsC_5F_{24.5}NXeBr_{2.5}$	AsF_9Xe_2
space group (No.)	$P\bar{1}$ (2)	$P\bar{1}$ (2)	*C2/c* (15)
a (Å)	7.831(3)	7.871(3)	25.756(3)
b (Å)	10.353(4)	10.473(4)	8.556(1)
c (Å)	13.282(5)	13.931(5)	15.356(2)
α (deg.)	75.179(9)	72.916(7)	90
β (deg.)	75.797(6)	75.900(7)	126.592(5)
γ (deg.)	73.135(7)	72.776(8)	90
V ($Å^3$)	979.0(6)	1033.0(7)	2716.9(6)
molecules/unit cell	2	2	12
mol. wt. (g mol^{-1})	911.55	945.55	508.52
calcd. density (g cm^{-3})	3.092	3.040	3.730
T (°C)	-122	-122	-127
μ (mm^{-1})	8.746	8.306	11.203
λ(Å) used for data collection	0.71073	0.71073	0.71073
final agreement factors[a]	$R_1 = 0.0473$ $wR_2 = 0.1188$	$R_1 = 0.0580$ $wR_2 = 0.1447$	$R_1 = 0.0389$ $wR_2 = 0.0758$

[a] R_1 is defined as $\Sigma||F_o| - |F_c||/\Sigma|F_o|$ for $I > 2\sigma(I)$; wR_2 is defined as $[\Sigma[w(F_o^2 - F_c^2)^2]/\Sigma w(F_o^2)^2]^{1/2}$ for $I > 2\sigma(I)$.

parameters are summarized in Appendix B. Important bond lengths and angles are listed in Table 3.2.

R–C≡N–XeF$^+$AsF$_6^-$ (R = H, (CH$_3$)$_3$C), CH$_3$C≡N–XeF$^+$AsF$_6^-$·HF, and HC≡NH$^+$AsF$_6^-$

The X-ray crystal structures of HC≡N–XeF$^+$AsF$_6^-$ (Figure 3.1) CH$_3$C≡N–XeF$^+$AsF$_6^-$·HF (Figure 3.2), and (CH$_3$)$_3$CC≡N–XeF$^+$AsF$_6^-$ (Figure 3.3) are in agreement with earlier Raman and multi-NMR spectroscopic findings[68,69] and provide among the first detailed structures containing formally sp-hybridized nitrogen centers that are bonded to xenon. The MeC≡N···Xe–C$_6$F$_5^+$ cation[66] has been previously reported, but the Xe–N interaction is considerably weaker than those in the present structures (*vide infra*). Knowledge of the detailed structures of HC≡N–XeF$^+$AsF$_6^-$ and HC≡NH$^+$AsF$_6^-$ (Figure 3.4) complement the recent theoretical investigations of the bonding in HC≡N–NgF$^+$ (Ng = Kr, Xe) at the SCF level using the theory of atoms in molecules.[88-95]

The structures consist of well-separated cations and AsF$_6^-$ anions with no evidence of significant contacts by means of Xe···F–As bridges. The AsF$_6^-$ anions are nearly octahedral with average As–F bond distances (HC≡N–XeF$^+$AsF$_6^-$, 1.715(6) Å; CH$_3$C≡N–XeF$^+$AsF$_6^-$·HF, 1.721(5) Å; (CH$_3$)$_3$CC≡N–XeF$^+$AsF$_6^-$, 1.727(7) Å; HC≡NH$^+$AsF$_6^-$, 1.722(11) Å) and *cis* F–As–F angles (HC≡N–XeF$^+$AsF$_6^-$, 88.95(9) – 91.05(10)°; CH$_3$C≡N–XeF$^+$AsF$_6^-$·HF, 88.9(3) – 91.6(3)°; (CH$_3$)$_3$CC≡N–XeF$^+$AsF$_6^-$, 88.8(2) – 91.2(2)°; HC≡NH$^+$AsF$_6^-$, 89.8(2) – 90.4(2)°) that are comparable to values found in the literature.[10,19,131]

Table 3.2 Experimental Geometries for $HC{\equiv}N{-}XeF^+AsF_6^-$, $HC{\equiv}NH^+AsF_6^-$, $CH_3C{\equiv}N{-}XeF^+AsF_6^-{\cdot}HF$, $(CH_3)_3CC{\equiv}N{-}XeF^+AsF_6^-$, *s*-$C_3F_3N_2N{-}XeF^+AsF_6^-\cdot 2.5BrF_5$, $C_5F_5N{-}XeF^+AsF_6^-\cdot 2.5BrF_5$, and $Xe_2F_3^+AsF_6^-$.

$HC{\equiv}N{-}XeF^+AsF_6^-$

Bond Lengths (Å)

	expt		expt
Xe(1)-F(1)	1.936(2)	As(1)-F(5)	1.721(2)
Xe(1)-N(1)	2.235(3)	As(1)-F(6)	1.723(2)
As(1)-F(2)	1.722(2)	As(1)-F(7)	1.733(2)
As(1)-F(3)	1.737(2)	N(1)-C(1)	1.116(4)
As(1)-F(4)	1.728(2)	C(1)-H(1)	0.90(5)

Bond Angles (deg.)

	expt		expt
F(1)-Xe(1)-N(1)	179.83(9)	F(3)-As(1)-F(5)	90.75(10)
Xe(1)-N(1)-C(1)	177.7(3)	F(3)-As(1)-F(6)	89.54(9)
N(1)-C(1)-H(1)	173(3)	F(3)-As(1)-F(7)	88.95(9)
F(2)-As(1)-F(3)	89.33(10)	F(4)-As(1)-F(5)	90.12(11)
F(2)-As(1)-F(4)	89.79(10)	F(4)-As(1)-F(6)	90.47(9)

Table 3.2 (continued)

F(2)-As(1)-F(5)	179.72(11)	F(4)-As(1)-F(7)	91.05(10)
F(2)-As(1)-F(6)	90.56(10)	F(5)-As(1)-F(6)	89.71(9)
F(2)-As(1)-F(7)	90.36(10)	F(5)-As(1)-F(7)	89.37(10)
F(3)-As(1)-F(4)	179.13(10)	F(6)-As(1)-F(7)	178.22(9)

$HC{\equiv}NH^{+}AsF_6^{-}$

Bond Lengths (Å)

	expt		expt
As(1)-F(1)	1.743(3)	As(1)-F(3)	1.708(3)
As(1)-F(2)	1.714(3)	N/C-C/N	1.103(11)

Bond Angles (deg.)

	expt
F(1)-As(1)-F(2)	89.8(2)
F(1)-As(1)-F(3)	90.2(2)
F(2)-As(1)-F(3)	90.4(2)

Table 3.2 (continued)

$CH_3C{\equiv}N{-}XeF^+AsF_6^-{\cdot}HF$

Bond Lengths (Å)			
	expt		expt
Xe(1)-F(1)	1.947(5)	As(1)-F(5)	1.712(6)
Xe(1)-N(1)	2.179(7)	As(1)-F(6)	1.713(6)
As(1)-F(2)	1.719(5)	As(1)-F(7)	1.741(5)
As(1)-F(3)	1.732(6)	N(1)-C(1)	1.120(11)
As(1)-F(4)	1.711(6)	C(1)-C(2)	1.451(13)

Bond Angles (deg.)			
	expt		expt
F(1)-Xe(1)-N(1)	178.7(3)	F(3)-As(1)-F(7)	89.4(3)
F(2)-As(1)-F(3)	89.4(3)	F(4)-As(1)-F(5)	91.6(3)
F(2)-As(1)-F(4)	90.8(3)	F(4)-As(1)-F(6)	91.2(4)
F(2)-As(1)-F(5)	90.4(3)	F(4)-As(1)-F(7)	179.5(3)
F(2)-As(1)-F(6)	178.0(3)	F(5)-As(1)-F(6)	89.4(3)
F(2)-As(1)-F(7)	88.9(3)	F(5)-As(1)-F(7)	88.9(3)

Table 3.2 (continued)

F(3)-As(1)-F(4)	90.2(3)	F(6)-As(1)-F(7)	89.1(3)
F(3)-As(1)-F(5)	178.3(3)	C(1)-N(1)-Xe(1)	175.0(8)
F(3)-As(1)-F(6)	90.7(3)	N(1)-C(1)-C(2)	178.8(10)

$(CH_3)_3CC{\equiv}N{-}XeF^+AsF_6^-$

Bond Lengths (Å)

	expt		expt
F(1)-Xe(1)	1.952(3)	As(1)-F(2)	1.736(3)
Xe(1)-N(1)	2.212(4)	As(1)-F(3)	1.705(3)
N(1)-C(1)	1.147(6)	As(1)-F(4)	1.716(3)
C(1)-C(2)	1.491(7)	As(1)-F(5)	1.708(3)
C(2)-C(3)	1.533(8)	As(1)-F(6)	1.714(3)
C(2)-C(4)	1.541(7)	As(1)-F(7)	1.713(4)
C(2)-C(5)	1.545(7)		

Table 3.2 (continued)

Bond Angles (deg.)

	expt		expt
F(1)-Xe(1)-N(1)	178.1(1)	F(2)-As(1)-F(6)	89.2(2)
C(1)-N(1)-Xe(1)	166.9(4)	F(2)-As(1)-F(7)	88.8(2)
N(1)-C(1)-C(2)	176.3(5)	F(3)-As(1)-F(4)	89.9(2)
C(1)-C(2)-C(3)	107.5(4)	F(3)-As(1)-F(5)	90.0(2)
C(1)-C(2)-C(4)	106.9(4)	F(3)-As(1)-F(6)	89.4(2)
C(1)-C(2)-C(5)	108.0(4)	F(3)-As(1)-F(7)	179.6(2)
C(3)-C(2)-C(4)	111.7(5)	F(4)-As(1)-F(5)	90.0(2)
C(3)-C(2)-C(5)	111.1(5)	F(4)-As(1)-F(6)	91.2(2)
C(4)-C(2)-C(5)	111.4(5)	F(4)-As(1)-F(7)	90.3(2)
F(2)-As(1)-F(3)	91.0(2)	F(5)-As(1)-F(6)	178.7(2)
F(2)-As(1)-F(4)	179.1(2)	F(5)-As(1)-F(7)	90.3(2)
F(2)-As(1)-F(5)	89.6(1)	F(6)-As(1)-F(7)	90.2(2)

Table 3.2 (continued)

s-$C_3F_3N_2N$–$XeF^+AsF_6^- \cdot 2.5BrF_5$

Bond Lengths (Å)			
	expt		expt
F(1)-Xe(1)	1.931(5)	As(1)-F(12)	1.738(4)
Xe(1)-N(1)	2.316(6)	Br(1)-F(13)	1.687(4)
N(1)-C(1)	1.335(9)	Br(1)-F(14)	1.765(5)
N(1)-C(5)	1.366(9)	Br(1)-F(15)	1.791(5)
C(1)-F(2)	1.301(8)	Br(1)-F(16)	1.777(5)
C(1)-N(3)	1.311(10)	Br(1)-F(17)	1.751(5)
N(3)-C(3)	1.308(10)	Br(2)-F(18)	1.693(5)
C(3)-F(4)	1.304(8)	Br(2)-F(19)	1.765(5)
C(3)-N(5)	1.334(10)	Br(2)-F(20)	1.747(5)
N(5)-C(5)	1.293(9)	Br(2)-F(21)	1.773(5)
C(5)-F(6)	1.296(8)	Br(2)-F(22)	1.773(5)
As(1)-F(7)	1.710(4)	Br(3)-F(23)	1.749(14)
As(1)-F(8)	1.734(4)	Br(3)-F(24)	1.77(2)
As(1)-F(9)	1.726(4)	Br(3)-F(25)	1.77(2)

Table 3.2 (continued)

As(1)-F(10)	1.726(4)	Br(3)-F(26)	1.75(2)
As(1)-F(11)	1.725(4)	Br(3)-F(27)	1.73(2)

Bond Angles (deg.)

	expt		expt
F(1)-Xe(1)-N(1)	178.6(2)	F(13)-Br(1)-F(14)	85.5(3)
C(1)-N(1)-C(5)	113.4(6)	F(13)-Br(1)-F(15)	83.6(3)
Xe(1)-N(1)-C(1)	122.0(5)	F(13)-Br(1)-F(16)	84.2(3)
Xe(1)-N(1)-C(5)	124.6(5)	F(13)-Br(1)-F(17)	85.2(3)
F(2)-C(1)-N(1)	115.0(6)	F(14)-Br(1)-F(15)	90.4(3)
F(2)-C(1)-N(3)	118.8(6)	F(14)-Br(1)-F(16)	169.6(3)
N(3)-C(1)-N(1)	126.2(7)	F(14)-Br(1)-F(17)	89.0(3)
C(1)-N(3)-C(3)	113.0(6)	F(15)-Br(1)-F(16)	89.3(2)
F(4)-C(3)-N(3)	116.4(7)	F(15)-Br(1)-F(17)	168.9(2)
F(4)-C(3)-N(5)	114.8(7)	F(16)-Br(1)-F(17)	89.3(3)
N(3)-C(3)-N(5)	128.8(7)	F(18)-Br(2)-F(19)	83.8(3)
C(3)-N(5)-C(5)	112.7(6)	F(18)-Br(2)-F(20)	84.5(3)
N(5)-C(5)-F(6)	119.7(6)	F(18)-Br(2)-F(21)	83.6(3)

Table 3.2 (continued)

N(5)-C(5)-N(1)	125.9(6)	F(18)-Br(2)-F(22)	84.0(3)
F(6)-C(5)-N(1)	114.3(7)	F(19)-Br(2)-F(20)	89.2(3)
F(7)-As(1)-F(8)	179.3(2)	F(19)-Br(2)-F(21)	167.4(2)
F(7)-As(1)-F(9)	91.0(2)	F(19)-Br(2)-F(22)	89.2(3)
F(7)-As(1)-F(10)	91.4(2)	F(20)-Br(2)-F(21)	90.7(3)
F(7)-As(1)-F(11)	90.0(2)	F(20)-Br(2)-F(22)	168.5(3)
F(7)-As(1)-F(12)	91.3(2)	F(21)-Br(2)-F(22)	88.4(3)
F(8)-As(1)-F(9)	88.4(2)	F(23)-Br(3)-F(24)	80.9(11)
F(8)-As(1)-F(10)	88.8(2)	F(23)-Br(3)-F(25)	85.1(11)
F(8)-As(1)-F(11)	89.8(2)	F(23)-Br(3)-F(26)	84.1(11)
F(8)-As(1)-F(12)	89.3(2)	F(23)-Br(3)-F(27)	79.9(11)
F(9)-As(1)-F(10)	90.3(2)	F(24)-Br(3)-F(25)	89.2(8)
F(9)-As(1)-F(11)	90.6(2)	F(24)-Br(3)-F(26)	164(2)
F(9)-As(1)-F(12)	177.7(2)	F(24)-Br(3)-F(27)	79.2(8)
F(10)-As(1)-F(11)	178.4(2)	F(25)-Br(3)-F(26)	94.6(8)
F(10)-As(1)-F(12)	89.5(2)	F(25)-Br(3)-F(27)	162(2)
F(11)-As(1)-F(12)	89.6(2)	F(26)-Br(3)-F(27)	93.1(8)

Table 3.2 (continued)

C_5F_5N–$XeF^+AsF_6^- \cdot 2.5BrF_5$

Bond Lengths (Å)			
	expt		expt
F(1)-Xe(1)	1.932(6)	As(1)-F(11)	1.724(5)
Xe(1)-N(1)	2.287(8)	As(1)-F(12)	1.699(6)
N(1)-C(1)	1.351(12)	Br(1)-F(13)	1.705(7)
N(1)-C(5)	1.349(12)	Br(1)-F(14)	1.790(7)
C(1)-F(2)	1.303(11)	Br(1)-F(15)	1.758(7)
C(1)-C(2)	1.370(14)	Br(1)-F(16)	1.763(7)
C(2)-F(3)	1.321(9)	Br(1)-F(17)	1.770(7)
C(2)-C(3)	1.385(14)	Br(2)-F(18)	1.682(7)
C(3)-F(4)	1.319(11)	Br(2)-F(19)	1.765(7)
C(3)-C(4)	1.377(13)	Br(2)-F(20)	1.763(7)
C(4)-F(5)	1.346(11)	Br(2)-F(21)	1.762(8)
C(4)-C(5)	1.352(14)	Br(2)-F(22)	1.755(7)
C(5)-F(6)	1.320(10)	Br(3)-F(23)	1.59(3)
As(1)-F(7)	1.723(6)	Br(3)-F(24)	1.71(2)

Table 3.2 (continued)

As(1)-F(8)	1.715(6)	Br(3)-F(25)	1.81(2)
As(1)-F(9)	1.721(6)	Br(3)-F(26)	1.69(2)
As(1)-F(10)	1.712(6)	Br(3)-F(27)	1.75(3)

Bond Angles (deg.)

	expt		expt
F(1)-Xe(1)-N(1)	178.8(3)	F(10)-As(1)-F(12)	89.7(3)
C(1)-N(1)-C(5)	117.9(9)	F(11)-As(1)-F(12)	178.2(3)
Xe(1)-N(1)-C(1)	121.0(7)	F(13)-Br(1)-F(14)	84.1(4)
Xe(1)-N(1)-C(5)	121.0(6)	F(13)-Br(1)-F(15)	84.4(4)
N(1)-C(1)-F(2)	115.6(9)	F(13)-Br(1)-F(16)	85.4(4)
F(2)-C(1)-C(2)	122.1(9)	F(13)-Br(1)-F(17)	84.4(4)
N(1)-C(1)-C(2)	122.3(9)	F(14)-Br(1)-F(15)	168.5(4)
C(1)-C(2)-F(3)	120.7(9)	F(14)-Br(1)-F(16)	90.2(4)
F(3)-C(2)-C(3)	120.7(8)	F(14)-Br(1)-F(17)	89.0(4)
C(1)-C(2)-C(3)	118.7(8)	F(15)-Br(1)-F(16)	89.5(4)
C(2)-C(3)-F(4)	119.8(9)	F(15)-Br(1)-F(17)	89.3(4)
F(4)-C(3)-C(4)	121.1(9)	F(16)-Br(1)-F(17)	169.7(4)

Table 3.2 (continued)

C(2)-C(3)-C(4)	119.1(9)	F(18)-Br(2)-F(19)	83.2(4)
C(3)-C(4)-F(5)	120.0(9)	F(18)-Br(2)-F(20)	84.6(4)
F(5)-C(4)-C(5)	120.6(9)	F(18)-Br(2)-F(21)	84.3(4)
C(3)-C(4)-C(5)	119.4(9)	F(18)-Br(2)-F(22)	84.4(4)
C(4)-C(5)-F(6)	121.8(9)	F(19)-Br(2)-F(20)	167.8(3)
F(6)-C(5)-N(1)	115.6(9)	F(19)-Br(2)-F(21)	89.7(5)
N(1)-C(5)-C(4)	122.6(9)	F(19)-Br(2)-F(22)	89.0(4)
F(7)-As(1)-F(8)	178.1(3)	F(20)-Br(2)-F(21)	89.1(4)
F(7)-As(1)-F(9)	90.0(3)	F(20)-Br(2)-F(22)	89.8(3)
F(7)-As(1)-F(10)	89.5(3)	F(21)-Br(2)-F(22)	168.7(4)
F(7)-As(1)-F(11)	90.0(3)	F(23)-Br(3)-F(24)	87(2)
F(7)-As(1)-F(12)	91.8(3)	F(23)-Br(3)-F(25)	86.5(14)
F(8)-As(1)-F(9)	90.5(3)	F(23)-Br(3)-F(26)	83.7(14)
F(8)-As(1)-F(10)	90.0(3)	F(23)-Br(3)-F(27)	86.8(14)
F(8)-As(1)-F(11)	88.2(3)	F(24)-Br(3)-F(25)	85.5(12)
F(8)-As(1)-F(12)	90.1(3)	F(24)-Br(3)-F(26)	89.1(12)
F(9)-As(1)-F(10)	178.8(3)	F(24)-Br(3)-F(27)	173(2)
F(9)-As(1)-F(11)	88.5(3)	F(25)-Br(3)-F(26)	169.1(12)

Table 3.2 (continued)

F(9)-As(1)-F(12)	91.3(3)	F(25)-Br(3)-F(27)	96.7(13)
F(10)-As(1)-F(11)	90.5(3)	F(26)-Br(3)-F(27)	87.5(12)

$Xe_2F_3^+AsF_6^-$

Bond Lengths (Å)

	expt		expt
Xe(1)-F(1)	2.157(3)	As(1)-F(9)	1.695(7)
Xe(1)-F(2)	1.929(6)	As(1)-F(10)	1.714(7)
Xe(2)-F(3)	1.908(7)	As(1)-F(11)	1.713(7)
Xe(2)-F(4)	2.142(7)	As(2)-F(12)	1.72(2)
Xe(3)-F(4)	2.148(7)	As(2)-F(13)	1.75(2)
Xe(3)-F(5)	1.908(6)	As(2)-F(14)	1.74(2)
As(1)-F(6)	1.708(7)	As(2)-F(12A)	1.73(1)
As(1)-F(7)	1.696(7)	As(2)-F(13A)	1.69(2)
As(1)-F(8)	1.723(7)	As(2)-F(14A)	1.71(2)

Table 3.2 (continued)

Bond Angles (deg.)

	expt		expt
F(1)-Xe(1)-F(2)	177.6(3)	F(8)-As(1)-F(11)	90.9(4)
F(3)-Xe(2)-F(4)	177.3(4)	F(9)-As(1)-F(10)	89.9(4)
Xe(2)-F(4)-Xe(3)	149.5(4)	F(9)-As(1)-F(11)	91.6(4)
F(4)-Xe(3)-F(5)	177.7(3)	F(10)-As(1)-F(11)	178.4(4)
Xe(1)-F(1)-Xe(1A)	148.6(4)	F(12)-As(2)-F(13)	90.2(7)
F(6)-As(1)-F(7)	90.8(5)	F(12)-As(2)-F(14)	89.3(8)
F(6)-As(1)-F(8)	179.0(4)	F(13)-As(2)-F(14)	89.7(10)
F(6)-As(1)-F(9)	91.4(4)	F(12)-As(2)-F(13A)	73.8(8)
F(6)-As(1)-F(10)	90.6(4)	F(12)-As(2)-F(14A)	116.0(9)
F(6)-As(1)-F(11)	89.5(4)	F(13)-As(2)-F(12A)	116.4(7)
F(7)-As(1)-F(8)	88.3(4)	F(13)-As(2)-F(14A)	100.6(10)
F(7)-As(1)-F(9)	177.8(4)	F(14)-As(2)-F(12A)	70.0(9)
F(7)-As(1)-F(10)	89.9(4)	F(14)-As(2)-F(13A)	67.2(10)
F(7)-As(1)-F(11)	88.5(4)	F(12A)-As(2)-F(13A)	91.8(7)
F(8)-As(1)-F(9)	89.5(4)	F(12A)-As(2)-F(14A)	89.6(9)
F(8)-As(1)-F(10)	88.9(4)	F(13A)-As(2)-F(14A)	87.4(10)

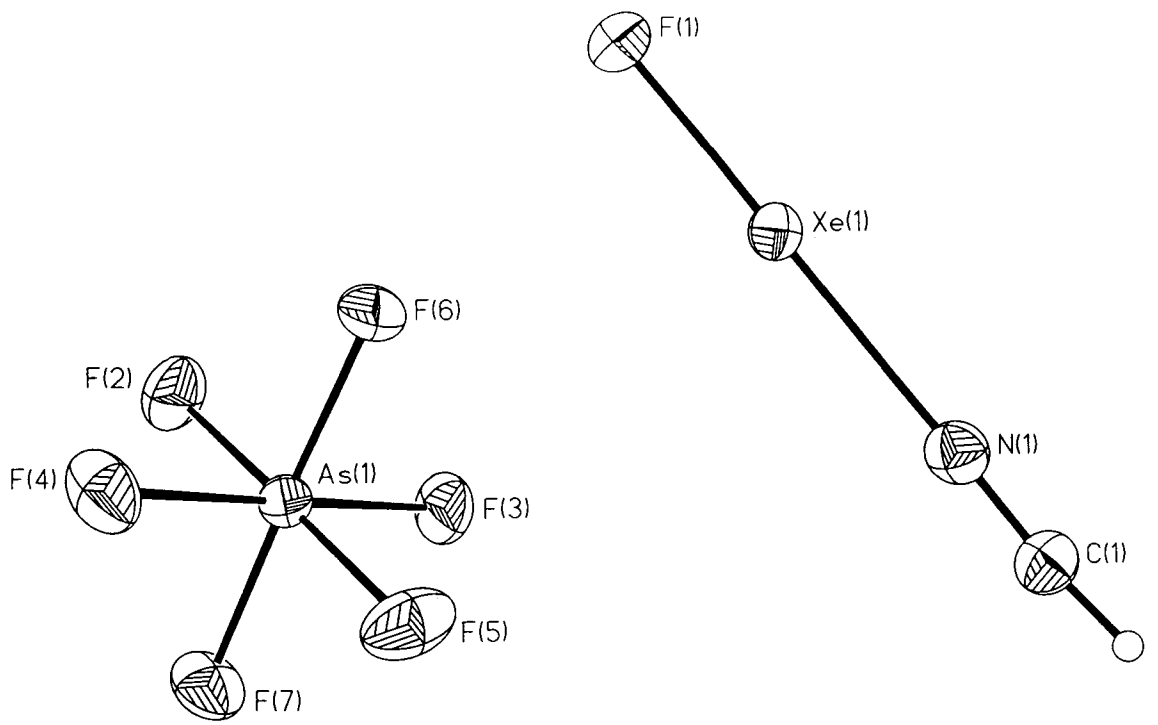

Figure 3.1 Structure of $HC{\equiv}N{-}XeF^{+}AsF_6^{-}$ showing thermal ellipsoids at the 50% probability level.

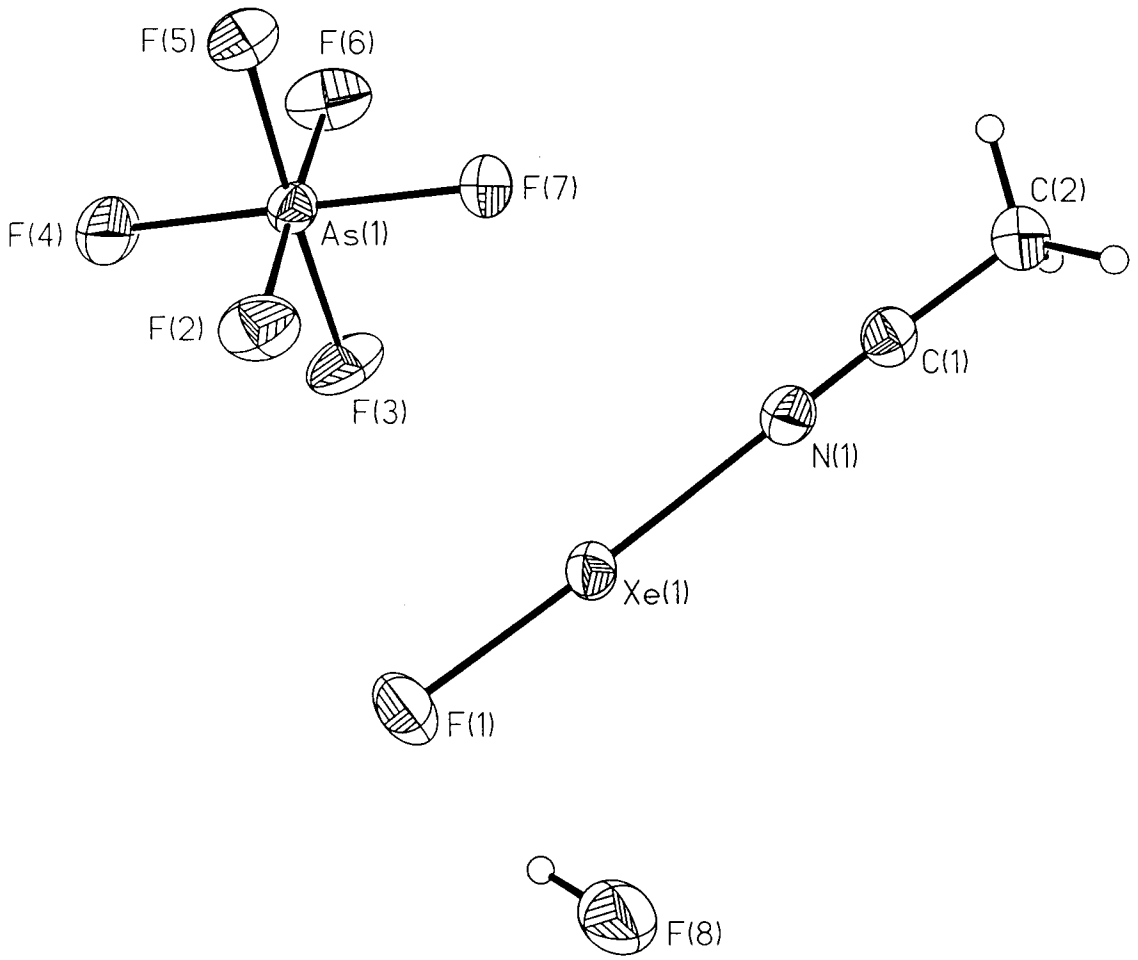

Figure 3.2 Structure of $CH_3C{\equiv}N{-}XeF^+AsF_6^-{\cdot}HF$ showing thermal ellipsoids at the 50% probability level.

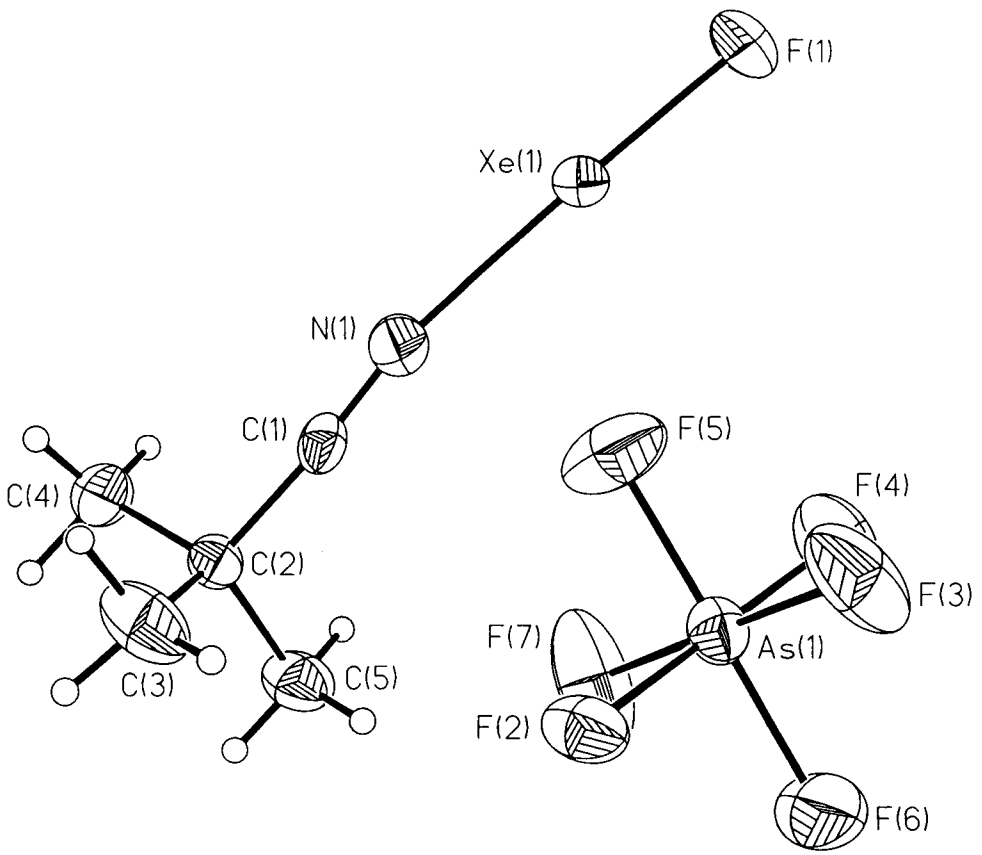

Figure 3.3 Structure of $(CH_3)_3CC{\equiv}N{-}XeF^+AsF_6^-$ showing thermal ellipsoids at the 50% probability level.

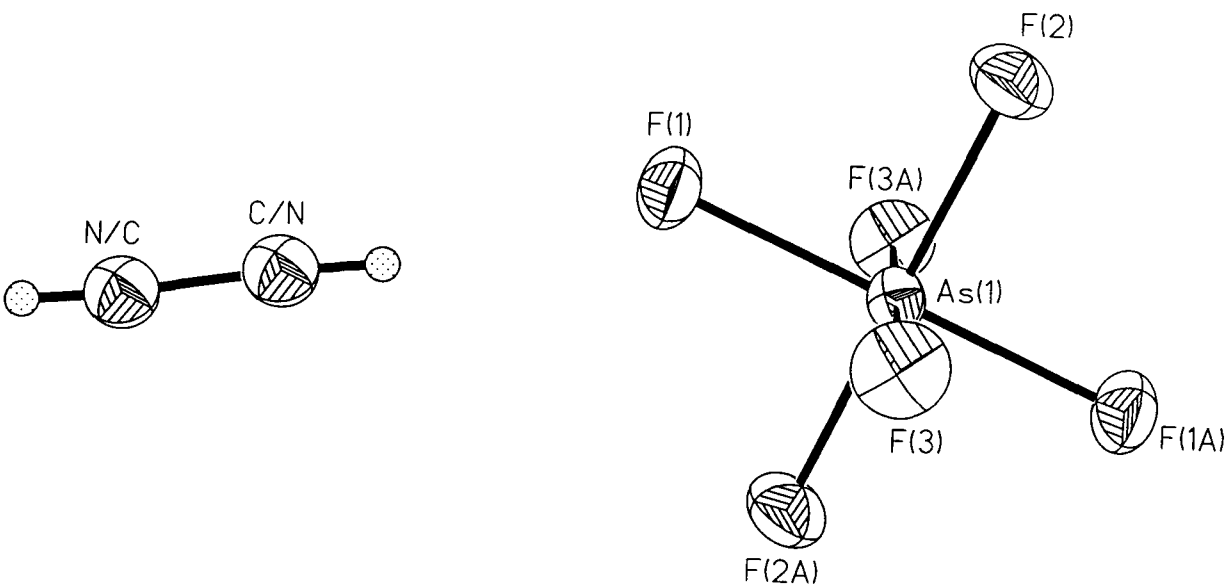

Figure 3.4 Structure of $HC{\equiv}NH^{+}AsF_6^{-}$ showing thermal ellipsoids at the 50% probability level.

The Xe–N bond lengths in $HC{\equiv}N{-}XeF^+AsF_6^-$ (2.235(3) Å), $(CH_3)_3CC{\equiv}N{-}XeF^+AsF_6^-$ (2.212(4) Å), and $CH_3C{\equiv}N{-}XeF^+AsF_6^-{\cdot}HF$ (2.179(7) Å) are significantly longer than that in $XeN(SO_2F)_2{}^+Sb_3F_{16}^-$ (2.02(1) Å),[20] but are much shorter than those in $[MeC{\equiv}N{\cdots}Xe{-}C_6F_5]^+$ (2.681(8) Å),[66] $[2,6\text{-}C_5H_3F_2N{\cdots}Xe{-}C_6F_5{}^+][AsF_6^-]$ (2.694(5) Å),[67] and in the calculated model of $HC{\equiv}N{-}XeF^+$ (2.421 Å).[88] Of the well-characterized Xe–N bonded adduct cations having formal sp-hybridization at the nitrogen atom, the Xe–N bond in $CH_3C{\equiv}N{-}XeF^+AsF_6^-$ has the highest degree of covalency. The covalent characters of the Xe–N bonds increase in the order $HC{\equiv}N{-}XeF^+AsF_6^-$ < $(CH_3)_3CC{\equiv}N{-}XeF^+AsF_6^-$ < $CH_3C{\equiv}N{-}XeF^+AsF_6^-$ and somewhat parallel the increasing ionic characters of the terminal Xe–F bonds. The Xe–F bond lengths in $HC{\equiv}N{-}XeF^+AsF_6^-$ (1.936(2) Å), $(CH_3)_3CC{\equiv}N{-}XeF^+AsF_6^-$ (1.952(3) Å), and $CH_3C{\equiv}N{-}XeF^+AsF_6^-{\cdot}HF$ (1.947(5) Å) are considerably longer than the terminal Xe–F bond lengths in $Xe_2F_3{}^+AsF_6^-$ (1.915(6) Å; *vide infra*), $XeF^+AsF_6^-$ (1.873(6) Å),[19] and $XeF^+Sb_2F_{11}^-$ (1.84(1) Å),[11] but are still shorter than those in XeF_2 (2.010(6) Å)[31] and $FXeN(SO_2F)_2$ (1.967(3) Å).[62] The structure of the $XeF^+Sb_2F_{11}^-$ salt represents the closest approximation to the free XeF^+ cation since it has a very weak fluorine bridge interaction between xenon and the weakly basic $Sb_2F_{11}^-$ anion (2.35 Å). By comparison, the reaction of the gas-phase XeF^+ ion with F^- to yield XeF_2 results in an increase in the Xe–F bond lengths by 0.100 Å,[56] while the reactions of $XeF^+AsF_6^-$ with HCN, $CH_3C{\equiv}N$, and

$(CH_3)_3CC{\equiv}N$ cause the Xe–F bond length to increase by only 0.063 Å, 0.074 Å, and 0.079 Å, respectively, with respect to that in $XeF^+AsF_6^-$ (1.873(6) Å).

In many ways HCN, with IP_1 = 13.80 eV, is archetypical of the other oxidatively resistant organic and perfluoro-organic nitrogen bases that form adducts with XeF^+ and, more recently, with KrF^+;[85] the most potent oxidative fluorinating agent known (EA: KrF^+, ~13.2 eV; XeF^+, ~10.9 eV). For this reason, the X-ray crystal structures of both $HC{\equiv}N{-}XeF^+AsF_6^-$ and $HC{\equiv}NH^+AsF_6^-$ are highly significant, particularly as they serve as comparisons in understanding the bonding in $HC{\equiv}N{-}KrF^+AsF_6^-$ previously ascribed by NMR spectroscopy[85] and theoretical calculations,[88-95] and whose preparation, although explosive above -50 °C in HF, was best achieved by the reaction of KrF_2 with $HC{\equiv}NH^+AsF_6^-$ in BrF_5.[85] While $HC{\equiv}N{-}XeF^+AsF_6^-$ has been characterized more recently in HF and BrF_5 solvents by multi-NMR spectroscopy and in the solid state by low-temperature Raman spectroscopy,[88] the $HC{\equiv}NH^+AsF_6^-$ salt was characterized as early as 1962 by conductivity measurements,[132] ^1H NMR spectroscopy,[133] and by multi-NMR spectroscopy in the strong acid system $FSO_3H{-}SbF_5{-}SO_2$.[134]

The C≡N bond lengths in $HC{\equiv}N{-}XeF^+AsF_6^-$ (1.116(4) Å), $HC{\equiv}NH^+AsF_6^-$ (1.103(11) Å), and $CH_3C{\equiv}N{-}XeF^+AsF_6^-{\cdot}HF$ (1.120(11) Å) are significantly shorter than those observed in the corresponding free HCN (observed in gas phase, 1.155 Å;[135] calculated, 1.15582(2) Å),[136] and CH_3CN (1.141(2) Å)[137] compounds. Additionally, the C≡N bond length observed in $HC{\equiv}N{-}XeF^+AsF_6^-$ is shorter than that calculated (1.127 Å).[88-95] The C≡N bond length in $(CH_3)_3CC{\equiv}N{-}XeF^+AsF_6^-$ (1.147(6) Å) could not be

compared with that in free $(CH_3)_3CC{\equiv}N$ since the crystal structure of the free base has not been determined, however, it is comparable with that in $NbCl_5((CH_3)_3CC{\equiv}N)$ (1.135 Å).[138] By analogy with the trends observed between the other XeF^+ adducts and the free nitriles, the C≡N bond length in free $(CH_3)_3CC{\equiv}N$ is expected to be longer than 1.147 Å. Decreases in the C≡N bond lengths upon coordination of a nitrile to a Lewis acid have also been encountered in $VCl_4(NCH)_2$ (1.12(1), 1.14(1) Å),[135] $TiCl_4(NCH)_2$ (1.11(1) Å),[139] $NbCl_5(NCH)$ (1.090(4) Å),[140] $Ag(NCH)_2^+SbF_6^-$ (1.093(4) Å),[141] $Cu(NO_3)_2(CH_3CN)_2$ (1.04(7) Å),[142] and $CH_3C{\equiv}N{\cdot}B(C_6F_5)_3$ (1.124(3) Å).[143]

The arrangement of atoms about nitrogen in $HC{\equiv}N{-}XeF^+AsF_6^-$ (177.7(3)°), $CH_3C{\equiv}N{-}XeF^+AsF_6^-{\cdot}HF$ (175.0(8)°), and $(CH_3)_3CC{\equiv}N{-}XeF^+AsF_6^-$ (166.9(4)°) are significantly distorted from linearity, and the C≡N–Xe angle in $(CH_3)_3CC{\equiv}N{-}XeF^+AsF_6^-$ exhibits the greatest distortion. Bent C≡N–E (E = inorganic main-group element) arrangements have also been encountered in $[(Me_3Sn)_4Mo(CN)_8]$ (C≡N–Sn = 163.7(5)°),[145] $[(Me_3Sn)_4W(CN)_8]$ (C≡N–Sn = 166.0(9)°),[145] $[(thf)_2Tl(\mu\text{-}NC)Mn(CO)(dppm)_2][PF_6]$ (average C≡N–Tl = 133.1(12)°),[146] $[InBr_3(DME)(MeCN)]$ (C≡N–In = 162.7(5)°),[147] and $[(Me_3Sn)_3Co(CN)_6]$ (average C≡N–Sn = 158(3)°),[148] and $[(Me_3Pb)_3Co(CN)_6]$ (average C≡N–Pb = 143(3)°),[148] although no explanations were given for the distortions. However, the observed C≡N–Ti deformation (178.1(8)°) in the transition metal complex, $TiCl_4(NCH)_2$, has previously been examined using semi-empirical calculations.[144] The results from this study may, in turn, be correlated to the title compounds and are discussed in further detail in **Correlations of the Structural**

Findings with Spectroscopic Results. The weak inter- and intramolecular contacts around the nitrogen atoms in the adduct salts are at the sum of their van der Waals radii (N, 1.55 Å; F, 1.35-1.50 Å)[36-38] (Figure 3.5). Due to the disorder, the H–C–N and H–N–C angles in $HC{\equiv}NH^+AsF_6^-$ are unreliable.

The N–Xe–F angles observed in $HC{\equiv}N{-}XeF^+AsF_6^-$ (179.83(9)°), $CH_3C{\equiv}N{-}XeF^+AsF_6^-{\cdot}HF$ (178.7(3) °), and $(CH_3)_3CC{\equiv}N{-}XeF^+AsF_6^-$ (178.1(1)°) are nearly linear. Without exception, linear arrangements of atoms about xenon are found in nearly all known Xe(II) compounds, such as $FXeN(SO_2F)_2$ (178.1(1)°)[62] and $XeN(SO_2F)_2{}^+Sb_3F_{16}^-$ (178.3(3)°),[20] and are consistent with the AX_2E_3 valence-shell electron-pair repulsion (VSEPR) model of the three lone pairs in equatorial positions with the bond pairs in axial positions about the central Xe(II) atom. Closest intermolecular fluorine contacts with the xenon atoms avoid the lone-pair electron density on xenon in the equatorial regions of the linear N–Xe–F arrangements (Figures 3.6 – 3.8) and are within the sum of their xenon and fluorine van der Waals radii (Xe···F = 3.63 Å).[36-38]

The packing arrangements of the $HC{\equiv}N{-}XeF^+AsF_6^-$, $CH_3C{\equiv}N{-}XeF^+AsF_6^-{\cdot}HF$, $(CH_3)_3CC{\equiv}N{-}XeF^+AsF_6^-$, and $HC{\equiv}NH^+AsF_6^-$ units in the lattice are illustrated in Figures 3.9, 3.10, 3.11, and 3.12, respectively. The crystal packings of $HC{\equiv}N{-}XeF^+AsF_6^-$, $CH_3C{\equiv}N{-}XeF^+AsF_6^-{\cdot}HF$, and $(CH_3)_3CC{\equiv}N{-}XeF^+AsF_6^-$ consist of ordered assemblies of discrete rows of cations separated by rows of anions along the *a*- and *c*-axes, respectively. The packing of $HC{\equiv}NH^+AsF_6^-$ molecules represents a body-

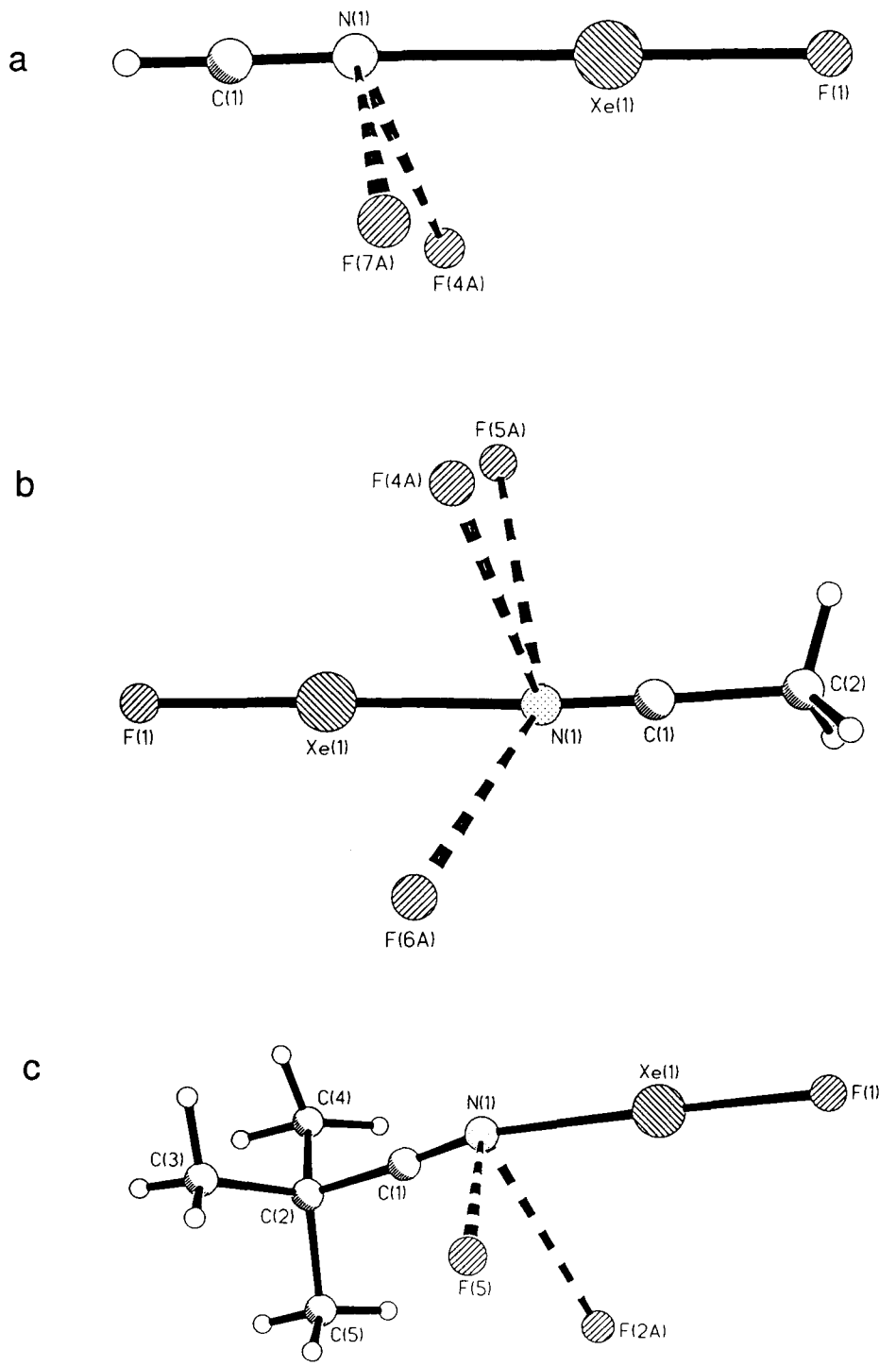

Figure 3.5 View of the closest fluorine contacts to the nitrogen atom in: (a) $HC{\equiv}N{-}XeF^{+}AsF_6^{-}$; (b) $CH_3C{\equiv}N{-}XeF^{+}AsF_6^{-}{\cdot}HF$; (c) $(CH_3)_3CC{\equiv}N{-}XeF^{+}AsF_6^{-}$. Dashed lines denote the N···F contacts.

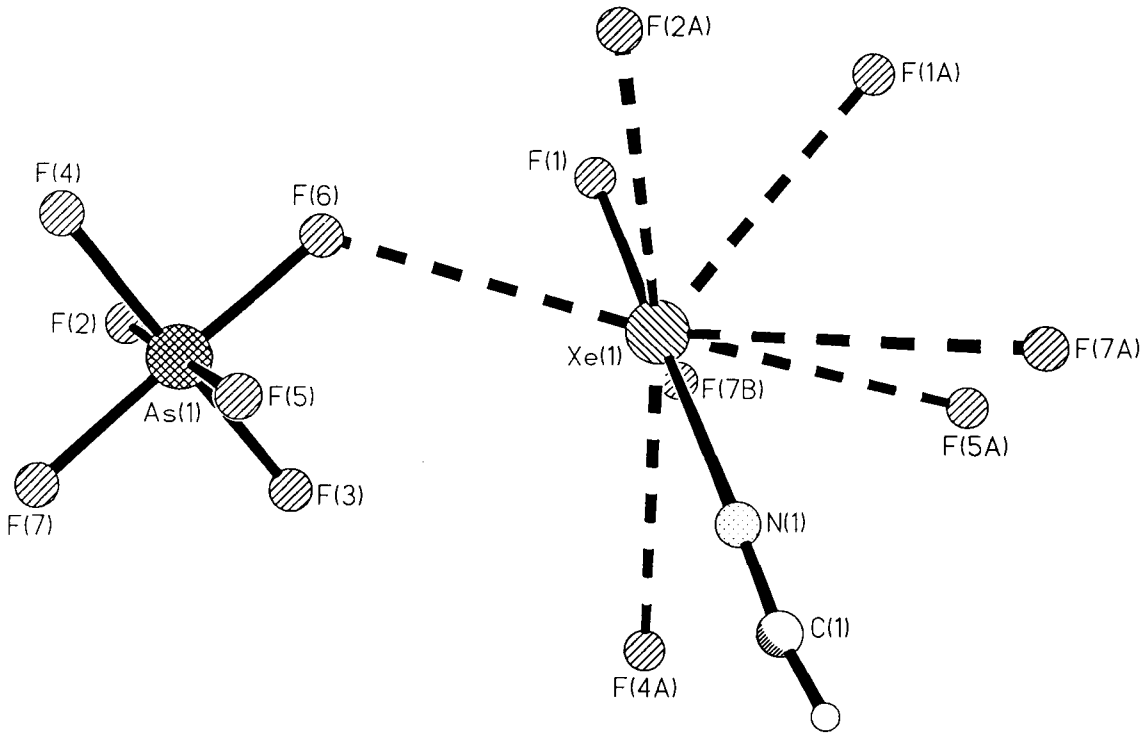

Figure 3.6 View of the closest fluorine contacts to the xenon atom in HC≡N–$XeF^+AsF_6^-$. Dashed lines denote the Xe···F contacts.

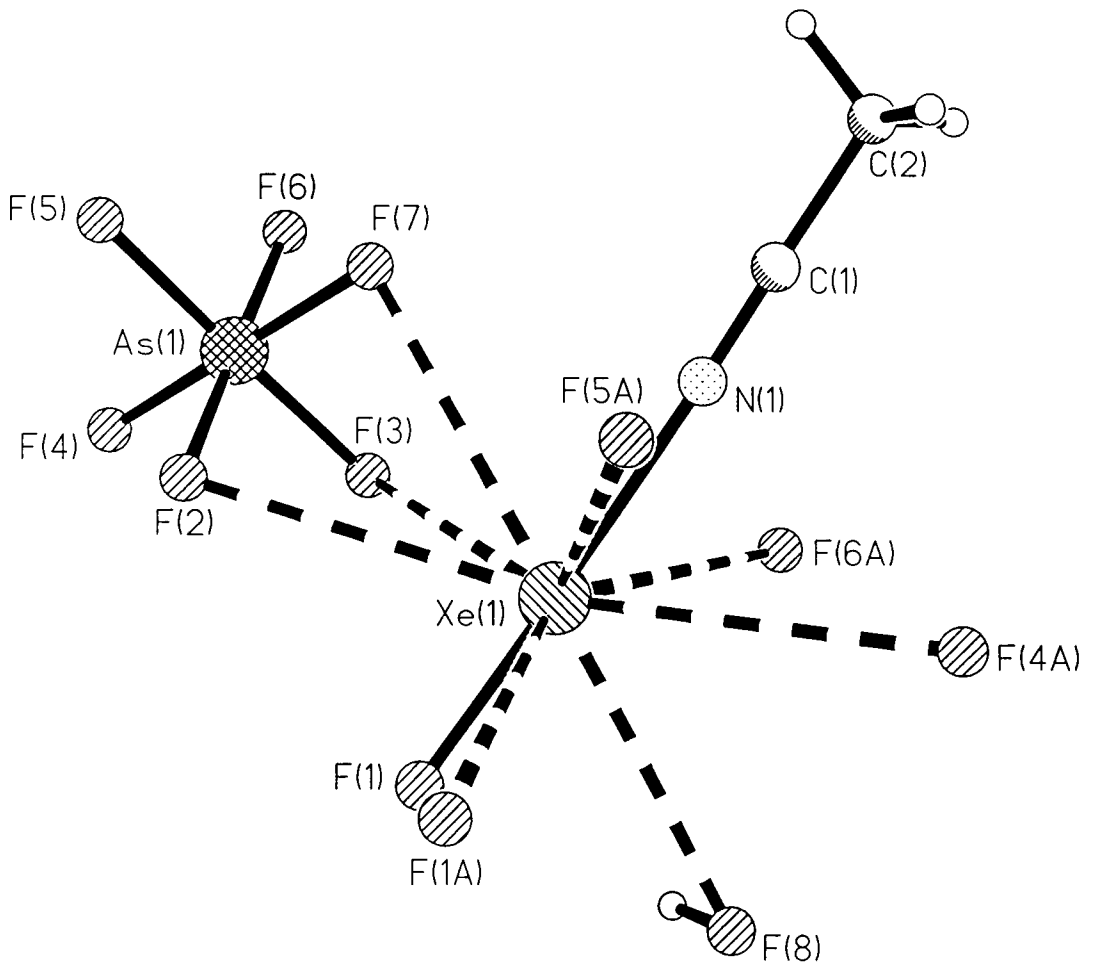

Figure 3.7 View of the closest fluorine contacts to the xenon atom in $CH_3C{\equiv}N{-}XeF^+AsF_6^-{\cdot}HF$. Dashed lines denote the Xe···F contacts.

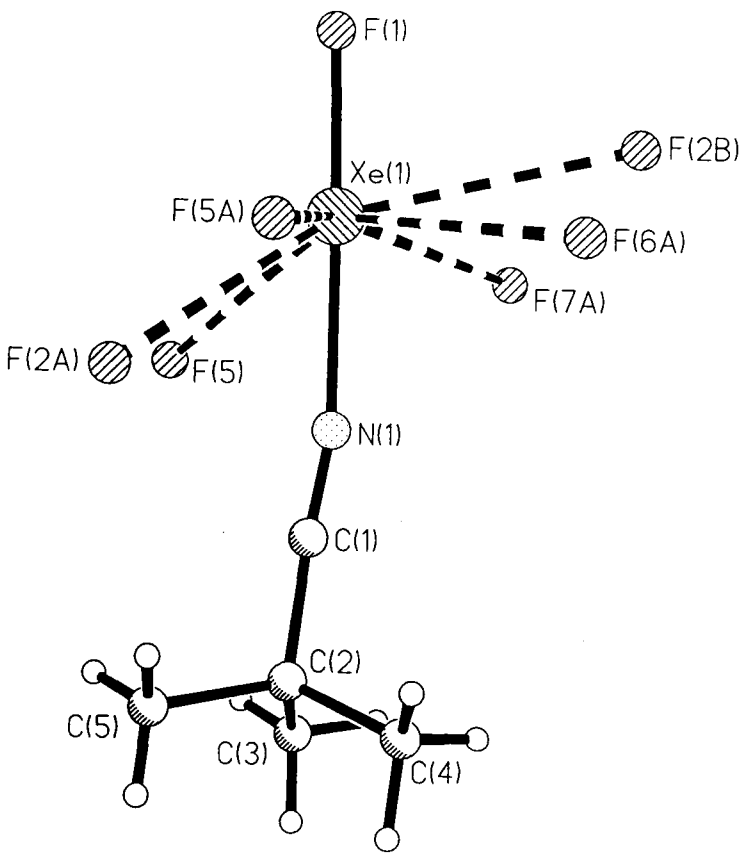

Figure 3.8 View of the closest fluorine contacts to the xenon atom in $(CH_3)_3CC{\equiv}N{-}XeF^+AsF_6^-$. Dashed lines denote the Xe···F contacts.

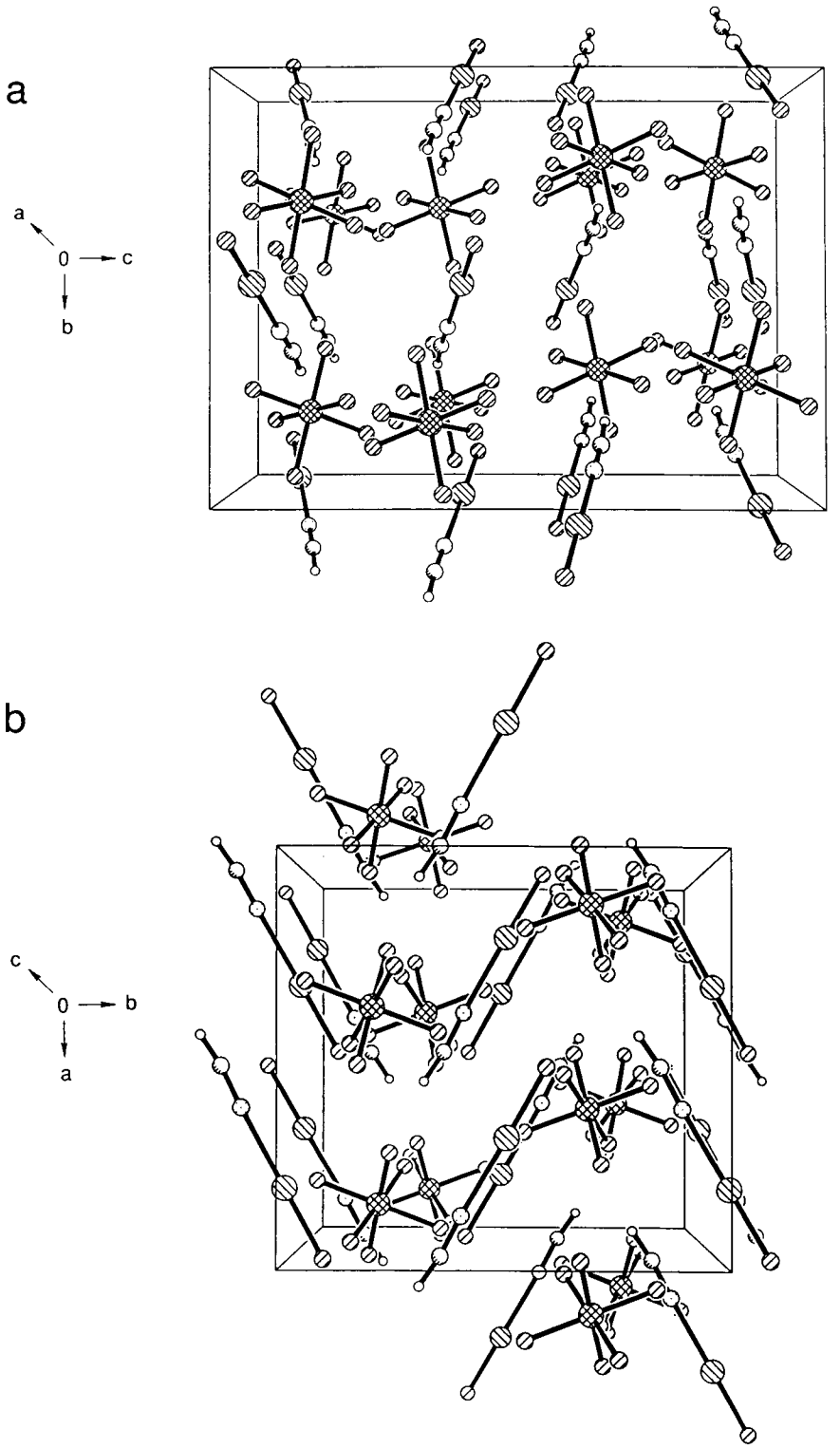

Figure 3.9 View of the $HC{\equiv}N{-}XeF^{+}AsF_6^{-}$ unit cell: (a) along the a-axis; (b) along the c-axis.

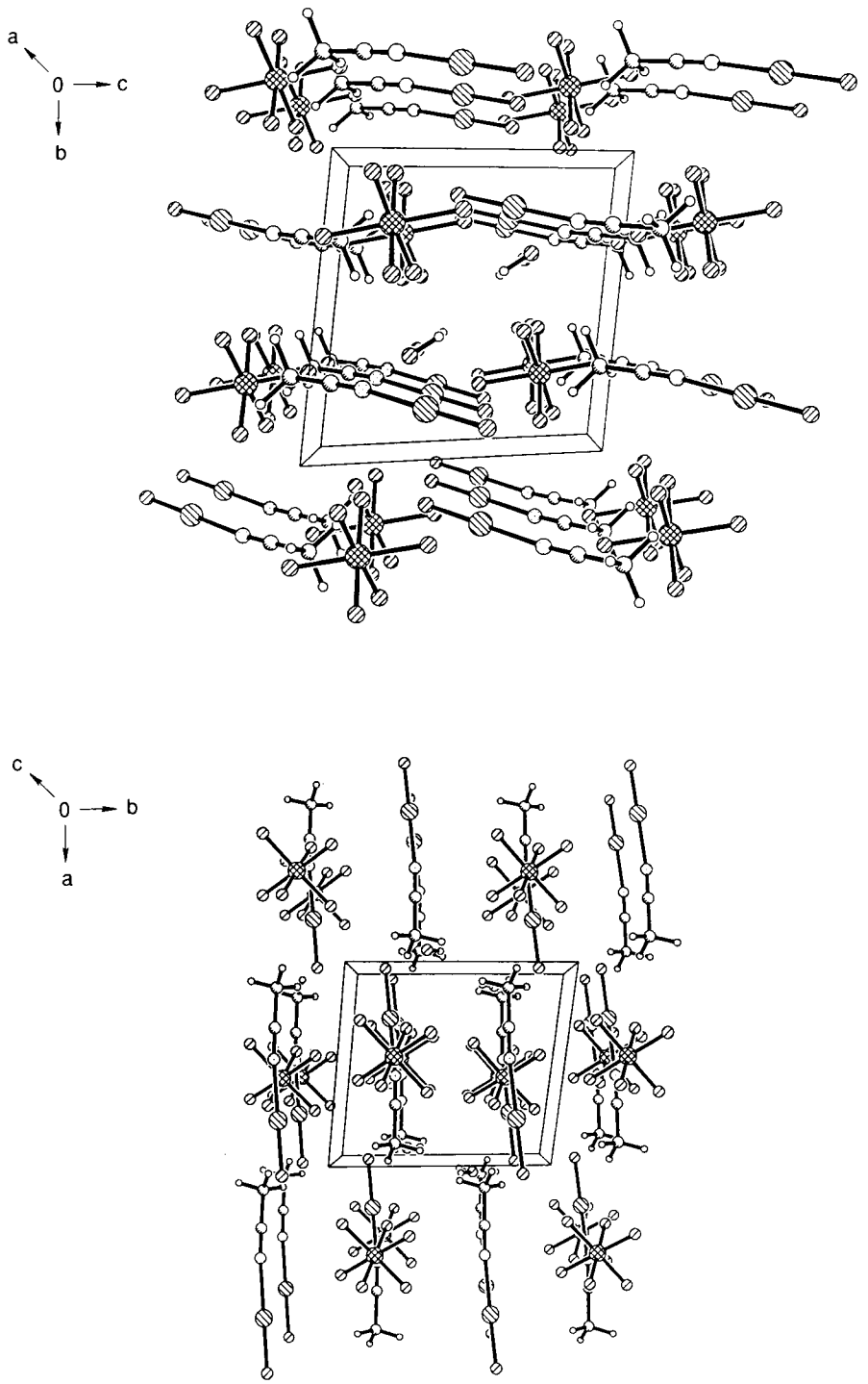

Figure 3.10 View of the $CH_3C{\equiv}N{-}XeF^+AsF_6^-{\cdot}HF$ unit cell: (a) along the a-axis; (b) along the c-axis.

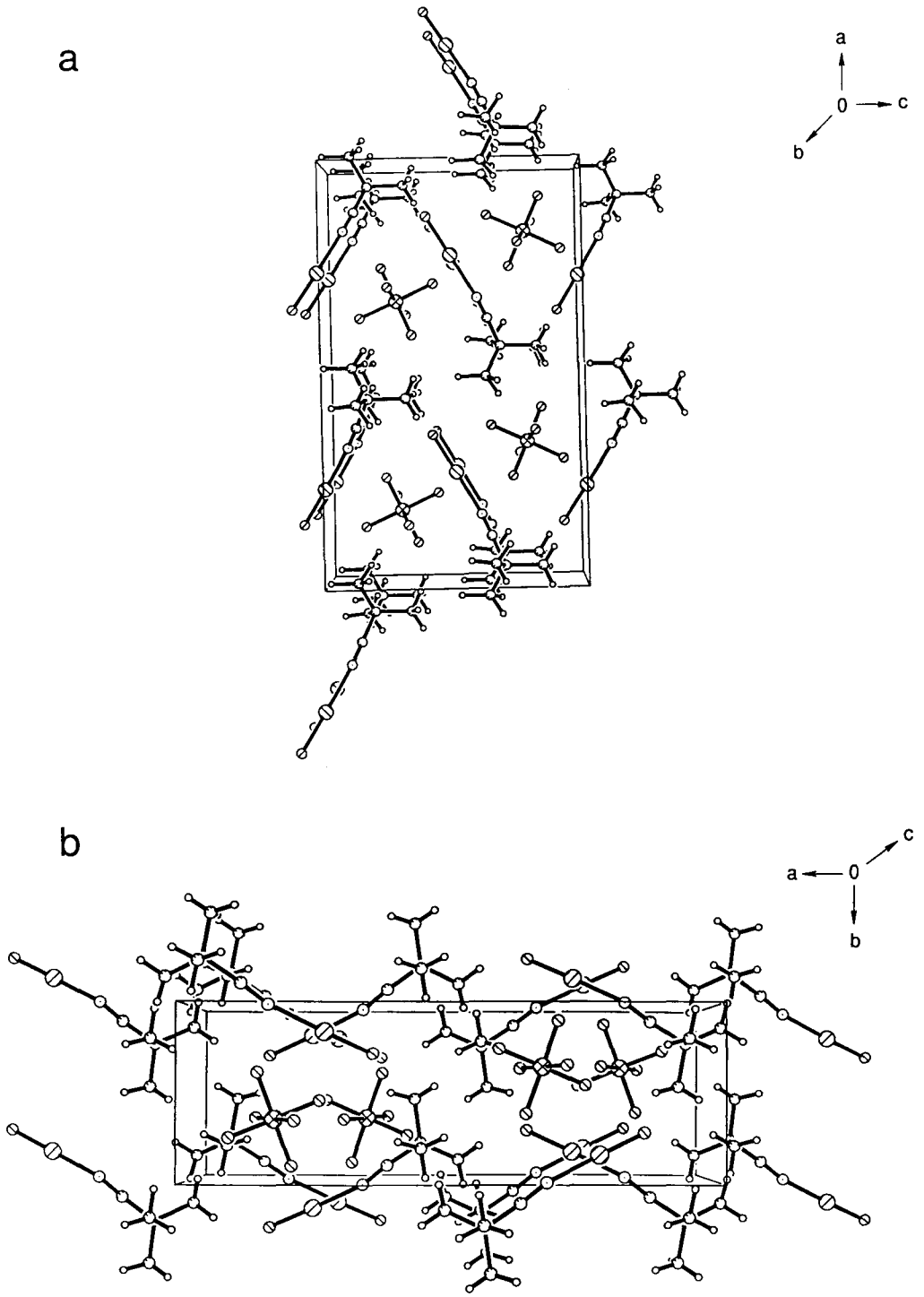

Figure 3.11 View of the $(CH_3)_3CC{\equiv}N{-}XeF^+AsF_6^-$ unit cell: (a) along the b-axis; (b) along the c-axis.

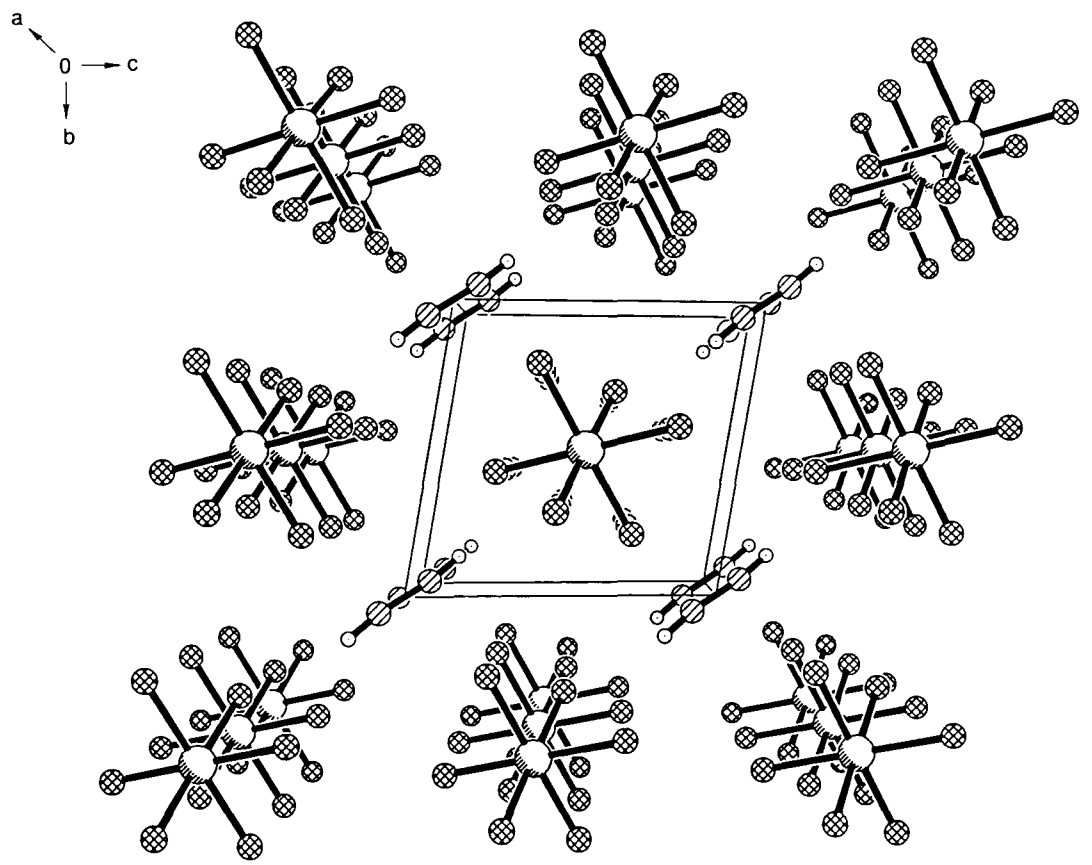

Figure 3.12 View of the $HC{\equiv}NH^{+}AsF_6^{-}$ unit cell along the a-axis.

centered cube with disordered cations on crystallographically imposed inversion centers at the corners of the cube and an AsF_6^- anion at the center.

s-$C_3F_3N_2N$–$XeF^+AsF_6^-$· 2.5BrF_5 and C_5F_5N–$XeF^+AsF_6^-$· 2.5BrF_5

The X-ray crystal structures of *s*-$C_3F_3N_2N$–$XeF^+AsF_6^-$·2.5BrF_5 (Figure 3.13) and C_5F_5N–$XeF^+AsF_6^-$·2.5BrF_5 (Figure 3.14) represent unique examples of Xe–N bonding in which XeF^+ functions as an aromatic substituent. The *s*-$C_3F_3N_2N$–XeF^+ [58] and C_5F_5N–XeF^+ [55] cations were previously characterized by multi-NMR and Raman spectroscopy and represent the first examples of noble gases bonded to an aromatic ring system. Subsequent to these, 2,6-$C_5H_3F_2N$···Xe–$C_6F_5^+$ [67] was characterized by X-ray crystallography. However, the Xe–N bonds characterized in the present structures are considerably more covalent than that in 2,6-$C_5H_3F_2N$···Xe–$C_6F_5^+$ (*vide infra*).

The structures of the s-$C_3F_3N_2N$–$XeF^+AsF_6^-$·2.5BrF_5 and C_5F_5N–$XeF^+AsF_6^-$· 2.5BrF_5 salts consist of well-separated anions and cations with no evidence of a bridge interaction between xenon and a fluorine atom of AsF_6^-. The AsF_6^- anions are octahedral with average As–F bond distances (*s*-$C_3F_3N_2N$–$XeF^+AsF_6^-$·2.5BrF_5, 1.726(4) Å; C_5F_5N–$XeF^+AsF_6^-$· 2.5BrF_5, 1.716(4) Å) and *cis* F–As–F bond angles (*s*-$C_3F_3N_2N$–$XeF^+AsF_6^-$·2.5BrF_5, 88.4(2) – 91.4(2)°; C_5F_5N–$XeF^+AsF_6^-$· 2.5BrF_5, 88.2(3) – 91.8(3)°) that are comparable to values found in the literature.[10,19,131]

The BrF_5 molecules, which crystallized with *s*-$C_3F_3N_2N$–$XeF^+AsF_6^-$ and C_5F_5N–$XeF^+AsF_6^-$, are the first high-quality X-ray structures of BrF_5 in the solid-state.

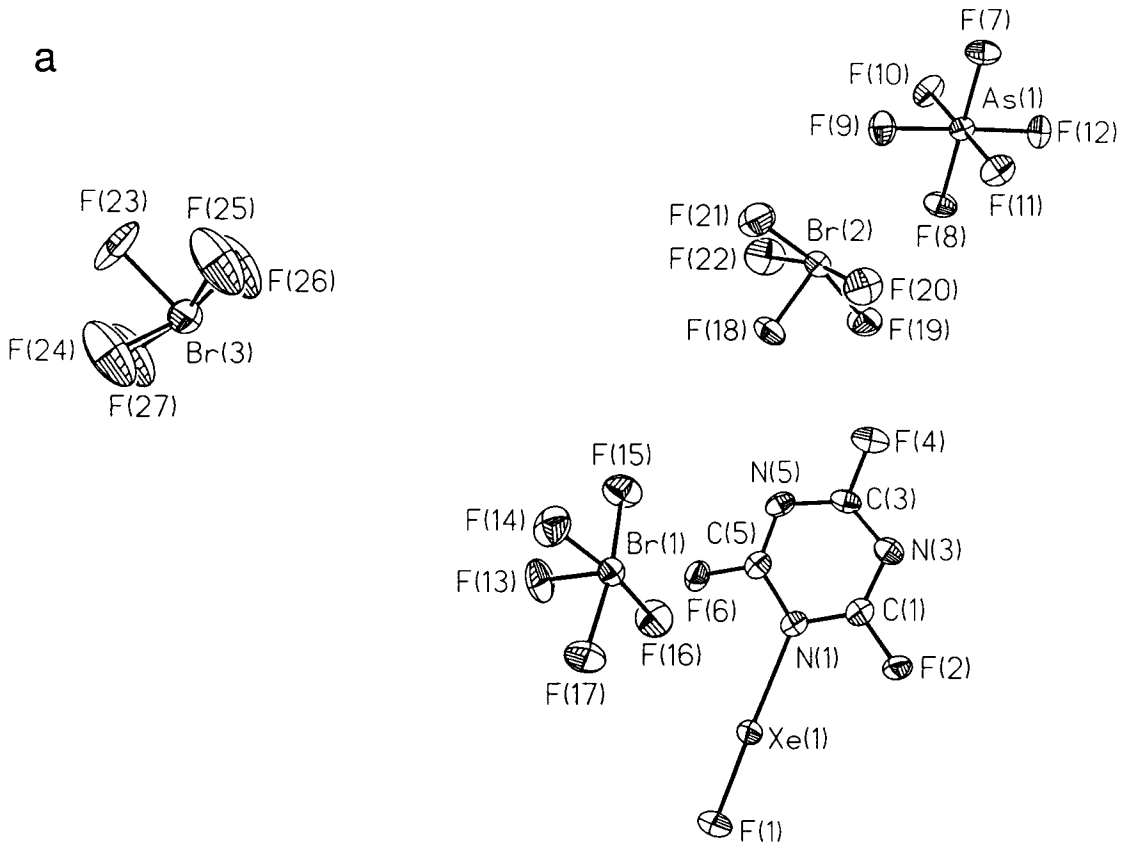

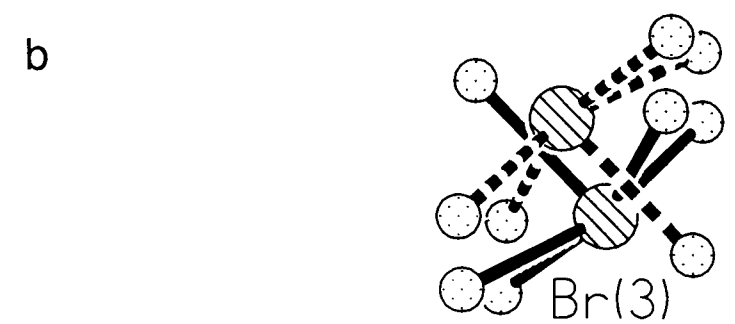

Figure 3.13 (a) Structure of *s*-$C_3F_3N_2N$–$XeF^+AsF_6^-$·2.5BrF_5 showing thermal ellipsoids at the 50% probability level; (b) Disordered model of Br(3) in *s*-$C_3F_3N_2N$–$XeF^+AsF_6^-$·2.5BrF_5.

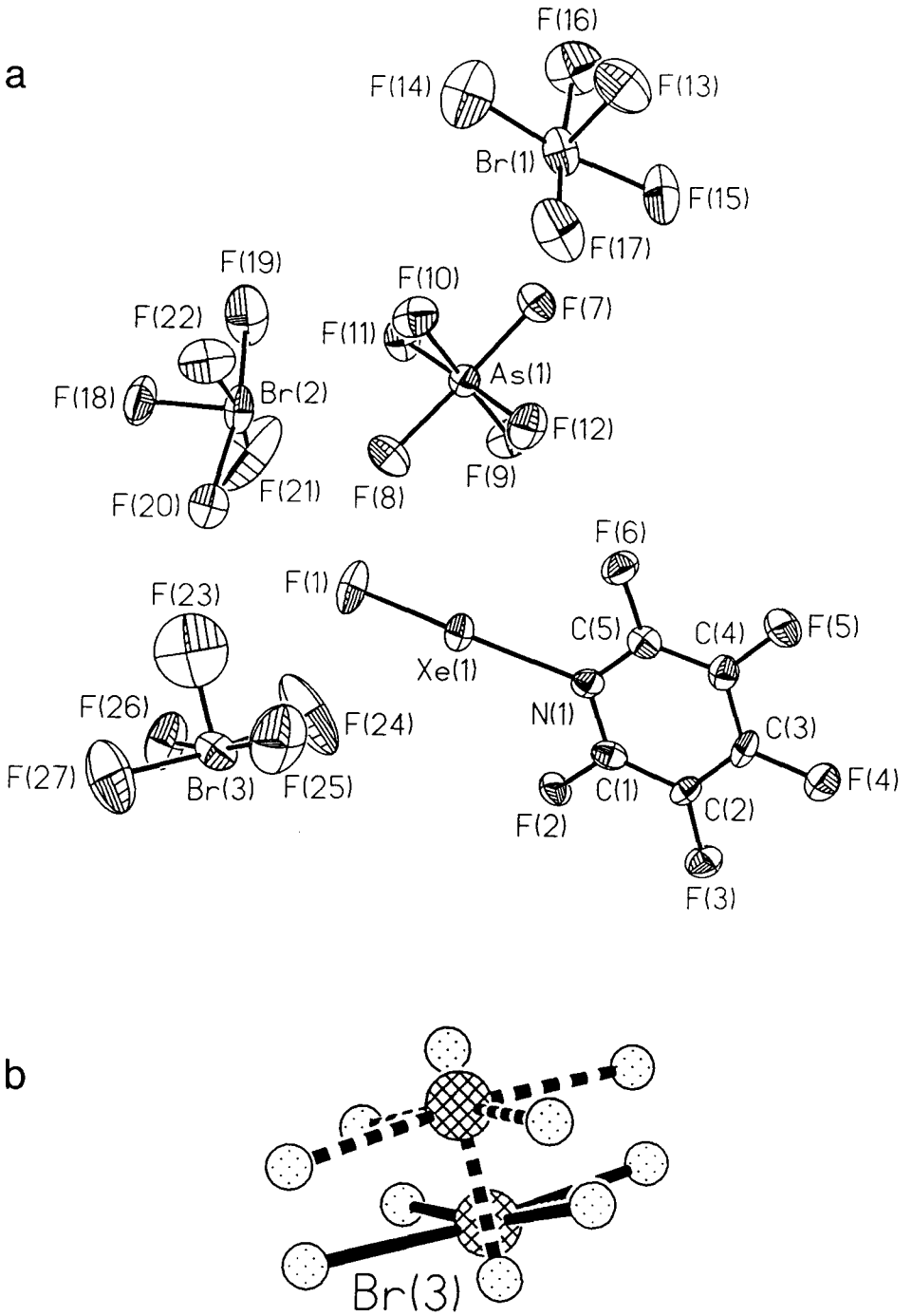

Figure 3.14 (a) Structure of C_5F_5N–$XeF^+AsF_6^-\cdot 2.5BrF_5$ showing thermal ellipsoids at the 50% probability level; (b) Disordered model of Br(3) in C_5F_5N–$XeF^+AsF_6^-\cdot 2.5BrF_5$.

The earliest report by Burbank and Bensey[149] in 1957 had a final R-factor that was significantly larger (0.184) than those in the present work (0.0473 and 0.0580) and precise values for the geometrical parameters were not reported. Geometrical data for the gas-phase molecular structure of BrF_5 was obtained in 1971 by Robiette *et al.*[150] from electron diffraction measurements. As previously reported, the BrF_5 molecules in the present work are square pyramidal (C_{4v}) with the central bromine atoms slightly below the plane of the four basal F atoms. The average apical (F_a) and basal (F_b) Br–F bond distances (s-$C_3F_3N_2N$–$XeF^+AsF_6^-$·2.5BrF_5, 1.690(3) Å and 1.768(5) Å; C_5F_5N–$XeF^+AsF_6^-$· 2.5BrF_5, 1.693(11) and 1.766(4) Å, respectively) and F_a–Br–F_b bond angles (s-$C_3F_3N_2N$–$XeF^+AsF_6^-$·2.5BrF_5, 84.3(3)°; C_5F_5N–$XeF^+AsF_6^-$· 2.5BrF_5, 84.3(4)°) are comparable to the previous reports (Br–F_a = 1.68 Å,[149] 1.689(8) Å;[150] $(Br–F_b)_{av}$ = 1.79 Å,[149] 1.774(3) Å;[150] $(F_a–Br–F_b)_{av}$ = 84.1°,[149] 84.8(1)° [150]). Detailed structural information for BrF_5 is significant since this molecule is often used as an illustration of the valence-shell electron pair repulsion theory,[151,152] in which distortions from idealized octahedral coordination with angles of 90° at the central atom are ascribed to the effect of the lone pair of electrons. In BrF_5 the large nonbonding electron density in the axial position opposite F_a causes the Br–F_b bonding pairs to lengthen as they pucker away, whereas, the valence electron lone pair is far away from the Br–F_a bond to affect it appreciably. In each structure of s-$C_3F_3N_2N$–$XeF^+AsF_6^-$·2.5BrF_5 and C_5F_5N–$XeF^+AsF_6^-$· 2.5BrF_5, the BrF_5 molecule that is shared between the unit cells suffers from a two-fold positional disorder of the atoms.

As observed for R–C≡N–$XeF^+AsF_6^-$ (R = H, CH_3, $(CH_3)_3C$) (*vide supra*), coordination of the perfluoro-organic nitrogen bases with XeF^+ serves to lower the effective positive charge at xenon to give Xe–N bond lengths (*s*-$C_3F_3N_2N$–$XeF^+AsF_6^-$·2.5BrF_5, 2.316(6) Å; C_5F_5N–$XeF^+AsF_6^-$, 2.287(7) Å) that are significantly shorter than those in MeCN···Xe–$C_6F_5^+$ (2.681(8) Å)[66] and 2,6-$C_5H_3F_2N$···Xe–$C_6F_5^+$ (2.694(5) Å),[67] but are longer and more ionic than those observed in $FXeN(SO_2F)_2$ (2.200(3) Å)[62] and $XeN(SO_2F)_2^+Sb_3F_{16}^-$ (2.02(1) Å).[20] Furthermore, the Xe–N bond lengths in *s*-$C_3F_3N_2N$–$XeF^+AsF_6^-$·2.5BrF_5 and C_5F_5N–$XeF^+AsF_6^-$·2.5BrF_5 are considerably longer than those found in R–C≡N–$XeF^+AsF_6^-$ (R = H, CH_3, $(CH_3)_3C$) (see previous section).

The Xe–F bond lengths in *s*-$C_3F_3N_2N$–$XeF^+AsF_6^-$·2.5BrF_5 (1.931(5) Å) and C_5F_5N–$XeF^+AsF_6^-$ (1.932(6) Å) are longer than the terminal Xe–F bond lengths in $Xe_2F_3^+AsF_6^-$ (1.915(6) Å; *vide infra*), $XeF^+AsF_6^-$ (1.873(6) Å),[19] and $XeF^+Sb_2F_{11}^-$ (1.84(1) Å),[11] but are shorter than those in XeF_2 (2.01(1) Å),[31] $FXeN(SO_2F)_2$ (1.967(3) Å),[62] and R–C≡N–$XeF^+AsF_6^-$ (R = H, CH_3, $(CH_3)_3C$; *vide supra*).

The N–Xe–F angles in *s*-$C_3F_3N_2N$–$XeF^+AsF_6^-$·2.5BrF_5 (178.6(2)°) and C_5F_5N–$XeF^+AsF_6^-$ (178.8(3)°) are nearly linear, as predicted by the AX_2E_3 VSEPR model of atoms about a central Xe atom, and are comparable to those angles observed in the R–C≡N–$XeF^+AsF_6^-$ (R = H, CH_3, $(CH_3)_3C$) salts (*vide supra*) and in $FXeN(SO_2F)_2$ (178.1(1)°). Weak intermolecular fluorine contacts with the xenon atoms (3.192 – 3.535 Å; see Appendix E) appear to avoid the lone-pair electron density on xenon expected in

the equatorial region of the N–Xe–F systems (Figure 3.15) and are near the sum of their xenon and fluorine van der Waals radii (3.63 Å).[36-38]

The Xe, C(1), and C(5) atoms in *s*-$C_3F_3N_2N$–$XeF^+AsF_6^-$·2.5BrF_5 and C_5F_5N–$XeF^+AsF_6^-$·2.5BrF_5 form trigonal-planar (sp^2) arrangements about nitrogen with a sum of bond angles of 360.0(5)° and 359.9(7)°, respectively, that are close to the ideal sum of 360° for a planar arrangement. These planar arrangements about the nitrogen atoms have been observed for the $XeNS_2$ groupings in $FXeN(SO_2F)_2$ (359.9(2)°)[62] and $XeN(SO_2F)_2^+Sb_3F_{16}^-$ (359.6(6)°),[20] and were attributed to the involvement of the nitrogen lone pair in partial sulfur-nitrogen π-bonding evidenced by their short S–N bond lengths (1.68(1) – 1.70(1) Å)[20,62] compared to values found in $NH_3^+SO_3^-$ (1.772 Å),[153] $K[NH_2SO_3]$ (1.666(6) Å),[154,155] $K_2[NH(SO_3)_2]$ (1.674(5) Å),[156,157] and $K_3[N(SO_3)_3]\cdot 2H_2O$ (1.71(2) Å).[158] The planar arrangements about nitrogen bonded to xenon and N–C bond lengths in *s*-$C_3F_3N_2N$–$XeF^+AsF_6^-$·2.5BrF_5 and C_5F_5N–$XeF^+AsF_6^-$·2.5BrF_5 indicate a significant measure of C–N double-bond character. The endocyclic C–N bond lengths in *s*-$C_3F_3N_2N$–$XeF^+AsF_6^-$·2.5BrF_5 (1.293(9) – 1.366(9) Å) and C_5F_5N–$XeF^+AsF_6^-$·2.5BrF_5 (1.349(12), 1.351(12) Å), and the C–C bond lengths in C_5F_5N–$XeF^+AsF_6^-$ (1.352(14) – 1.385(14) Å), are within 3σ of those reported for chemically similar bonds in *s*-$C_3F_3N_3$·AsF_5 (C–N, 1.279(14) – 1.340(13) Å)[159] and $((CH_3)_3N)_2Pt(CH_3)(C_5F_5N)^+$ (average: C–N, 1.340(6) Å; C–C, 1.366(8) Å).[160] The C–N and C–C bonds in these compounds exhibit considerable double-bond character since they are much shorter than the sum of their single bond covalent radii (C, 0.77 Å; N, 0.75 Å) and those in H_3C–NH_2

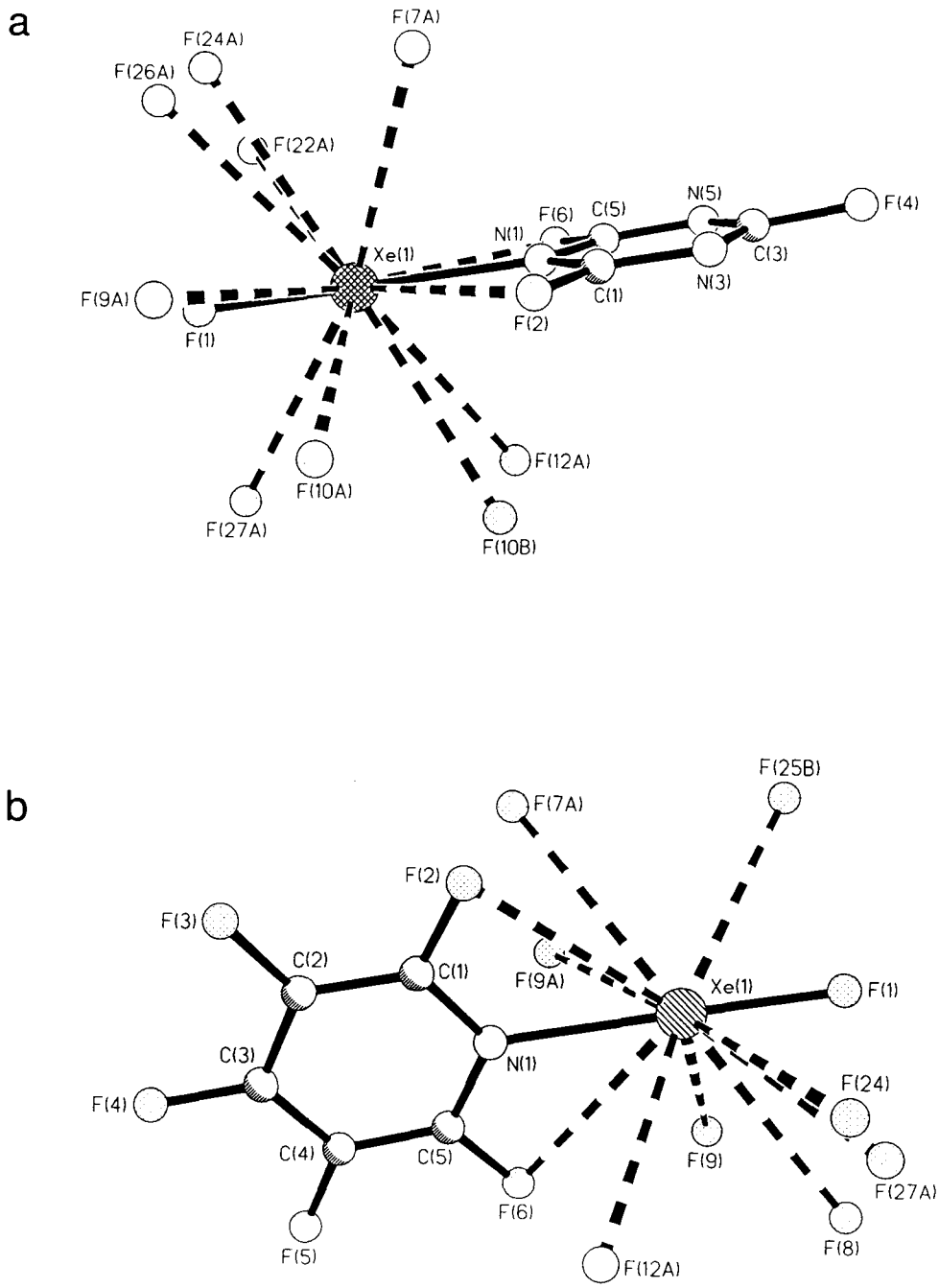

Figure 3.15 View of the closest fluorine contacts to xenon: (a) in *s*-$C_3F_3N_2N$–$XeF^+AsF_6^-\cdot 2.5BrF_5$; (b) in C_5F_5N–$XeF^+AsF_6^-\cdot 2.5BrF_5$. Dashed lines denote the Xe···F contacts.

(C–N, 1.471 Å) and $H_3C–CH_3$ (C–C, 1.5351 Å), respectively, where there are no electrons on nitrogen or carbon available for π-bonding.

The average C–F bond distances in $C_5F_5N–XeF^+AsF_6^-·2.5BrF_5$ (1.322(10) Å) and $((CH_3)_3N)_2Pt(CH_3)(C_5F_5N)^+$ (1.327(8) Å) are considerably more ionic than those found in *s*-$C_3F_3N_2N–XeF^+AsF_6^-·2.5BrF_5$ (1.300(8) Å) and *s*-$C_3F_3N_3·AsF_5$ (1.296(11) Å) possibly due to the repulsive or electron-withdrawing effect by the fluorines which are in close proximity to each other (2.715 – 2.738 Å) and are within the sum of two fluorine van der Waals radii (F···F, 2.70 – 3.00 Å). The average N–C–F bond angles in the structures (*s*-$C_3F_3N_2N–XeF^+AsF_6^-·2.5BrF_5$, 116.5(7)°; $C_5F_5N–XeF^+AsF_6^-·2.5BrF_5$, 115.6(9)°) are in agreement with each other within experimental error and are comparable to those in *s*-$C_3F_3N_3·AsF_5$ (116.4(2)°) and $((CH_3)_3N)_2Pt(CH_3)(C_5F_5N)^+$ (116.2(6)°). However, unlike in the latter compounds, the N–C–F angles nearest the xenon atoms in the $C_3F_3N_2N–XeF^+AsF_6^-·2.5BrF_5$ (115.0(6) and 114.3(7)°) and $C_5F_5N–XeF^+AsF_6^-·2.5BrF_5$ (115.6(9) and 115.6(9)°) structures are bent towards xenon. The observed angle distortions towards xenon may contribute to the stability of the adduct cations and is discussed in further detail in **Correlations of the Structural Findings with Spectroscopic Results.**

The *s*-$C_3F_3N_2N–XeF^+AsF_6^-·2.5BrF_5$, $C_5F_5N–XeF^+AsF_6^-·2.5BrF_5$, *s*-$C_3F_3N_3·AsF_5$, and $((CH_3)_3N)_2Pt(CH_3)(C_5F_5N)^+$ compounds are the only known examples with crystallographically well-characterized *s*-$C_3F_3N_3$ and C_5F_5N bases. Since geometrical parameters for the free bases are not available, it is not certain whether coordination of

these strongly basic perfluoro-organic nitrogen bases with XeF^+ results in significant decreases in the C–N and/or C–F bond lengths of the aromatic ring.

The arrangements of s-$C_3F_3N_2N$–$XeF^+AsF_6^-$·2.5BrF_5 and C_5F_5N–$XeF^+AsF_6^-$·2.5BrF_5 molecules in their respective crystal lattices are illustrated in Figures 3.16 and 3.17, respectively. The planar s-$C_3F_3N_2N$–XeF^+ and C_5F_5N–XeF^+ cations pack in alternating orientations along the c-axes separated by AsF_6^- anions and BrF_5 molecules, with the disordered BrF_5 molecules lying on crystallographically imposed inversion centers.

$Xe_2F_3^+AsF_6^-$

The crystal structures of the title compounds are reported in this work for the first time, with the exception of $Xe_2F_3^+AsF_6^-$ whose room temperature structure had been previously reported by Bartlett *et al.* in 1974.[21] The crystallization of $Xe_2F_3^+AsF_6^-$ during the preparation of $(CH_3)_3CC{\equiv}N$–$XeF^+AsF_6^-$ was unintentional, however, even though the room temperature structure reported previously is in good agreement with the low-temperature structure described in this Chapter (*vide infra*), more accurate geometrical parameters for $Xe_2F_3^+AsF_6^-$ are listed in Table 3.2. As in the previous structure,[21] there are two crystallographically non-equivalent $Xe_2F_3^+$ cations and two AsF_6^- anions (Figure 3.18). The lower R-factor in the present work is partially due to the refinement of a two-fold orientationally disordered AsF_6^- anion that was missed in the previous determination. The AsF_6^- anions are octahedral with As–F bond distances

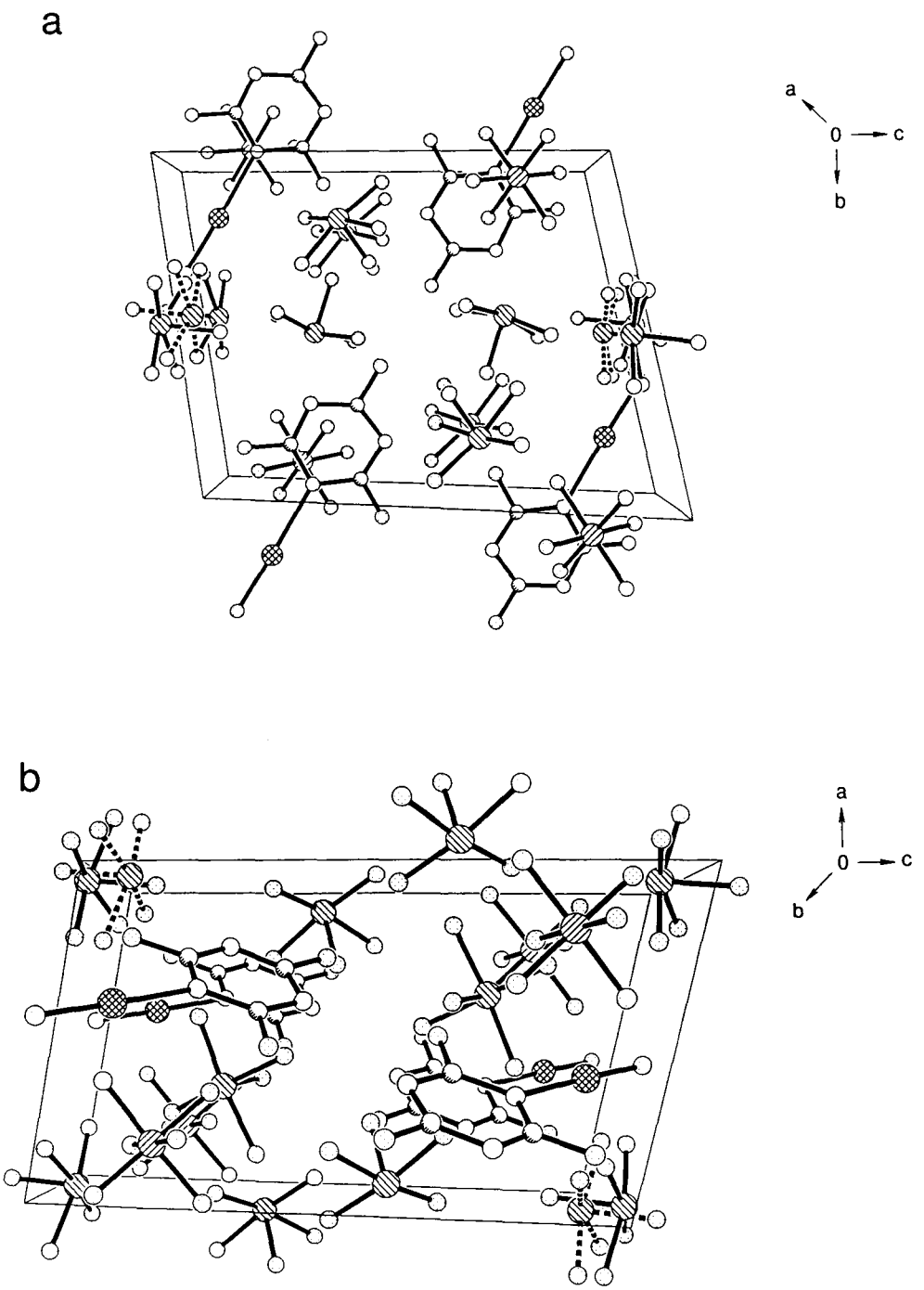

Figure 3.16 View of the *s*-$C_3F_3N_2N$–$XeF^+AsF_6^-$·2.5BrF_5 unit cell: (a) along the a-axis; (b) along the b-axis.

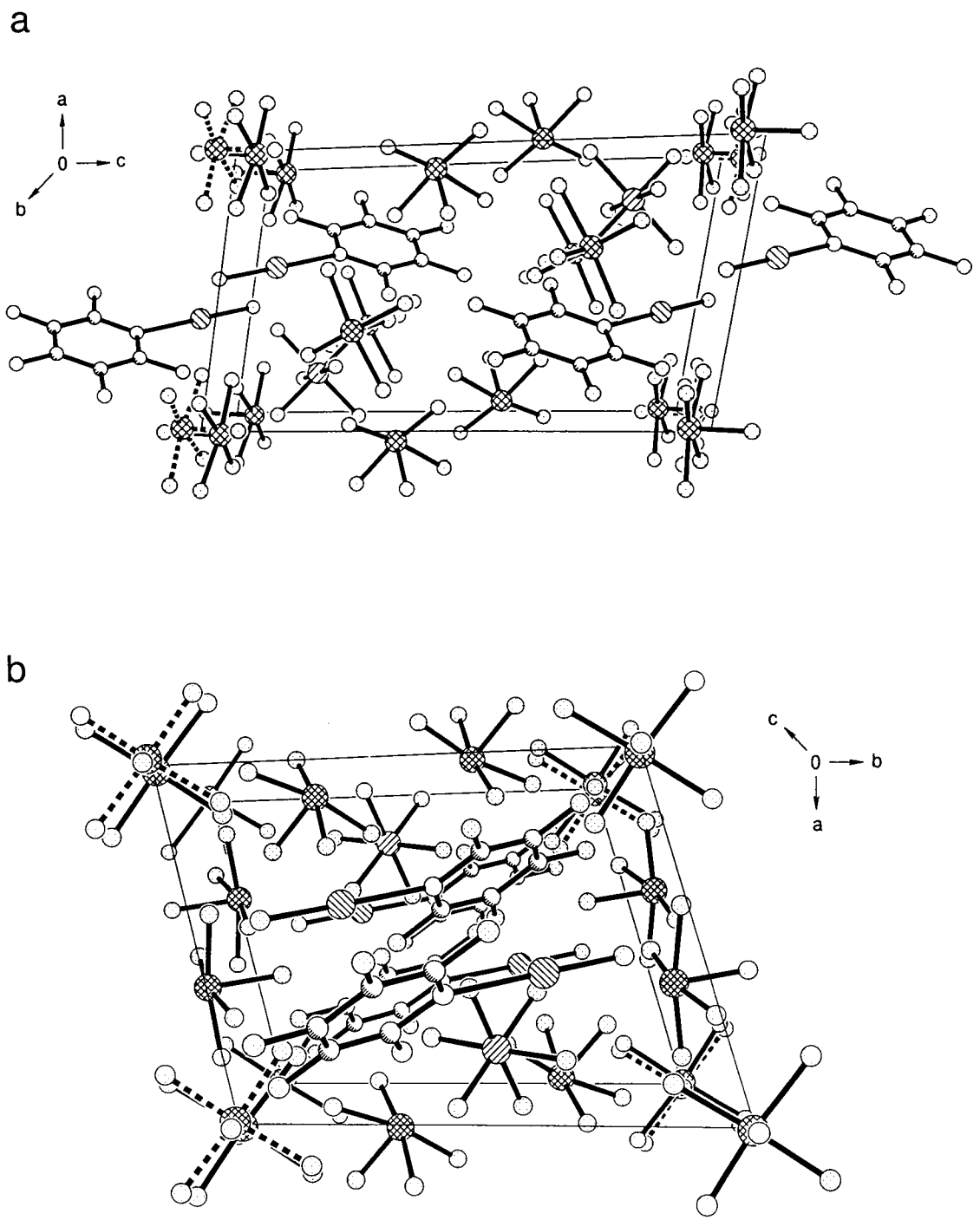

Figure 3.17 View of the C_5F_5N–$XeF^+AsF_6^-$·2.5BrF_5 unit cell: (a) along the b-axis; (b) along the c-axis.

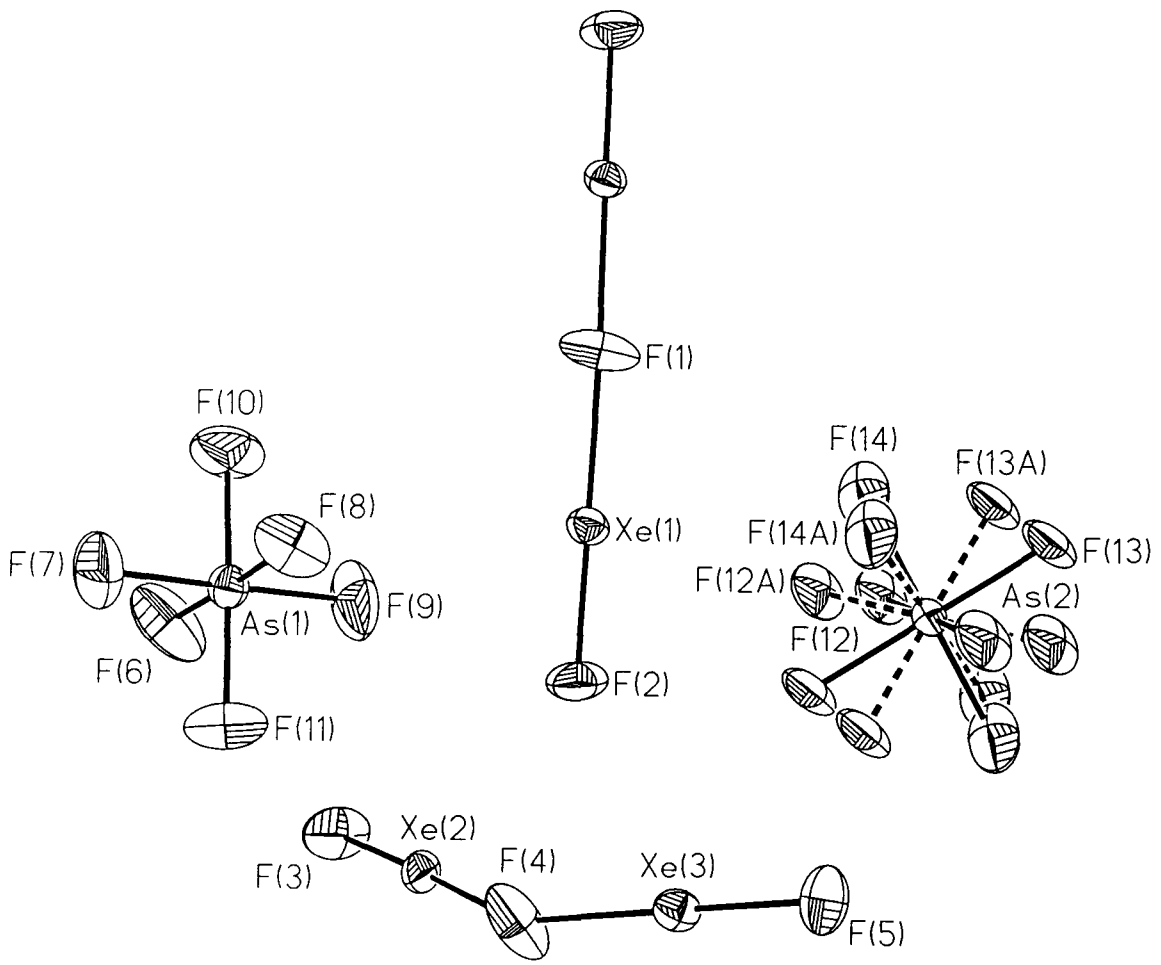

Figure 3.18 Structure of $Xe_2F_3^+AsF_6^-$ showing thermal ellipsoids at the 50% probability level and the disordered model of As(2).

(average, 1.708(7), 1.72(2) Å) and *cis* F–As–F bond angles (87.4(10) – 91.8(7)°) comparable to values found in the literature.[10,19,131] The cations are planar, V-shaped, and symmetrical about the bridging F atom, with each F–Xe–F component being essentially linear (average, 177.5(3)°). The linear arrangements about the xenon atoms are consistent with the AX_2E_3 valence-shell electron-pair repulsion (VSEPR) arrangement of bonding pairs in the axial positions and the lone electron pairs in the equatorial positions. The average terminal Xe–F (1.915(6) Å) and bridging Xe–F (2.149(7) Å) bond distances compare well with those reported (1.90(3) Å and 2.14(3) Å, respectively)[21] and with values found in the literature.[19,122] The average bridge Xe···F···Xe angle (149.1(4)°) is comparable to the reported value (150.2(8)°), however it is significantly larger than the expected 109.5° angle for the tetrahedral AX_2E_2 VSEPR arrangement of bonding and lone electron pairs. The extended structure of $Xe_2F_3^+AsF_6^-$ consists of rows of cations in alternating orientations separated by rows of anions (Figure 3.19).[21] Two long contacts (2.948 – 3.011 Å) are observed between each bridging fluorine atom with the terminal fluorine atoms of other cations as a consequence of closest packing (Figure 3.20). There are also several long fluorine contacts with the xenon atoms (listed in Appendix D) that are within the sum of the fluorine and xenon van der Waals radii (Xe···F = 3.63 Å) and are as short as 3.214 Å in length (Figure 3.21). The fluorine contacts appear to avoid regions about xenon perpendicular to the linear F–Xe–F plane where the lone pair electron density is expected. Contrary to the previous report, the crystal structure

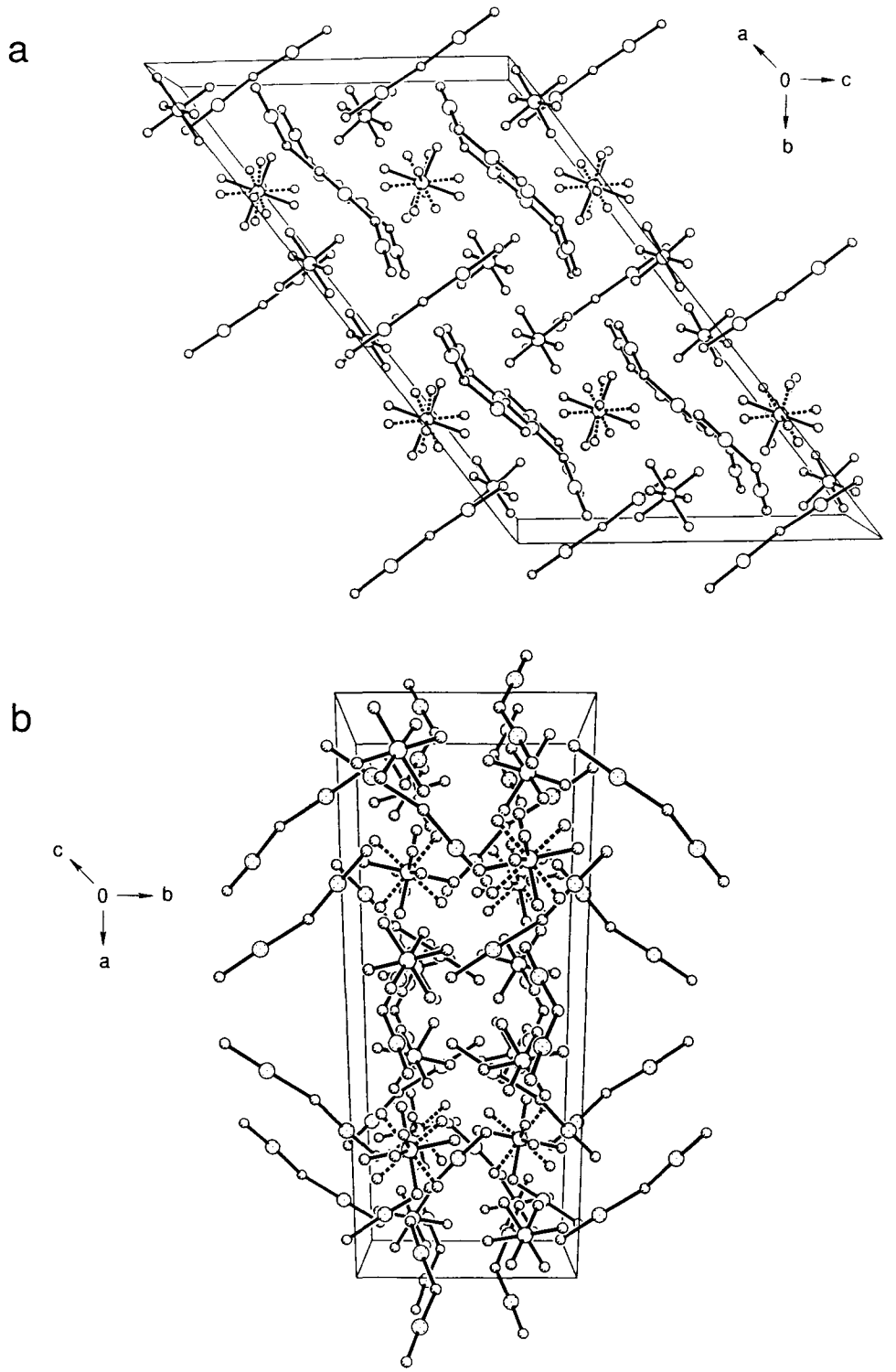

Figure 3.19 View of the $Xe_2F_3^+AsF_6^-$ unit cell: (a) along the a-axis; (b) along the c-axis.

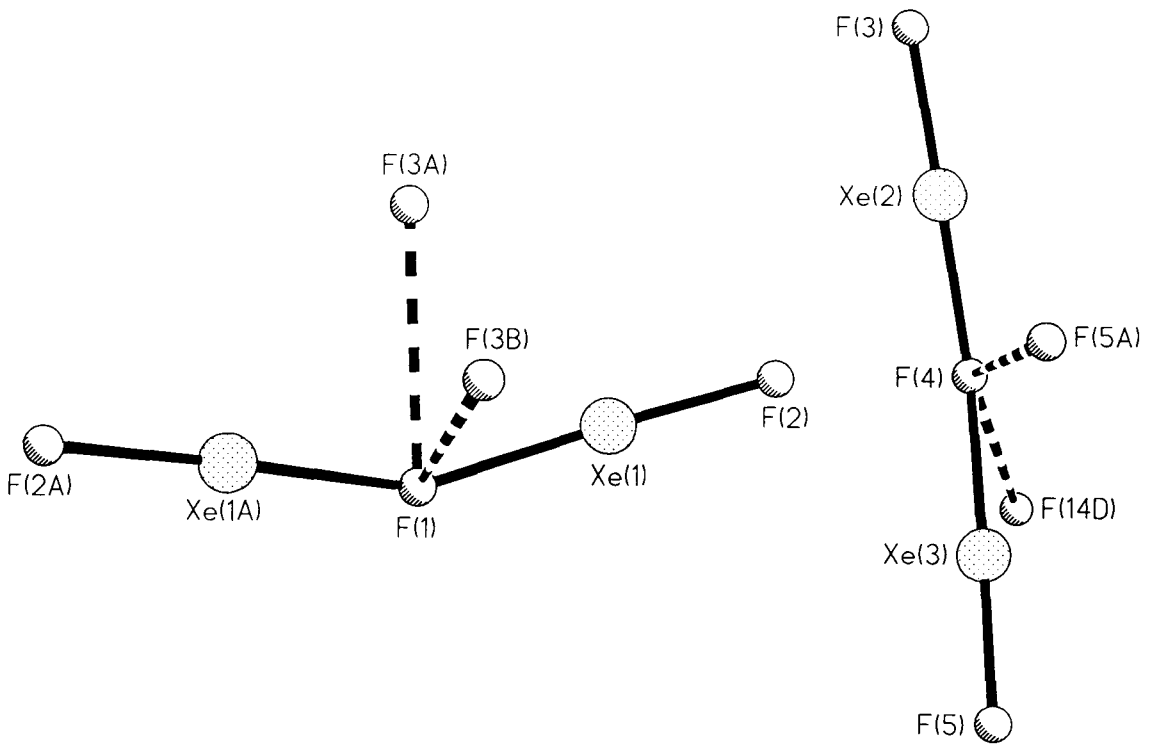

Figure 3.20 View of the closest fluorine contacts to the bridging fluorine atom in $Xe_2F_3^+AsF_6^-$. Dashed lines denote the F···F contacts.

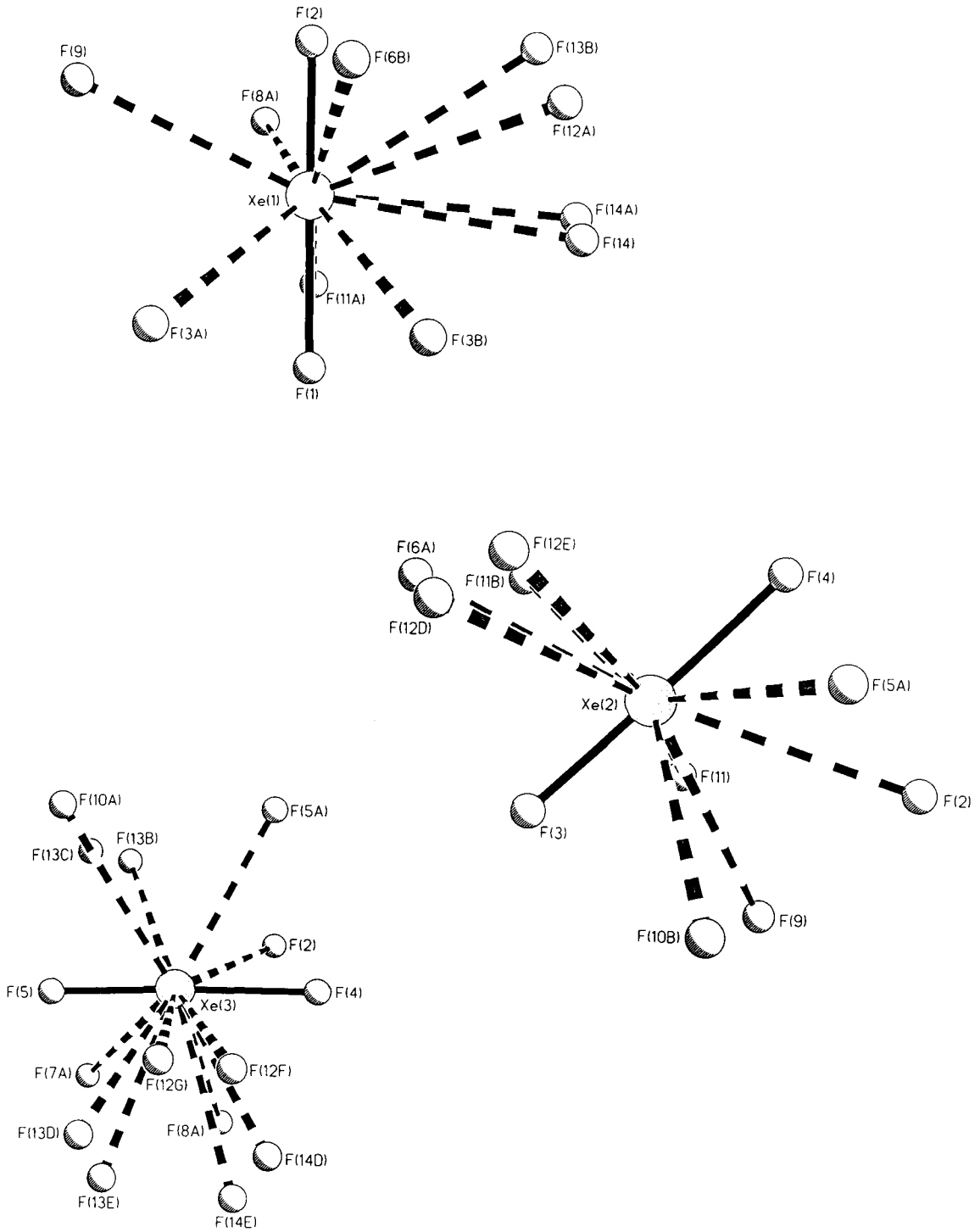

Figure 3.21 View of the closest fluorine contacts to the xenon atoms in $Xe_2F_3^+AsF_6^-$. Dashed lines denote the Xe···F contacts.

observed in the present work was refined in the conventional space group *C2/c* rather than in the space group *I2/a*.[21,161]

Correlations of the Structural Findings with Spectroscopic Results

$R–C{\equiv}N–XeF^{+}AsF_6^{-}$ (R = H, $(CH_3)_3C$), $CH_3C{\equiv}N–XeF^{+}AsF_6^{-}{\cdot}HF$, and $HC{\equiv}NH^{+}AsF_6^{-}$

The order of increasing ionic character in the Xe–F bonds parallels the increase in the covalent nature of the Xe–N bonds. The Xe–N bond becomes progressively more covalent and the Xe–F bond more ionic with increasing basicity of the nitrogen base. This trend correlates with previous measurements of ν(Xe–L) (L = F, N) provided by Raman spectroscopy, which signify increased covalency of the Xe–L bonds with shifts to higher frequency, and *vice versa* (Table 3.3). The relative covalent characters of the Xe–L bonds may also be correlated with ^{129}Xe and ^{19}F chemical shifts and with $^{1}J(^{129}Xe–^{19}F)$ and $^{1}J(^{129}Xe–^{14/15}N)$ spin-spin couplings (Table 3.3). On ascending Table 3.3, the values of $\delta(^{19}F)$ and $^{1}J(^{129}Xe–^{19}F)$ increase and the values of $\delta(^{129}Xe)$ and $^{1}J(^{129}Xe–^{14}N)$ decrease as the Xe–N bond covalency increases and the terminal Xe–F bond covalency decreases. The qualitative trends in bond lengths and associated spectroscopic parameters support earlier views and theoretical calculations that the Xe–N bonds in the cations may be thought of as classical Lewis acid-base donor-acceptor bonds[88-95] and that the bonding could be rationalized in terms of valence bond structures I and II, where the latter is the least important contributing structure due to the high charge

Table 3.3 Comparison of Some X-Ray Crystallographic, Raman, and NMR Parameters for the $HC{\equiv}N{-}XeF^+$,[68,69] $CH_3C{\equiv}N{-}XeF^+$,[69] $(CH_3)_3CC{\equiv}N{-}XeF^+$,[44] *s*-$C_3F_3N_2N{-}XeF^+$,[72] and $C_5F_5N{-}XeF^+$ [70] Cations.

	X-ray Crystallography (Å)		Raman (cm^{-1})[b]		NMR[c]			
Cation[a]	Xe–F	Xe–N	ν(Xe–F)	ν(Xe–N)	δ(^{129}Xe), ppm	δ(^{19}F), ppm[d]	^1J(^{129}Xe-^{19}F), Hz	^1J(^{129}Xe-^{14}N), Hz
$CH_3C{\equiv}N{-}XeF^+$	1.947(5)	2.179(7)	559		-1708	-185.5	6020	313
$(CH_3)_3CC{\equiv}N{-}XeF^+$	1.952(3)	2.212(4)	565	401	-1721	-184.3	6024	309
$HC{\equiv}N{-}XeF^+$	1.936(2)	2.235(3)	564	328, 335	-1555 (-1570)	-198.4 (-193.1)	6150 (6181)	336 (334)
$C_5F_5N{-}XeF^+$	1.932(6)	2.287(8)	528	401, 419	-1871.9 (-1922.5)	-148.3 (-139.6)	5936 (5926)	236
s-$C_3F_3N_2N{-}XeF^+$	1.931(5)	2.316(6)	544	313	-1807.9 (-1862.4)	-154.9 (-145.6)	5909 (5932)	245

[a] All cations have AsF_6^- as the counterion.
[b] Recorded at –196 °C as powdered samples.
[c] Chemical shifts are referenced with respect to the neat liquids $XeOF_4$ (^{129}Xe) and $CFCl_3$ (^{19}F) at 24 °C in $HF(BrF_5)$; a positive sign denotes the chemical shift of the resonance in question occurs to higher frequency of (is more shielded than) the resonance of the reference substance. The NMR spectra for the $HC{\equiv}N{-}XeF^+$,[68,69] $CH_3C{\equiv}N{-}XeF^+$,[69] $(CH_3)_3CC{\equiv}N{-}XeF^+$,[44] *s*-$C_3F_3N_2N{-}XeF^+$,[72] and $C_5F_5N{-}XeF^+$ [70] cations were recorded at -10 (-58), -10, -30, -5 (-50), and -30 (-30) °C, respectively.
[d] Refers to the terminal fluorine on the xenon atom.

$$[L\ {}^{+}Xe{-}F] \quad \leftrightarrow \quad [L{-}Xe^{2+}\ F^{-}]$$

I II

localization on xenon.[68,88] Implicit in this description of the Xe–N bond is a considerable degree of ionic character, which appears to be a dominant feature of the stability of the adduct cations.[68,88] The ability of XeF^+ to act as a "hard" Lewis acid was shown to be related to "the presence of holes in the valence shell charge concentrations of the xenon atoms that expose their cores," [88] such that the mechanism of formation of the Xe–N bonds in the adduct salts is similar to the formation of a hydrogen bond; *i.e.*, the mutual penetration of outer diffuse non-bonded densities in Xe and N is facilitated by their dipolar and quadrupolar polarizations, which remove density along their axis of approach, to yield a final density in the interatomic surface that is only slightly greater than the sum of the unperturbed densities.[88]

The shortening of the C≡N bond lengths upon protonation of HCN to give $HC{\equiv}NH^+AsF_6^-$ and upon adduct formation of the nitriles with XeF^+ to give the $R{-}C{\equiv}N{-}XeF^+AsF_6^-$ compounds correlates well with ^{13}C and $^{14/15}N$ NMR spectroscopic measurements summarized in Table 3.4. Despite solvent and temperature dependencies, generally, with increasing Lewis acidity of the ligand ($H^+ < XeF^+ < KrF^+$) on moving down the table, the ^{13}C and ^{14}N nuclei become less deshielded, the values of $^1J(^{13}C\text{-}^1H)$ increase, and the values for $^1J(^{14}N\text{-}^{13}C)$ decrease.

Semi-empirical calculations[144] of the electronic distribution in the transition metal complex, $TiCl_4(NCH)_2$, have previously been carried out to explain the observed C≡N–Ti

Table 3.4 Comparison of Some X-Ray Crystallographic and NMR Parameters for HCN,[163] $HC{\equiv}NH^+AsF_6^-$,[44,134] and $HC{\equiv}N{-}NgF^+AsF_6^-$ (Ng = Xe, Kr).[68,69,85]

	X-ray Crystallography (Å)		NMR[a]				
Cation	H–C	C≡N	$\delta(^{13}C)$, ppm	$\delta(^{14}N)$, ppm	$\delta(^{15}N)$, ppm	$^1J(^{13}C\text{-}^1H)$, Hz	$^1J(^{14}N\text{-}^{13}C)$, Hz
HCN	1.0655	1.1532	83.7			269	
$HC{\equiv}NH^+$		1.103(11)	97.1	-240.3		325	41
$HC{\equiv}N{-}XeF^+$	0.90(5)	1.116(4)	104.1	-235.1	(-230.2)	308	22
$HC{\equiv}N{-}KrF^+$			(98.5)		(-200.8)		

[a] Chemical shifts are referenced with respect to the neat liquids $XeOF_4$ (^{129}Xe) and $CFCl_3$ (^{19}F) at 24 °C; a positive sign denotes the chemical shift of the resonance in question occurs to higher frequency of (is more shielded than) the resonance of the reference substance. The NMR spectra for HCN,[163] $HC{\equiv}NH^+$, $HC{\equiv}N{-}XeF^+$ [68,69], and $HC{\equiv}N{-}KrF^+$ [85] and were recorded at -90 °C in $FSO_3H{-}SbF_5{-}SO_2$, 25 °C in HF, -10°C in HF (BrF_5), and -57 °C in (BrF_5) respectively.

deformation (178.1(8)°) in the compound. The calculations indicated that a considerable degree of electronic density remained on the nitrogen atom. Consequently, it was predicted that the nitrogen atom does not use pure sp-hybrid orbitals, rather the orbitals have partial sp^2 character. The reduced coupling constant $^1K(Xe–N)$ allows assessment of the relative degrees of hybridization for the nitrogen orbitals bonded to xenon and may be calculated according to equation (3.15), where h is Planck's constant, and $\gamma(^{14}N)$ and

$$^1K(Xe–N) = 4\pi^2[^1J(^{129}Xe–^{14}N)] / [h\gamma(^{14}N)\gamma(^{129}Xe)] \quad (3.15)$$

$\gamma(^{129}Xe)$ are the gyromagnetic ratios of the coupled nuclei. According to the Fermi contact mechanism, which is usually the dominant mechanism for scalar couplings that involve heavy nuclei, the magnitude of $^1K(Xe–N)$ decreases as the %s character of the nitrogen valence orbitals decreases. A comparison of the reduced coupling constants $^1K(Xe–N)$ for $HC{\equiv}N–XeF^+AsF_6^-$ (1.389 $NA^{-2}m^{-3}{\times}10^{22}$), $CH_3C{\equiv}N–XeF^+AsF_6^-{\cdot}HF$ (1.296 $NA^{-2}m^{-3}{\times}10^{22}$), and $(CH_3)_3CC{\equiv}N–XeF^+AsF_6^-$ (1.279 $NA^{-2}m^{-3}{\times}10^{22}$) with that of $FXeN(SO_2F)_2$ (0.913 $NA^{-2}m^{-3}{\times}10^{22}$) containing a formal sp^2-hybridized nitrogen center indicates that the %s character decreases in the order $HC{\equiv}N–XeF^+AsF_6^-$ > $CH_3C{\equiv}N–XeF^+AsF_6^-{\cdot}HF$ > $(CH_3)_3CC{\equiv}N–XeF^+AsF_6^-$ and follows the trend of increasing C≡N–Xe distortion (*vide supra*). Consequently, resonance structure IV is preferred over III in $(CH_3)_3CC{\equiv}N–XeF^+AsF_6^-$ due to the positive inductive effect of the $(CH_3)_3C$ group

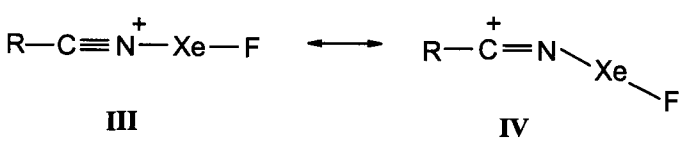

III IV

where the stabilization of the positive charge is greatest on C(1). The partial sp^2 characters of the nitrogen atoms in these adducts are further exhibited by the arrangement of the weak inter- and intramolecular contacts (*i.e.*, at the sum of their van der Waals radii (N, 1.55 Å; F, 1.35-1.50 Å))[36-38] around the nitrogen atom that appear to avoid the predicted electronic density on nitrogen (Figure 3.5).

s-$C_3F_3N_2N$–$XeF^+AsF_6^-\cdot 2.5BrF_5$ and C_5F_5N–$XeF^+AsF_6^-\cdot 2.5BrF_5$

Although the Xe–F bond lengths are not significantly different in the *s*-$C_3F_3N_2N$–$XeF^+AsF_6^-\cdot 2.5BrF_5$ and C_5F_5N–$XeF^+AsF_6^-\cdot 2.5BrF_5$ salts, the increase in covalent nature of the Xe–N bonds parallel the increase in $\delta(^{19}F)$, $^1J(^{129}Xe\text{-}^{19}F)$, and ν(Xe–N) values and the decrease in $\delta(^{129}Xe)$, $^1J(^{129}Xe\text{-}^{14}N)$, and ν(Xe–F) values (Table 3.3), as illustrated for R–C≡N–$XeF^+AsF_6^-$ (*vide supra*). Similar to R–C≡N–$XeF^+AsF_6^-$, the Xe–N bonds in *s*-$C_3F_3N_2N$–$XeF^+AsF_6^-\cdot 2.5BrF_5$ and C_5F_5N–$XeF^+AsF_6^-\cdot 2.5BrF_5$ may also be represented as classical Lewis acid-base donor-acceptor bonds.[88] However, along with valence bond structures V and VI (illustrated for *s*-$C_3F_3N_2N$–XeF^+, where VI is the

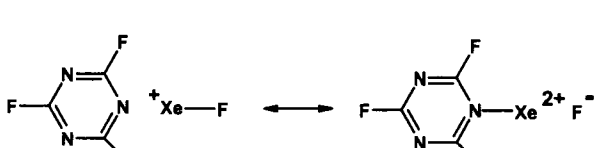

V **VI**

least important contributing structure), the bonding description of *s*-$C_3F_3N_2N$–$XeF^+AsF_6^-\cdot 2.5BrF_5$ and C_5F_5N–$XeF^+AsF_6^-\cdot 2.5BrF_5$ may also be represented as a resonance hybrid of valence bond structures VII and VIII, respectively. This additional

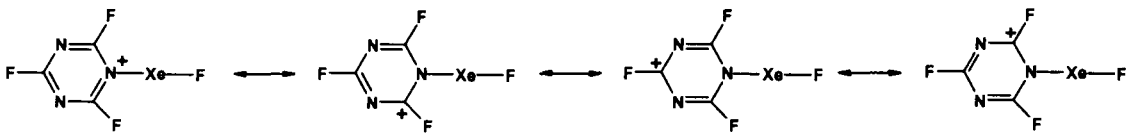

VII

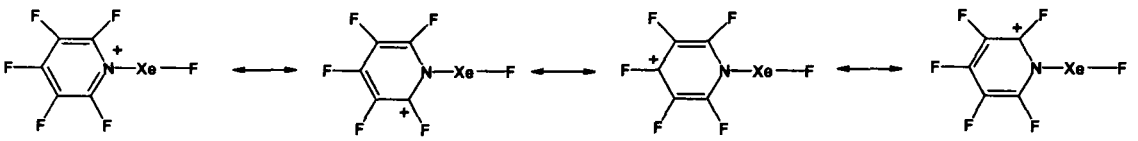

VIII

resonance effect, as well as the general electron-withdrawing effect by the fluorine substituents, the Coulombic interaction between F(2) and F(6) with xenon (structures IX and X) based on the distortion of N–C–F angles towards xenon, and significant ionic

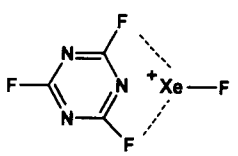

IX

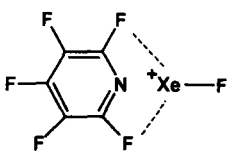

X

character of the Xe–N bonds, contribute to the higher thermal stability of these compounds when compared with the R–C≡N–$XeF^+AsF_6^-$ compounds. Similar arguments have previously been used to explain the relative stabilities of the Xe(2,6-$F_2C_6H_3)^+$ and MeCN···Xe–$C_6F_5^+$ cations among other $XeAr^+$ (Ar = 2-FC_6H_4, 4-FC_6H_4) derivatives having fewer fluorine atoms.[66,162]

Summary

The X-ray crystal structures of R–C≡N–$XeF^+AsF_6^-$ (R = H, CH_3, $(CH_3)_3C$), *s*-$C_3F_3N_2N$–$XeF^+AsF_6^-$·2.5BrF_5, and C_5F_5N–$XeF^+AsF_6^-$·2.5BrF_5 described in this Chapter

represent the first series of definitively characterized Xe–N bonded adducts derived from the interaction of the Lewis acid cation, XeF^+, with a variety of oxidatively resistant organic or fluoro-organic Lewis nitrogen bases. The structures support early evidence[68-70] by low-temperature Raman and NMR spectroscopy of covalent bonding between xenon(II) and formally sp- or sp^2-hybridized nitrogen. Their stabilities are attributed to the high effective group electronegativities of the nitrogen base donor ligands that have the ability to withstand the high electron affinity of the XeF^+ cation (10.9 eV).

By comparison of the geometrical parameters in the structures, the covalent nature of the Xe–N bonds increase in the order: s-$C_3F_3N_2N$–$XeF^+AsF_6^-$·2.5BrF_5 < C_5F_5N–$XeF^+AsF_6^-$·2.5BrF_5 < $HC{\equiv}N$–$XeF^+AsF_6^-$ < $(CH_3)_3CC{\equiv}N$–$XeF^+AsF_6^-$ < $CH_3C{\equiv}N$–$XeF^+AsF_6^-$·HF, indicating that s-$C_3F_3N_2N$–$XeF^+AsF_6^-$·2.5BrF_5 contains the most ionic Xe–N bond known to this series. Additionally, as the covalent nature of Xe–N bonds increase, base strengths of the nitrogen ligand groups increase, covalent characters of the Xe–F bonds decrease, the effective electronegativities of the nitrogen atoms decrease, and the Xe nuclei become more shielded in the ^{129}Xe NMR spectra (see Table 3.3). Therefore, among the nitrogen electron donor centers investigated, namely those having formal sp- and sp^2-hybridizations, the effective electronegativities of those in the nitrile bases are lower. This is reflected in the lower relative thermal stabilities of the R–C≡N–$XeF^+AsF_6^-$ (R = H, CH_3, $(CH_3)_3C$) adducts when compare with s-$C_3F_3N_2N$–$XeF^+AsF_6^-$[72] and C_5F_5N–$XeF^+AsF_6^-$.[70]

CHAPTER 4

THE STRUCTURAL CHARACTERIZATION OF F_5TeNH_2, $F_5TeNH_3^+AsF_6^-$, AND $F_5TeN(H)Xe^+AsF_6^-$

INTRODUCTION

Since the first reported Xe–N bond in $FXeN(SO_2F)_2$ was definitively characterized in this laboratory by multi-NMR spectroscopy, Raman spectroscopy, and X-ray crystallography,[62,63,164] other imidodisulfurylfluoride Xe-N bonded species have been characterized by multi-NMR spectroscopy, namely $Xe[N(SO_2F)_2]_2$,[63,64] $F[XeN(SO_2F)_2]_2^+$,[20,63] $XeN(SO_2F)_2^+AsF_6^-$,[20] and $XeN(SO_2F)_2^+Sb_3F_{16}^-$.[20] The salt, $XeN(SO_2F)_2^+Sb_3F_{16}^-$, has also been characterized by X-ray crystallography. The ability of the imidodisulfurylfluoride ligand to form stable bonds to xenon is attributed to its high electronegativity and resistance to oxidative attack.

More recently, the Lewis acidity of the XeF^+ cation has been utilized in the preparation of novel Xe–N bonded adduct cations, $D–Xe–F^+$, by its reaction with oxidatively resistant organo- and fluoro-organo nitrogen bases (D) in HF according to equation (4.1).[34,70] In these acid-base reactions, XeF^+ functions as an electron-pair

$$D + XeF^+AsF_6^- + HF \longrightarrow D–XeF^+AsF_6^- + HF \qquad (4.1)$$

acceptor for the lone pair on the nitrogen base of the ligand. Because of the strong oxidizing power of XeF^+, only oxidatively resistant bases whose first adiabatic ionization

potentials (IP_1) exceed the electron affinity of XeF^+ (10.9 eV) are resistant to oxidation, allowing the isolation of D–$XeF^+AsF_6^-$ at low temperatures.[34,70] The Xe–N bonded compounds which have been prepared by the reaction of XeF^+ with neutral bases in HF or by reactions of XeF_2 with the protonated base in BrF_5 include R–C≡N–$XeF^+AsF_6^-$ (R = H, alkyl, fluoroalkyl, C_6F_5),[68,69,72] *s*-$C_3F_3N_2N$–$XeF^+AsF_6^-$,[72] C_5F_5N–$XeF^+AsF_6^-$,[70] and $R_FC_5F_4N$–$XeF^+AsF_6^-$ (R_F = 2-CF_3, 4-CF_3).[70] In Chapter 3, the detailed structures of several of these thermally unstable Xe–N bonded adduct salts have been obtained for the first time. All of these adduct cations involve ligands in which the nitrogen bonded to xenon is formally sp- or sp^2-hybridized. Besides the partially characterized salt, $F_5SN(H)Xe^+AsF_6^-$,[26] which can be prepared by solvolysis of $F_3S{\equiv}NXeF^+AsF_6^-$ in HF solvent, there are no examples of formally sp^3-hybridized nitrogen atoms bonded to xenon and none that have been characterized by X-ray crystallography.

Significant progress has been made in noble-gas chemistry as a result of recent developments in this laboratory that have led to reliable and routine methods for the low-temperature growing and mounting of thermally unstable and air-sensitive single crystals. In the present work, the syntheses and detailed structural characterizations by low-temperature single crystal X-ray diffraction of $F_5TeN(H)Xe^+AsF_6^-$, $F_5TeNH_3^+AsF_6^-$, and F_5TeNH_2 are described. The synthesis of $F_5TeN(H)Xe^+AsF_6^-$ by the reaction of $XeF^+AsF_6^-$ with F_5TeNH_2 in HF solvent, using the method of Schrobilgen and Whalen,[26] represents the first example where an inorganic ammonium base is utilized as a precursor to a compound containing a Xe–N bond. The $F_5TeN(H)Xe^+$ cation is isolobal with the

F_5ChOXe^+ cations (Ch = Se, Te) and represents the second example where xenon(II) is bonded to formally sp^3-hybridized nitrogen and the first to have been characterized by X-ray crystallography.[34]

Prior to this work, natural abundance and 99.5% ^{15}N-enriched $F_5TeN(H)Xe^+AsF_6^-$,[26] $F_5TeNH_3^+AsF_6^-$,[26] and F_5TeNH_2 [123] had been characterized by ^1H, ^{15}N, ^{19}F, ^{125}Te, and ^{129}Xe NMR spectroscopy and by Raman spectroscopy. In the case of the $F_5TeN(H)Xe^+$ cation, the NMR and Raman spectroscopic findings were consistent with a strong covalent bonding interaction between xenon and nitrogen along with a weak Xe···F–As fluorine bridge interaction between the cation and the anion.[26] In order to better characterize the nature of the Xe–N bond in $F_5TeN(H)Xe^+AsF_6^-$, its synthesis and spectroscopic characterizations have been complemented in the present study by X-ray structural characterizations of $F_5TeN(H)Xe^+AsF_6^-$, $F_5TeNH_3^+AsF_6^-$, and F_5TeNH_2 combined with local density functional theory (LDFT/DZVP) calculations on $F_5TeN(H)Xe^+AsF_6^-$, $F_5TeNH_3^+AsF_6^-$, and F_5TeNH_2.

The primary amine, F_5TeNH_2, is isoelectronic with the strong acid F_5TeOH and is thought to be among the least electronegative nitrogen-donor ligands to form compounds with xenon(II).[123,165] The low electronegativity of the ligand is reflected in the thermal instability of $F_5TeN(H)Xe^+AsF_6^-$.[26] Despite the low basicity of the nitrogen in F_5TeNH_2, it may be protonated in anhydrous HF solvent to give $F_5TeNH_3^+$, which is present in equilibrium with XeF_2 and $F_5TeN(H)Xe^+$ during the synthesis of $F_5TeN(H)Xe^+$ [see equations (4.4) – (4.6)].[26] In the present Chapter, the effect of the protonation of

F_5TeNH_2 on the bonding of the F_5TeN group was also investigated by the X-ray crystal structures and theoretical calculations of F_5TeNH_2 and $F_5TeNH_3^+AsF_6^-$.

RESULTS AND DISCUSSION

Preparation of F_5TeNH_2, $F_5TeNH_3^+AsF_6^-$, and $F_5TeN(H)Xe^+AsF_6^-$

Aminotellurium(VI) pentafluoride, F_5TeNH_2, has been prepared according to the method of Seppelt and Lentz [equations (4.2) and (4.3)].[123] The amine is a volatile,

$$TeF_6 + (CH_3)_3SiNHSi(CH_3)_3 \longrightarrow F_5TeNHSi(CH_3)_3 + (CH_3)_3SiF \quad (4.2)$$

$$F_5TeNHSi(CH_3)_3 + HF \longrightarrow F_5TeNH_2 + (CH_3)_3SiF \quad (4.3)$$

colorless solid that is moderately soluble in SO_2, and is a suitable candidate for single crystal growth.

The $F_5TeNH_3^+AsF_6^-$ and $F_5TeN(H)Xe^+AsF_6^-$ salts were prepared by the reaction of stoichiometric amounts of $XeF^+AsF_6^-$ and F_5TeNH_2 in anhydrous HF solvent according to the method of Whalen[26] [equations (4.4), (4.5), and (4.6)]. The F_5TeNH_2

$$XeF^+AsF_6^- + HF \rightleftharpoons XeF_2 + H_2F^+AsF_6^- \quad (4.4)$$

$$F_5TeNH_2 + H_2F^+AsF_6^- \rightleftharpoons F_5TeNH_3^+AsF_6^- + HF \quad (4.5)$$

$$F_5TeNH_3^+AsF_6^- + XeF_2 \rightleftharpoons F_5TeN(H)Xe^+AsF_6^- + 2HF \quad (4.6)$$

base was protonated in HF acidified with $XeF^+AsF_6^-$ forming $F_5TeNH_3^+AsF_6^-$ and XeF_2 according to equations (4.4) and (4.5). The $F_5TeNH_3^+AsF_6^-$ salt undergoes an HF elimination reaction with XeF_2 to form $F_5TeN(H)Xe^+AsF_6^-$ [eq (4.6)]. Both

$F_5TeN(H)Xe^+AsF_6^-$ and $F_5TeNH_3^+AsF_6^-$ crystallize from anhydrous HF at *ca.* -50 °C as yellow and colorless needles, respectively.

X-ray Crystal Structures of F_5TeNH_2, $F_5TeNH_3^+AsF_6^-$, and $F_5TeN(H)Xe^+AsF_6^-$

A summary of the refinement results and other crystallographic information are given in Table 4.1. The final atomic coordinates and equivalent isotropic thermal parameters are summarized in Appendix B. Important bond lengths and angles for F_5TeNH_2, $F_5TeN(H)Xe^+AsF_6^-$, and $F_5TeNH_3^+AsF_6^-$ are listed in Table 4.2 along with the calculated values (see **Computational Results**). The values related to $F_5TeNH_3^+AsF_6^-$ and F_5TeNH_2 are given in parentheses and square brackets, respectively. Unless otherwise mentioned, the values for F_5TeNH_2 are for the low-temperature (-113 °C) phase structure.

The structure of $F_5TeNH_3^+AsF_6^-$ (Figure 4.1) consists of well-separated $F_5TeNH_3^+$ cations and AsF_6^- anions, whereas in $F_5TeN(H)Xe^+AsF_6^-$ (Figure 4.2) each AsF_6^- anion is fluorine-bridged to a $F_5TeN(H)Xe^+$ cation through a short Xe···F bridge bond (2.580(3) Å). The AsF_6^- anion in $F_5TeNH_3^+AsF_6^-$ is octahedral about arsenic with all *cis* F–As–F angles approximately equal to 90° and an average As–F bond distance of 1.722(3) Å that is comparable to values found in the literature.[10,19,21,131] The AsF_6^- anion in $F_5TeN(H)Xe^+AsF_6^-$ has a distorted octahedral geometry with the bridging As–F bond length longer (1.740(4) Å) than the others (average, 1.696(9) Å). Similar As–F bridge

Table 4.1 Summary of Crystal Data and Refinement Results for $F_5TeNH_3^+AsF_6^-$, $F_5TeN(H)Xe^+AsF_6^-$, and F_5TeNH_2.

	$F_5TeNH_3^+AsF_6^-$	$F_5TeN(H)Xe^+AsF_6^-$	F_5TeNH_2	F_5TeNH_2
empirical formula	$H_3AsF_{11}NTe$	$HAsF_{11}NTeXe$	H_2F_5NTe	H_2F_5NTe
space group (No.)	$P2_1/m$ (11)	$P\bar{1}$ (2)	$I\bar{4}3m$ (217)	$P2_1$ (4)
a (Å)	6.6397(2)	5.3898(3)	6.404(5)	5.163 (2)
b (Å)	17.0068(1)	7.0580(3)	6.404(5)	9.083 (4)
c (Å)	11.1684(3)	12.5326(4)	6.404(5)	5.262 (2)
α (deg.)	90	86.736(3)	90	90
β (deg.)	105.636(2)	84.064(3)	90	112.223 (8)
γ (deg.)	90	85.531(3)	90	90
V (Å^3)	1214.47(5)	472.18(4)	262.6(4)	228.4 (2)
molecules/unit cell	6	2	2	2
mol. wt. (g mol^{-1})	428.55	557.84	238.63	477.25
calcd. density (g cm^{-3})	3.516	3.924	3.018	3.469
T (°C)	-109	-109	-5	-113
μ (mm^{-1})	7.889	10.295	5.665	6.512
wavelength (Å)	0.71073	0.71073	0.71073	0.71073
final agreement factors[a]	$R_1 = 0.0271$ $wR_2 = 0.0735$	$R_1 = 0.0373$ $wR_2 = 0.0946$	$R_1 = 0.0324$ $wR_2 = 0.1001$	$R_1 = 0.0415$ $wR_2 = 0.1132$

[a] R_1 is defined as $\Sigma||F_o| - |F_c||/\Sigma|F_o|$ for $I > 2\sigma(I)$.
wR_2 is defined as $[\Sigma[w(F_o^2 - F_c^2)^2]/\Sigma w(F_o^2)^2]^{1/2}$ for $I > 2\sigma(I)$.

Table 4.2 Experimental and Calculated Geometries for $F_5TeNH_3^+AsF_6^-$, $F_5TeN(H)Xe^+AsF_6^-$, and F_5TeNH_2.

$F_5TeNH_3^+AsF_6^-$ [a]

	Bond Lengths (Å)			
	expt	LDFT/DZVP		expt
Te(1)-N(1)	2.049(3)	2.154	As(1)-F(9)	1.707(2)
Te(1)-F(1)	1.810(2)	1.867	As(1)-F(10)	1.732(2)
Te(1)-F(2)	1.814(2)	1.888	As(1)-F(11)	1.724(2)
Te(1)-F(3)	1.815(2)	1.889	As(2)-F(12)	1.716(2)
Te(2)-N(2)	2.043(2)	2.154	As(2)-F(13)	1.734(2)
Te(2)-F(4)	1.815(2)	1.888	As(2)-F(14)	1.729(2)
Te(2)-F(5)	1.819(2)	1.889	As(2)-F(15)	1.709(2)
Te(2)-F(6)	1.819(2)	1.888	As(3)-F(16)	1.721(2)
Te(2)-F(7)	1.815(2)	1.888	As(3)-F(17)	1.722(2)
Te(2)-F(8)	1.806(2)	1.867	As(3)-F(18)	1.721(2)
			As(3)-F(19)	1.727(2)

Table 4.2 (continued)

Bond Angles (deg.)

	expt	LDFT/DZVP		expt
F(1)-Te(1)-F(2)	91.33(8)	94.9	F(10)-As(1)-F(10A)	180.0
F(1)-Te(1)-F(2A)	91.32(8)	95.2	F(10)-As(1)-F(11)	89.87(8)
F(1)-Te(1)-F(3)	91.29(8)	94.9	F(10)-As(1)-F(11A)	90.13(8)
F(1)-Te(1)-F(3A)	91.29(8)	95.2	F(10A)-As(1)-F(11A)	89.87(8)
F(1)-Te(1)-N(1)	179.77(11)	179.8	F(11)-As(1)-F(9A)	89.69(9)
F(2)-Te(1)-F(2A)	90.57(12)	89.7	F(11)-As(1)-F(10A)	90.13(8)
F(2)-Te(1)-F(3)	89.28(9)	89.4	F(11)-As(1)-F(11A)	180.0
F(2)-Te(1)-F(3A)	177.39(8)	169.9	F(12)-As(2)-F(13)	89.61(8)
F(2)-Te(1)-N(1)	88.84(9)	85.0	F(12)-As(2)-F(13A)	89.61(8)
F(3)-Te(1)-F(2A)	177.39(8)	169.9	F(12)-As(2)-F(14)	90.19(8)
F(3)-Te(1)-F(3A)	90.75(12)	89.5	F(12)-As(2)-F(14A)	90.19(8)
F(3)-Te(1)-N(1)	88.55(9)	85.3	F(12)-As(2)-F(14A)	90.19(8)
F(2A)-Te(1)-F(3A)	89.28(9)	89.7	F(12)-As(2)-F(15)	179.57(11)
F(2A)-Te(1)-N(1)	88.84(9)	84.6	F(13)-As(2)-F(13A)	90.24(11)
F(3A)-Te(1)-N(1)	88.55(9)	84.9	F(13)-As(2)-F(14)	89.82(8)
F(4)-Te(2)-F(5)	177.57(7)	169.9	F(13)-As(2)-F(14A)	179.79(9)
F(4)-Te(2)-F(6)	90.20(8)	89.7	F(13A)-As(2)-F(14A)	89.82(8)

Table 4.2 (continued)

F(4)-Te(2)-F(7)	90.26(8)	89.7
F(4)-Te(2)-F(8)	91.70(9)	95.2
F(4)-Te(2)-N(2)	89.17(10)	84.6
F(5)-Te(2)-F(6)	89.55(8)	89.5
F(5)-Te(2)-F(7)	89.94(8)	89.4
F(5)-Te(2)-F(8)	90.72(9)	94.9
F(5)-Te(2)-N(2)	88.41(9)	85.3
F(6)-Te(2)-F(7)	178.59(7)	169.9
F(6)-Te(2)-F(8)	90.57(8)	95.2
F(6)-Te(2)-N(2)	89.75(8)	84.9
F(7)-Te(2)-F(8)	90.75(8)	94.9
F(7)-Te(2)-N(2)	88.92(8)	85.0
F(8)-Te(2)-N(2)	179.07(8)	179.8
F(9)-As(1)-F(9A)	180.0	
F(9)-As(1)-F(10)	89.43(9)	
F(9)-As(1)-F(10A)	90.57(9)	
F(9)-As(1)-F(11)	90.31(9)	
F(9)-As(1)-F(11A)	89.69(9)	
F(14)-As(2)-F(13A)	179.79(9)	
F(14)-As(2)-F(14A)	90.11(12)	
F(14)-As(2)-F(15)	90.11(8)	
F(15)-As(2)-F(13A)	90.09(8)	
F(15)-As(2)-F(14A)	90.11(8)	
F(16)-As(3)-F(17)	90.74(8)	
F(16)-As(3)-F(17A)	90.74(8)	
F(16)-As(3)-F(18)	89.43(8)	
F(16)-As(3)-F(18A)	89.43(8)	
F(16)-As(3)-F(19)	179.03(10)	
F(17)-As(3)-F(17A)	90.30(11)	
F(17)-As(3)-F(18)	89.19(9)	
F(17)-As(3)-F(18A)	179.46(7)	
F(17)-As(3)-F(19)	89.95(8)	
F(17A)-As(3)-F(18A)	89.19(9)	
F(18)-As(3)-F(17A)	179.46(7)	
F(18)-As(3)-F(18A)	91.33(11)	
F(18)-As(3)-F(19)	89.89(8)	

Table 4.2 (continued)

F(9A)-As(1)-F(10A)	89.43(9)	F(19)-As(3)-F(17A)	89.95(8)
F(9A)-As(1)-F(11A)	90.32(9)	F(19)-As(3)-F(18A)	89.89(8)
F(10)-As(1)-F(9A)	90.57(9)		

$F_5TeN(H)Xe^+AsF_6^-$

	Bond Lengths (Å)					
	expt	LDFT/DZVP[b]			expt	LDFT/DZVP[b]
Te(1)-N(1)	1.982(5)	2.025	[2.108]	As(1)-F(6)	1.697(4)	1.730
Te(1)-F(1)	1.791(4)	1.891	[1.873]	As(1)-F(7)	1.701(3)	1.731
Te(1)-F(2)	1.805(4)	1.919	[1.909]	As(1)-F(8)	1.686(4)	1.763
Te(1)-F(3)	1.819(3)	1.915	[1.902]	As(1)-F(9)	1.684(4)	1.717
Te(1)-F(4)	1.820(3)	1.907	[1.904]	As(1)-F(10)	1.712(3)	1.759
Te(1)-F(5)	1.801(4)	1.898	[1.886]	As(1)-F(11)	1.740(4)	1.978
N(1)-H(1)	0.93(6)	1.044	[1.051]			
Xe(1)-N(1)	2.044(4)	2.149	[2.108]			
Xe(1)-F(11)	2.580(3)					

Table 4.2 (continued)

Bond Angles (deg.)

	expt	LDFT/DZVP[b]		expt	LDFT/DZVP[b]
F(1)-Te(1)-F(2)	88.8(2)	87.2	F(6)-As(1)-F(7)	90.1(2)	91.0
F(1)-Te(1)-F(3)	89.6(2)	90.6	F(6)-As(1)-F(8)	176.8(2)	167.6
F(1)-Te(1)-F(4)	91.5(2)	90.9	F(6)-As(1)-F(9)	91.9(2)	97.1
F(1)-Te(1)-F(5)	88.4(2)	88.1	F(6)-As(1)-F(10)	89.1(2)	89.7
F(1)-Te(1)-N(1)	176.6(2)	178.5	F(6)-As(1)-F(11)	88.9(2)	84.6
F(2)-Te(1)-F(3)	90.4(2)	90.7	F(7)-As(1)-F(8)	91.9(2)	89.4
F(2)-Te(1)-F(4)	89.7(2)	89.0	F(7)-As(1)-F(9)	92.8(2)	96.6
F(2)-Te(1)-F(5)	177.2(2)	175.4	F(7)-As(1)-F(10)	176.4(2)	168.4
F(2)-Te(1)-N(1)	94.2(2)	94.2	F(7)-As(1)-F(11)	89.0(2)	84.9
F(3)-Te(1)-F(4)	178.9(2)	178.5	F(8)-As(1)-F(9)	90.5(2)	95.1
F(3)-Te(1)-F(5)	89.6(2)	89.7	F(8)-As(1)-F(10)	88.8(2)	87.5
F(3)-Te(1)-N(1)	88.8(2)	89.7	F(8)-As(1)-F(11)	88.6(2)	83.1
F(4)-Te(1)-F(5)	90.4(2)	90.7	F(9)-As(1)-F(10)	90.8(2)	94.9
F(4)-Te(1)-N(1)	90.1(2)	88.8	F(9)-As(1)-F(11)	178.1(2)	177.6
F(5)-Te(1)-N(1)	88.6(2)	90.4	F(10)-As(1)-F(11)	87.4(2)	83.6
Te(1)-N(1)-Xe(1)	115.1(2)	113.0			
Te(1)-N(1)-H(1)	109(4)	105.3			

Table 4.2 (continued)

Xe(1)-N(1)-H(1)	107(4)	105.1
F(11)-Xe(1)-N(1)	171.6(2)	
As(1)-F(11)-Xe(1)	128.1(2)	

F_5TeNH_2 (-113 °C)[c]

Bond Lengths (Å)

	expt	LDFT/DZVP		expt	LDFT/DZVP
Te(1)-N(1)	1.94(2)	1.975	Te(1)-F(3)	1.85(2)	1.912
Te(1)-F(1)	1.83(2)	1.900	Te(1)-F(4)	1.85(2)	1.912
Te(1)-F(2)	1.854(6)	1.923	Te(1)-F(5)	1.855(6)	1.902

Bond Angles (deg.)

	expt	LDFT/DZVP2		expt	LDFT/DZVP2
F(1)-Te(1)-F(2)	85.3(8)	85.2	F(2)-Te(1)-N(1)	91.5(10)	95.6
F(1)-Te(1)-F(3)	85.5(3)	89.7	F(3)-Te(1)-F(4)	174.1(11)	179.3
F(1)-Te(1)-F(4)	88.9(11)	89.7	F(3)-Te(1)-F(5)	87.7(8)	89.8
F(1)-Te(1)-F(5)	88.6(7)	86.3	F(3)-Te(1)-N(1)	89.9(12)	90.3

Table 4.2 (continued)

F(1)-Te(1)-N(1)	174.4(11)	179.2	F(4)-Te(1)-F(5)	90.3(8)	89.8
F(2)-Te(1)-F(3)	90.9(8)	90.1	F(4)-Te(1)-N(1)	95.8(4)	90.3
F(2)-Te(1)-F(4)	90.5(8)	90.1	F(5)-Te(1)-N(1)	94.5(9)	92.9
F(2)-Te(1)-F(5)	173.9(7)	171.5			

F_5TeNH_2 (-5 °C)

	Bond Lengths (Å)
	expt
Te(1)-N/F	1.82(2)

[a] The calculated values reported are for the free ions $F_5TeNH_3^+$ and AsF_6^-. Other observed and calculated bond lengths (Å) for $F_5TeNH_3^+$: N(1)-H(1A, 1B): obs. 0.820/ calc. 1.042

N(2)-H(2A, 2B, 2C): obs. 0.833/ calc. 1.042

[b] The calculated values reported are for the ion pair $F_5TeN(H)Xe^+AsF_6^-$ and the free ion $F_5TeN(H)Xe^+$ [square brackets].

[c] Other observed and calculated bond lengths (Å) for F_5TeNH_2: N(1)-H(1A, 1B, 1C): obs. 0.900/ calc. 1.033

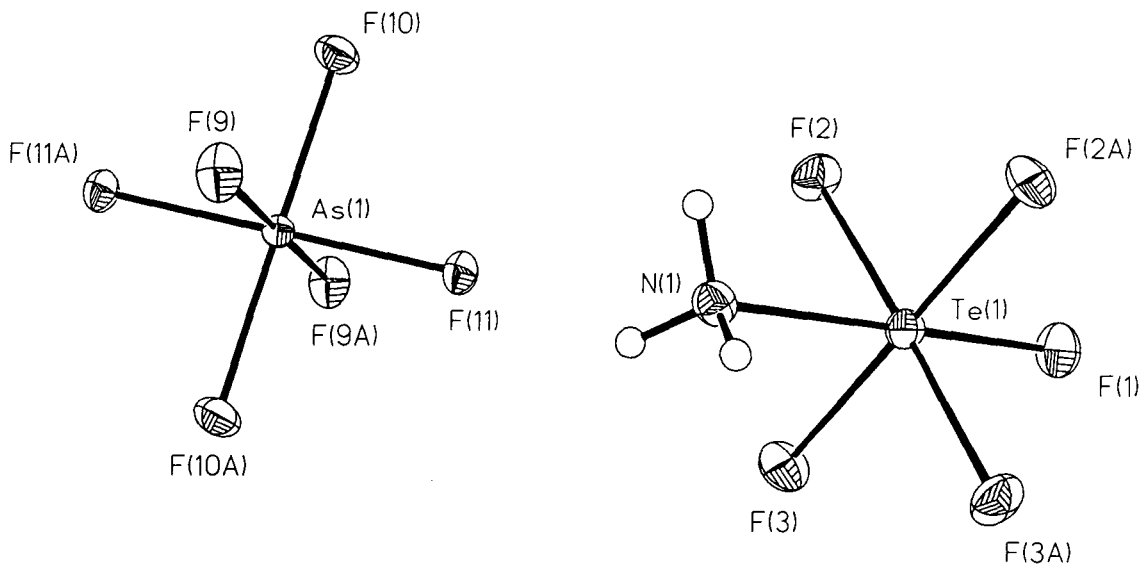

Figure 4.1 Structure of $F_5TeNH_3^+AsF_6^-$ showing thermal ellipsoids at the 50% probability level.

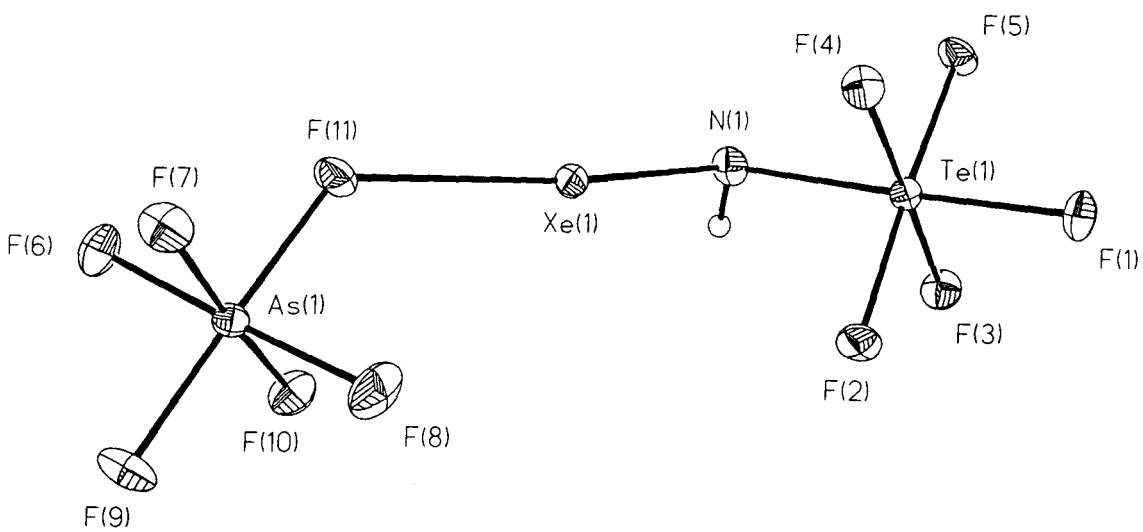

Figure 4.2 Structure of $F_5TeN(H)Xe^+AsF_6^-$ showing thermal ellipsoids at the 50% probability level.

bond lengths have been encountered in $HF{\cdot}HO{-}TeF_4{-}O{-}Xe^+AsF_6^-$ (1.771(1) Å),[166] $XeF_5^+AsF_6^-$ (1.74(2)-1.75(2) Å),[21] and $XeF^+AsF_6^-$ (1.813(6) Å),[19] where one or more fluorine atoms of the AsF_6^- anion are bridged to the xenon atom.

In all three structures, the environment around the tellurium atom is pseudo-octahedral, with Te–N (1.982(5) (2.043(3), 2.049(3)) [1.94(2)] Å) and Te–F (average, 1.807(6) (1.814(2)) [1.85(5)] Å) bond lengths comparable to those reported for other F_5TeN compounds.[123,167] The Te–F/N bond length of 1.82(2) Å in the disordered structure of F_5TeNH_2 at -5 °C (Figure 4.3b) is, within 3σ, an average value of the Te–F and Te–N bond lengths observed for F_5TeNH_2 at -113 °C (1.90(6) Å) (Figures 4.3a). The slightly longer Te–N bond lengths found in the $F_5TeNH_3^+$ cation, as compared to that found in $F_5TeN(H)Xe^+$, can be rationalized in terms of increased bond polarities anticipated upon substitution of the hydrogen atoms with the more electronegative xenon atom and is further discussed in a subsequent section (see **Correlations of the Structural Findings with Spectroscopic Results**). Protonation of F_5TeNH_2 to give $F_5TeNH_3^+$ leads to a shortening of the Te–F bonds and a lengthening of the Te–N bond (Table 4.2), as was previously predicted from the differences in the Raman and ^{19}F NMR spectral parameters of natural abundance and 99.5% ^{15}N-enriched F_5TeNH_2 and $F_5TeNH_3^+$ (see **Correlations of the Structural Findings with Spectroscopic Results**).[26]

Although there are several examples of Xe–N bonded compounds that have been characterized by X-ray crystallography, $F_5TeN(H)Xe^+AsF_6^-$ is the first structurally, well-characterized compound where xenon(II) is directly bonded to a formally sp^3-hybridized

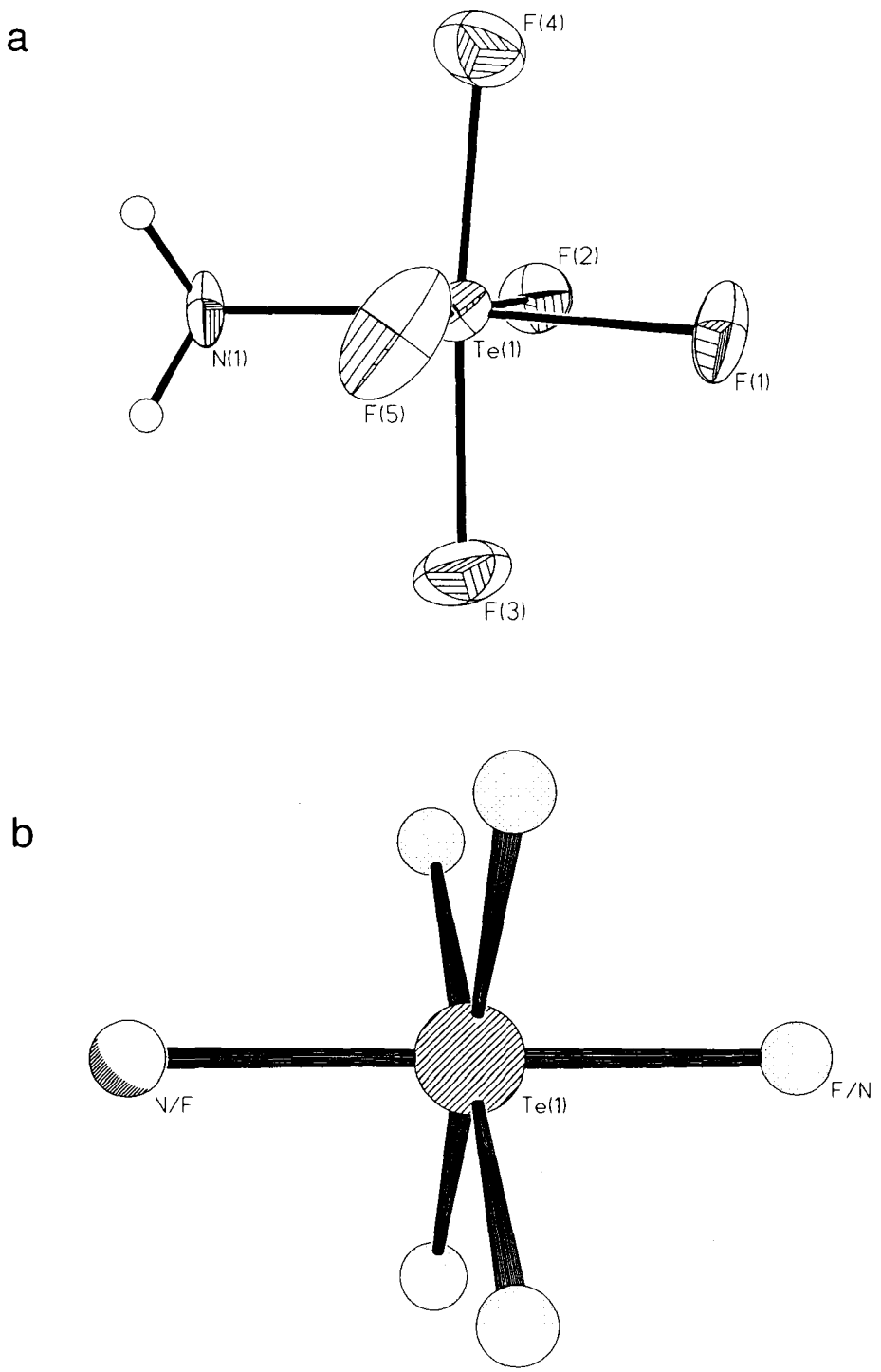

Figure 4.3 (a) Structure of F_5TeNH_2 at -113 °C showing thermal ellipsoids at the 50% probability level; (b) Disordered model of F_5TeNH_2 at -5 °C.

nitrogen atom. The only other example of xenon(II) bonded to an sp^3-hybridized nitrogen occurs in the $F_5SN(H)Xe^+AsF_6^-$ salt which has been identified exclusively by Raman and NMR spectroscopy.[26,34] The Xe–N bond length in $F_5TeN(H)Xe^+AsF_6^-$ (2.044(4) Å) is comparable to that observed in $XeN(SO_2F)_2^+Sb_3F_{16}^-$ (2.02(1) Å),[20] but is shorter than those in $FXeN(SO_2F)_2$ (2.200(3) Å),[62] $MeCN\cdots Xe–C_6F_5^+(C_6F_5)_2BF_2^-$ (2.681(8) Å),[66] $2,6\text{-}C_5H_3F_2N\cdots Xe–C_6F_5^+AsF_6^-$ (2.694(5) Å),[67] and also, $HC{\equiv}N–XeF^+AsF_6^-$ (2.235(3) Å), $CH_3C{\equiv}N–XeF^+AsF_6^-\cdot HF$ (2.179(7) Å), $(CH_3)_3CC{\equiv}N–XeF^+AsF_6^-$ (2.212(4) Å), $s\text{-}C_3F_3N_2N–XeF^+AsF_6^-\cdot 2.5BrF_5$ (2.316(6) Å), and $C_5F_5N–XeF^+AsF_6^-\cdot 2.5BrF_5$ (2.287(8) Å) (see Chapter 3). Consequently, the Xe–N bond length in $F_5TeN(H)Xe^+AsF_6^-$ is one of the most covalent observed thus far (r_{cov}: Xe, 1.30 Å; N, 0.75 Å; r_{vdW}: Xe, 2.20 Å; N, 1.50 – 1.60 Å).[36] The highly covalent nature of the Xe–N bond results from the low electronegativity, or low valence s-character (sp^3-hybridization), of the nitrogen atom in the parent base F_5TeN, and is consistent with the long bond length observed for Te–N. Partial π-bonding between nitrogen and xenon in the $F_5TeN(H)Xe^+$ cation is reasonable (see **Correlations of the Structural Findings with Spectroscopic Results**) by analogy with the $R–Xe^+$ (R = C_6F_5,[66,168,169] $2,6\text{-}F_2C_6H_3$,[162] $2\text{-}FC_6H_4$,[162] $4\text{-}FC_6H_4$,[162] $2,4,6\text{-}F_3C_6H_2$ [170]) cations, where the fluorine and carbon atoms closest to the xenon atom on the aryl ring are deshielded in the ^{19}F and ^{13}C NMR spectra, respectively, consistent with Xe–C π-bonding.[26]

The Xe···F bridge bond length (2.580(3) Å) in $F_5TeN(H)Xe^+AsF_6^-$ is much longer than the more covalent terminal Xe–F bond distances in $FXeN(SO_2F)_2$ (1.967(3) Å),[62]

$HC{\equiv}N{-}XeF^{+}AsF_6^{-}$ (1.936(2) Å), $CH_3C{\equiv}N{-}XeF^{+}AsF_6^{-}{\cdot}HF$ (1.947(5) Å), $(CH_3)_3CC{\equiv}N{-}XeF^{+}AsF_6^{-}$ (1.952(3) Å), *s*-$C_3F_3N_2N{-}XeF^{+}AsF_6^{-}{\cdot}2.5BrF_5$ (1.931(5) Å), and $C_5F_5N{-}XeF^{+}AsF_6^{-}{\cdot}2.5BrF_5$ (1.932(6) Å). However, it is comparable to the bridging Xe···F bond distances in the $XeN(SO_2F)_2{}^{+}Sb_3F_{16}^{-}$ (2.457(8) Å),[20] $XeF^{+}AsF_6^{-}$ (2.212(5) Å),[19] $XeF_5{}^{+}AsF_6^{-}$ (2.65(2)-2.83(2) Å),[21] $XeF_3{}^{+}SbF_6^{-}$ (2.49-2.71 Å),[9] and $XeOF_3{}^{+}SbF_6^{-}$ (2.449(10)-2.589(10) Å)[122] salts, and is considerably shorter than the sums of the Xe and F van der Waals radii (Xe, 2.20 Å; F, 1.35-1.50 Å).[36-38] The X-ray crystal structures of several Xe–N bonded compounds described in Chapter 3, as well as theoretical calculations of $HC{\equiv}NXeF^{+}$,[88-95] have shown that the covalent character of the Xe–N bond increases as the Xe–F bond becomes more ionic. This is evidenced in $F_5TeN(H)Xe^{+}AsF_6^{-}$ by the very short, covalent Xe–N bond length of 2.044(4) Å and long Xe···F bridge contact of 2.580(3) Å to the AsF_6^{-} anion.

The Xe, Te, and H atoms in $F_5TeN(H)Xe^{+}AsF_6^{-}$ form a near tetrahedral (sp^3) arrangement about nitrogen with a sum of bond angles of 331.1(3)° that is only slightly larger than the ideal sum of tetrahedral angles (3 × 109.5° = 328.5°), whereas the $XeNS_2$ moieties in $FXeN(SO_2F)_2$ [62] and $XeN(SO_2F)_2{}^{+}Sb_3F_{16}^{-}$ [20] are virtually planar (sp^2) having bond angle sums about nitrogen of 359.9(2)° and 359.6(6)°, respectively. The trigonal planar geometries at nitrogen observed in $FXeN(SO_2F)_2$ and $XeN(SO_2F)_2{}^{+}Sb_3F_{16}^{-}$ have been attributed to the involvement of the nitrogen lone pair in partial sulfur-nitrogen π-bonding and is evident from their short S–N bond lengths (1.68(1) – 1.70(1) Å)[62,63] compared to values found in the literature.[154-158]

The N–Xe···F angle (171.6(2)°) observed in $F_5TeN(H)Xe^+AsF_6^-$ is significantly smaller than that previously reported for $XeN(SO_2F)_2^+Sb_3F_{16}^-$ (178.3(3)°).[20] The distortion from the ideal linear arrangement of the atoms is uncommon in Xe(II) compounds and is inconsistent with the VSEPR rules for the AX_2E_3 formulation of the three lone pairs in equatorial positions with the bond pairs in axial positions about the central Xe(II) atom.[20,151] However, the N–Xe···F arrangement in $F_5TeN(H)Xe^+AsF_6^-$ appears to be bent so that significant intra- and intermolecular close contacts around the xenon atom in the crystal avoid the lone-pair electron density on xenon in the N–Xe···F system. This is well-illustrated along the *b*- and *c*-axes of the extended arrangement of $F_5TeN(H)Xe^+AsF_6^-$ molecules in the unit cell where there appears to be ample space surrounding the xenon atoms for the three equatorial lone electron pairs (Figure 4.4). The closest fluorine contacts to xenon (Xe···F(4) = 3.169 Å, Xe···F(11A) = 3.281 Å, Xe···F(8B) = 3.265 Å, and Xe···F(10E) = 3.260 Å), which are somewhat smaller than the sum of their van der Waals radii (Xe···F = 3.63 Å),[36-38] are greater than 30° from the hypothetical plane perpendicular to the N–Xe···F axis and containing the three valence electron lone pairs on xenon. The Xe···F–As bridge bond angle of 128.1(2)° is comparable to those in $XeF^+AsF_6^-$ (134.8(2)°),[19] $XeF_5^+AsF_6^-$ (127.3(2)°),[21] and $HF{\cdot}HO{-}TeF_4{-}OXe^+AsF_6^-$ (133.0(4)°).[166] This angle is expected to be easily distorted by crystal packing.

The arrangement of $F_5TeNH_3^+AsF_6^-$ molecules in the lattice is illustrated in Figure 4.5. The AsF_6^- anions occupy the corners of the unit cell along both the *a*- and *c*-

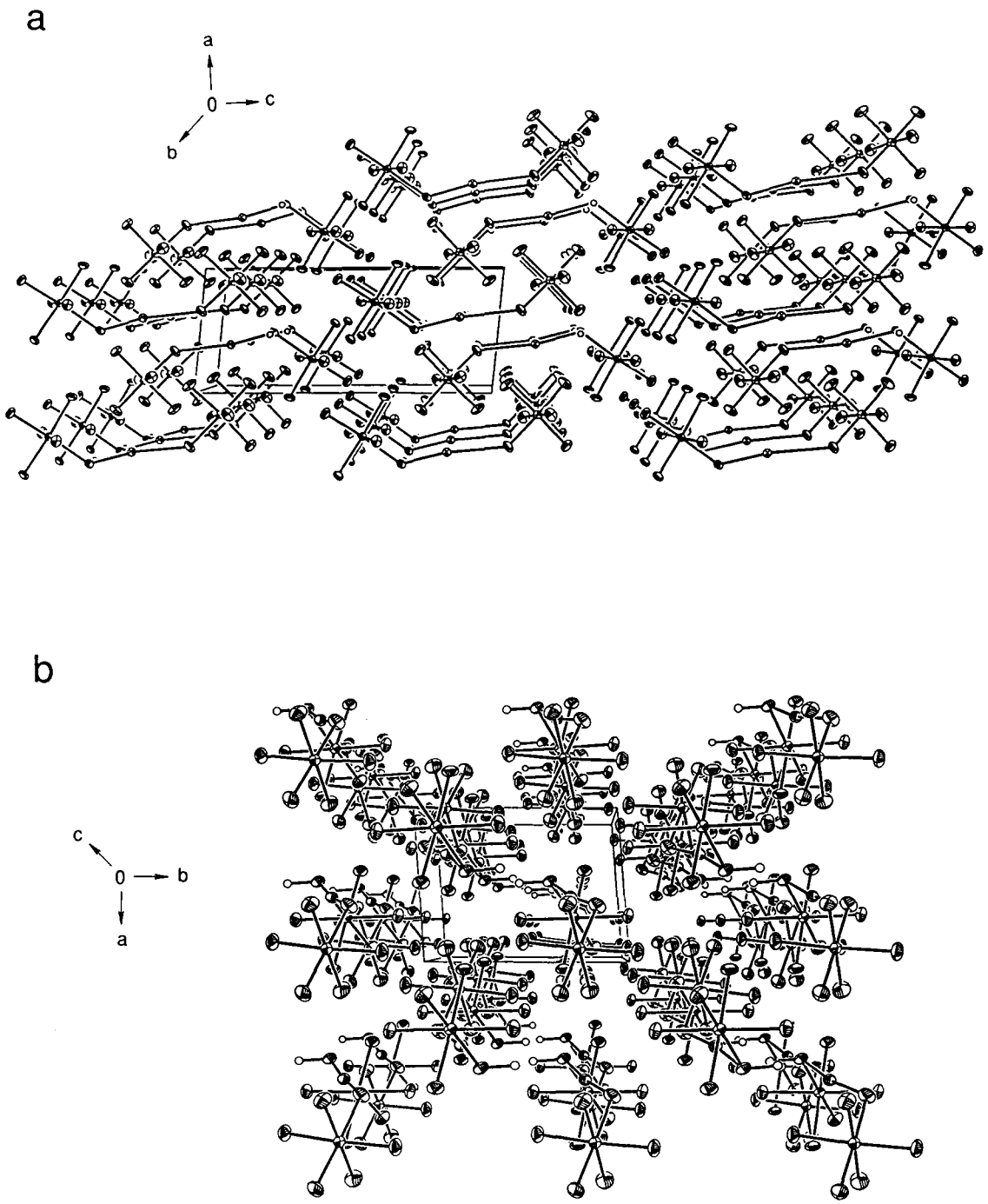

Figure 4.4 View of the $F_5TeN(H)Xe^+AsF_6^-$ unit cell: (a) along the b-axis; (b) along the c-axis.

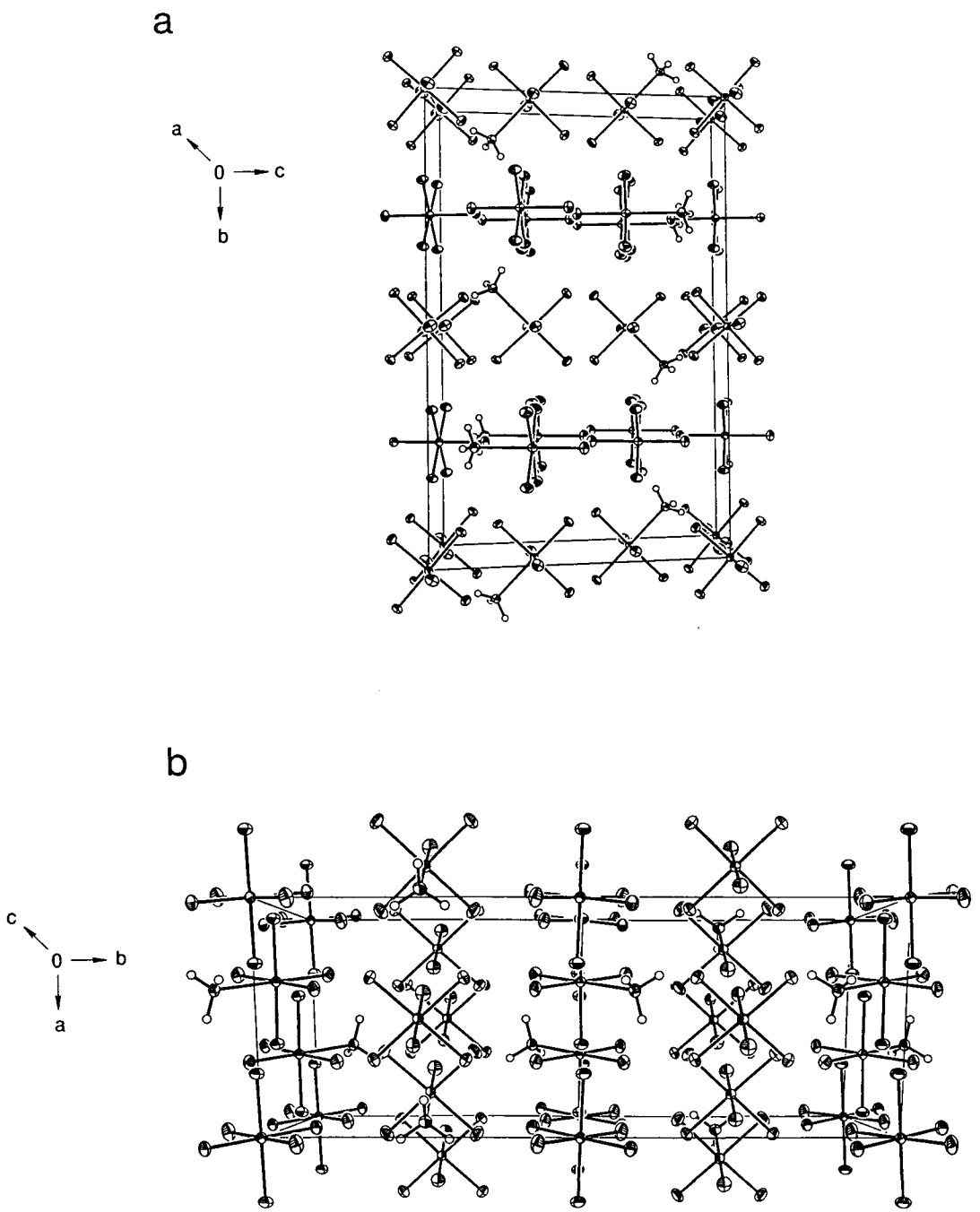

Figure 4.5 View of the $F_5TeNH_3^+AsF_6^-$ unit cell: (a) along the a-axis; (b) along the c-axis.

axes. The closest intra- and intermolecular contacts are N(1)···F(17) = 2.844 Å, N(1)···F(18) = 2.909 Å, N(2)···F(13) = 2.828 Å, N(2)···F(14) = 2.855 Å, N(2)···F(19) = 2.831 Å, N(1) ···F(2) = 2.709 Å, N(1)···F(3) = 2.703 Å, N(2)···F(4) = 2.713 Å, N(2)···F(5) = 2.698 Å, N(2)···F(6) = 2.730 Å, and N(2)···F(7) = 2.707 Å. All contacts are within the sum of their van der Waals radii (NH_4^+, 1.51 Å;[37] F, 1.50-1.60 Å).[36-38]

Arrangements of F_5TeNH_2 molecules in the lattices of the low- and high-temperature phases are illustrated in Figures 4.6a and 4.6b, respectively. The molecular units at low-temperature (-113 °C) pack in similar orientations along the *c*-axis and alternate orientations along the *b*-axis. The packing of the high-temperature (-5 °C) phase of F_5TeNH_2 is that of a simple body-centered cube having a coordination number of 8. The closest intra- and intermolecular contacts observed for F_5TeNH_2 at -113 °C are N(1)···F(3A) = 3.073 Å and N(1)···F(6A) = 3.020 Å. These contacts are at the limit of the sum of their van der Waals radii (NH_4^+, 1.51 Å;[37] F, 1.50-1.60 Å).[36-38]

Computational Results for F_5TeNH_2, $F_5TeNH_3^+AsF_6^-$, and $F_5TeN(H)Xe^+AsF_6^-$

Preliminary calculations at the local density functional theory (LDFT/DZVP) level were done for the title compounds. The $F_5TeNH_3^+$ cation of $F_5TeNH_3^+AsF_6^-$ was treated as a free ion, and the $F_5TeN(H)Xe^+AsF_6^-$ salt was treated as an ion-pair and as separate anion and cation entities. Although the global geometries are in reasonable agreement, the calculated bond lengths are all significantly longer than those observed (see Table 4.2). In $F_5TeNH_3^+$ and F_5TeNH_2 the calculated Te–N bond lengths were too

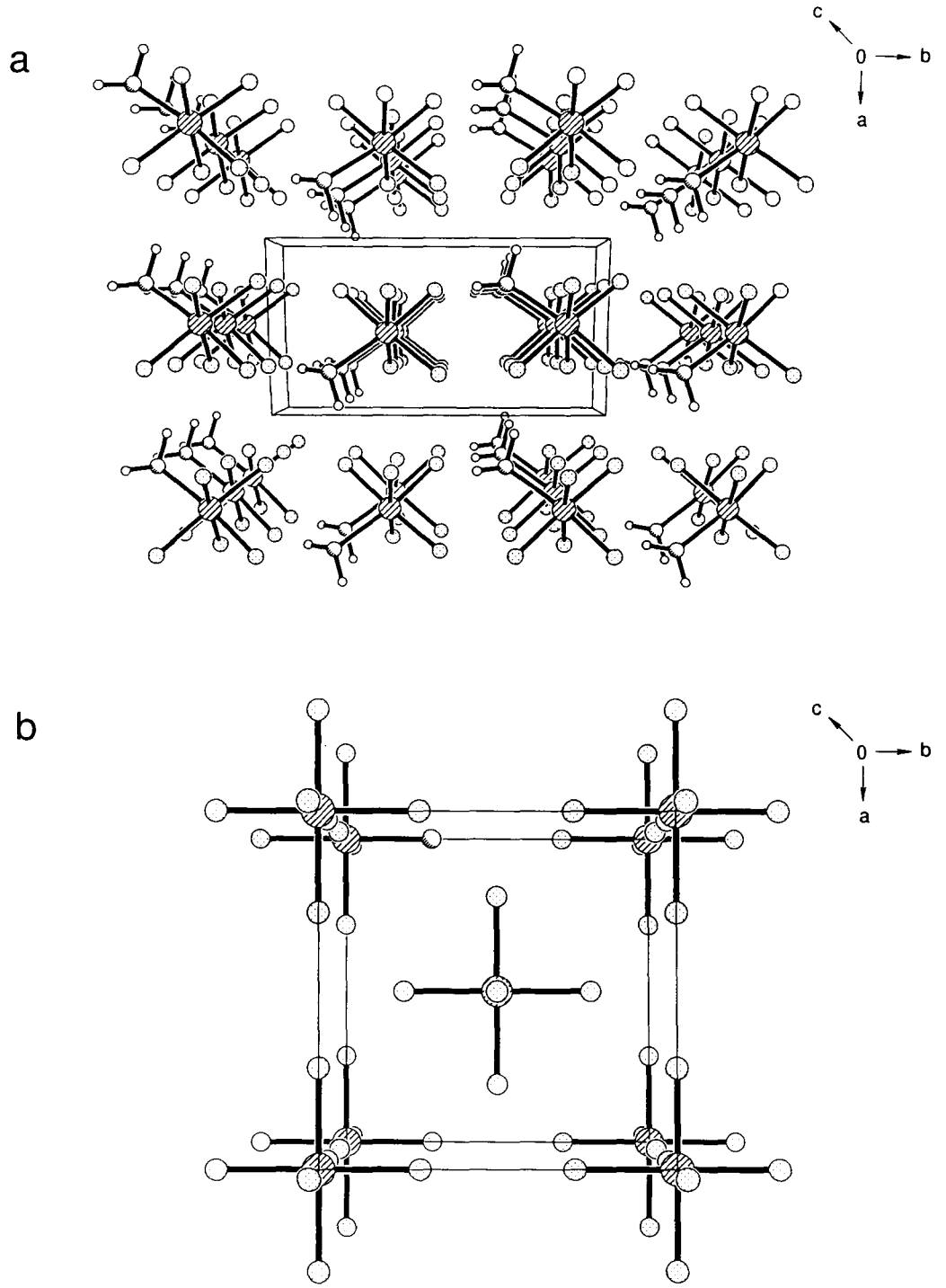

Figure 4.6 View of the F_5TeNH_2 unit cell along the c-axis: (a) at -113 °C (b) at -5 °C.

long by 0.105 – 0.111 Å and 0.035 Å, respectively, and the Te–F bond lengths were too long by 0.057 – 0.074 Å and 0.047 – 0.070 Å, respectively. The calculated Te–N, Te–F, Xe–N, and As–F bond lengths in $F_5TeN(H)Xe^+AsF_6^-$ when treated as an ion-pair are too long by 0.043 Å, 0.087 – 0.114 Å, 0.105 Å, and 0.030 – 0.238 Å, respectively. With the exception of the Te–N bond, the bond lengths calculated for the free ions of $F_5TeN(H)Xe^+AsF_6^-$ are slightly smaller than those determined for the ion-pair model. Due to the discrepancies between observed and calculated geometries, the calculations are now being redone at the Hartree-Fock level which was previously used successfully to calculate the geometries and vibrational frequencies of the F_5TeO^- anion.[171]

Correlations of the Structural Findings with Spectroscopic Results

The $F_5TeN(H)Xe^+AsF_6^-$, $F_5TeNH_3^+AsF_6^-$, and F_5TeNH_2 compounds, whose X-ray crystal structures have been determined in this work, had previously been characterized by Raman and multi-NMR spectroscopy. Prior to the X-ray crystal structures, these techniques served as the only probes for evaluating the bonding in these species. The Raman and ^{19}F NMR spectral parameters of natural abundance and 99.5% ^{15}N-enriched F_5TeNH_2 and $F_5TeNH_3^+$ are consistent with the observed shortening of the Te–F bonds and the lengthening of the Te–N bond when F_5TeNH_2 (Te–F_{av}, 1.85(4) Å; Te–N, 1.94(2) Å) is protonated to give $F_5TeNH_3^+$ (Te–F_{av}, 1.814(2) Å; Te–N, 2.043(3) and 2.049(3) Å). Table 4.3 lists some available X-ray crystallographic, Raman, and NMR data for the title compounds, as well as for FO_2SNH_2,[172] $FO_2SNH_3^+$,[26] $HOChF_5$ (Ch

Table 4.3 Comparison of Some X-Ray Crystallographic, Raman, and NMR Parameters for F_5TeNH_2, $F_5TeNH_3^+$, F_5ChOH, F_5ChO^-, FO_2SNH_2, and $FO_2SNH_3^+$ (Ch = Se, Te).

	X-ray Crystallography (Å)		Raman (cm^{-1})[a]			NMR		
Cation	$(Te–F)_{av}$	Te–N	$\nu(Ch\text{-}F_{ax})$	$\nu_{sym}(Ch\text{-}F_{eq})$	$\nu(Ch\text{-}L)$	$\delta(^{19}F_A)$, ppm[b]	$\delta(^{19}F_B)$, ppm[b]	$^1J(^{125}Te\text{-}^{15}N)$, Hz
$F_5TeN(H)Xe^+AsF_6^-$[c]	1.807(6)	1.982(5)	719.6 [719.3]	672.3 [666.1]		-51.9	-43.2	333
F_5TeNH_2[40, d]	1.85(4)	1.94(2)	582.7 [572.9]	619.6 [619.4]	761.0 [752.9]	-37.8	-42.8	231
$F_5TeNH_3^+AsF_6^-$[26, e]	1.814(2)	2.043(3), 2.049(3)	730.2 [729.3]	682.9 [682.2]	566.5 [550.8]	-55.6	-30.2	48
$[N(n\text{-}Bu)_4]^+F_5TeO^-$[97,176, f]			576	645	867	-19.0	-36.8	
$N(CH_3)_4^+F_5TeO^-$[175, g]			583, 650	583, 650	868	-19.1	-36.9	
F_5TeOH[109,173]			735	685	735	-44.3	-46.6	
$K^+F_5SeO^-$[96,109,177, h]			559	649	919	121.1	78.4	
F_5SeOH[96,109, i]			625	685	753	82.7	64.8	
FO_2SNH_2[172, j]		1.60(1)				964.5		
$FO_2SNH_3^+$[26]						709.9		

Table 4.3 (continued)

[a] Raman spectra were performed on the neat compounds using 514.5-nm excitation at ambient temperatures unless otherwise specified. Values in square brackets are for 99.5% ^{15}N-enriched samples. L denotes the oxygen or nitrogen ligand atom.

[b] Chemical shifts are referenced with respect to the neat liquid $CFCl_3$ (^{19}F) at ambient temperatures unless otherwise specified: a positive sign denotes the chemical shift of the resonance in question occurs to higher frequency of (is more shielded than) the resonance of the reference substance; A and B denote the axial and equatorial environments of the ChF_5 group, respectively.

[c] Raman spectra recorded at -165 °C. ^{19}F NMR spectra recorded at -44 °C in BrF_5 solvent.

[d] Raman spectra recorded at -150 °C. ^{19}F NMR spectra recorded at -44 °C in BrF_5 solvent.

[e] ^{19}F NMR spectra recorded at -50 °C in BrF_5 solvent.

[f] ^{19}F NMR spectra recorded in CH_2Cl_2 solvent.

[g] ^{19}F NMR spectra recorded in CH_3CN solvent at -10 °C.

[h] Raman spectra recorded in CH_3CN solvent.

[i] ^{19}F NMR spectra recorded in CH_3CN solvent.

[j] Bond lengths obtained from electron diffraction.

= Se, Te),[96,109,173] and salts of the form $M^+OChF_5^-$,[96,97,109,175,176,177] where the Ch–O bonds in the salts are significantly more ionic than the O–H bond in $HOChF_5$. The increase in the Te–N bond length on protonation of F_5TeNH_2 is analogous to the Ch–O (Ch = Se, Te) and S–N bond length changes reflected by Raman and ^{19}F NMR spectroscopy which occur in the $M^+OChF_5^-$ anions and in FO_2SNH_2 upon protonation to give the F_5ChOH acids and $FO_2SNH_3^+$, respectively. Protonation of F_5TeNH_2, $OChF_5^-$ (Ch = Se, Te), and FO_2SNH_2 generally results in greater shielding of the ^{19}F NMR resonances, smaller ^{125}Te-^{15}N coupling constant, a decrease in the ν(Ch-L) (L = N, O ligand atom) stretching frequencies, and an increase in the $\nu_{sym}(Ch\text{-}F_{eq})$ and $\nu_{sym}(Ch\text{-}F_{ax})$ stretching frequencies. By analogy with bonding predictions previously made for the acid/base pairs, namely F_5ChOH/F_5ChO^- and $FO_2SNH_3^+/FO_2SNH_2$,[26] the trends observed in the experimental data on comparison of $F_5TeNH_3^+$ and F_5TeNH_2 imply some degree of Te–N π-bonding in F_5TeNH_2 that decreases upon protonation of the nitrogen lone pair.

Schleyer and Reed[178] have recently examined hypervalent bonding in a series of 32-valence-electron X_3AY species (CF_4, F_3NO, F_3SN, etc.) and generalized their findings to *n*-coordinate 8*n*-valence electron species (HF_2^-, F_4SO, F_5TeO^-, etc.) as well as their reduced analogues (SF_4, IF_6^-, ClF_3, etc.). Based on their studies, it was concluded that the bonding description for F_5TeO^- was also applicable to the isoelectronic, but hypothetical, F_5TeN^{2-} anion. The latter anion is isoelectronic with its protonated forms, F_5TeNH_2 and $F_5TeNH_3^+$, and the $F_5TeN(H)Xe^+$ cation is isoelectronic with respect to the F_5TeN–moiety. Based on Schleyer and Reed's bonding analyses, the three center 4-

electron σ_{TeF}-bonding in these F_5TeN systems (see Scheme I) are expected to be significantly ionic, and the strongly polar σ^*_{TeF} orbitals are more effective electron acceptors than the valence d-orbitals on Te. Negative $\pi_N \rightarrow \sigma^*_{TeF}$ type hyperconjugation, which results in π_{TeN} bonding, may be an important contributor to multiple bonding between Te and N. This is illustrated by Structure I for $F_5TeN(H)Xe^+AsF_6^-$, which is

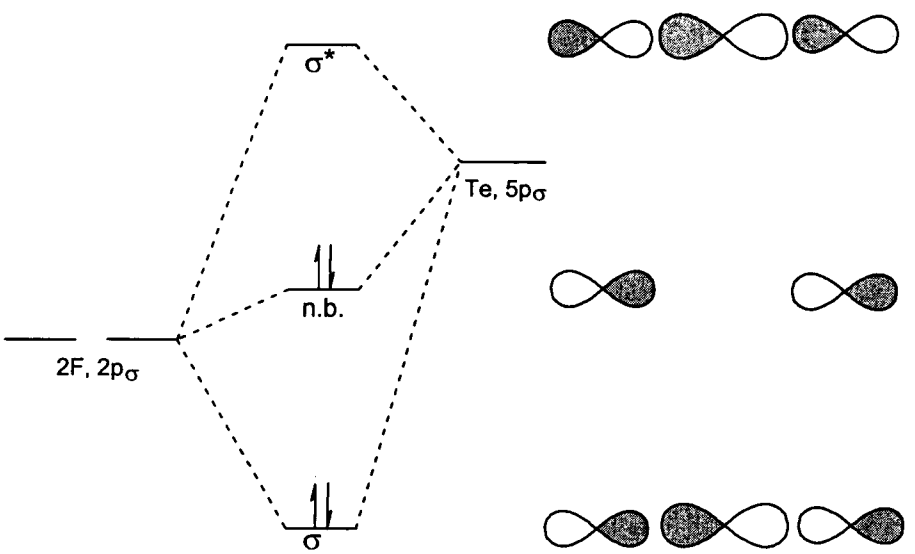

Scheme I

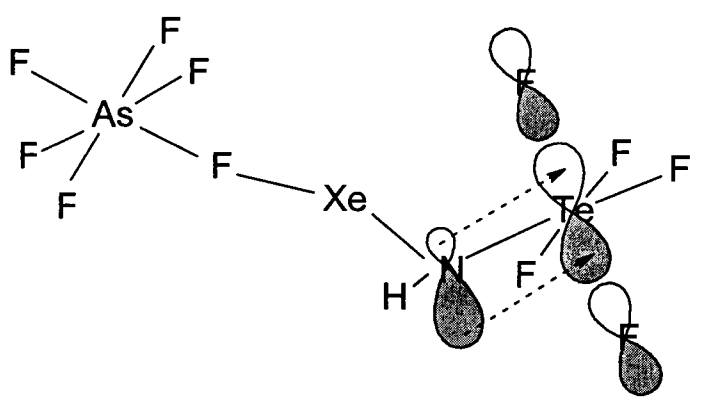

Structure I

similar for F_5TeNH_2. The d-orbitals play only a secondary role in the π-bonding and serve to polarize the σ^*_{TeF} orbitals, which enhances π_{TeN} bonding and diminishes σ^*_{TeF} antibonding interactions. Consequently, protonation of the lone pair in F_5TeNH_2 turns off the π_{TeN}-bonding interaction of the lone pair resulting in a longer Te–N bond and shorter Te–F bonds. Similar effects on the Te–N bond length are observed for $F_5TeN(H)Xe^+$ when compared to $F_5TeNH_3^+$. As observed in the crystal structures of these compounds, the effect of negative hyperconjugation in $F_5TeN(H)Xe^+$ and F_5TeNH_2 when compared to $F_5TeNH_3^+$ is also reflected in the $^1J(^{125}Te\text{-}^{15}N)$ coupling constants which decrease from 333 Hz ($F_5TeN(H)Xe^+$) and 231 Hz (F_5TeNH_2) to 48 Hz upon protonation of the nitrogen lone electron pair to give $F_5TeNH_3^+$ (see Table 4.3).

The hybridization at nitrogen (*i.e.*, %s character, where 50.0, 33.3, and 25.0 represent sp, sp^2, and sp^3 valence orbital hybridizations, respectively) may be evaluated by an empirical equation (4.7) derived by Binsch *et al.*[179] based on the proportionality of

$$\% s = 0.43\,[^1J(^{15}N\text{-}^1H)] - 6 \qquad (4.7)$$

$^1J(^{15}N\text{-}^1H)$ and the s characters of the hybrid orbitals which make up the N–H bond as shown in equation (4.8). Equation (4.8) is a more complex expression for the Fermi

$$^1J(^{15}N\text{-}^1H) \propto \gamma(^{15}N)\gamma(^1H)(\Delta E)^{-1}(\alpha_N)^2(\alpha_H)^2\,|\psi_{N(2s)}(0)|^2\,|\psi_{H(1s)}(0)|^2 \qquad (4.8)$$

contact contribution to the one bond $^{15}N\text{-}^1H$ coupling constant, where $\gamma(^{15}N)$ and $\gamma(^1H)$ are the gyromagnetic ratios of the coupled nuclei, ΔE is the average excitation energy, $(\alpha_N)^2$ and $(\alpha_H)^2$ are the s characters of the hybrid orbitals which make up the N–H bond, and the $|\psi(0)|$ terms represent the magnitudes of the valence s orbitals at the appropriate nuclei. Using equation (4.7) and the $^1J(^{15}N\text{-}^1H)$ values for $F_5TeNH_3^+$ (76 Hz), F_5TeNH_2

(71 Hz), and $F_5TeN(H)Xe^+$ (62 Hz), the %s hybridizations at the nitrogen atoms were determined to be 26.7, 24.5, and 20.7, respectively. The smaller %s character observed for the nitrogen valence hybrid orbitals in F_5TeNH_2 and $F_5TeN(H)Xe^+$ when compared to $F_5TeNH_3^+$ is due to the involvement of the nitrogen electron lone pair in π_{TeN} bonding. In turn, the smaller %s character for $F_5TeN(H)Xe^+$ relative to F_5TeNH_2 implies a higher degree of π_{TeN} interaction in $F_5TeN(H)Xe^+$.

The combined Raman and ^{19}F, ^{1}H, ^{129}Xe, and ^{125}Te NMR spectroscopic data successfully predict the highly covalent nature of the Xe–N bond (2.044(4) Å) together with the ionic Xe···F bridging bond (2.580(3) Å) in $F_5TeN(H)Xe^+AsF_6^-$.[26] Table 4.4 lists some available X-ray crystallographic and NMR parameters for $F_5TeN(H)Xe^+AsF_6^-$, as well as for $XeOTeF_5^+AsF_6^-$, $XeF^+AsF_6^-$, and several other Xe–N bonded compounds. The compounds are listed in order of decreasing Xe–N covalent bond and Xe–F ionic bond characters. Although the ^{129}Xe NMR chemical shifts of xenon(II) compounds are highly solvent and temperature dependent leading to some obvious discrepancies, generally, these bond length trends are paralleled by decreased shielding of the ^{129}Xe resonances, a decrease in the magnitude of $^{1}J(^{129}Xe\text{-}^{19}F)$, and increased ^{19}F chemical shifts for the terminal Xe–F group. The highly shielded ^{129}Xe NMR resonances for the $F_5TeN(H)Xe^+$ and $F_5SN(H)Xe^+$ cations relative to the other compounds are consistent with their having the most covalent Xe–N bonds and highest degree of Xe···F ionic bond character, *i.e.*, no formal Xe–F bond exists in solutions. The ^{129}Xe NMR resonances and X-ray data for the isoelectronic $F_5TeN(H)Xe^+$ and F_5TeOXe^+ cations, as well as for XeF^+, also reflect the higher electronegativity of the $OTeF_5$ and F ligands compared to the

Table 4.4 Comparison of Some X-Ray Crystallographic, Raman, and NMR Parameters for $F_5TeN(H)Xe^+$, XeF^+, $XeOTeF_5^+$, and Several Xe–N Bonded Cations.

	X-ray Crystallography (Å)		NMR[b]			
Cation[a]	Xe–F	Xe–N	$\delta(^{129}Xe)$, ppm	$\delta(^{19}F)$, ppm[c]	$^1J(^{129}Xe\text{-}^{19}F)$, Hz[c]	$^1J(^{129}Xe\text{-}^{15}N)$, Hz
$F_5SN(H)XeF^+$ [34,26]			-2886			
$F_5TeN(H)Xe^+$	2.580(3)[d]	2.044(4)	-2841 (-2902)			138 (142)
$XeOTeF_5^+$ [53,55,56]	2.24(3)[d]		[-1521] {-1472}			
XeF^+ [19]	2.212(5)[d]		[-991]	[-243.5]	[6350]	
$(CH_3)_3CC{\equiv}N\text{–}XeF^+$ [68,69,72]	1.952(3)	2.212(4)	-1721	-184.3	6024	309
$HC{\equiv}N\text{–}XeF^+$ [68,69,72]	1.936(2)	2.235(3)	-1555 (-1570)	-198.4 (-193.1)	6150 (6181)	336 (334)
$C_5F_5N\text{–}XeF^+$ [70]	1.932(6)	2.287(8)	-1871.9 (-1922.5)	-148.3 (-139.6)	5936 (5926)	236
$s\text{-}C_3F_3N_2N\text{–}XeF^+$ [72]	1.931(5)	2.316(6)	-1807.9 (-1862.4)	-154.9 (-145.6)	5909 (5932)	245

[a] All cations have AsF_6^- as the counterion.

[b] Chemical shifts are referenced with respect to the neat liquids $XeOF_4$ (^{129}Xe) and $CFCl_3$ (^{19}F) at 24 °C; a positive sign denotes the chemical shift of the resonance in question occurs to higher frequency of (is more shielded than) the resonance of the reference substance. The NMR spectra were recorded in HF (BrF_5) [HSO_3F] {SbF_5}. The NMR spectra for the $F_5TeN(H)Xe^+$, XeF^+, $XeOTeF_5^+$, $HC{\equiv}N\text{–}XeF^+$,[68,69] $(CH_3)_3CC{\equiv}N\text{–}XeF^+$,[44] $s\text{-}C_3F_3N_2N\text{–}XeF^+$,[72] $C_5F_5N\text{–}XeF^+$,[70] and $F_5SN(H)XeF^+$ [34] cations were recorded at -45 (-45), [-96], [-94.6]{30}, -10 (-58), -30, -5 (-50), -30 (-30), and (-20) °C, respectively.

[c] Refers to the terminal fluorine on the xenon atom, except in the $F_5TeN(H)Xe^+$, $XeOTeF_5^+$, and XeF^+ cations where it refers to the bridging fluorine on arsenic.

[d] Refers to the bridging fluorine on arsenic.

$F_5TeN(H)$ group, and subsequent higher Lewis acidities for $XeOTeF_5^+$ and XeF^+ (see Chapter 5). Evidence for the low Lewis acid strength of $F_5TeN(H)Xe^+$, as compared to $XeOTeF_5^+$, is indicated by its inability to form Lewis acid-base adducts $B–XeN(H)TeF_5^+$ (B = C_5F_5N, *s*-$C_3F_3N_2N$, CH_3CN), by the strongly basic behavior of the parent compound, F_5TeNH_2, which could be quantitatively protonated in HF,[26] and by the shorter Xe···F bridge bond length in $XeOTeF_5^+$ (see Table 4.4 and Chapter 5).

CHAPTER 5

STRUCTURAL STUDIES OF SOME XENON(II) DERIVATIVES OF THE $OChF_5$ (Ch = Te, Se) GROUPS

INTRODUCTION

Xenon(II) derivatives of the bulky and highly electronegative $OTeF_5$ and $OSeF_5$ ligands have been studied extensively. The $OTeF_5$ group has an effective group electronegativity (3.88 on the Pauling scale)[45,47] approaching that of F (4.00)[48] and is capable of stabilizing nearly all of the same oxidation states as F. Likewise, the effective electronegativity of the $OSeF_5$ group approaches that of F, however, it is expected to be somewhat less than that for $OTeF_5$ based on Mössbauer data and ^{125}Te and ^{129}Xe NMR spectroscopic measurements.[41] Consequently, nearly all of the chemistry of $OTeF_5$ and $OSeF_5$ compounds has been developed by analogy with the existing fluorides.[181]

The synthetic potentials of the $OTeF_5$ and $OSeF_5$ group were made possible with the discovery of the strong $HOTeF_5$ [182] and $HOSeF_5$ [183] acids in 1964 and 1972, respectively [eqs (5.1) and (5.2)]. The chemistry of the $OSeF_5$ ligand is less extensive

$$Te(OH)_6 + 5HSO_3F \longrightarrow 5H_2SO_4 + HOTeF_5 \quad (5.1)$$

$$3SeO_2F_2 + 4HF \longrightarrow 2HOSeF_5 + H_2SeO_4 \quad (5.2)$$

because $HOSeF_5$ [41] is a stronger oxidizer and is considerably more toxic and difficult to prepare and purify than $HOTeF_5$.

Typically, $OChF_5$ compounds of Xe(II) have been structurally characterized by ^{19}F NMR, infrared, and Raman spectroscopy. While there are several X-ray crystal structures of $OTeF_5$ compounds, a number are complicated by orientational disorders resulting from the nearly spherical shape of the $OTeF_5$ group. In such cases, the disordered atoms appear with very large librational parameters, resulting in inaccurate geometrical parameters.

In the present work, the structural characterizations by single crystal X-ray diffraction of the $F_5ChOXe^+AsF_6^-$ salts and of the neutral $Xe(OChF_5)_2$ compounds were undertaken and described. The Lewis acidities of the F_5ChOXe^+ cations approach that of XeF^+ and are isolobal with the $F_5TeN(H)Xe^+$ cation described in Chapter 4. Although the F_5TeOXe^+ cation has been previously characterized by Raman and NMR spectroscopy,[53,55,56] the crystal structures of both $F_5ChOXe^+AsF_6^-$ salts were unknown. Detailed characterizations of these salts were also carried out in this work by Raman spectroscopy and by local density functional theory (LDFT/DZVP) calculations.

The $Xe(OChF_5)_2$ derivatives, on the other hand, have been previously examined by X-ray crystallography. However, no structural details for $Xe(OTeF_5)_2$ [50] have been reported and those reported for $Xe(OSeF_5)_2$ [51] are clearly affected by a three-fold orientational disorder of O and F atoms. Structural characterizations have been carried

out in order to obtain complete and precise data for comparison with the structures of the $F_5ChOXe^+AsF_6^-$ salts.

RESULTS AND DISCUSSION

Preparation of $XeOChF_5^+AsF_6^-$ and $Xe(OChF_5)_2$ (Ch = Te, Se)

In the present work, Sladky's synthesis of $XeOTeF_5^+AsF_6^-$ [53,55] had been repeated according to equation (5.5). The precursor, $Xe(OTeF_5)_2$, was also prepared, however, the synthetic approach used [eqs (5.3) – (5.4)][41] differs from Sladky's[107] original synthesis

$$3XeF_2 + 2B(OTeF_5)_3 \longrightarrow 3Xe(OTeF_5)_2 + 2BF_3 \quad (5.3)$$

$$Xe(OTeF_5)_2 + XeF_2 \longrightarrow 2FXeOTeF_5 \quad (5.4)$$

$$FXeOTeF_5 + AsF_5 \longrightarrow XeOTeF_5^+AsF_6^- \quad (5.5)$$

[eqs (5.6) – (5.7)] and has the advantage of avoiding equilibrium mixtures. The original

$$XeF_2 + HOTeF_5 \rightleftharpoons FXeOTeF_5 + HF \quad (5.6)$$

$$FXeOTeF_5 + HOTeF_5 \rightleftharpoons Xe(OTeF_5)_2 + HF \quad (5.7)$$

preparation requires that a large excess of $HOTeF_5$ be used to completely displace HF and give $Xe(OTeF_5)_2$ that is free of $FXeOTeF_5$.

The corresponding $Xe(OSeF_5)_2$ and $XeOSeF_5^+AsF_6^-$ compounds were prepared in quantitative yield according to the methods of Seppelt[50] and Schrobilgen,[128] respectively [eqs (5.8), (5.9), and (5.10)].[50] Both $OSeF_5$ derivatives are readily sublimable yellow

$$2SeO_2F_2 + 3XeF_2 \longrightarrow Xe(OSeF_5)_2 + 2Xe + O_2 \quad (5.8)$$

$$Xe(OSeF_5)_2 + XeF_2 \longrightarrow 2FXeOSeF_5 \quad (5.9)$$

$$FXeOSeF_5 + AsF_5 \longrightarrow XeOSeF_5^+AsF_6^- \quad (5.10)$$

solids at room temperature. The volatilities of the $XeOChF_5^+AsF_6^-$ and $Xe(OChF_5)_2$ compounds lead to crystal growth by sublimation under static vacuum.

X-ray Crystal Structures of $XeOChF_5^+AsF_6^-$ and $Xe(OChF_5)_2$ (Ch = Te, Se)

A summary of the refinement results and other crystallographic information are given in Table 5.1. The final atomic coordinates and equivalent isotropic thermal parameters are summarized in Appendix B. Important bond lengths and angles are listed in Table 5.2 along with the calculated values (see **Computational Results**).

The crystal structures of $XeOTeF_5^+AsF_6^-$ and $XeOSeF_5^+AsF_6^-$ are reported in this work for the first time. Both compounds are found to be isostructural and present the same four-fold orientational disorder of the fluorine and oxygen atoms (Figures 5.1 and 5.2). On the contrary, $Xe(OTeF_5)_2$[50] and $Xe(OSeF_5)_2$[51] had been previously studied by X-ray crystallography. Although no geometrical parameters had been reported for $Xe(OTeF_5)_2$, a geometry was deduced from a single crystal study using precession camera data; the study was also corroborated by powder data.[51] Even though the gross geometry reported was analogous to the one described in this paper (*vide infra*, Figure 5.3), the crystallographic parameters differ markedly (space group *Cmca*, a = 9.83(5) Å, b = 8.73(5) Å, c = 12.97(5) Å, Z = 4, V = 1114 Å^3) and suggest that the crystalline material

Table 5.1 Summary of Crystal Data and Refinement Results for $XeOTeF_5^+AsF_6^-$, $XeOSeF_5^+AsF_6^-$, $Xe(OTeF_5)_2$, and $Xe(OSeF_5)_2$.

	$XeOTeF_5^+AsF_6^-$	$XeOSeF_5^+AsF_6^-$	$Xe(OTeF_5)_2$	$Xe(OSeF_5)_2$
empirical formula	$AsF_{11}OTeXe$	$AsF_{11}OSeXe$	$F_{10}O_2Te_2Xe$	$F_{10}O_2Se_2Xe$
space group (No.)	*P4/n* (85)	*P4/n* (85)	$P2_1/c$ (14)	$R\bar{3}$ (148)
a (Å)	6.13560(10)	6.1195(7)	10.289(2)	8.3859(6)
b (Å)	6.13560(10)	6.1195(7)	9.605(2)	8.3859(6)
c (Å)	13.8232(2)	13.0315(2)	10.478(2)	12.0355(13)
α (deg.)	90	90	90	90
β (deg.)	90	90	106.599(4)	90
γ (deg.)	90	90	90	120
V ($Å^3$)	520.383(14)	488.01(8)	992.3(3)	732.98(11)
molecules/unit cell	2	2	4	3
mol. wt. (g mol^{-1})	558.82	510.18	608.50	511.22
calcd. density (g cm^{-3})	3.566	3.472	4.073	3.474
T (°C)	-60	-113	-127	-45
μ (mm^{-1})	9.347	10.766	9.368	11.108
λ (Å) used for data coll.	0.71073	0.71073	0.71073	0.71073
final agreement factors[a]	$R_1 = 0.0453$	$R_1 = 0.0730$	$R_1 = 0.0680$	$R_1 = 0.0534$
	$wR_2 = 0.1345$	$wR_2 = 0.1664$	$wR_2 = 0.1589$	$wR_2 = 0.1676$

[a] R_1 is defined as $\Sigma||F_o| - |F_c||/\Sigma|F_o|$ for $I > 2\sigma(I)$. wR_2 is defined as $[\Sigma[w(F_o^2 - F_c^2)^2]/\Sigma w(F_o^2)^2]^{1/2}$ for $I > 2\sigma(I)$.

Table 5.2 Experimental and Calculated Geometries for $XeOTeF_5^+AsF_6^-$ and $XeOSeF_5^+AsF_6^-$, and Experimental Geometries for $Xe(OTeF_5)_2$ and $Xe(OSeF_5)_2$.

$XeOTeF_5^+AsF_6^-$

		Bond Lengths (Å)			
	expt	LDFT/DZVP		expt	LDFT/DZVP
As(1)-F(6)	1.72(2)	1.709	Te(1)-F(1)	1.80(2)	1.892
As(1)-F(7)	1.69(2)	1.745	Te(1)-F(2)	1.81(2)	1.912
As(1)-F(8)	1.74(2)	1.751	Te(1)-F(3)	1.82(2)	1.896
As(1)-F(9)	1.72(2)	1.731	Te(1)-F(4)	1.84(2)	1.897
As(1)-F(10)	1.72(2)	1.729	Te(1)-F(5)	1.79(3)	1.910
As(1)-F(11)	1.81(2)	2.074	Te(1)-O(1)	1.85(3)	1.947
Xe(1)-O(1)	1.96(4)	2.107			
Xe(1)-F(11)	2.24(3)	2.142			
		Bond Angles (deg.)			
	expt	LDFT/DZVP		expt	LDFT/DZVP
As(1)-F(11)-Xe(1)	135(1)	123.5	F(6)-As(1)-F(7)	89(4)	97.5
Te(1)-O(1)-Xe(1)	128(2)	116.8	F(6)-As(1)-F(8)	101(2)	97.7

Table 5.2 (continued)

O(1)-Te(1)-F(1)	175(1)	179.0	F(6)-As(1)-F(9)	91(5)	97.8
O(1)-Te(1)-F(2)	93(2)	91.9	F(6)-As(1)-F(10)	86(3)	98.3
O(1)-Te(1)-F(3)	89(2)	89.1	F(6)-As(1)-F(11)	175(3)	179.8
O(1)-Te(1)-F(4)	93(2)	90.6	F(7)-As(1)-F(8)	85(1)	87.3
O(1)-Te(1)-F(5)	99(2)	91.3	F(7)-As(1)-F(9)	176(2)	164.7
O(1)-Xe(1)-F(11)	174(1)	178.8	F(7)-As(1)-F(10)	96(3)	89.5
F(1)-Te(1)-F(2)	92(2)	89.1	F(7)-As(1)-F(11)	96(2)	82.5
F(1)-Te(1)-F(3)	87(3)	89.8	F(8)-As(1)-F(9)	99(2)	89.0
F(1)-Te(1)-F(4)	85(4)	89.3	F(8)-As(1)-F(10)	172(2)	164.0
F(1)-Te(1)-F(5)	85(3)	88.7	F(8)-As(1)-F(11)	81(2)	82.5
F(2)-Te(1)-F(3)	165(3)	178.9	F(9)-As(1)-F(10)	80(4)	89.9
F(2)-Te(1)-F(4)	90(2)	90.4	F(9)-As(1)-F(11)	84(2)	82.3
F(2)-Te(1)-F(5)	67(2)	88.2	F(10)-As(1)-F(11)	91(3)	81.5
F(3)-Te(1)-F(4)	105(2)	90.0			
F(3)-Te(1)-F(5)	98(3)	91.4			
F(4)-Te(1)-F(5)	154(2)	177.6			

Table 5.2 (continued)

$XeOSeF_5^+AsF_6^-$

Bond Lengths (Å)					
	expt	LDFT/DZVP		expt	LDFT/DZVP
As(1)-F(6)	1.73(4)	1.710	Se(1)-F(1)	1.72(4)	1.733
As(1)-F(7)	1.69(2)	1.745	Se(1)-F(2)	1.65(4)	1.759
As(1)-F(8)	1.76(3)	1.753	Se(1)-F(3)	1.70(3)	1.736
As(1)-F(9)	1.71(2)	1.729	Se(1)-F(4)	1.72(5)	1.738
As(1)-F(10)	1.74(3)	1.729	Se(1)-F(5)	1.70(3)	1.756
As(1)-F(11)	1.80(4)	2.066	Se(1)-O(1)	1.74(4)	1.787
Xe(1)-O(1)	2.04(4)	2.111			
Xe(1)-F(11)	2.31(4)	2.147			

Bond Angles (deg.)					
	expt	LDFT/DZVP		expt	LDFT/DZVP
As(1)-F(11)-Xe(1)	129(2)	121.6	F(6)-As(1)-F(7)	89(2)	97.3
Se(1)-O(1)-Xe(1)	120(3)	116.3	F(6)-As(1)-F(8)	101(2)	97.3
O(1)-Se(1)-F(1)	171(3)	178.7	F(6)-As(1)-F(9)	98(2)	97.9

Table 5.2 (continued)

O(1)-Se(1)-F(2)	94(3)	92.8	F(6)-As(1)-F(10)	86(2)	98.3
O(1)-Se(1)-F(3)	94(3)	89.1	F(6)-As(1)-F(11)	176(1)	179.4
O(1)-Se(1)-F(4)	76(3)	90.1	F(7)-As(1)-F(8)	86(2)	87.3
O(1)-Se(1)-F(5)	92(3)	91.9	F(7)-As(1)-F(9)	173(2)	164.7
O(1)-Xe(1)-F(11)	174(2)	179.1	F(7)-As(1)-F(10)	95(1)	89.6
F(1)-Se(1)-F(2)	95(2)	88.4	F(7)-As(1)-F(11)	95(2)	82.2
F(1)-Se(1)-F(3)	76(2)	89.7	F(8)-As(1)-F(9)	93(1)	89.0
F(1)-Se(1)-F(4)	106(2)	89.5	F(8)-As(1)-F(10)	173(2)	164.4
F(1)-Se(1)-F(5)	87(2)	88.5	F(8)-As(1)-F(11)	81(2)	82.4
F(2)-Se(1)-F(3)	168(2)	178.1	F(9)-As(1)-F(10)	85(2)	90.0
F(2)-Se(1)-F(4)	72(2)	90.0	F(9)-As(1)-F(11)	78(2)	82.7
F(2)-Se(1)-F(5)	98(2)	89.2	F(10)-As(1)-F(11)	92(2)	82.0
F(3)-Se(1)-F(4)	102(2)	90.0			
F(3)-Se(1)-F(5)	90(2)	90.7			
F(4)-Se(1)-F(5)	164(3)	177.9			

Table 5.2 (continued)

$Xe(OTeF_5)_2$

Bond Lengths (Å)			
	expt		expt
Xe(1)-O(1)	2.119(11)	Xe(2)-O(2)	2.112(12)
O(1)-Te(1)	1.843(11)	O(2)-Te(2)	1.842(11)
Te(1)-F(1)	1.843(10)	Te(2)-F(6)	1.855(11)
Te(1)-F(2)	1.835(10)	Te(2)-F(7)	1.830(10)
Te(1)-F(3)	1.850(11)	Te(2)-F(8)	1.848(11)
Te(1)-F(4)	1.823(9)	Te(2)-F(9)	1.825(10)
Te(1)-F(5)	1.849(9)	Te(2)-F(10)	1.835(9)

Bond Angles (deg.)			
	expt		expt
Te(1)-O(1)-Xe(1)	122.3(5)	Te(2)-O(2)-Xe(2)	121.2(6)
O(1)-Te(1)-F(1)	177.7(5)	O(2)-Te(2)-F(6)	178.8(5)
O(1)-Te(1)-F(2)	95.1(5)	O(2)-Te(2)-F(7)	92.6(5)
O(1)-Te(1)-F(3)	91.0(5)	O(2)-Te(2)-F(8)	92.1(5)

Table 5.2 (continued)

O(1)-Te(1)-F(4)	91.2(5)	O(2)-Te(2)-F(9)	90.8(5)
O(1)-Te(1)-F(5)	91.9(5)	O(2)-Te(2)-F(10)	93.5(5)
F(1)-Te(1)-F(2)	87.0(5)	F(6)-Te(2)-F(7)	88.2(5)
F(1)-Te(1)-F(3)	86.8(5)	F(6)-Te(2)-F(8)	87.2(5)
F(1)-Te(1)-F(4)	87.8(5)	F(6)-Te(2)-F(9)	88.2(5)
F(1)-Te(1)-F(5)	89.1(4)	F(6)-Te(2)-F(10)	87.5(5)
F(2)-Te(1)-F(3)	173.8(5)	F(7)-Te(2)-F(8)	175.3(5)
F(2)-Te(1)-F(4)	90.5(5)	F(7)-Te(2)-F(9)	91.4(5)
F(2)-Te(1)-F(5)	88.8(4)	F(7)-Te(2)-F(10)	89.1(5)
F(3)-Te(1)-F(4)	89.9(5)	F(8)-Te(2)-F(9)	88.8(5)
F(3)-Te(1)-F(5)	90.4(4)	F(8)-Te(2)-F(10)	90.3(5)
F(4)-Te(1)-F(5)	176.9(5)	F(9)-Te(2)-F(10)	175.6(4)
O(1)-Xe(1)-O(1A)	180	O(2)-Xe(2)-O(2A)	180

Table 5.2 (continued)

$Xe(OSeF_5)_2$

Bond Lengths (Å)			
	expt		expt
Xe(1)-O(1)	2.16(3)	Se(1)-F(2)	1.55(3)
O(1)-Se(1)	1.54(2)	Se(1)-F(3)	1.742(11)
Se(1)-F(1)	1.68(3)		

Bond Angles (deg.)			
	expt		expt
Se(1)-O(1)-Xe(1)	123.9(13)	F(1)-Se(1)-F(2)	92(2)
O(1)-Se(1)-F(1)	155(2)	F(1)-Se(1)-F(3)	80(2)
O(1)-Se(1)-F(2)	107(2)	F(2)-Se(1)-F(3)	167(2)
O(1)-Se(1)-F(3)	84.5(14)	O(1)-Xe(1)-O(1A)	180

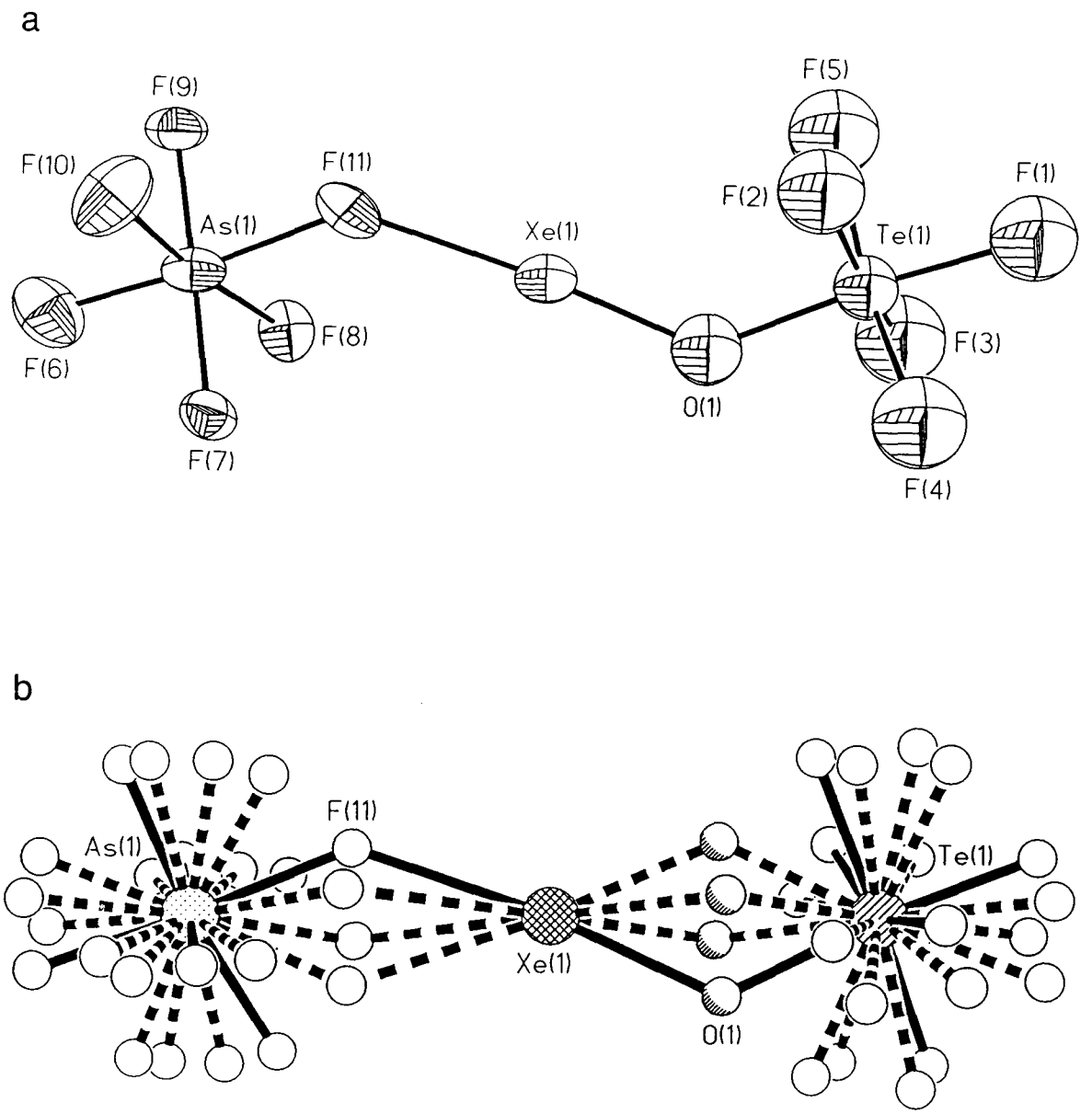

Figure 5.1 (a) Structure of $XeOTeF_5^+AsF_6^-$ as refined by least squares showing thermal ellipsoids at the 30% probability level; (b) disordered model of $XeOTeF_5^+AsF_6^-$.

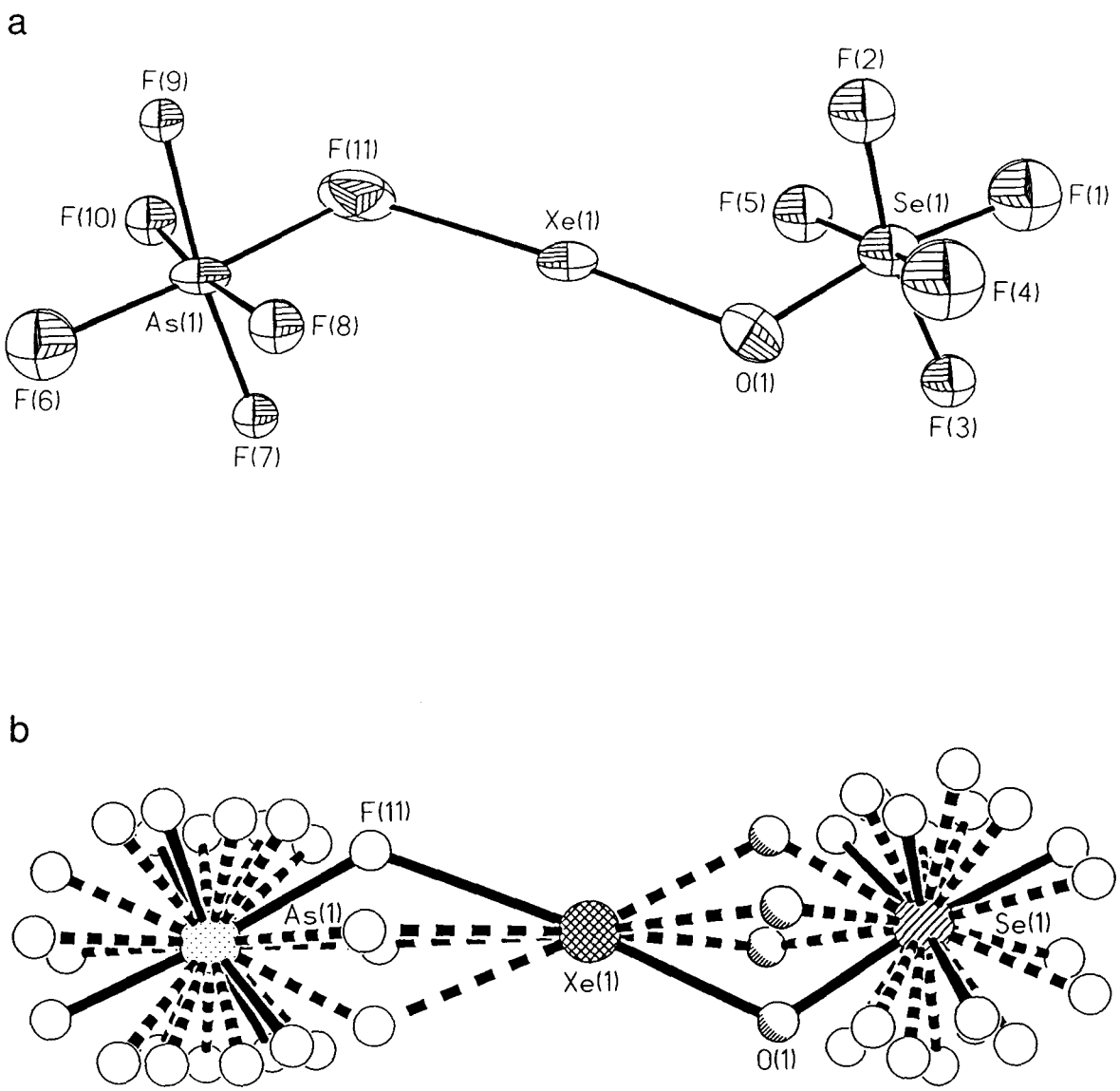

Figure 5.2 (a) Structure of $XeOSeF_5^+AsF_6^-$ as refined by least squares showing thermal ellipsoids at the 30% probability level; (b) disordered model of $XeOSeF_5^+AsF_6^-$.

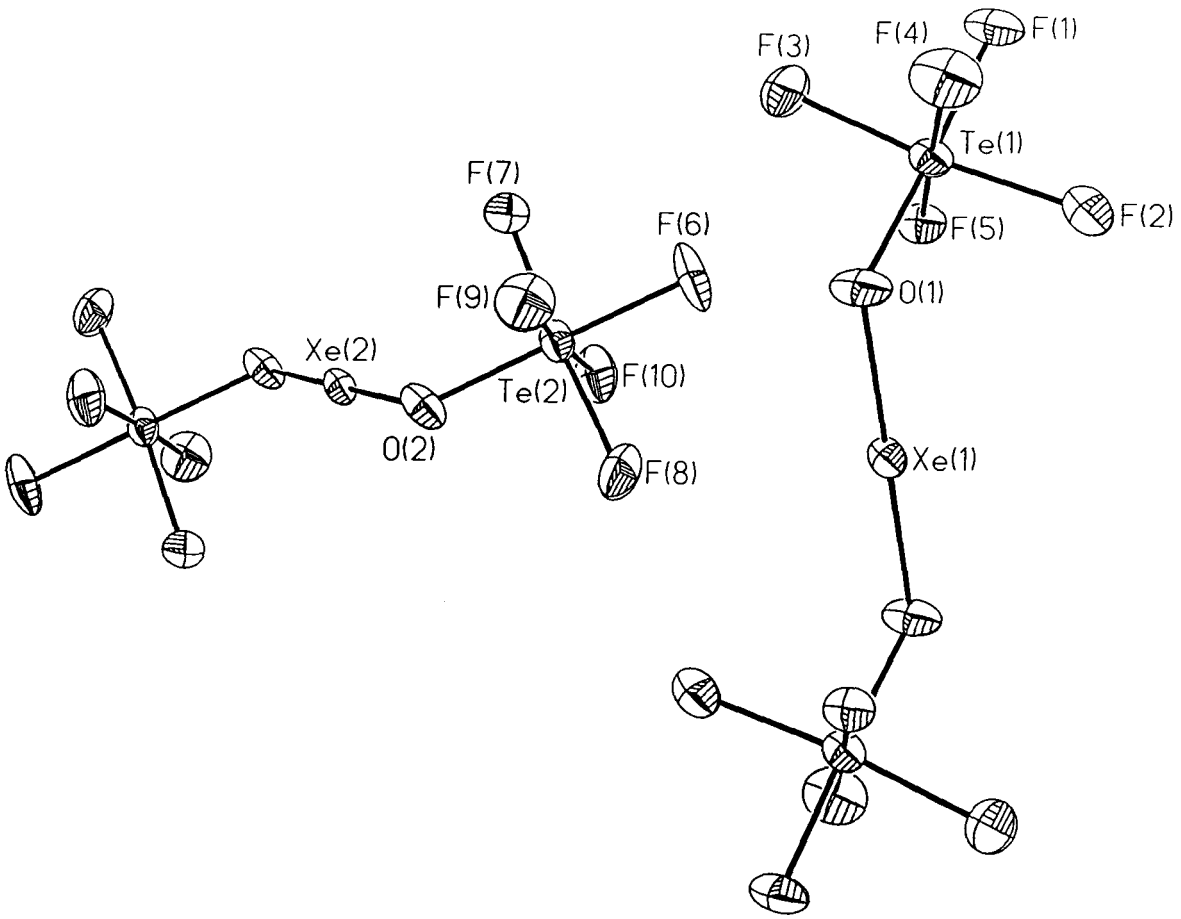

Figure 5.3 Structure of $Xe(OTeF_5)_2$ showing thermal ellipsoids at the 50% probability level.

studied by Sladky[51] was $Xe(OTeF_5)_2$ co-crystallized with another compound (cf. Table 5.1). From the synthetic scheme used by Sladky [eqs (5.6) and (5.7)], the two most likely components are $FXeOTeF_5$ or $HOTeF_5$. However, based on the difference in volume between the two cells, 120 $Å^3$, only one $FXeOTeF_5$ or one $HOTeF_5$ would be expected, which is not compatible with the *Cmca* space group. Athough it is very unlikely, based on equations (5.6) and (5.7), four XeF_2 molecules would account for a volume of 120 $Å^3$ and would be able to occupy the special positions (*2/m*).[174,198] The disordered room temperature structure of $Xe(OSeF_5)_2$ reported by Templeton *et al.* is comparable to the crystal structure observed in the present work (Figure 5.4) with the exception of a difference in Laue symmetries and smaller thermal parameters obtained in the present study.[50]

Three of the four structures reported in the present work suffer from orientational disorders of the fluorine and oxygen atoms [four-fold disorder for the $XeOChF_5^+AsF_6^-$ salts (Ch = Te, Se) and three-fold disorder for $Xe(OSeF_5)_2$] which may influence the geometrical parameters to some extent. All three compounds crystallized in a high symmetry space group (*P4/n* and $R\bar{3}$) which require the molecular axes to have only one orientation, allowing for the disorder to occur (Figures 5.5 and 5.7). On the other hand, $Xe(OTeF_5)_2$ crystallized in a lower symmetry space group ($P2_1/c$) which requires the molecular axes to have two alternating orientations, disfavoring disorder (Figure 5.6). It is somehow surprising to see that, unlike $XeOTeF_5^+AsF_6^-$ and $XeOSeF_5^+AsF_6^-$, $Xe(OTeF_5)_2$ and $Xe(OSeF_5)_2$ pack differently. Such differences in the packing

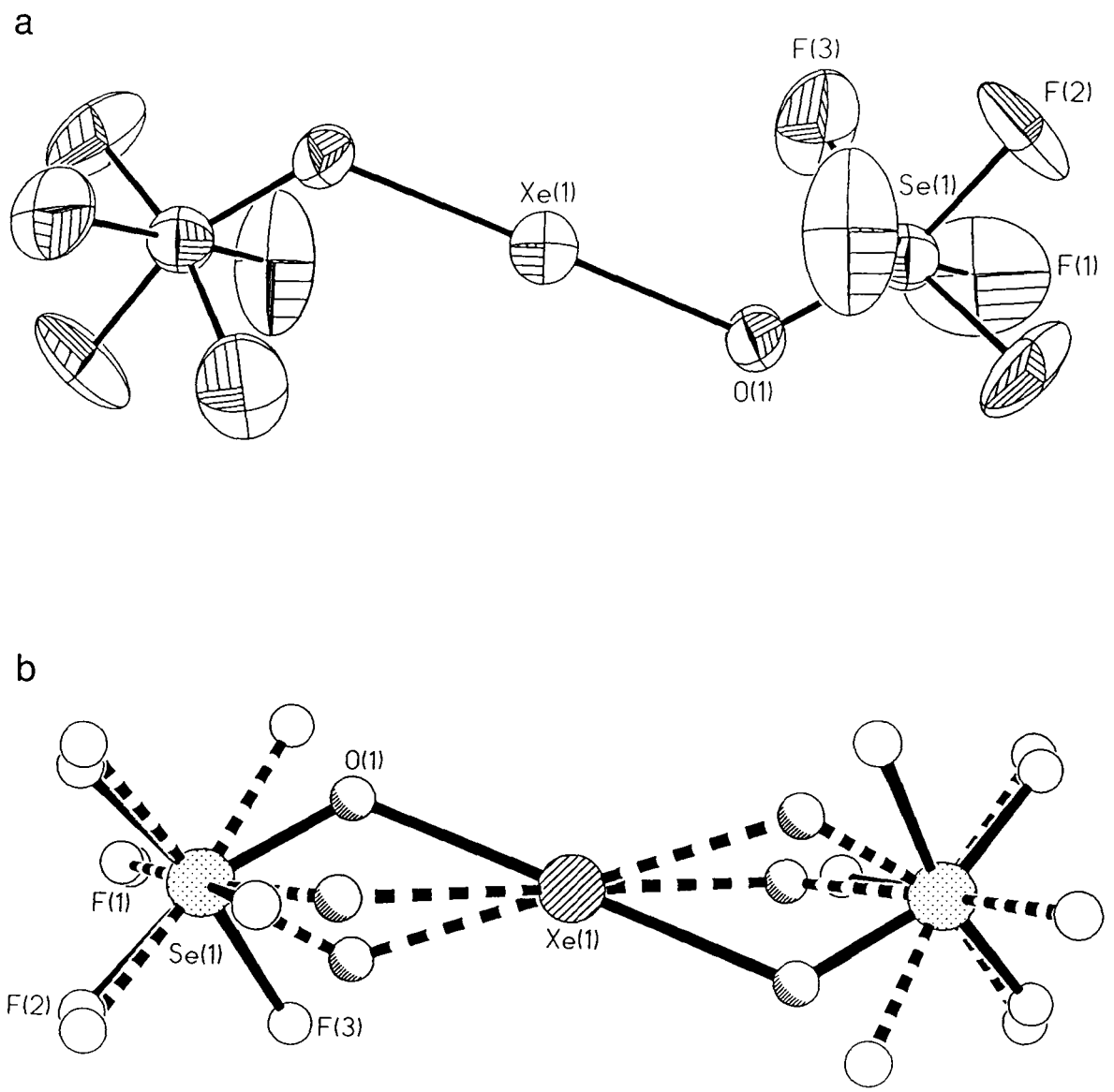

Figure 5.4 (a) Structure of $Xe(OSeF_5)_2$ as refined by least squares showing thermal ellipsoids at the 30% probability level; (b) disordered model of $Xe(OSeF_5)_2$.

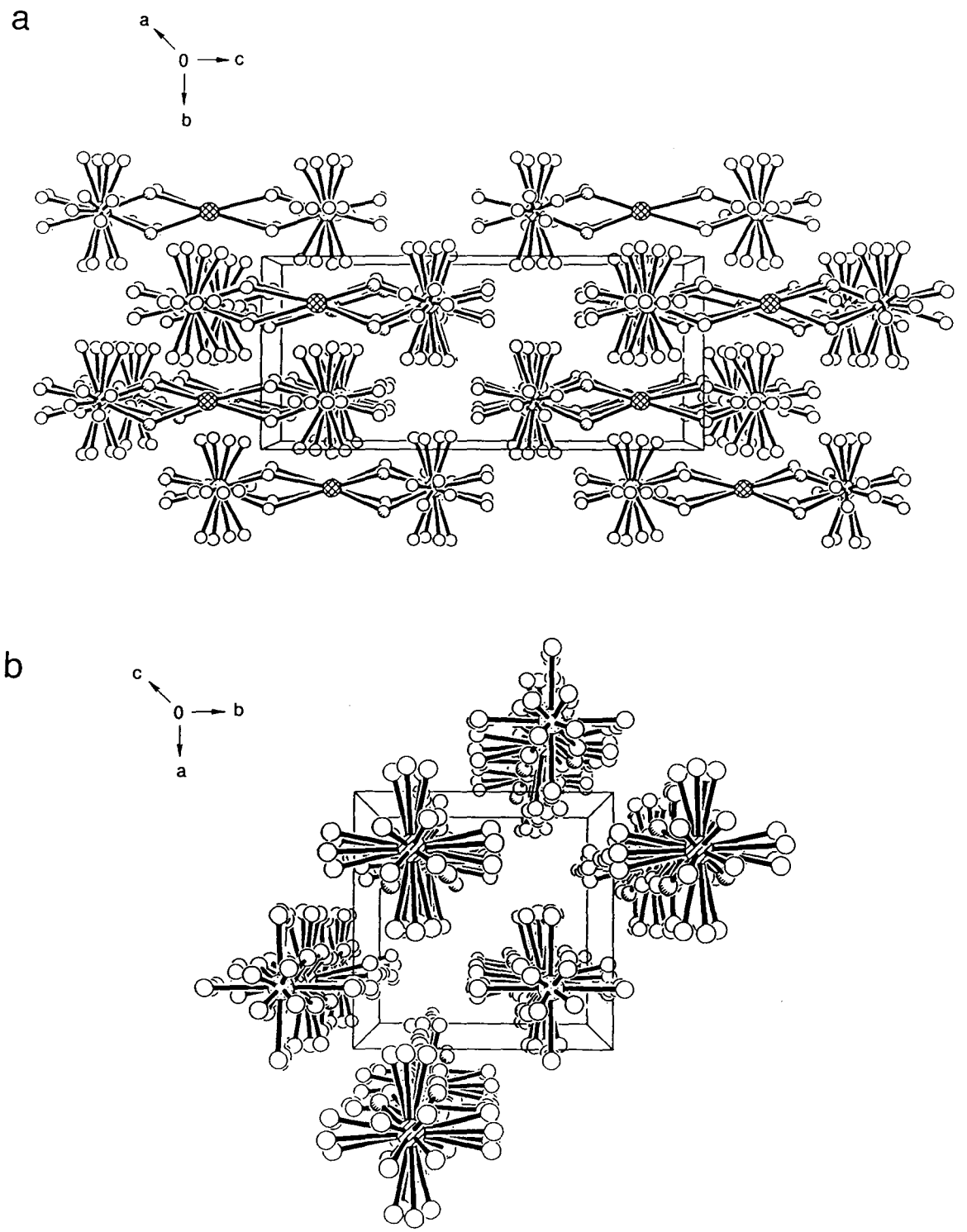

Figure 5.5 View of the $XeOTeF_5^+AsF_6^-$ unit cell, which is identical to $XeOSeF_5^+AsF_6^-$: (a) along the a-axis; (b) along the c-axis.

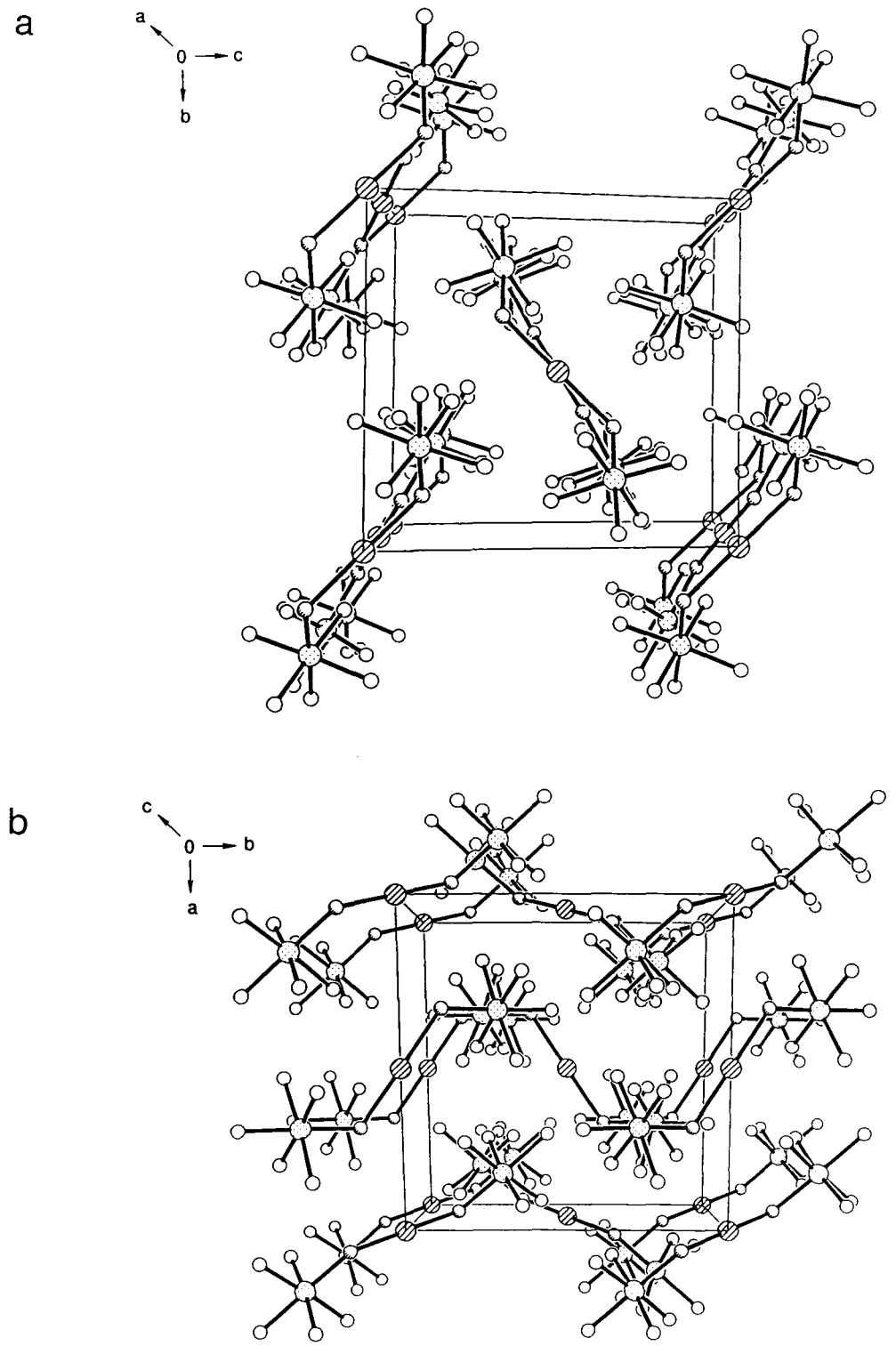

Figure 5.6 View of the $Xe(OTeF_5)_2$ unit cell: (a) along the a-axis; (b) along the c-axis.

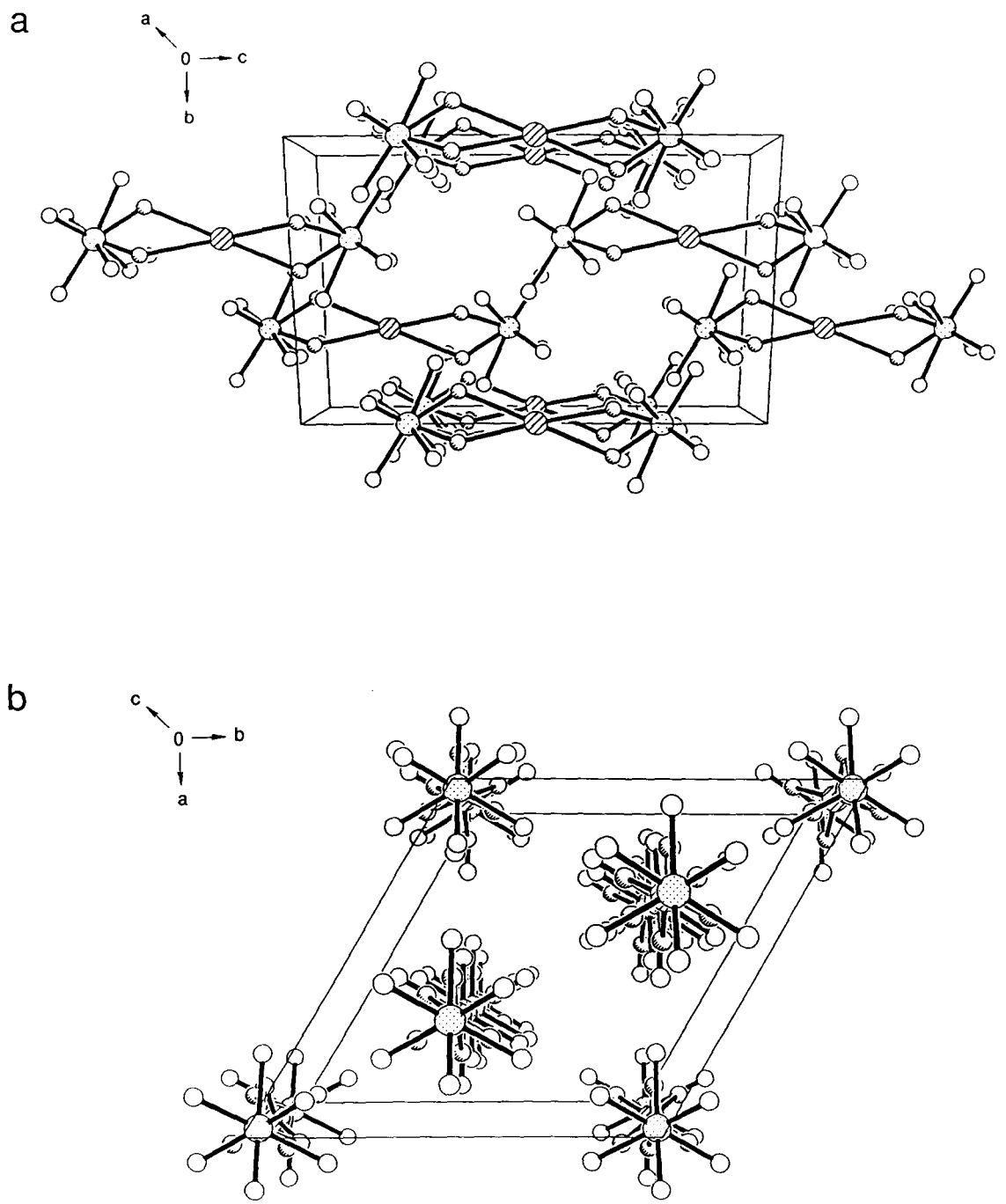

Figure 5.7 View of the $Xe(OSeF_5)_2$ unit cell: (a) along the a-axis; (b) along the c-axis.

arrangements of closely analogous compounds has also been observed for KrF_2 (space group $P4_2/mnm$)[174] and XeF_2 (space group $I4/mmm$),[198] which pack with two perpendicular orientations in the krypton compound and all parallel orientations in the xenon compound.[50] Even though the $Xe(OSeF_5)_2$ structure is disordered, its preferred eclipsed orientation of atoms along Se–O–Xe–O–Se is the same as for the well resolved structure of $Xe(OTeF_5)_2$ (Figures 5.8). All close fluorine contacts with xenon are at the limit of the sum of their van der Waals radii (Xe···F = 3.63 Å).[36-38]

In the $XeOChF_5^+AsF_6^-$ salts, each AsF_6^- anion is fluorine-bridged to the $XeOChF_5^+$ cation through short Xe···F contacts ($XeOTeF_5^+AsF_6^-$, 2.24(3) Å; $XeOSeF_5^+AsF_6^-$, 2.31(4) Å) comparable to that observed in the fluorine analogue, $XeF^+AsF_6^-$ (2.212(5) Å),[19] but shorter than that in the more recently characterized, isoelectronic $F_5TeN(H)Xe^+AsF_6^-$ (2.580(3) Å) salt described in Chapter 4. It has been previously established for $XeF^+AsF_6^-$ [19] and $XeF^+Sb_2F_{11}^-$,[34] when compared to XeF_2,[198] that the longer the bridging anion-cation contact, the more covalent the bonding strength is between xenon and the ligand atom, L (L = O, F, N). This trend reflects the markedly shorter Xe–O bonds in the $XeOChF_5^+AsF_6^-$ ($XeOTeF_5^+AsF_6^-$, 1.96(4) Å; $XeOSeF_5^+AsF_6^-$, 2.04(4) Å) salts when compared to those in the neutral $Xe(OChF_5)_2$ ($Xe(OTeF_5)_2$, 2.119(11) and 2.112(12) Å; $Xe(OSeF_5)_2$, 2.16(3) Å) and $FXeOSO_2F$ (2.16 Å)[166] compounds.

The AsF_6^- anions in $XeOChF_5^+AsF_6^-$ have distorted octahedral geometries about their arsenic atoms, with bridging As–F bond lengths that are longer ($XeOTeF_5^+AsF_6^-$,

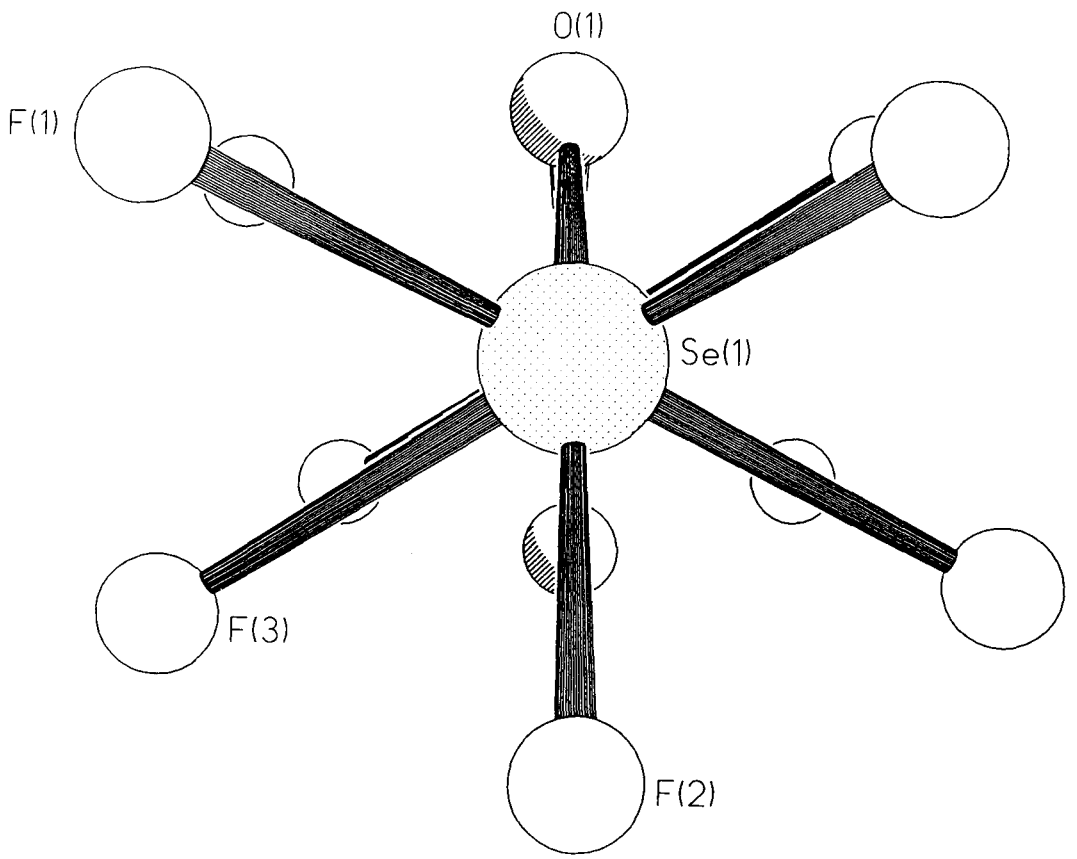

Figure 5.8 Eclipsed orientation of the $Xe(OSeF_5)_2$ structure, which is identical to $Xe(OTeF_5)_2$, along Se–O–Xe–O–Se.

1.81(2) Å; $XeOSeF_5^+AsF_6^-$, 1.80(4) Å) than the others (average: $XeOTeF_5^+AsF_6^-$, 1.72(2) Å; $XeOSeF_5^+AsF_6^-$, 1.73(2) Å). The lengthening of As–F bonds in AsF_6^- anions where short anion-cation contacts exist through Xe···F–As fluorine bridges has also been encountered in $HF{\cdot}HO{-}TeF_4{-}O{-}Xe^+AsF_6^-$ (1.771(1) Å), $XeF_5^+AsF_6^-$ (1.74(2)-1.75(2) Å), $XeF^+AsF_6^-$ (1.813(6) Å), and more recently, in $F_5TeN(H)Xe^+AsF_6^-$ (1.740(4) Å).

In all structures, the geometries around the tellurium or selenium atoms are pseudo-octahedral with *cis*- F–Ch–F and F–Ch–O angles deviating significantly from 90° in $XeOTeF_5^+AsF_6^-$, $XeOSeF_5^+AsF_6^-$, and $Xe(OSeF_5)_2$ possibly due to the disorders. The F–Te–F and F–Te–O bond angles in the ordered structure of $Xe(OTeF_5)_2$ are all equal to 90° within experimental error. Although the Se–O (1.54(2) Å) and Se–F (average: 1.66(6) Å) bond lengths in $Xe(OSeF_5)_2$ are significantly affected by the disorder, the Te–O ($XeOTeF_5^+AsF_6^-$, 1.85(3) Å; $Xe(OTeF_5)_2$, 1.843(11) and 1.842(11) Å), Te–F (average: $XeOTeF_5^+AsF_6^-$, 1.81(1) Å; $Xe(OTeF_5)_2$, 1.839(4) Å), Se–O ($XeOSeF_5^+AsF_6^-$, 1.74(4) Å), and Se–F (average: $XeOSeF_5^+AsF_6^-$, 1.70(1) Å) bond lengths in $XeOTeF_5^+AsF_6^-$, $XeOSeF_5^+AsF_6^-$, and $Xe(OTeF_5)_2$ are in agreement with values reported for other $OTeF_5$ and $OSeF_5$ compounds.[184,185,187-190]

Other than the $Xe(OChF_5)_2$ compounds, whose O–Xe–O angles are constrained to be 180°, the angles around the xenon atoms deviate by a maximum of 5° from linearity within experimental error, a deviation possibly resulting from the disordered nature of the structures. The near linear arrangement of atoms about xenon in $Xe(OChF_5)_2$ and in the ion-paired $XeOChF_5^+AsF_6^-$ structures is consistent with the AX_2E_3 valence-shell electron-

pair repulsion (VSEPR) arrangement of bonding pairs in the axial positions and the lone electron pairs in the equatorial positions. Significant intra- and intermolecular close contacts around the xenon atom in the crystal packing appear to avoid the lone-pair electron density in the F_5ChO–Xe···F and F_5ChO–Xe–$OChF_5$ systems (Figures 5.5 – 5.7).

The $OChF_5$ groups in $Xe(OChF_5)_2$ and the $OChF_5$ and AsF_6 groups in $XeOChF_5^+AsF_6^-$ are arranged *trans* to each other about the central xenon atom and have Xe–O–Ch and Xe···F–As angles significantly less than 180° [(As–F–Xe: $XeOTeF_5^+AsF_6^-$, 135(1)°; $XeOSeF_5^+AsF_6^-$, 129(2)°), (Xe–O–M: $XeOTeF_5^+AsF_6^-$, 128(2)°; $XeOSeF_5^+AsF_6^-$, 120(3)°; $Xe(OTeF_5)_2$, 122.3(5)° and 121.2(6)°; $Xe(OSeF_5)_2$, 123.9(13)°)]. The bent arrangement of atoms about the bridging fluorine or oxygen atoms is in accord with the VSEPR model, which states that the two bonding pairs and two electron pairs should form a tetrahedral AX_2E_2 arrangement as in the H_2O molecule. Based on this model the predicted angle between the bonds is 109.5°. The significantly larger angles observed in the title compounds and the *trans* arrangement of $OChF_5$ and AsF_6 groups about the xenon atom may be based on space filling principles of these bulky groups and has also been encountered in $Xe(OTeF_5)_4$ (Xe–O–Te = 125.1(3), 127.7(3)°) and $FXeOSO_2F$ (Xe–O–S = 123.7°).[185]

Computational Results for $XeOChF_5^+AsF_6^-$ (Ch = Te, Se)

At this stage, preliminary calculations have been carried out at the LDFT/DZVP level for the salts as fluorine bridged ion-pairs. Although the global geometries are in reasonable agreement with the observed ones, there are some noticeable discrepancies. The greatest discrepancies (see Table 5.2) are found at the bridging fluorine where the calculated As–F bridging bond is too long by 0.26 Å for both $F_5ChOXe^+AsF_6^-$ salts, and the Xe···F bridging bond is too short by 0.10 Å for $F_5TeOXe^+AsF_6^-$ and by 0.16 Å for $F_5SeOXe^+AsF_6^-$. In addition, the Xe–O bond is too long by 0.15 Å for $F_5TeOXe^+AsF_6^-$ and by 0.07 Å for $F_5SeOXe^+AsF_6^-$. The bonds around the Te atom are also too long (0.01 – 0.11 Å), while the terminal As–F bond lengths are in good agreement with experiment.

Structural Characterization of $XeOChF_5^+AsF_6^-$ (Ch = Te, Se) by Raman Spectroscopy

The low-temperature solid-state Raman spectra of $XeOTeF_5^+AsF_6^-$ and $XeOSeF_5^+AsF_6^-$ are shown in Figures 5.9 and 5.10, respectively. The observed frequencies and their assignments are summarized in Table 5.3, along with the calculated frequencies.

The Raman frequencies for $XeOTeF_5^+AsF_6^-$ have previously been reported.[53,56] The $XeOChF_5^+$ cations (C_1 point symmetry) possess 18 fundamental modes of vibration belonging to the irreducible representations $\Gamma = 18A$. A factor-group analysis (Table 5.4)

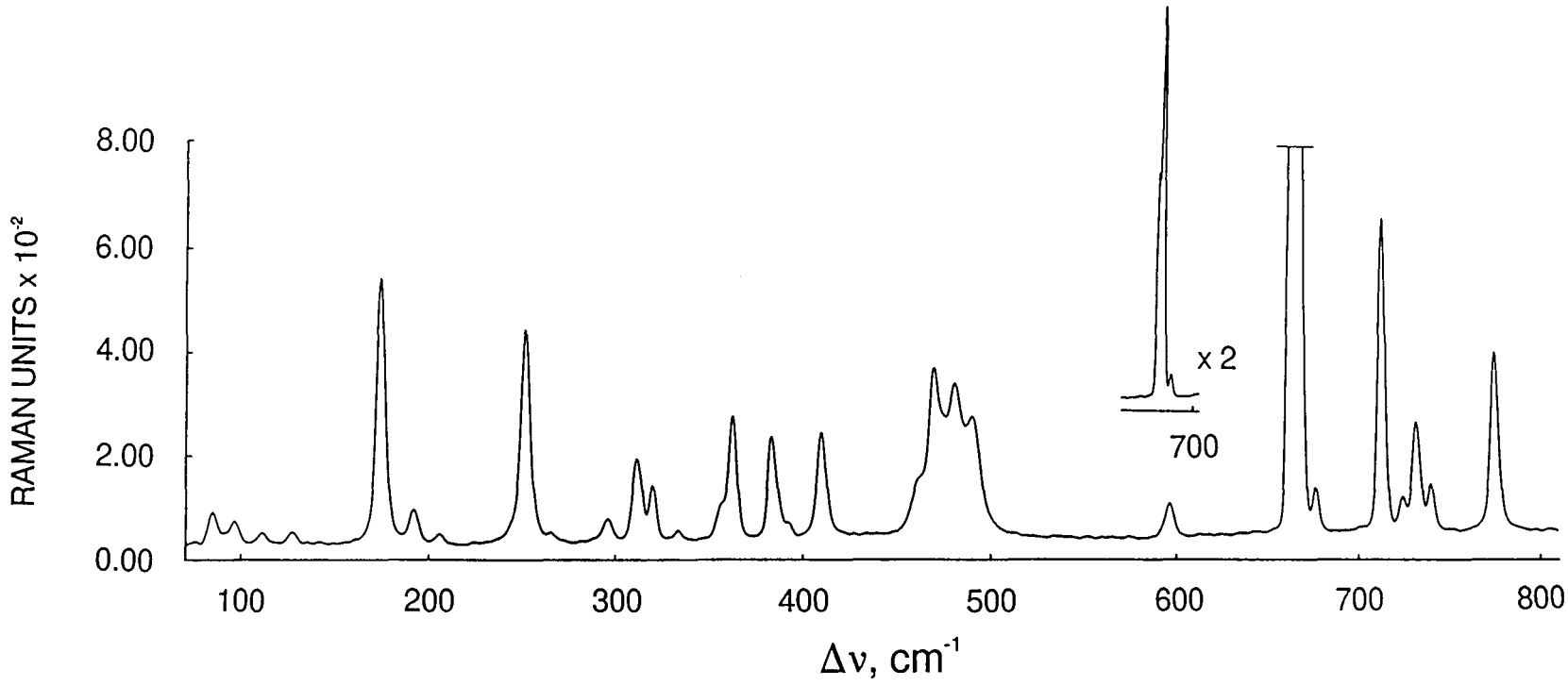

Figure 5.9 Raman spectrum of microcrystalline $XeOTeF_5^+AsF_6^-$ recorded in a Pyrex melting point tube at -145 °C using 1064-nm excitation.

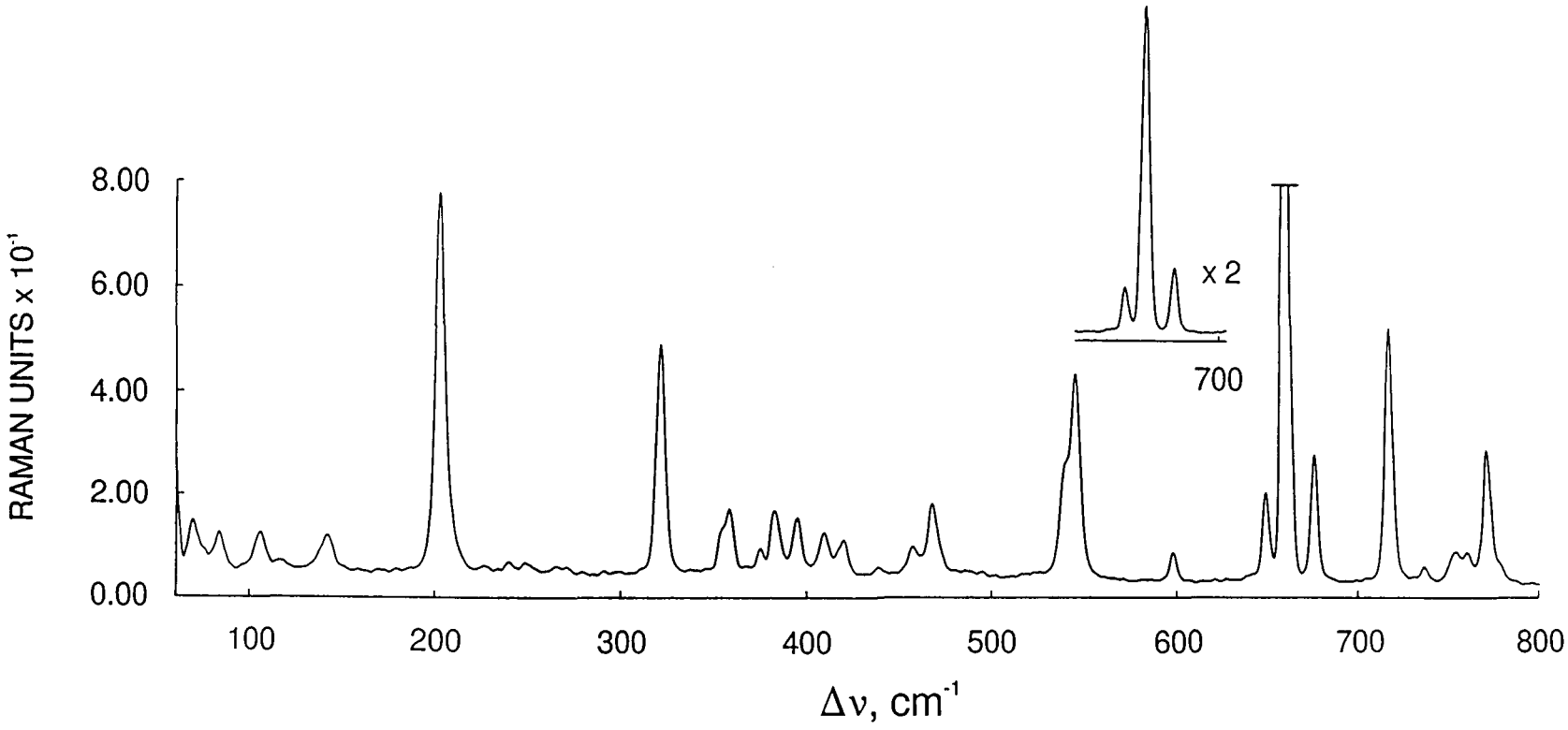

Figure 5.10 Raman spectrum of microcrystalline $XeOSeF_5^+AsF_6^-$ recorded in a Pyrex melting point tube at -145 °C using 1064-nm excitation.

Table 5.3 Experimental Raman and Calculated Vibrational Frequencies, Assignments, and Mode Descriptions for $XeOTeF_5^+AsF_6^-$ and $XeOSeF_5^+AsF_6^-$

frequencies (cm^{-1})				assignments[c]
$XeOTeF_5^+AsF_6^-$		**$XeOSeF_5^+AsF_6^-$**		
exp[a]	LDFT/DZVP[b]	exp[a]	LDFT/DZVP[b]	
775 (24)	740 (127)			(F9As) – (F1As) – (F7As)
		779(3), sh 771 (21) 760 (4) 754 (4)	740 (120)	(F9As – F1As)
739 (6) 731 (13)	739 (138)	736 (2) 730 (<1)	737 (133)	(F1As + F9As)
724 (4) 712 (41) 701 (1)	735 (140)			(F10As) – (F8As) + some (F1As)
		717 (39)	734 (133)	(F8As – F10As)
667 (100)	674 (95)			(F5Te – F4Te) + (F2Te – F3Te)
		659 (100)	714 (137)	(F5Se – F4Se)
			711 (142)	(F2Se – F3Se)

Table 5.3 (continued)

662 (58), sh	672 (217)			(F1Te – OTe) + asym other (FTe)
	672 (190)			(F1Te – OTe) – asym other (FTe)
		649 (14)	702 (359)	(F1Se – OSe)
676 (6)	650 (10)	676 (20)	648 (19)	FAs sym
	630 (68)			(F1Te) + (OTe)
	605 (3)			(F2Te + F3Te) – (F5Te + F4Te)
			601 (27)	(F2Se + F3Se) – (F1Se + OSe)
	600 (8)			F_4Te + some AsF sym
			641 (59)	F_4Se sym
596 (<1)	599 (9)	598 (4)	598 (7)	(F10As + F8As) – (F9As + F7As)
			596 (5)	(F10As + F8As) – (F9As + F7As); 596 / 598 strongly coupled
491 (14) 481(17)	486 (131)			(OXe – F_bXe)
		545 (32) 539 (16), sh	534 (59)	OXe

Table 5.3 (continued)

470 (19) 462 (7) , sh	442 (74)			(OXe + F_bXe)
		468 (10) 458 (5)	449 (101)	(F_bXe – F_bAs)
		438 (2)		d
		420 (5)		d
409 (12)		409 (6)		d
392 (2)		395 (8)		d
383 (12)		382 (9)	387 (100)	F_4Se umbrella + $\nu(F_bXe)$
		374 (3)	368 (30)	$OSeF_5$ out-of-phase bend
			366 (10)	($OSeF_5$ in-plane – F3SeF4)
362 (14)	358 (23)			$\nu(AsF_b)$ + F7AsF8 in-plane bend
		358 (9)	360 (23)	$\nu(AsF_b)$ + F10AsF8
355 (4), sh	351 (4)			F8AsF9 bend
		355 (6), sh	350 (1)	(F10AsF7 + F8AsF9)
	347 (38)			F7AsF10 – F8AsF9 + F_bAsF1 bends

Table 5.3 (continued)

			346 (37)	F10AsF7 – F8AsF9
333 (1)				d
320 (6)	326 (21)	322 (35)	330 (17) 325 (0)	F7AsF9 + F8AsF_b + XeF_bAs bends
311 (9)				d
295 (3)	298 (59)		287 (227)	F_4As out-of-plane bend + F_4Te out-of-plane bend + ν(AsF_b)
	275 (3)	271 (1)	276 (1)	F9AsF_b – F7AsF_b – F10AsF_b + F8AsF_b bends
264 (1)	265 (292)	265 (1)	269 (192)	F_4As out-of-plane bend – F_4Te out-of-plane bend + ν(AsF_b)
	263 (82)			F3TeF1 + F5TeF4
	260 (81)			F5TeF1 + F2TeF3
251 (28)	250 (1)	248 (2)	249 (9)	F10AsF1
	249 (4)			$OTeF_4$ bend really like an O out-of-plane bend
	239 (0)	240 (2)	240 (1)	F4TeF3 – F5TeF2
223 (<1)		226 (1)		d

Table 5.3 (continued)

205 (1)	203 (2)	203 (58)	213 (1)	F_bAsF7 bend really like an F_b out-of-plane bend
192 (4)	199 (18)		196 (1) 184 (9)	F5TeF2 – F3TeF4
174 (34)				d
	166 (0)			F2TeF4 – F2TeF3
	160 (0)		159 (0)	F10AsF8 – F9AsF7
	155 (2)			F9AsF7 – F5TeF4
	138 (0)	142 (5)	134 (1)	F5TeF3 – F2TeF4 + F1TeO
127 (1)	120 (0)		119 (1)	F10AsF_b – F'AsF_b (rock of AsF_5 group about F10–F8 axis)
111 (1)	106 (2)	117 (2) 106 (5)	118 (1)	rock of TeF_5 group about the F5–F4 axis

Table 5.3 (continued)

96 (3) 84 (4) 75 (<1)	97 (1)	95 (<1) 83 (5) 75 (3), sh 69 (7)	 73 (0) 65 (0)	rock of TeF_5 group about the F3–F2 axis – $OXeF_b$ bend
	62 (0)		59 (1)	AsF_5 group – F_bXe bend – TeF_5 group – OXe bend
	47 (0)			TeF_5 group torsion about TeO – AsF_5 group torsion about AsF_b
	44 (2)			TeF_5 group – OXe bend – AsF_5 group – FXe bend
			42 (1)	SeF_5 group – OXe bend – AsF_5 group – FXe bend, AsF_5 group wag
	37 (0)			AsF_5 group wag wrt Xe
	28 (1)			TeF_5 group wag wrt Xe
			24 (1)	SeF_5 group wag

[a] Powdered spectra recorded in Pyrex glass capillaries at -145 °C using 1064-nm excitation. Values in parentheses denote relative Raman intensities; sh = shoulder.

[b] Infrared intensities, in km mol^{-1}, are given in parentheses.

[c] The $XeOChF_5^+$ cations have C_s local site symmetry, the AsF_6^- cations have C_{4v} local site symmetry. F_b denotes the bridging fluorine atoms.

[d] Unassigned bands.

Table 5.4 Correlation Diagram for the Vibrational Modes of the Free $XeOChF_5^+$ Cations (Ch = Te, Se) to those in Crystalline $XeOChF_5^+AsF_6^-$.[a]

	Free Cation Symmetry, C_1	Site Symmetry, C_4	Crystal Symmetry, C_{4h}		
24T, 24R, $8(\nu_1 - \nu_{18})$	A	A_1	A_g (Ra)	3T, 3R	$(\nu_1 - \nu_{18})$
			B_g (i.a.)	3T, 3R	$(\nu_1 - \nu_{18})$
		B_1	E_g (Ra)	6T, 6R	$(\nu_1 - \nu_{18})$
			A_u (IR)	3T, 3R	$(\nu_1 - \nu_{18})$
		E_2	B_u (i.a.)	3T, 3R	$(\nu_1 - \nu_{18})$
			E_u (IR)	6T, 6R	$(\nu_1 - \nu_{18})$

Table 5.5 Correlation Diagram for the Vibrational Modes of the Free AsF_6^- Anions to those in Crystalline $XeOChF_5^+AsF_6^-$ (Ch = Te, Se).[a]

	Free Anion Symmetry, C_{4v}	Site Symmetry, C_4	Crystal Symmetry, C_{4h}		
8T, $8(\nu_1 - \nu_4)$	A_1	A	A_g (Ra)	4T, 4R	$4(\nu_1 - \nu_4)$
			B_g (Ra)		$4(\nu_5 - \nu_7)$
8R	A_2				
$8(\nu_5 - \nu_6)$	B_1	B	E_g (Ra)	8T, 8R	$4(\nu_8 - \nu_{11})$
			A_u (IR)	4T, 4R	$4(\nu_1 - \nu_4)$
$8\nu_7$	B_2				
		E	B_u (i.a.)		$4(\nu_5 - \nu_7)$
16T, 16R, $8(\nu_8 - \nu_{11})$	E		E_u (IR)	8T, 8R	$4(\nu_8 - \nu_{11})$

[a] The factor group analyses for the cations and the anions are treated separately, and although Z = 2, the analysis is treated for Z = 8 because of the four-fold disorder. The symbols T and R denote translatory and rotatory (external) modes, respectively, and Ra, IR, and i.a. in parentheses denote Raman and infrared activity, and inactivity, respectively.

correlating the C_1 point symmetry of the $XeOChF_5^+$ cations to the site symmetry (C_4) and to the crystallographic symmetry (C_{4h}) reveals that each vibrational mode should be split into an A_g and an E_g Raman-active component, and an A_u and an E_u infrared-active component under the crystal symmetry.

The AsF_6^- anions (C_{4v} point symmetry) possess 18 fundamental modes of vibration belonging to the irreducible representations $\Gamma = 4A_1 \oplus 2B_1 \oplus B_2 \oplus 4E$. The C_{4v} point symmetry of the AsF_6^- anion was correlated to the site symmetry (C_4) and to the crystallographic symmetry (C_{4h}) (Table 5.5). No bands are predicted to be split in the Raman spectrum.

The vibrational assignments for $XeOChF_5^+AsF_6^-$ were obtained from calculations at the LDFT/DZVP level and were compared with the assignments for $Xe(OTeF_5)_2$,[51,56] F_5TeOF,[191] $N(CH_3)_4^+TeOF_5^-$,[171] $XeOTeF_5^+Sb_2F_{11}^-$,[56] and the previously reported $XeOTeF_5^+AsF_6^-$ salt.[53,56] The discrepancies between the observed and calculated geometries (see Table 5.2 and **Computational Results for $XeOChF_5^+AsF_6^-$**) are reflected in the vibrational modes involving those bonds which were too short or too long relative to the calculated values and are found respectively too high or too low in frequency. The calculated modes involving the terminal As–F bonds, however, are in good agreement with experiment.

Some discrepancies are also noted between the calculated assignments for the $XeOChF_5^+AsF_6^-$ salts in the present work and those given for $Xe(OTeF_5)_2$,[51,56] F_5TeOF,[191] $N(CH_3)_4^+TeOF_5^-$,[171] $XeOTeF_5^+Sb_2F_{11}^-$,[56] and the previously reported $XeOTeF_5^+AsF_6^-$

salt.[53,56] In particular, the modes for the AsF_6^- anion are now found at higher frequency bands than those corresponding to the TeF_5 group. The calculations are currently being redone at the Hartree-Fock level which was previously used successfully to calculate the geometries and vibrational frequencies of the F_5TeO^- anion.[171]

Correlations of the Structural Findings with Spectroscopic Results and Bonding

The bonding in the neutral XeL_2 and cationic XeL^+ species (L = $OChF_5$) may be represented by valence bond schemes I and II, respectively, where structures $[L^-\ Xe^{2+}\ L^-]$

$$L^-\ Xe^{2+}\ L^- \quad \leftrightarrow \quad L{-}Xe^+\ L^- \quad \leftrightarrow \quad L^-\ {}^+Xe{-}L$$

I

$$L\ Xe^{2+}\ F^- \quad \leftrightarrow \quad L{-}Xe^{2+}\ F^- \quad \leftrightarrow \quad L\ {}^+Xe{-}F$$

II

and $[L\ Xe^{2+}\ F^-]$ are the least important contributing structures.[12] Accordingly, the XeL_2 molecules have formal Xe–L bond orders of ½, whereas the formal bond order for the XeL^+ cations is between ½ and 1. Prior to this work, the strengths of the bridging Xe···F and Xe–O bonds in the title compounds had been assessed by multi-NMR spectroscopy.[42,45,56,58,60] Table 5.6 lists some X-ray crystallographic and NMR parameters for $XeOChF_5^+AsF_6^-$,[53,55,56] $Xe(OChF_5)_2$,[42,45,60] $XeF^+AsF_6^-$,[19] XeF_2,[45,183,186] and $F_5TeN(H)Xe^+AsF_6^-$.[26] Despite solvent and temperature dependencies of the ^{129}Xe chemical shifts, generally, as the Xe···F bond becomes more ionic on moving down the

Table 5.6 Comparison of Some X-Ray Crystallographic, Raman, and NMR Parameters for $XeOChF_5^+AsF_6^-$, $Xe(OChF_5)_2$, $XeF^+AsF_6^-$, XeF_2, and $F_5TeN(H)Xe^+AsF_6^-$ (Ch = Se, Te).

	X-ray Crystallography (Å)		NMR[c]			
Cation[a]	Xe···F [a]	Xe–L [b]	Solvent (Temp. °C)	$\delta(^{129}Xe)$, ppm	δ(L), ppm[c]	$^1J(^{129}Xe\text{-}L)$, Hz
$XeF^+AsF_6^-$ [19]	2.212(5)[d]	F, 1.873(6)	HSO_3F (-96)	-991	^{19}F, -243.5	^{19}F, 6615
			SbF_5 (30)	-574		
$XeOTeF_5^+AsF_6^-$ [53,55,56]	2.24(3)	O, 1.96(4)	HSO_3F (-94.6)	-1521		
			SbF_5 (25)	-1472		
$XeOSeF_5^+AsF_6^-$ [58]	2.31(4)	O, 2.04(4)	BrF_5 (30)	-1438		
$F_5TeN(H)Xe^+AsF_6^-$ [26]	2.580(3)[d]	N, 2.044(4)	HF (-45)	-2841		^{15}N, 138
			BrF_5 (-45)	-2902		^{15}N, 142
XeF_2 [45,186,183]		F, 2.14(14)	HF (30)	-1592	^{19}F, -199.6	^{19}F, 5652
			BrF_5 (30)	-1750	^{19}F, -181.8	^{19}F, 5616
$Xe(OTeF_5)_2$ [42,45,60]		O, 2.119(11)	$CFCl_3$ (30)	-2447.4		
		O, 2.112(12)	SO_2ClF (-16)	-2327	^{17}O, 152.1	
$Xe(OSeF_5)_2$ [60]		O, 2.16(3)	$CFCl_3$, (30)	-2200		

[a] Refers to the bridging fluorine on arsenic.

[b] L denotes the oxygen, fluorine, or nitrogen ligand atom.

[c] Chemical shifts are referenced with respect to the neat liquids $XeOF_4$ (^{129}Xe) and $CFCl_3$ (^{19}F) at 24 °C; a positive sign denotes the chemical shift of the resonance in question occurs to higher frequency of (is more shielded than) the resonance of the reference substance.

table for $XeF^+AsF_6^-$, $XeOChF_5^+AsF_6^-$, and $F_5TeN(H)Xe^+AsF_6^-$, the formal charge on xenon is increased and the xenon nucleus becomes more shielded. In the cases where both fluorine atoms in XeF_2 are replaced by $OChF_5$ groups that provide bonds of greater covalent character than the Xe–F bonds, the ^{129}Xe shieldings increase. The differences between ionic strengths of the Xe···F bridging bonds in the $OChF_5$, F, and $F_5TeN(H)$ analogues correlate with the relative electronegativities of these groups, and subsequent Lewis acidities of the cations, $F_5TeN(H)Xe^+$, $XeChOTeF_5^+$, and XeF^+. Based on the trends, the relative electronegativities increase in the following order, as expected from previous studies:[45,46]

$$F_5TeN(H) > OSeF_5 > OTeF_5 > F$$

CHAPTER 6

As(II) AND Sb(III) DERIVATIVES OF THE $OTeF_5$ GROUP

INTRODUCTION

The pentafluorooxotellurate, $OTeF_5$, group resembles fluorine in its ability to stabilize high oxidation states. This is attributed to its high effective group electronegativity resulting from the inductive effect of five fluorines on tellurium,[41] and is demonstrated by the recent syntheses of the $B(OTeF_5)_4^-$,[108] $Pd(OTeF_5)_4^{2-}$,[109] $Ti(OTeF_5)_6^{2-}$,[110] $I(OTeF_5)_4^-$,[111] $Te(OTeF_5)_5^-$,[112] $Pn(OTeF_5)_6^-$ (Pn = As, Sb, Bi),[107] $Nb(OTeF_5)_6^-$,[110] and *cis*-$ReO_2(OTeF_5)_4^-$[113] anions. Compared to their fluorine analogues, BF_4^- and PnF_6^-, the $OTeF_5$ derivatives are weakly coordinating, stable with respect to fluoride abstraction, and virtually never form fluorine bridges. However, $OTeF_5$ derivatives can undergo various decomposition reactions with loss of a whole ligand. The elimination of $TeOF_4$ is common in coordinatively unsaturated compounds, whereas in coordinatively highly saturated compounds, TeF_6 and $F_5TeOTeF_5$ are eliminated with formation of oxo-derivatives, $O_nM(OTeF_5)_m$.[41]

For pentacoordinate AX_5 and AX_4E systems, intramolecular rearrangements that simultaneously interchange the axial and equatorial ligands by means of the Berry pseudorotation mechanism are common.[192] Intramolecular exchange by this process in PF_4^-,[116] SF_4,[117-119] PF_5,[120] and PF_3X_2 (X = Br, Cl)[121] has been studied in detail by

variable-temperature NMR spectroscopy and the activation energy barriers ($\Delta G^{\ddagger}$) have been calculated. The barriers for the two-site intramolecular exchange in these complexes were sufficiently high to reduce the exchange to a frequency that was slow enough on the NMR time scale at low temperatures to permit the observation of separate axial and equatorial environments. Until recently, however, the only known pseudo-trigonal bipyramidal main-group $OTeF_5$ derivative whose intramolecular exchange barrier had been determined was $Te(OTeF_5)_4$.[115]

The present work extends the known chemistry of main-group $OTeF_5$ derivatives by the syntheses and detailed structural characterizations by ^{19}F and ^{125}Te NMR spectroscopy and by Raman spectroscopy of the pnicogen anions, $Pn(OTeF_5)_4^-$ (Pn = Sb, As), as their $N(CH_3)_4^+$ and $N(CH_2CH_3)_4^+$ salts. The $Sb(OTeF_5)_4^-$ anion has previously been prepared as an intermediate in the synthesis of $Sb(OTeF_5)_6^-$,[107] however, this is the first time it is fully characterized. The $Pn(OTeF_5)_4^-$ anions, which contain fewer $OTeF_5$ groups than the previously characterized weakly coordinating $Pn(OTeF_5)_6^-$ (Pn = Sb, As, Bi) anions,[107] are expected to have pseudo-trigonal bipyramidal geometries with two equatorial and two axial $OTeF_5$ ligands that undergo intramolecular exchange in solution. X-ray crystal structure determination of $Sb(OTeF_5)_4^-$ has been attempted in this work.

RESULTS AND DISCUSSION

Preparation of the $Pn(OTeF_5)_4^-$ (Pn = Sb, As) Anions

The $Sb(OTeF_5)_4^-$ and $As(OTeF_5)_4^-$ anions were prepared as salts of both the $N(CH_3)_4^+$ and $N(CH_2CH_3)_4^+$ cations by the reaction of the appropriate $Pn(OTeF_5)_3$

derivative (Pn = Sb or As) with a stoichiometric amount of $NR_4^+OTeF_5^-$ (R = CH_3, CH_2CH_3) in SO_2ClF solvent according to equation (6.1). The reactions proceed at

$$Pn(OTeF_5)_3 + NR_4^+OTeF_5^- \xrightarrow{SO_2ClF,\ 25\ ^\circ C} NR_4^+Pn(OTeF_5)_4^- \qquad (6.1)$$

ambient temperature and yield white solids upon removal of SO_2ClF solvent *in vacuo*. This synthetic route is analogous to that used for the preparation of the $Te(OTeF_5)_5^-$ [112] and $Pn(OTeF_5)_6^-$ (Pn = As, Sb, Bi)[107] anions.

The $As(OTeF_5)_4^-$ anion is thermally less stable than $Sb(OTeF_5)_4^-$ in CH_3CN and SO_2ClF solvents, as determined by ^{125}Te and ^{19}F NMR spectroscopy (see **Decomposition of $N(CH_2CH_3)_4^+As(OTeF_5)_4^-$ in SO_2ClF**). Both $Sb(OTeF_5)_4^-$ salts were highly soluble in the solvents SO_2ClF, CH_3CN, CH_2Cl_2, and Freon-114 and all attempts to crystallize $Sb(OTeF_5)_4^-$ from these solvents produced the less soluble $Sb(OTeF_5)_5^{2-}$ anion instead (see **X-Ray Crystal Structure of $[N(CH_3)_4^+]_2[Sb(OTeF_5)_5^{2-}]$**).

Characterization of the $Pn(OTeF_5)_4^-$ (Pn = Sb, As) Anions by Raman Spectroscopy

The Raman spectra of the title compounds as their $N(CH_3)_4^+$ and $N(CH_2CH_3)_4^+$ salts are shown in Figures 6.1 – 6.5. The observed frequencies and their assignments are summarized in Table 6.1. Spectral assignments are tentative owing to uncertainties regarding the degree of vibrational coupling among the $OTeF_5$ modes of the ligands, anticipated strong coupling among vibrational modes associated with the Pn–O–Te (Pn = Sb, As) moieties, the degrees of site symmetry lowering resulting in removal of degeneracy for the E-modes (*vide infra*), as well as vibrational coupling within the unit

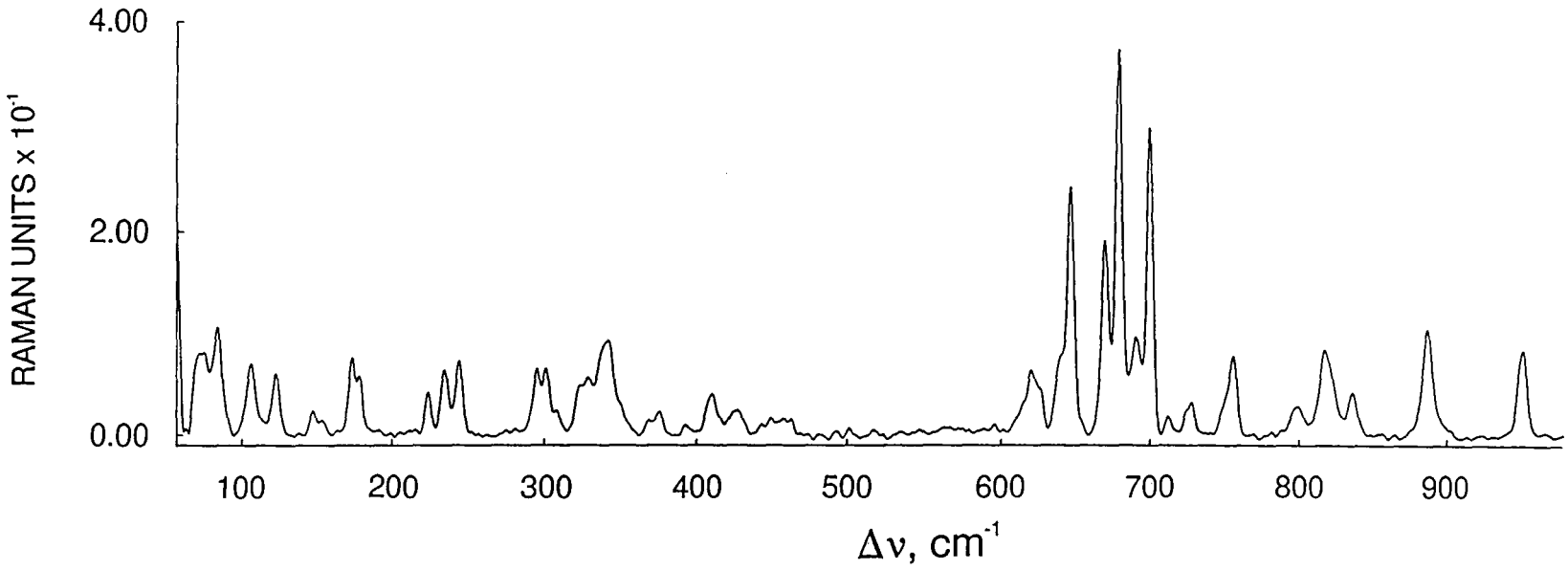

Figure 6.1 Raman spectrum of microcrystalline $N(CH_3)_4^+Sb(OTeF_5)_4^-$ recorded in 5-mm glass NMR tubes at -140 °C using 1064-nm excitation. The high-frequency bands of the $N(CH_3)_4^+$ cation are not shown but are listed in Table 6.1.

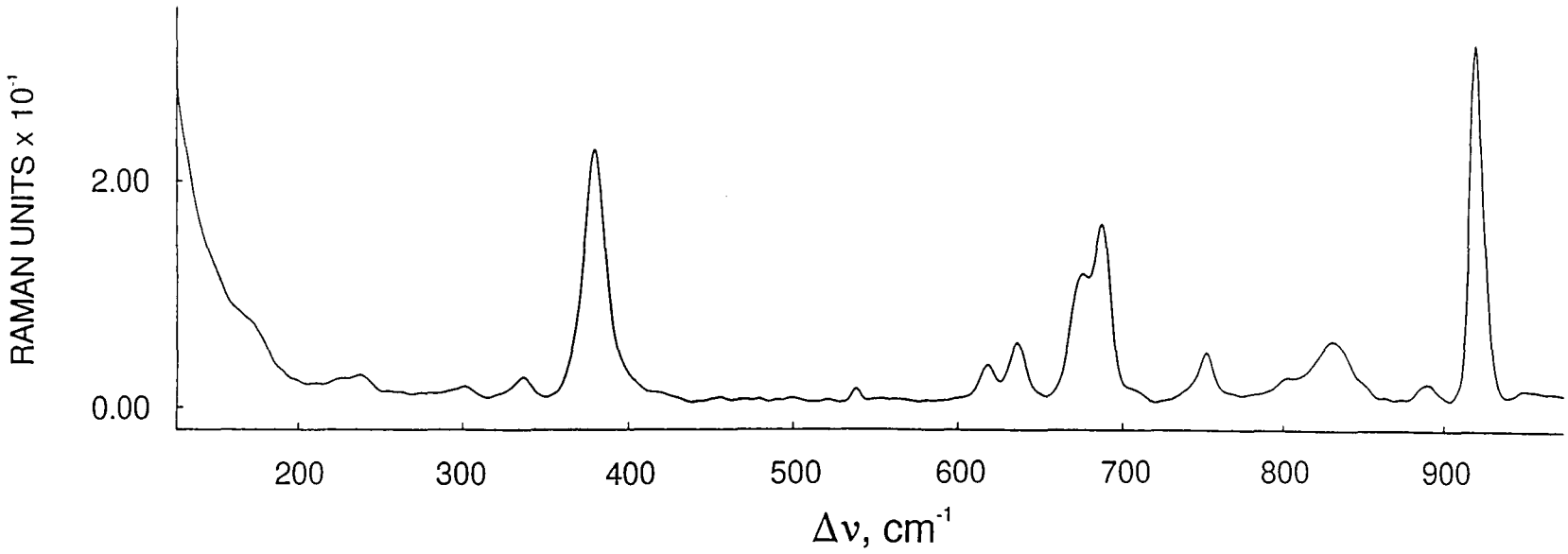

Figure 6.2 Raman spectrum of $N(CH_3)_4^+Sb(OTeF_5)_4^-$ in CH_3CN solvent recorded in 5-mm glass NMR tubes at 30 °C using 1064-nm excitation. The high-frequency bands of the $N(CH_3)_4^+$ cation are not shown but are listed in Table 6.1.

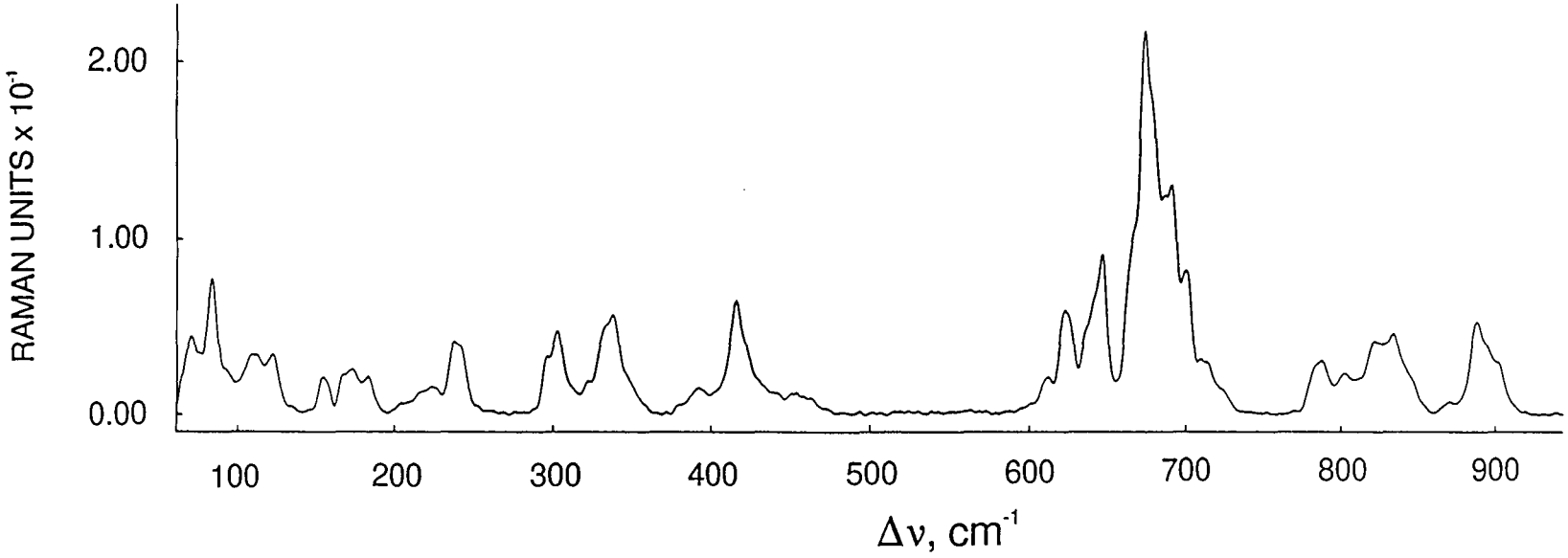

Figure 6.3 Raman spectrum of microcrystalline $N(CH_2CH_3)_4^+Sb(OTeF_5)_4^-$ recorded in 5-mm glass NMR tubes at -140 °C using 1064-nm excitation. The high-frequency bands of the $N(CH_2CH_3)_4^+$ cation are not shown but are listed in Table 6.1.

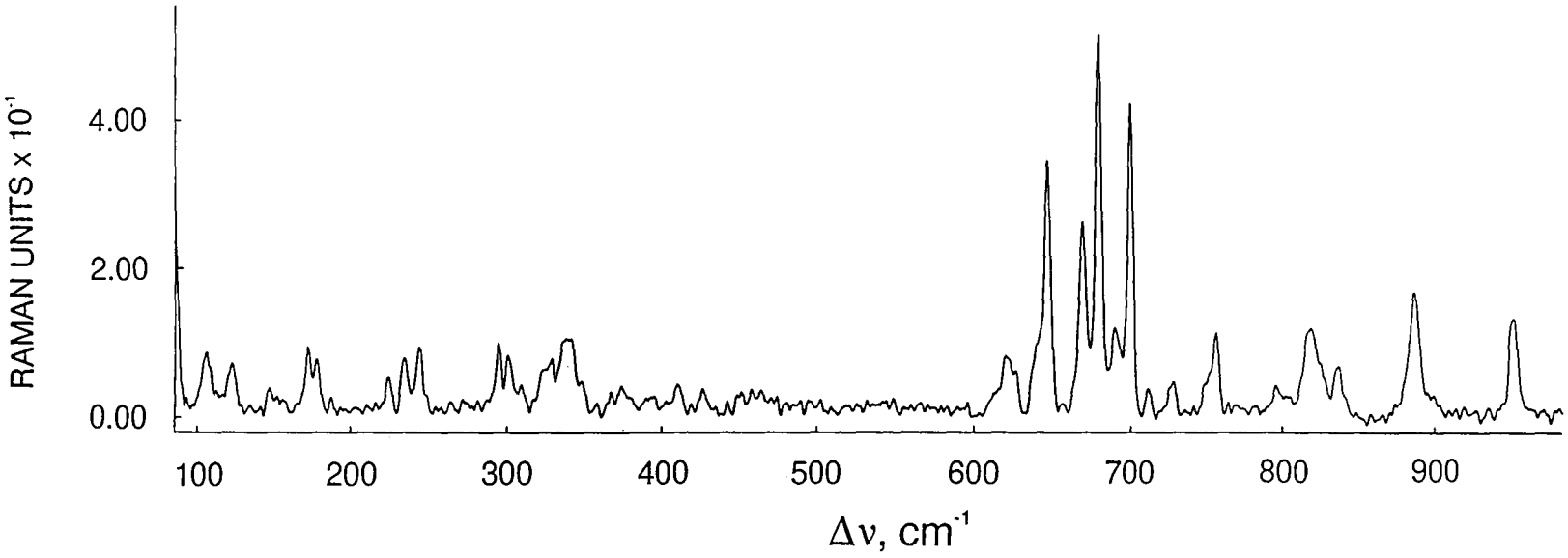

Figure 6.4 Raman spectrum of microcrystalline $N(CH_3)_4^+As(OTeF_5)_4^-$ recorded in Pyrex capillaries at -140 °C using 1064-nm excitation. The high-frequency bands of the $N(CH_3)_4^+$ cation are not shown but are listed in Table 6.1.

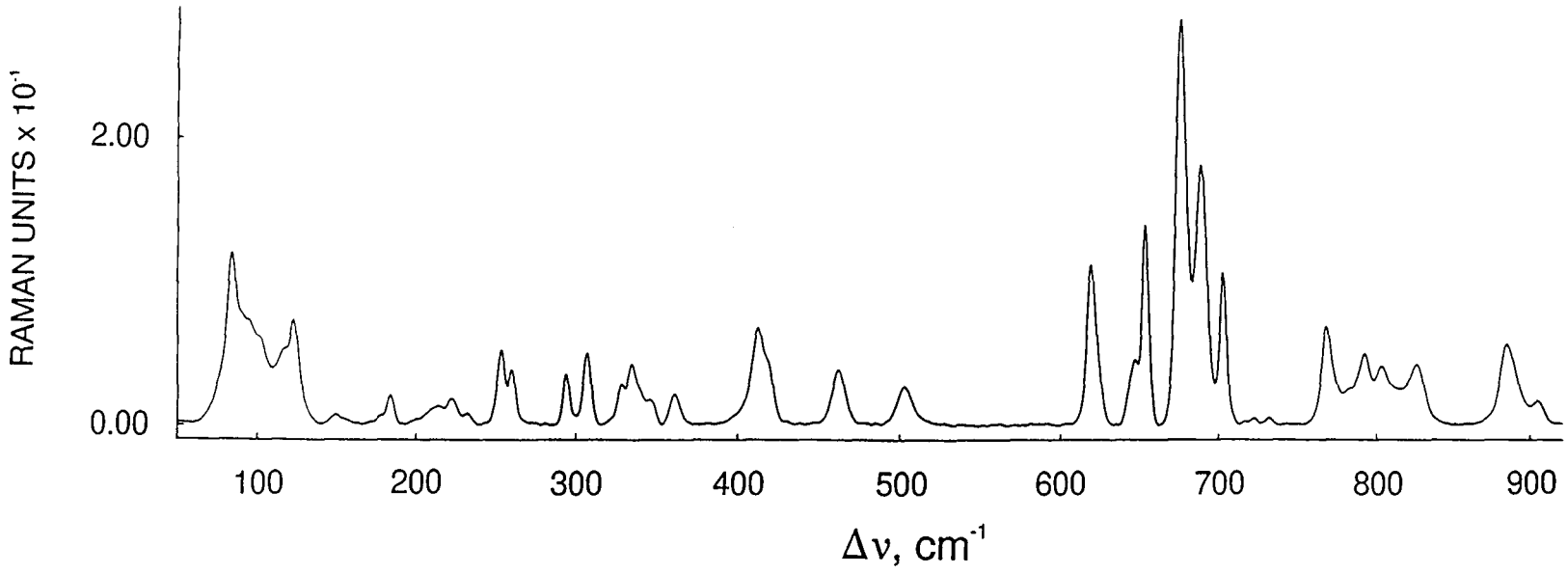

Figure 6.5 Raman spectrum of microcrystalline $N(CH_2CH_3)_4^+As(OTeF_5)_4^-$ recorded in 5-mm glass NMR tubes at -166 °C using 1064-nm excitation. The high-frequency bands of the $N(CH_2CH_3)_4^+$ cation are not shown but are listed in Table 6.1.

Table 6.1 Experimental Vibrational Frequencies, Assignments, and Mode Descriptions for $N(CH_3)_4^+Sb(OTeF_5)_4^-$, $N(CH_2CH_3)_4^+Sb(OTeF_5)_4^-$, $N(CH_3)_4^+As(OTeF_5)_4^-$, and $N(CH_2CH_3)_4^+As(OTeF_5)_4^-$.

freq, cm^{-1}					assignments	
$N(CH_3)_4^+Sb(OTeF_5)_4^-$		$N(CH_2CH_3)_4^+$ $Sb(OTeF_5)_4^-$	$N(CH_3)_4^+$ $As(OTeF_5)_4^-$	$N(CH_2CH_3)_4^+$ $As(OTeF_5)_4^-$		
solid[a]	solution[b]	solid[a,e]	solid[c]	solid[d,e]	cation	anion
3052 (10)			3062 (8)		$\nu_5(E)$, $\nu_{as}(CH_3)$;	
3044 (8), sh	3040 (1)		3050 (29)		$\nu_{13}(T_2)$, $\nu_{as}(CH_3)$	
			3043 (20), sh			
				3023 (6), sh	$\nu_1(A_1)$, $\nu_s(CH_3)$	
2991 (16)	3003 (5)	3004 (15)	2991 (54)	3003 (21)		
		2994 (12), sh				
			2970 (7), sh		$\nu_{14}(T_2)$, $\nu_{as}(CH_3)$	
2965 (5)		2966 (10)	2965 (15)	2967 (10)		
2932 (9)	2943 (100)	2951 (14)	2932 (32)	2951 (20)	$2\nu_6(E)$, $2\nu_2(A_1)$	
				2921 (3)	e	
2905 (2)		2901 (4)		2901 (4)		
	2879 (<1)	2880 (1)	2874 (4)	2879 (1)	$\nu_6(E)$, $\nu_{16}(T_2)$	
2827 (4)	2858 (3)		2826 (12)		$2\nu_{16}(T_2)$	
	2843 (<1)					

Table 6.1 (continued)

		2774 (1)		2774 (1)	e
		2755 (<1)		2756 (1)	
	2732 (3)				
			2477 (12)		
				2330 (1)	
	2293 (5)		2228 (15)		
	2252 (51)				
	2204 (<1)				
	2083 (<1)				
			2027 (23)		
		1491 (3)		1493 (3)	
				1479 (2)	
1453 (27)	1452 (2)	1464 (24)	1453 (33)	1463 (21)	$\nu_2(A_1)$, $\delta(CH_3)$;
		1446 (2)		1441 (1)	$\nu_6(E)$, $\delta_{as}(CH_3)$
1422 (4)	1409 (1)	1407 (2)	1422 (5)	1403 (2)	$\nu_{16}(T_2)$, $\delta_{as}(CH_3)$
		1391 (4)		1391 (3)	e
	1374 (5)			1378 (1)	
1301 (3)		1300 (11)	1290 (4)	1298 (10)	$\nu_{17}(T_2)$,$\delta_{rock}(CH_3)$
1293 (3)					
1170 (4)		1176 (5)	1170 (6)	1177 (3)	$\nu_7(E)$, $\delta_{rock}(CH_3)$
		1120 (15)		1119 (12)	e
1069 (2)		1070 (5)		1071 (2)	

Table 6.1 (continued)

		998 (12)		1019 (1) 1000 (7) 994 (4), sh 986 (1), sh	$\nu_{18}(T_2)$, $\delta_{as}(CN_4)$	
953 (23)			953 (26)			
	919 (11)	902 (14) 895 (19), sh		905 (6)	e	
886 (29)	889 (<1)	888 (24) 869 (4)	886 (33)	885 (20)		
		845 (10), sh	840 (7), sh			
836 (12) 821 (20), sh	830 (2)	833 (22)	836 (14) 824 (15), sh	826 (15)		
817 (23)		821 (19)	818 (23)			
	800 (<1), sh	802 (11)	804 (6)	803 (10)		
799(9)		787 (14)	796 (9)	792 (18) 783 (9), sh	$\nu_3(A_1)$, $\nu_s(CN_4)$	
756 (22) 750 (11), sh	751 (2)		756 (22) 750 (12), sh	768 (24)		$\nu_1(A_1)$, ν(TeF)
728 (10) 724 (8), sh		723 (7)	728 (9)	732 (2) 722 (2)		f
712 (6)		713 (14) 709 (15)	711 (8)	716 (1)		
		700 (38)		703 (37)		
700 (80)		691 (61)	699 (82)			
690 (27)	687 (6)	687 (58)	689 (23)	689 (64)		

Table 6.1 (continued)

		679 (84), sh				$\nu_2(A_1)$,
679 (100)	674 (4)	674 (100)	679 (100)	677 (100)		$\nu_s(TeF_4)$
669 (52)		668 (49), sh	669 (47)			f
646 (65)	636 (2)	646 (42)	646 (67)	654 (49)		$\nu_5(B_1)$, $\nu_{as}(TeF_4)$
638 (22), sh		637 (22), sh	639 (19), sh	647 (16)		f
626 (13), sh		623 (27)	626 (12), sh			
619 (18)	617 (1)	611 (10)	619 (16)	619 (39)		
614 (10), sh			613 (7), sh			
596 (4)		601 (3)				
501 (3)				503 (10)		
463 (5)		463 (5)	464 (6)	462 (14)		
458 (5)		453 (5)	457 (7)		$\nu_{19}(T_2)$, $\delta(CN_4)$	
449 (5)		451 (5)	451 (6)			
443 (4)		441 (6)				$\nu_3(A_1)$,
425 (7)		421 (19), sh	426 (7)			ν(TeO)
416 (5), sh				418 (17), sh		coupled
410 (12)		416 (30)	410 (8)	412 (24)		with
392 (4)		392 (7)				ν(Pn-O)
375 (7)	380 (8)	379 (3)	374 (8)		$\nu_8(E)$, $\delta(CN_4)$	
367 (4)			367 (6)	361 (8)		
349 (9), sh		346 (11), sh	348 (9)	346 (6)		$\nu_9(E)$,
341 (25)	336 (<1)	337 (26)	339 (20)	334 (15)		$\delta(FTeF_4)$

Table 6.1 (continued)

329 (15)		332 (23), sh	328 (15)	328 (10)	$\nu_{10}(E)$,
322 (13)		320 (9)	323 (12), sh	321 (1), sh	$\delta(OTeF_4)$
308 (7)		311 (8), sh	309 (8)	306 (17)	$\nu_4(A_1)$,
301 (18)	300 (<1)	302 (21)	300 (16)		$\delta_s(FTeF_4)$
295 (18)		295 (15)	295 (19)	293 (12)	
				260 (13)	$\nu_7(B_2)$,
			248 (5), sh		$\delta_{sciss}(TeF_4)$
244 (20)		242 (18)	243 (18)	253 (18)	
234 (17)	236 (<1)	238 (19)	234 (15)	232 (3)	$\nu_{11}(E)$,
224 (12)		223 (7)	223 (10)	222 (7)	$\delta_{as}(TeF_4)$
		216 (6)		213 (4)	
		205 (3)	187 (5)	199 (2), sh	
178 (11)		183 (10)	178 (15)	184 (7)	δ(TeOPn)
173 (20)	170 (3)	173 (11)	172 (18)	177 (3), sh	
		166 (10)			
		154 (9)	156 (4)	155 (2), sh	
152 (4)			151 (5)		
147 (6)			147 (7)	149 (3)	
123 (15)		121 (15)	122 (14)	122 (25)	
		111 (15)	108 (13), sh	116 (18), sh	lattice modes + τ(TeOPn)
106 (19)		108 (15)	106 (16)	102 (22), sh	
		91 (12)		94 (26), sh	
				90 (27), sh	
83 (28)		83 (35)		84 (42)	
73 (21)		71 (20)		75 (11), sh	

[a] Spectra were recorded on microcrystalline powders in 5-mm glass NMR tubes at -140 °C using 1064-nm excitation.

[b] Spectra were recorded in CH_3CN solvent in 5-mm glass NMR tubes at 30 °C using 1064-nm excitation.

[c] Spectra were recorded on microcrystalline powders in Pyrex capillaries at -140 °C using 1064-nm excitation.

[d] Spectra were recorded on microcrystalline powders in 5-mm glass NMR tubes at -166 °C using 1064-nm excitation.

[a-d] Values in parentheses denote relative intensities and sh denotes a shoulder.

[e] Bands associated with the $N(CH_2CH_3)_4^+$ cation cannot be assigned in all cases.

[f] Unassigned bands.

cell (factor group splitting). Moreover, it has not been possible to distinguish between the vibrational modes of the axial and equatorial $OTeF_5$ groups. The assignments of the frequencies of the $OTeF_5$ groups have been aided by comparison with the assignments for $N(CH_3)_4^+TeOF_5^-$,[171] for which *ab initio* calculations and a normal coordinate analysis confirm the correctness of the assignments, and with the assignments for F_5TeOF [191] and the $M(OTeF_5)_6^-$ (M = As, Sb, Bi)[107] anions. Assignments were made under C_{4v} symmetry for the $OTeF_5$ group which has 15 vibrations, $4A_1 \oplus 2B_1 \oplus B_2 \oplus 4E$, all of which are Raman active (A_1 and E are infrared active).

Modes corresponding to the Pn–O and Te–O stretching modes are expected to be intense in the Raman spectra and strongly vibrationally coupled as a result of the large masses of the Pn and Te atoms.[107] The assignments of these modes were aided by comparison with the strongly coupled and intense Pn–O, Xe–O, and Te–O stretching modes in the $Pn(OTeF_5)_6^-$ anions (Pn = As, Sb, Bi; 392-443 cm^{-1}),[107] $Xe(OTeF_5)_2$ (428, 442 cm^{-1}),[51] $FXeOTeF_5$ (457 cm^{-1}),[56] $XeOTeF_5^+$ (487 cm^{-1}),[53] and $Te(OTeF_5)_4$ (461 cm^{-1}).[112] The assignments of the Pn–O–Te bends have also been made by comparison with those of the $Pn(OTeF_5)_6^-$ anions (118-140 cm^{-1}),[107] $Xe(OTeF_5)_2$ (133 cm^{-1}),[51] $XeOTeF_5^+$ (174 cm^{-1}),[53] $Te(OTeF_5)_4$ (173 cm^{-1}),[112] and $Te(OTeF_5)_5^-$ (177 cm^{-1}) and are tentative.[112] The Pn–O–Te torsions are tentatively assigned to moderately intense low-frequency bands at 71-116 cm^{-1}.

The assignments for the $N(CH_3)_4^+$ cation are based on those for the free $N(CH_3)_4^+$ cation, which belongs to the point group T_d and has 19 fundamental vibrational bands,

$3A_1 \oplus A_2 \oplus 4E \oplus 4T_1 \oplus 7T_2$. Of these, the T_2 modes are infrared active and A_1, E, and T_2 modes are Raman active. Explicit assignments for the $N(CH_2CH_3)_4^+$ cation are not given but the frequencies are listed in Table 6.1 opposite related $N(CH_3)_4^+$ vibrational modes. The assignments of the $N(CH_3)_4^+$ cations in the present work are largely based upon a previous study by Kabisch[193] of the deviations of the Raman spectra of the free $N(CH_3)_4^+$ cation from the T_d selection rules in various salts of known crystal structures, providing empirical rules for estimating, from vibrational spectra, the degree of $N(CH_3)_4^+$ cation distortion.[107] It has been shown that a correlation exists between the degree of cation distortion and the position of the CH stretching band, $\nu_5(E)$, which varies in frequency from 3008 cm^{-1} for the most distorted $N(CH_3)_4^+$ cation in $N(CH_3)_4^+I^-$ to 3042 cm^{-1} for the least distorted case in $N(CH_3)_4^+ClO_4^-$.[107] Accordingly, it was concluded from the high-frequency positions of this line for all salts in the present work (3040-3062 cm^{-1}) that the distortion of the $N(CH_3)_4^+$ cations from tetrahedral symmetry was minimal.

The assignments for CH_3CN in the Raman spectrum of $N(CH_3)_4^+Sb(OTeF_5)_4^-$ recorded in CH_3CN solution at room temperature were made by comparison with the Raman spectrum and corresponding assignments for free CH_3CN.[194,195]

There are several bands in the Raman spectra of the $Pn(OTeF_5)_4^-$ salts that do not appear in the Raman spectra of $OTeF_5$ derivatives found in the literature. For the $N(CH_2CH_3)_4^+Pn(OTeF_5)_4^-$ salts, some of these bands may be attributed to the $N(CH_2CH_3)_4^+$ cation. Otherwise, the bands may occur from binary and combination bands which are normally expected to be weak in the Raman spectrum or they may be attributed to the impurity $F_5TeOTeF_5$ (*vide infra*).

Characterization of the $Pn(OTeF_5)_4^-$ (Pn = Sb, As) Anions in Solution by ^{125}Te and ^{19}F NMR Spectroscopy

The ^{125}Te and ^{19}F NMR spectra of the $Pn(OTeF_5)_4^-$ (M = Sb, As) anions as their $N(CH_3)_4^+$ salts in CH_3CN at -40 °C are shown in Figures 6.6 and 6.7, and their NMR parameters are listed in Tables 6.2 and 6.3. The labels, A and B, denote axial and equatorial groups, respectively. The ^{125}Te NMR spectra display a doublet-of-quintets arising from ^{125}Te-^{19}F spin-spin coupling. The ^{19}F NMR spectra reveal a single second order AB_4 pattern, in which the A and B parts are well-separated from each other and their ^{125}Te satellites. The AB_4 patterns are characteristic of $OTeF_5$ derivatives with chemical shifts and $^2J(^{19}F_A$-$^{19}F_B)$ values falling within the range for other $OTeF_5$ derivatives. In the ^{19}F NMR spectrum of the $As(OTeF_5)_4^-$ anion (Figure 6.7b), the ^{125}Te satellites (labeled b) overlap with the A part. Although the ^{125}Te satellites in the ^{19}F NMR spectrum of $Sb(OTeF_5)_4^-$ are better resolved, the A part is noticeably broader such that the transition is obscured (Figure 6.6b). At room temperature, the lines in this region of the ^{19}F NMR spectrum of $Sb(OTeF_5)_4^-$ become narrower and significantly more resolved (Figure 6.6c).

The valence-shell electron-pair repulsion (VSEPR) model[13] predicts that the $Pn(OTeF_5)_4^-$ anions should be based upon a trigonal bipyramidal arrangement of four bond pairs and an electron lone pair with two axial and two equatorial $OTeF_5$ groups, as in the core of the isovalent $Te(OTeF_5)_4$ molecule.[112] The observation of only one AB_4 pattern in the ^{19}F NMR spectra and one doublet-of-quintet pattern in the ^{125}Te NMR

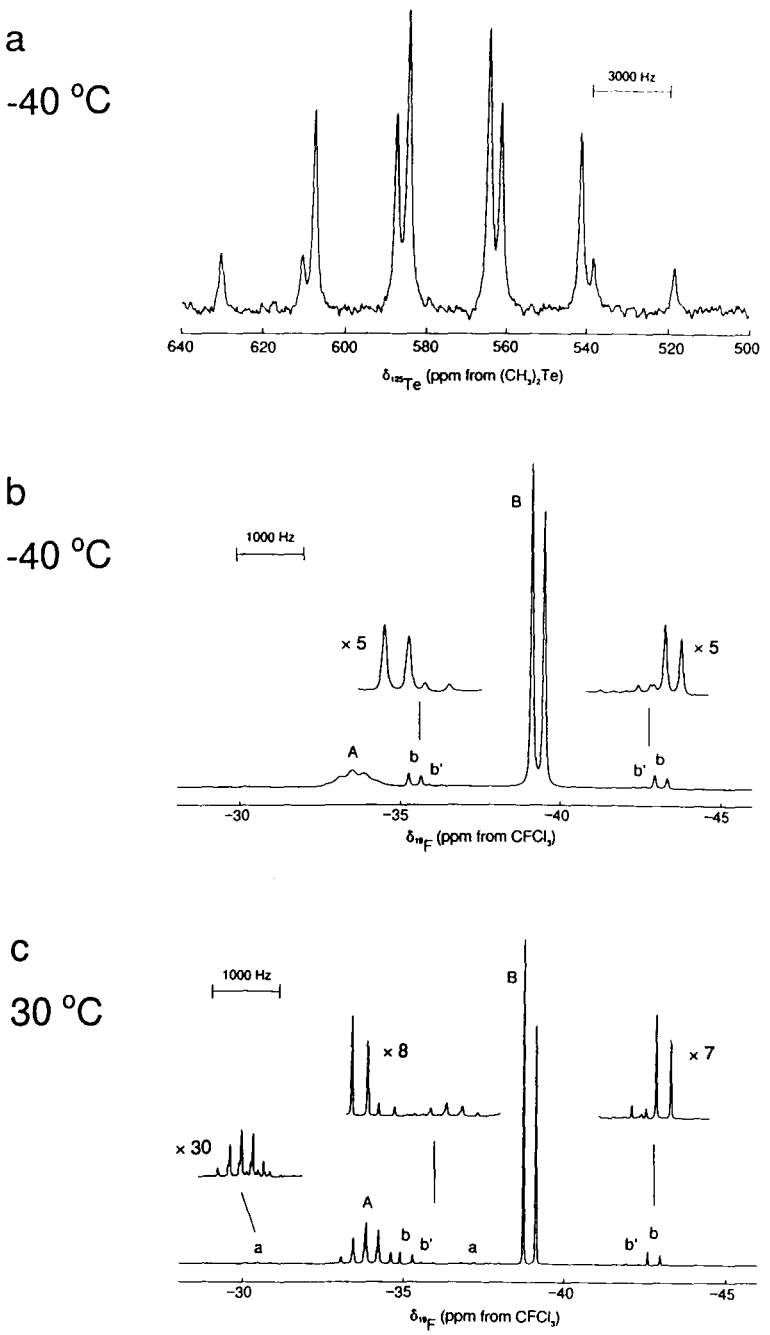

Figure 6.6 NMR spectra of $N(CH_3)_4^+Sb(OTeF_5)_4^-$ in CH_3CN: (a) ^{125}Te (157.790 MHz), recorded at -40 °C; (b) ^{19}F (470.592 MHz), recorded at -40 °C; (c) ^{19}F 470.592 MHz), recorded at 30 °C. A and B denote the axial and equatorial $OTeF_5$ groups, respectively, a and b indicate satellites resulting from the couplings $^1J(^{19}F_A\text{-}^{125}Te)$ and $^1J(^{19}F_B\text{-}^{125}Te)$, respectively, primes denote ^{123}Te satellites where they can be observed, and asterisks, *, denote impurities.

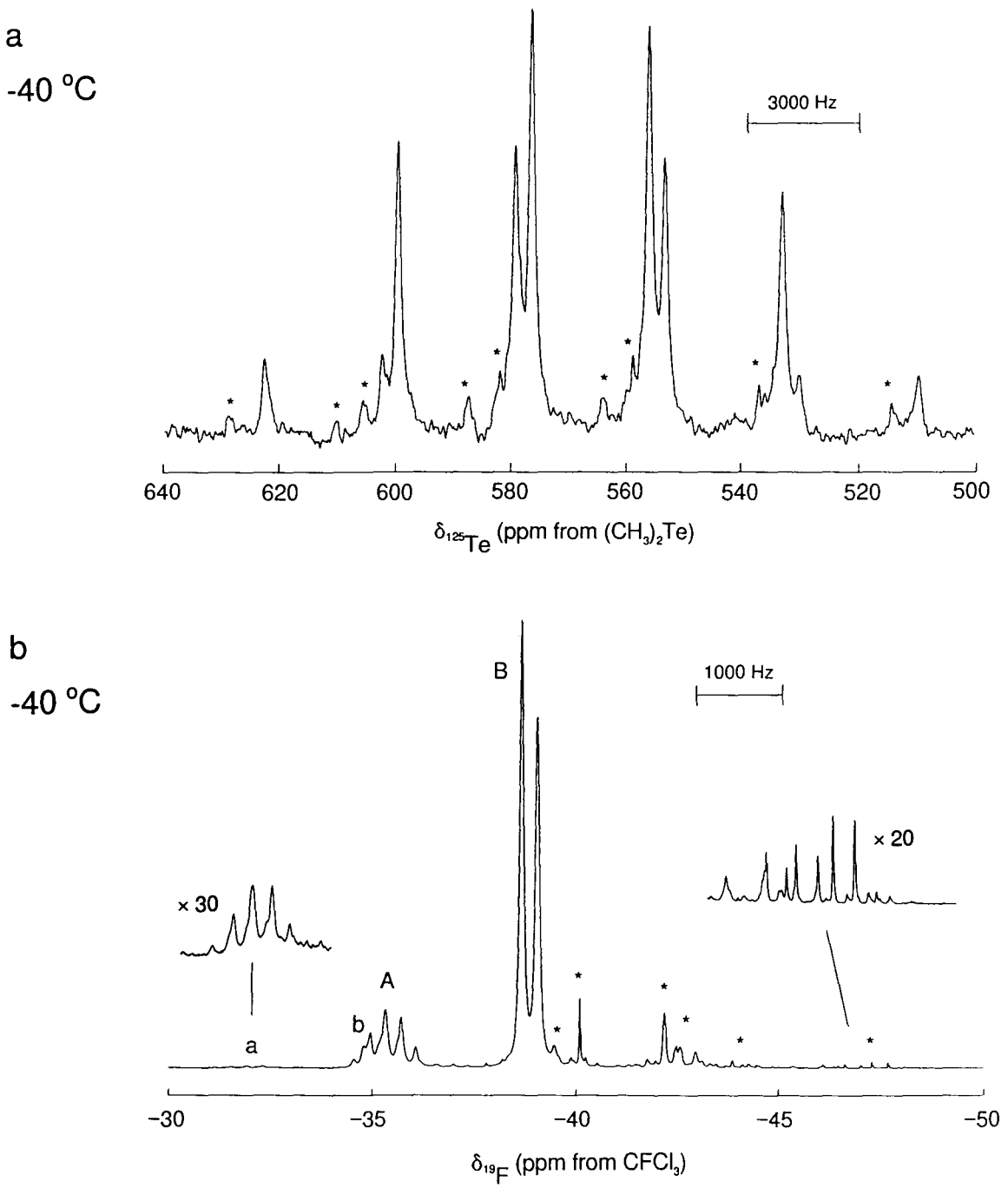

Figure 6.7 NMR spectra of $N(CH_3)_4^+As(OTeF_5)_4^-$ in CH_3CN: (a) ^{125}Te (157.790 MHz), recorded at -40 °C; (b) ^{19}F (470.592 MHz), recorded at -40 °C. A and B denote the axial and equatorial $OTeF_5$ groups, respectively, a and b indicate satellites resulting from the couplings $^1J(^{19}F_A\text{-}^{125}Te)$ and $^1J(^{19}F_B\text{-}^{125}Te)$, respectively, and asterisks, *, denote impurities.

Table 6.2 ^{19}F and ^{125}Te NMR Chemical Shifts for the $Pn(OTeF_5)_4^-$ (Pn = Sb, As) Anions.[a]

Compound	Solvent	Chemical Shifts (ppm)			T (°C)
		$\delta(^{19}F)_A$	$\delta(^{19}F)_B$	$\delta(^{125}Te)$	
$N(CH_3)_4^+Sb(OTeF_5)_4^-$	CH_3CN	-33.4	-39.3	574.5	-40
		-33.8	-38.9	c	30
$N(CH_3)_4^+As(OTeF_5)_4^-$	CH_3CN	-35.4	-38.9	566.1	-40
$N(CH_2CH_3)_4^+Sb(OTeF_5)_4^-$	SO_2ClF	b	-38.7	572.2	-122.5
		-35.4	-38.7	572.6	-85
		-36.6	-38.4	574.0	30
$N(CH_2CH_3)_4^+As(OTeF_5)_4^-$	SO_2ClF	b	~-38.3	~575/585[b]	-120
		-37.3	-38.6	567.3	-82.8

[a] ^{19}F (470.592 MHz) and ^{125}Te (157.790 MHz) NMR spectra of the samples were recorded in 5-mm medium-walled glass NMR tubes.

[b] Resonances are overlapping with ^{125}Te satellites and are not reported.

[c] ^{125}Te NMR spectrum were not acquired because the sample undergoes slow decomposition at room temperature.

Table 6.3 ^{19}F and ^{125}Te NMR Spin-Spin Coupling Constants for the $Pn(OTeF_5)_4^-$ (Pn = Sb, As) Anions.[a]

Compound	Solvent	Coupling Constants (Hz)					T (°C)
		$^2J(^{19}F_A - ^{19}F_B)$	$^1J(^{19}F_A - ^{125}Te)$	$^1J(^{19}F_B - ^{125}Te)$	$^1J(^{19}F_A - ^{123}Te)$	$^1J(^{19}F_B - ^{123}Te)$	
$N(CH_3)_4^+Sb(OTeF_5)_4^-$	CH_3CN	182	3155	3634	b	3015	-40
		180	3163	3627	2625	3009	30
$N(CH_3)_4^+As(OTeF_5)_4^-$	CH_3CN	181	3220	3661	b	b	-40
$N(CH_2CH_3)_4^+$	SO_2ClF	164	b	3608	b	2917	-122.5
$Sb(OTeF_5)_4^-$		175	3239	3617	b	~3160	-85
		163	3260	3603	b	3162	30
$N(CH_2CH_3)_4^+$	SO_2ClF	b	b	b	b	b	-120
$As(OTeF_5)_4^-$		159	3306	3650	b	b	-82.8

[a] ^{19}F (470.592 MHz) and ^{125}Te (157.790 MHz) NMR spectra of the samples were recorded in 5-mm medium-walled glass NMR tubes.

[b] Resonances are too weak or are overlapping with other signals and are not reported.

spectra, rather than the two expected for a static trigonal bipyramidal structure, demonstrates that all of the $OTeF_5$ ligands have been rendered equivalent on the NMR time scale as the result of a relatively fast intramolecular exchange of $OTeF_5$ groups. Based on the trigonal bipyramidal model, the mechanism by which fluxionality occurs is likely that of the classical Berry pseudorotation involving a square-pyramidal C_{4v} transition state. This mechanism has previously been used to explain the observed exchange behavior of axial and equatorial ligands in the isovalent SF_4,[117-119] PF_4^-,[116] and $Te(OTeF_5)_4$ [115] molecules. For these species, the activation energy barrier to the intramolecular fluorine and teflate exchange processes was high enough that the exchange could be slowed down sufficiently on the NMR time scale to observe separate axial and equatorial environments. The broadened signal observed at -40 °C in the ^{19}F NMR spectrum of $Sb(OTeF_5)_4^-$ in CH_3CN (Figure 6.6b) indicates that this anion has a higher activation energy barrier to intramolecular exchange than $As(OTeF_5)_4^-$ making it the more suitable candidate for a variable temperature ^{19}F and ^{125}Te NMR study aimed at slowing down the fluxional process at low-temperature (*vide infra*).

The ^{125}Te and ^{19}F NMR spectra for the $Pn(OTeF_5)_4^-$ (Pn = Sb, As) anions have also been obtained in SO_2ClF solvent as their $N(CH_2CH_3)_4^+$ salts and their NMR parameters at several temperatures are given in Tables 6.2 and 6.3. The appearance of the spectra was found to be solvent dependent (Figures 6.8 – 6.11). The ^{19}F and ^{125}Te NMR spectra at temperatures above -85 °C display the expected AB_4 and doublet-of-quintet patterns, respectively, indicative of a fluxional AX_4E system. However, in SO_2ClF, the chemical shift difference between $^{19}F_A$ and $^{19}F_B$ is smaller ($\delta(\nu_{AB})_{avg}$ = 2.1

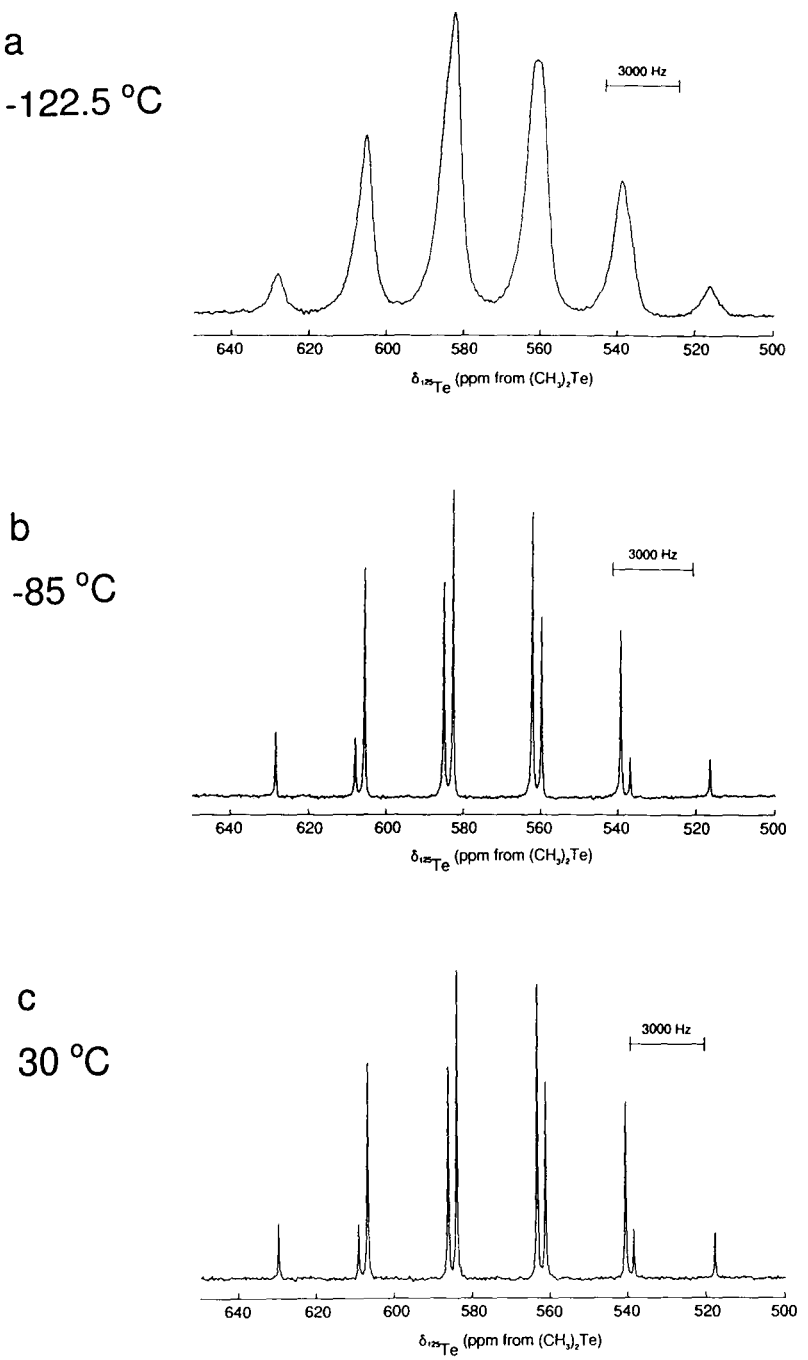

Figure 6.8 ^{125}Te NMR spectra (157.790 MHz) of $N(CH_2CH_3)_4^+Sb(OTeF_5)_4^-$ in SO_2ClF: (a) recorded at -122.5 °C; (b) recorded at -85 °C; (c) recorded at 30 °C.

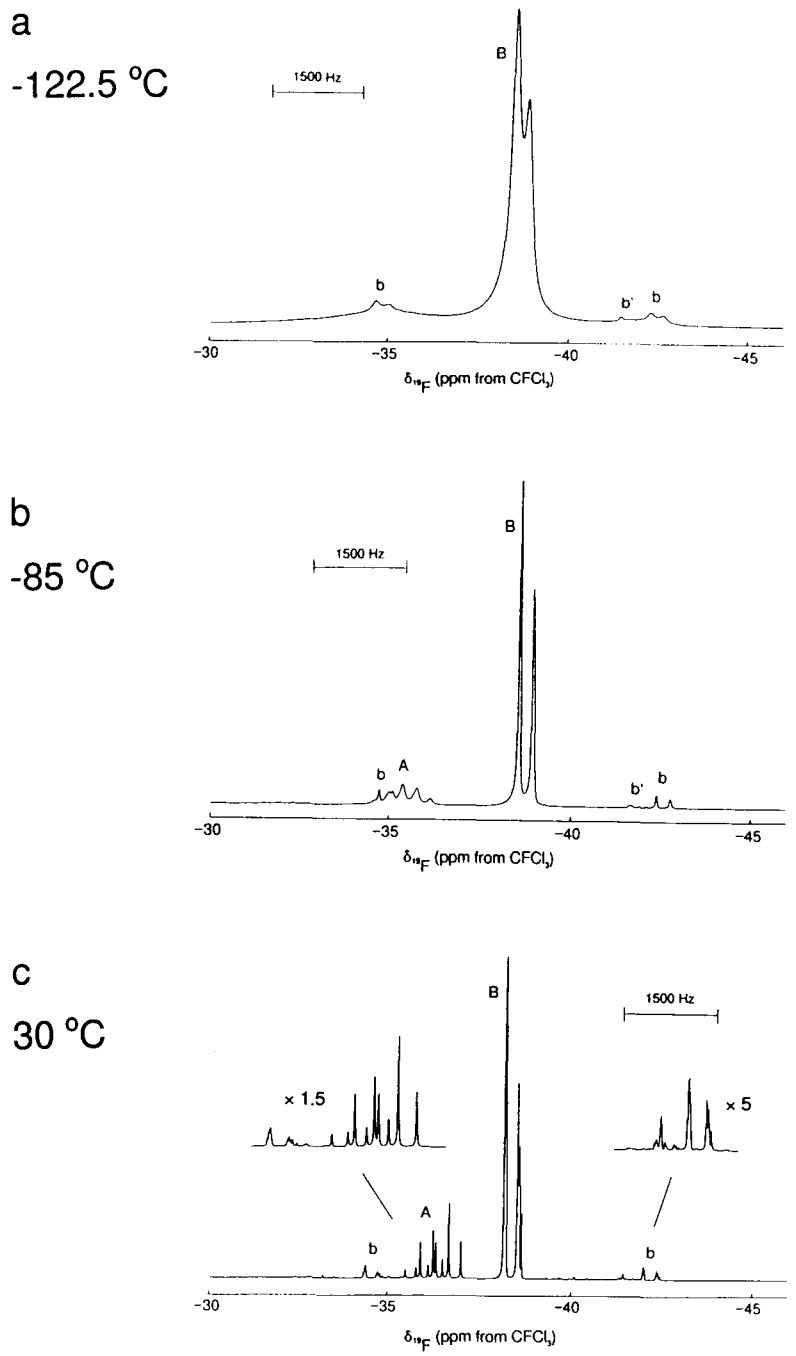

Figure 6.9 ^{19}F NMR spectra (470.592 MHz) of $N(CH_2CH_3)_4^+Sb(OTeF_5)_4^-$ in SO_2ClF: (a) recorded at -122.5 °C; (b) recorded at -85 °C; (c) recorded at 30 °C. A and B denote the axial and equatorial $OTeF_5$ groups, respectively, a and b indicate satellites resulting from the couplings $^1J(^{19}F_A\text{-}^{125}Te)$ and $^1J(^{19}F_B\text{-}^{125}Te)$, respectively, primes denote ^{123}Te satellites where they can be observed, and asterisks, *, denote impurities.

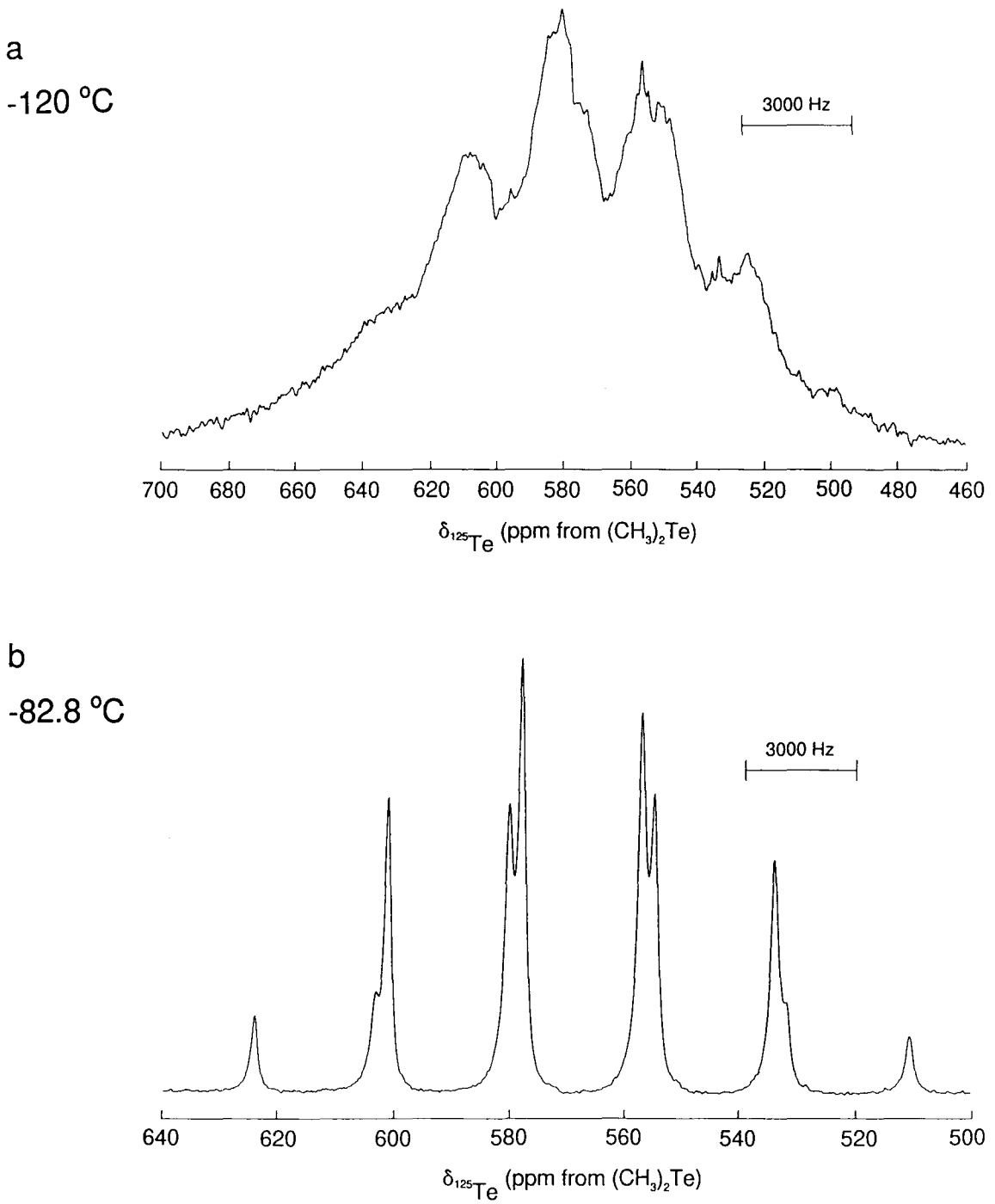

Figure 6.10 ^{125}Te NMR spectra (157.790 MHz) of $N(CH_2CH_3)_4^+As(OTeF_5)_4^-$ in SO_2ClF: (a) recorded at -120 °C; (b) recorded at -82.8 °C.

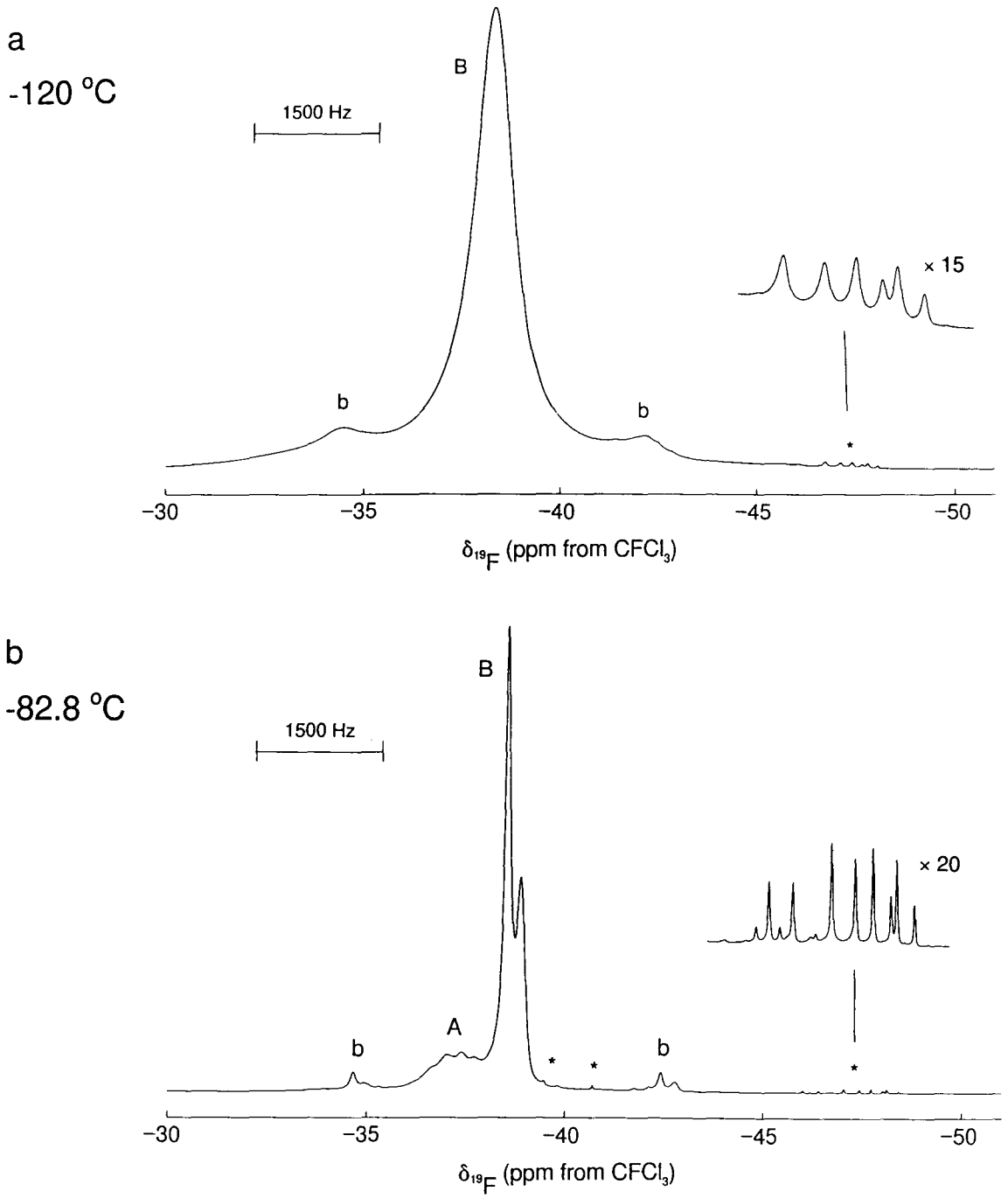

Figure 6.11 ^{19}F NMR spectra (470.592 MHz) of $N(CH_2CH_3)_4^+As(OTeF_5)_4^-$ in SO_2ClF: (a) recorded at -120 °C; (b) recorded at -82.8 °C. A and B denote the axial and equatorial $OTeF_5$ groups, respectively, a and b indicate satellites resulting from the couplings $^1J(^{19}F_A\text{-}^{125}Te)$ and $^1J(^{19}F_B\text{-}^{125}Te)$, respectively, and asterisks, *, denote impurities.

ppm) than in CH_3CN ($\delta(\nu_{AB})_{avg}$ = 4.8 ppm) and consequently the second-order effects are more severe. That is, the multiplets in the ^{125}Te NMR spectra have greater asymmetry and those in the ^{19}F NMR spectra exhibit additional second order splittings associated with the coupling of the AB_4 spin systems to $^{125,123}Te$. The smaller chemical shift difference is primarily due to a shift of $^{19}F_A$ to lower frequency with greater solvent polarity, while the chemical shift of $^{19}F_B$ is less affected. A similar effect is observed for the $Sb(OTeF_5)_6^-$ anion when dissolved in the same solvents.[107]

In contrast to the ^{125}Te and ^{19}F NMR spectra observed above -80 °C for the $Pn(OTeF_5)_4^-$ anions in SO_2ClF, the spectra at *ca.* -120 °C are very broad. The ^{19}F NMR spectra of the anions give rise to a single AB_4 pattern with the A part concealed beneath $^{125,123}Te$ satellites (Figures 6.9 and 6.11). The B_4 part of the spectrum for the $As(OTeF_5)_4^-$ anion is a single broad line, thereby indicating that the chemical shifts of F_A and F_B are overlapping at this temperature. The ^{125}Te NMR spectrum of the $As(OTeF_5)_4^-$ anion at this temperature (Figure 6.10) displays two sets of very broad overlapping pseudo-sextets, whereas the spectrum of $Sb(OTeF_5)_4^-$ (Figure 6.8) appears as a single, broad pseudo-sextet. The appearance of the AB_4 patterns in the ^{19}F NMR spectra and that of the doublet-of-quintets in the ^{125}Te NMR spectra indicate that the $Pn(OTeF_5)_4^-$ (Pn = Sb, As) anions are labile in SO_2ClF and are consistent with intramolecular exchange by means of a pseudorotation. The appearance of the spectra also suggest that the activation energy barrier to intramolecular exchange is much higher for the $As(OTeF_5)_4^-$ anion in SO_2ClF than for $Sb(OTeF_5)_4^-$ since the two chemically different $OTeF_5$ environments (*i.e.*, axial and equatorial) appear to coalesce at a higher temperature for the $As(OTeF_5)_4^-$

anion (≈ -120 °C) when compared to $Sb(OTeF_5)_4^-$ (<< -120 °C). Unfortunately, these barriers could not be determined below -124 °C; the freezing point of SO_2ClF.

In addition to the resonances attributed to the $Pn(OTeF_5)_4^-$ anions, other weak resonances were observed in the ^{19}F and ^{125}Te NMR spectra of the anions. In order to determine their origins, the ^{19}F and ^{125}Te NMR spectra of the synthetic precursors were recorded, namely $Pn(OTeF_5)_3$ (Pn = Sb, As) and $N(CH_2CH_3)_4^+OTeF_5^-$. The ^{19}F and ^{125}Te NMR parameters obtained for $As(OTeF_5)_3$ in SO_2ClF (Figure 6.12), and for $Sb(OTeF_5)_3$ (Figure 6.13) and $N(CH_2CH_3)_4^+OTeF_5^-$ (Figure 6.14) in CH_3CH_2CN, are given in Table 6.4. The ^{125}Te NMR spectra of these compounds display a single doublet-of-quintet pattern expected for the coupling of the ^{125}Te to the ^{19}F ligands. Each ^{19}F NMR spectrum reveals an AB_4 pattern and $^{125,123}Te$ satellites characteristic of the $OTeF_5$ group. The ^{19}F and ^{125}Te NMR chemical shifts and $^2J(^{19}F_A\text{-}^{19}F_B)$ values for these resonances are comparable to values reported in the literature for the $Pn(OTeF_5)_3$ and $N(CH_2CH_3)_4^+OTeF_5^-$ compounds, respectively.[107] However, in addition to the signals observed for $Sb(OTeF_5)_3$ and $As(OTeF_5)_3$, the ^{19}F and ^{125}Te NMR spectra of both compounds also reveal resonances attributable to $F_5TeOTeF_5$ [$\delta(^{19}F_A)$ = -47.9 ppm, $\delta(^{19}F_B)$ = -39.7 ppm, $\delta(^{125}Te)$ = 576.7 ppm, $^1J(^{19}F_A\text{-}^{19}F_B)$ = 182 Hz].[107] Several other weaker resonances were observed, but they could not be identified.

The resonances attributed to the $F_5TeOTeF_5$ impurity are significantly more intense in the ^{19}F and ^{125}Te NMR spectra of the $As(OTeF_5)_4^-$ anion as compared to those in the spectra of $Sb(OTeF_5)_4^-$. The presence of intense $F_5TeOTeF_5$ signals, as well as

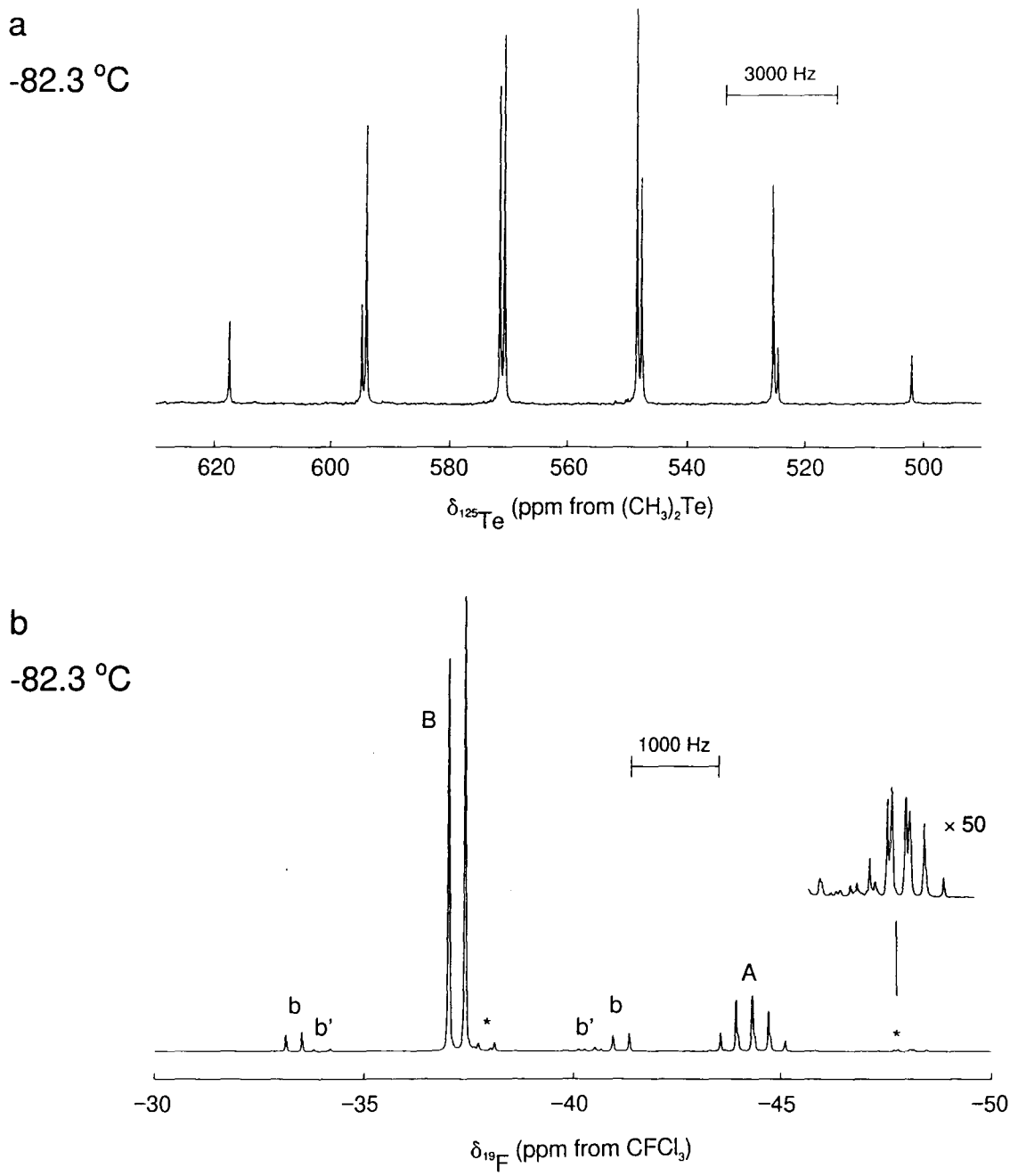

Figure 6.12 NMR spectra of $As(OTeF_5)_3$ in SO_2ClF: (a) ^{125}Te (157.790 MHz), recorded at -82.3 °C; (b) ^{19}F (470.592 MHz), recorded at -82.3 °C. A and B denote the axial and equatorial $OTeF_5$ groups, respectively, a and b indicate satellites resulting from the couplings $^1J(^{19}F_A\text{-}^{125}Te)$ and $^1J(^{19}F_B\text{-}^{125}Te)$, respectively, primes denote ^{123}Te satellites where they can be observed, and asterisks, *, denote impurities.

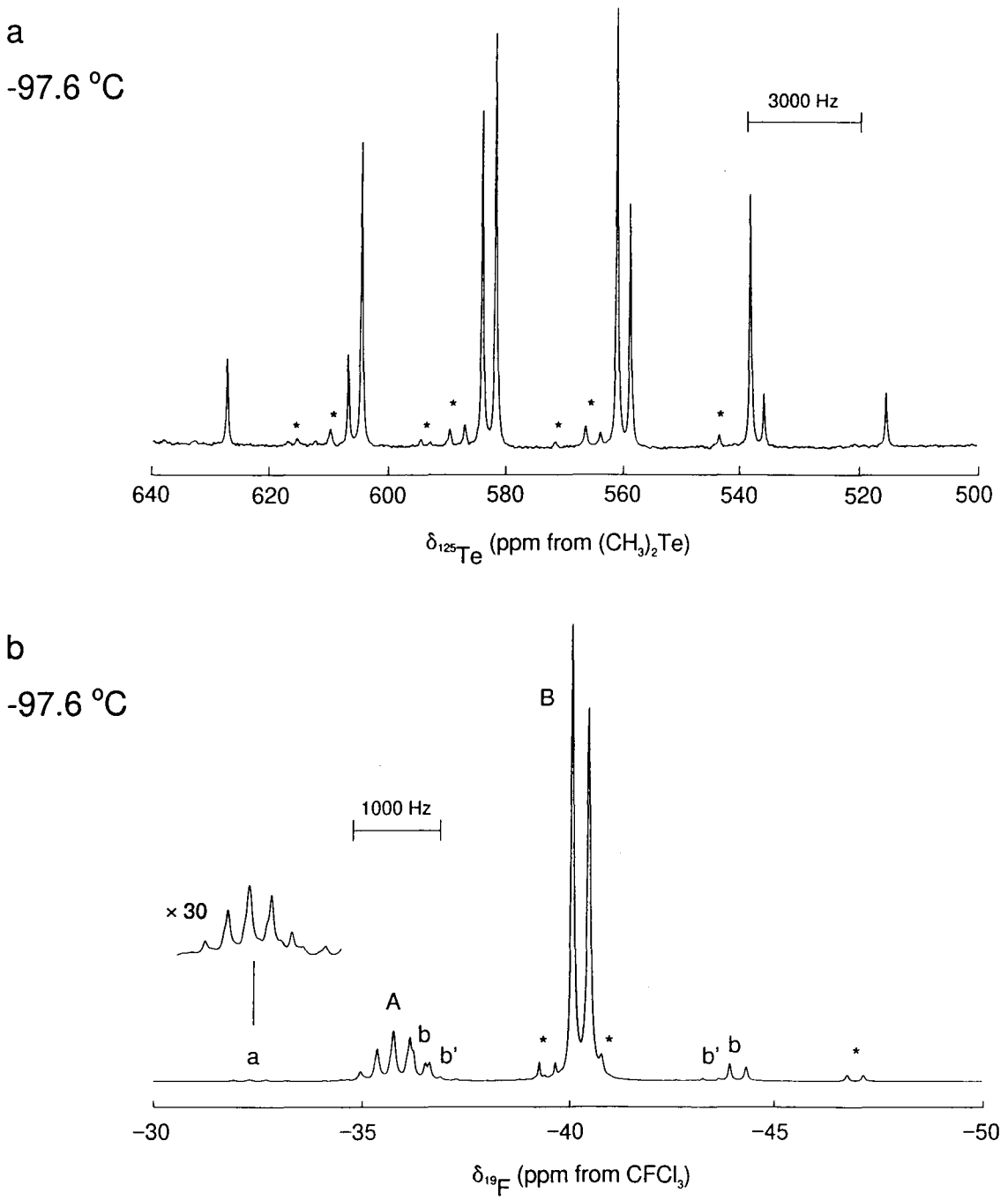

Figure 6.13 NMR spectra of $Sb(OTeF_5)_3$ in CH_3CH_2CN: (a) ^{125}Te (157.790 MHz), recorded at -97.6 °C; (b) ^{19}F (470.592 MHz), recorded at -97.6 °C. A and B denote the axial and equatorial $OTeF_5$ groups, respectively, a and b indicate satellites resulting from the couplings $^1J(^{19}F_A\text{-}^{125}Te)$ and $^1J(^{19}F_B\text{-}^{125}Te)$, respectively, primes denote ^{123}Te satellites where they can be observed, and asterisks, *, denote impurities.

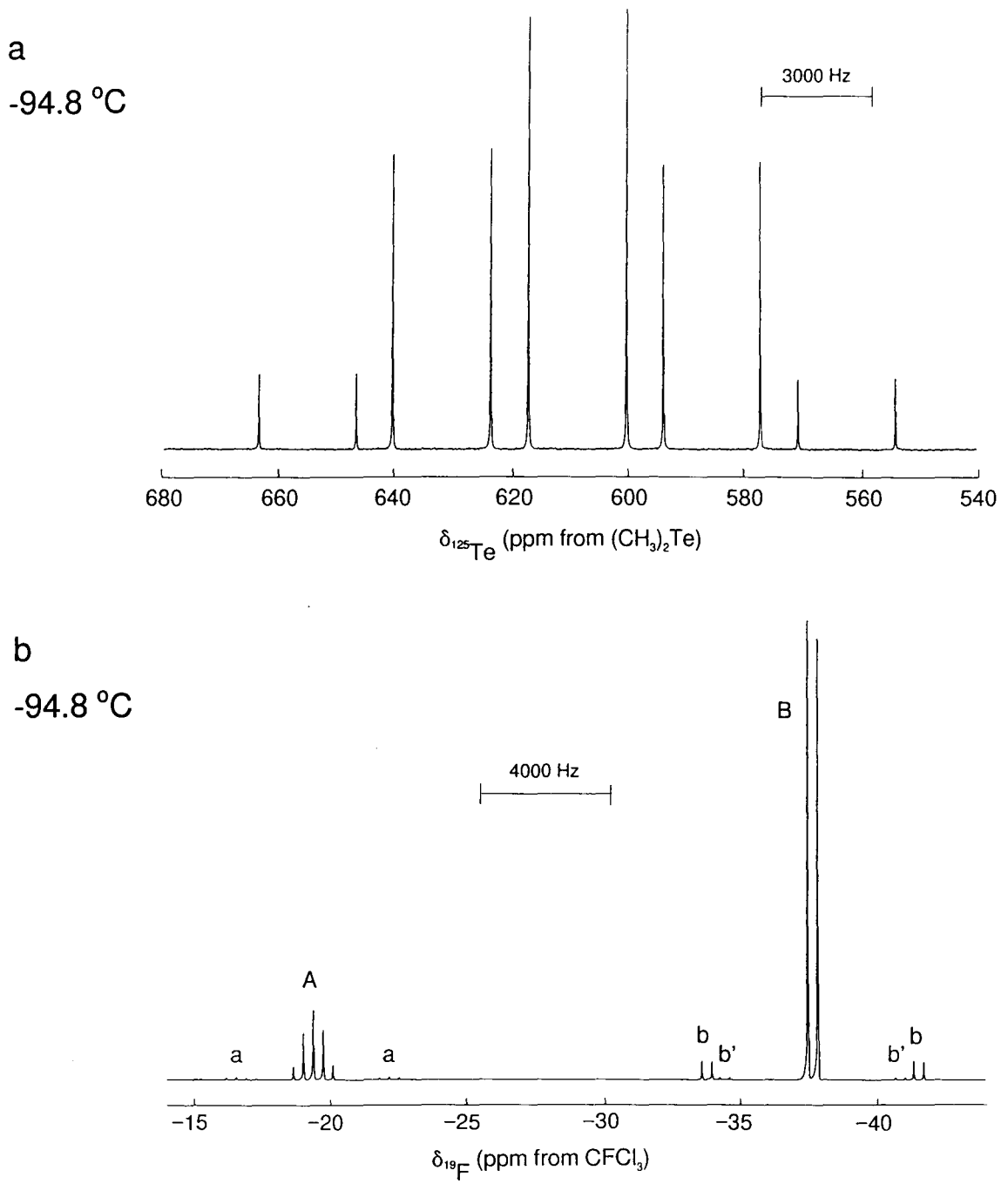

Figure 6.14 NMR spectra of $N(CH_2CH_3)_4^+OTeF_5^-$ in CH_3CH_2CN: (a) ^{125}Te (157.790 MHz), recorded at -94.8 °C; (b) ^{19}F (470.592 MHz), recorded at -94.8 °C. A and B denote the axial and equatorial $OTeF_5$ groups, respectively, a and b indicate satellites resulting from the couplings $^1J(^{19}F_A\text{-}^{125}Te)$ and $^1J(^{19}F_B\text{-}^{125}Te)$, respectively, and primes denote ^{123}Te satellites where they can be observed.

Table 6.4 ^{19}F and ^{125}Te NMR Parameters for the Starting Materials used in the Preparation of the $Pn(OTeF_5)_4^-$ (Pn = Sb, As) Anions.[a]

Chemical Shifts

Compound	Solvent	Chemical Shifts (ppm)			T (°C)
		$\delta(^{19}F)_A$	$\delta(^{19}F)_B$	$\delta(^{125}Te)$	
$As(OTeF_5)_3$	SO_2ClF	-44.3	-37.3	559.5	-82.3
$Sb(OTeF_5)_3$	CH_3CH_2CN	-35.8	-40.3	571.4	-97.6
$N(CH_2CH_3)_4^+OTeF_5-$	CH_3CH_2CN	-19.4	-37.7	608.7	-94.8

Coupling Constants

Compound	Solvent	Coupling Constants (Hz)					T (°C)
		$^2J(^{19}F_A-^{19}F_B)$	$^1J(^{19}F_A-^{125}Te)$	$^1J(^{19}F_B-^{125}Te)$	$^1J(^{19}F_A-^{123}Te)$	$^1J(^{19}F_B-^{123}Te)$	
$As(OTeF_5)_3$	SO_2ClF	182	2553	3676	b	2978	-82.3
$Sb(OTeF_5)_3$	CH_3CH_2CN	185	3251	3608	b	2991	-97.6
$N(CH_2CH_3)_4^+OTeF_5^-$	CH_3CH_2CN	171	2651	3659	b	3035	-94.8

[a] ^{19}F (470.592 MHz) and ^{125}Te (157.790 MHz) NMR spectra of the samples were recorded in 5-mm medium-walled glass NMR tubes.

[b] Resonances are too weak and are not reported.

other weaker signals, indicate that the $As(OTeF_5)_4^-$ anion is considerably less stable in solution than $Sb(OTeF_5)_4^-$ (*vide infra*).

Decomposition of $N(CH_2CH_3)_4^+As(OTeF_5)_4^-$ in SO_2ClF

The stepwise decomposition of $N(CH_2CH_3)_4^+As(OTeF_5)_4^-$ in SO_2ClF was studied in detail by ^{19}F and ^{125}Te NMR spectroscopy and the spectra are illustrated in Figures 6.15 and 6.16, respectively. The ^{19}F and ^{125}Te NMR data for the $As(OTeF_5)_4^-$ anion following decomposition are given in Tables 6.5 and 6.6, respectively. Spectra were recorded on the solution quenched at -82 °C after the solution was heated (≥ 30 °C) for varying periods of time. As the solution of $N(CH_2CH_3)_4^+As(OTeF_5)_4^-$ in SO_2ClF was heated, a new AB_4 pattern developed in the ^{19}F NMR spectrum and a doublet-of-quintets also grew in the ^{125}Te NMR spectrum with chemical shifts and coupling constants [$\delta(^{19}F_A) = -49.0$ ppm, $\delta(^{19}F_B) = -39.1$ ppm, $\delta(^{125}Te) = 571.7$ ppm, $^1J(^{19}F_A\text{-}^{19}F_B) = 182$ Hz] (Table 6.7) in good agreement with those reported in the literature for $F_5TeOTeF_5$ [$\delta(^{19}F_A) = -48.9$ ppm, $\delta(^{19}F_B) = -38.9$ ppm, $^1J(^{19}F_A\text{-}^{19}F_B) = 182$ Hz].[107] With continued heating of the sample, the spectral lines from the $F_5TeOTeF_5$ impurity intensified and several new signals appeared. The other impurities present in the sample could not be identified due to extensive spectral overlap and broadening, however, they may correspond to $O{=}As(OTeF_5)_2^-$, $O{=}AsOTeF_5$, or $OTeF_5^-$ produced as decomposition products according to equations (6.2) and (6.3). The percentage of the major impurity

$$As(OTeF_5)_4^- \longrightarrow O{=}As(OTeF_5)_2^- + F_5TeOTeF_5 \qquad (6.2)$$

Figure 6.15 ^{125}Te NMR spectra (157.790 MHz) of $N(CH_2CH_3)_4^+As(OTeF_5)_4^-$ in SO_2ClF recorded at -82 °C [30 °C for (f)] following decomposition: (a) 5 min at 30 °C + 5 min at 50 °C; (b) 5 min at 30°C + 35 min at 50 °C; (c) 5 min at 30°C + 95 min at 50 °C; (d) 5 min at 30 °C + 95 min at 50 °C + 60 min at 60 °C; (e) 5 min at 30 °C + 95 min at 50 °C + 300 min at 60 °C; (f) 5 min at 30°C + 95 min at 50 °C + 300 min at 60 °C.

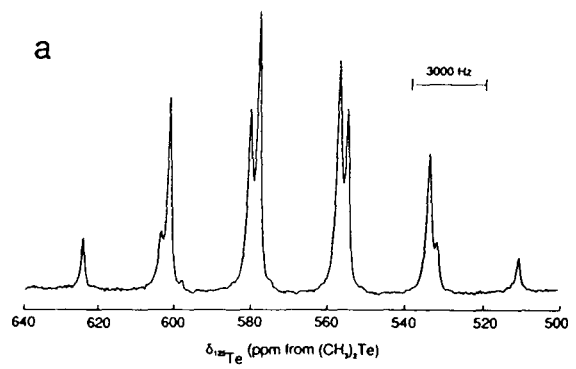
a
3000 Hz
640
620
600
580
560
540
520
500
δ125Te (ppm from (CH3)2Te)

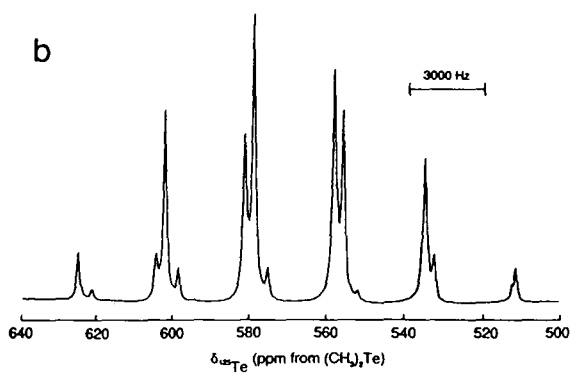
b
3000 Hz
640
620
600
580
560
540
520
500
δ125Te (ppm from (CH3)2Te)

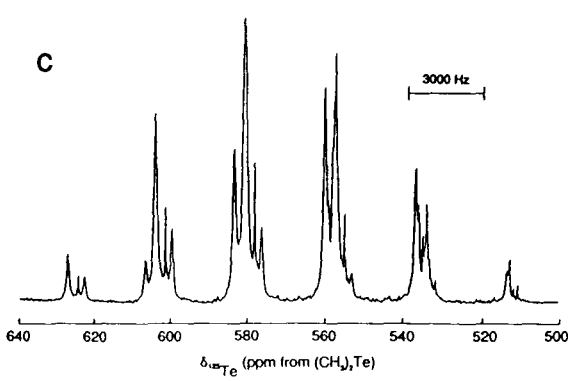
c
3000 Hz
640
620
600
580
560
540
520
500
δ125Te (ppm from (CH3)2Te)

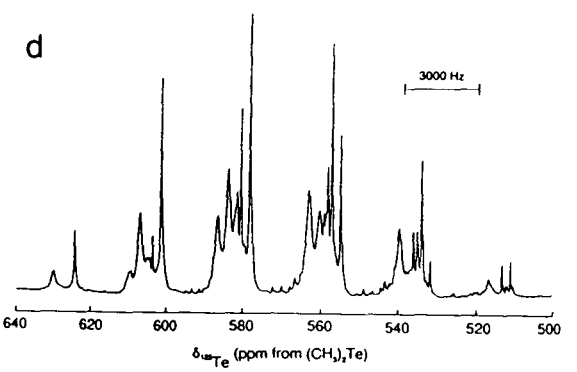
d
3000 Hz
640
620
600
580
560
540
520
500
δ125Te (ppm from (CH3)2Te)

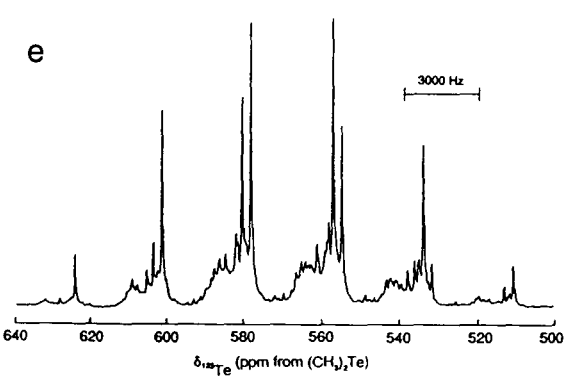
e
3000 Hz
640
620
600
580
560
540
520
500
δ125Te (ppm from (CH3)2Te)

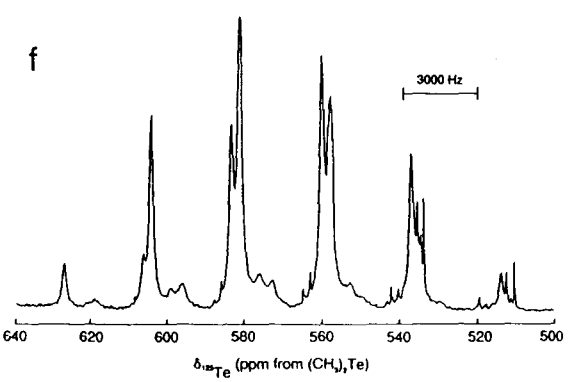
f
3000 Hz
640
620
600
580
560
540
520
500
δ125Te (ppm from (CH3)2Te)

Figure 6.16 ^{19}F NMR spectra (470.592 MHz) of $N(CH_2CH_3)_4^+As(OTeF_5)_4^-$ in SO_2ClF recorded at -82 °C [30 °C for (g)] following decomposition: (a) 5 min at 30 °C; (b) 5 min at 30 °C + 5 min at 50 °C; (c) 5 min at 30°C + 35 min at 50 °C; (d) 5 min at 30 °C + 95 min at 50 °C; (e) 5 min at 30 °C + 95 min at 50 °C + 60 min at 60 °C; (f) 5 min at 30°C + 95 min at 50 °C + 300 min at 60 °C; (g) 5 min at 30°C + 95 min at 50 °C + 300 min at 60 °C.

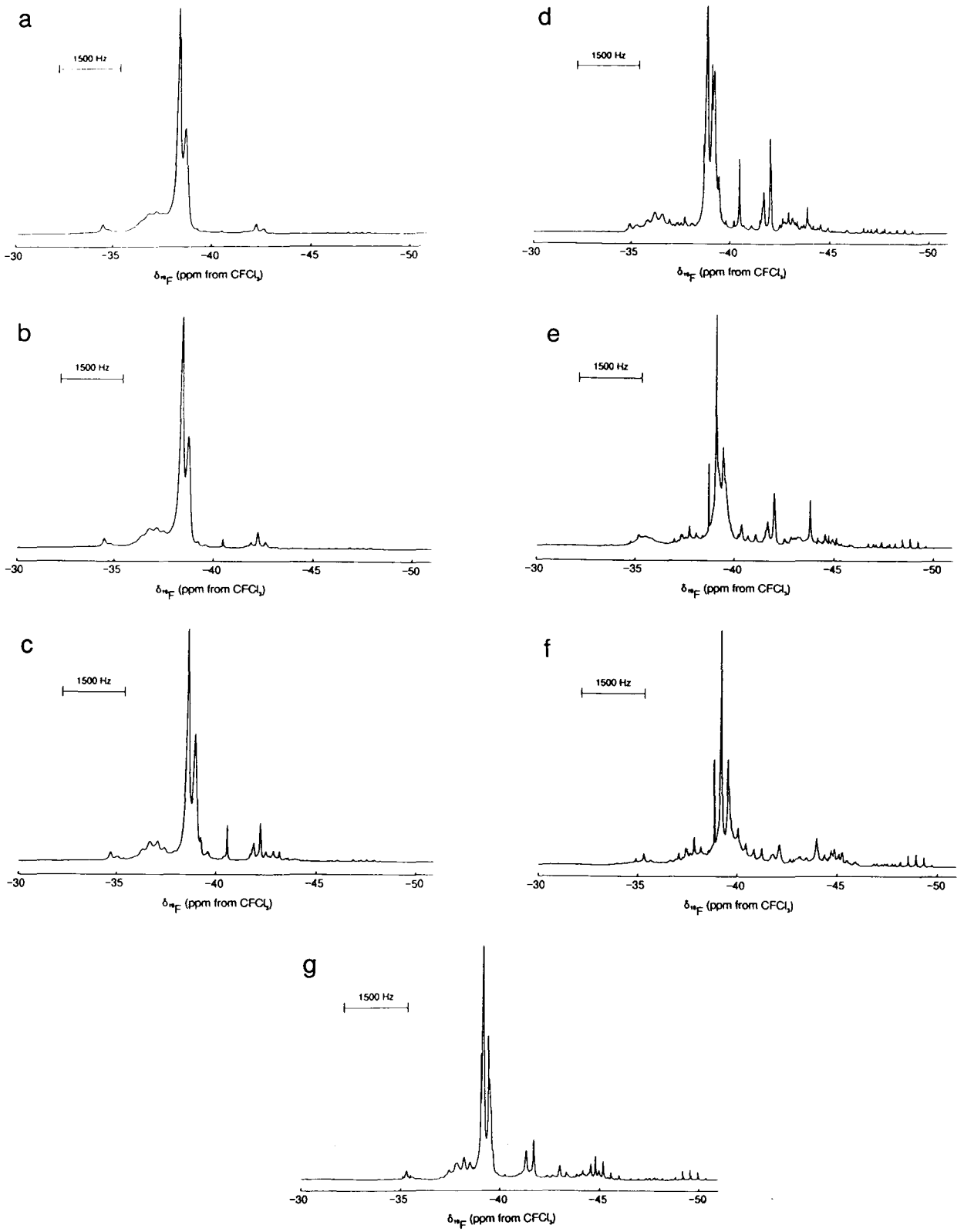
a
1500 Hz
-30
-35
-40
-45
-50
δ19F (ppm from CFCl3)
d
1500 Hz
-30
-35
-40
-45
-50
δ19F (ppm from CFCl3)
b
1500 Hz
-30
-35
-40
-45
-50
δ19F (ppm from CFCl3)
e
1500 Hz
-30
-35
-40
-45
-50
δ19F (ppm from CFCl3)
c
1500 Hz
-30
-35
-40
-45
-50
δ19F (ppm from CFCl3)
f
1500 Hz
-30
-35
-40
-45
-50
δ19F (ppm from CFCl3)
g
1500 Hz
-30
-35
-40
-45
-50
δ19F (ppm from CFCl3)

Table 6.5 ^{19}F and ^{125}Te NMR Chemical Shifts for $N(CH_2CH_3)_4^+As(OTeF_5)_4^-$ in SO_2ClF as a Function of Warming Time.[a]

Warming Time (Temp.) [min. (°C)]	Chemical Shifts (ppm)			T (°C) at which Spectrum was Acquired
	$\delta(^{19}F)_A$	$\delta(^{19}F)_B$	$\delta(^{125}Te)$	
5 (30)	-37.2	-38.5	b	-82
5 (30) + 5 (50)	-37.2	-38.6	567.5	-82
5 (30) + 35 (50)	-37.1	-38.8	568.3	-82
5 (30) + 95 (50)	~-37.0	-38.5	567.6	-82
5 (30) + 95 (50) + 60 (60)	~-37.8	-39.3	567.6	-82
5 (30) + 95 (50) + 300 (60)	-37.3	-39.4	567.4	-82
5 (30) + 95 (50) + 300 (60)	-38.2	-39.4	570.3	30

[a] ^{19}F (470.592 MHz) and ^{125}Te (157.790 MHz) NMR spectra of the samples were recorded in 5-mm medium-walled glass NMR tubes.

[b] ^{125}Te NMR spectrum was not acquired because the sample undergoes slow decomposition at room temperature.

Table 6.6 ^{19}F and ^{125}Te NMR Spin-Spin Coupling Constants for $N(CH_2CH_3)_4^+As(OTeF_5)_4^-$ in SO_2ClF as a Function of Warming Time. [a]

Warming Time (Temp.) [min. (°C)]	Coupling Constants (Hz)[b]			T (°C) at which Spectrum was Acquired
	$^2J(^{19}F_A - ^{19}F_B)$	$^1J(^{19}F_A - ^{125}Te)$	$^1J(^{19}F_B - ^{125}Te)$	
5 (30)	159	b	3654	-82
5 (30) + 5 (50)	158	3309	3653	-82
5 (30) + 35 (50)	166	3305	3661	-82
5 (30) + 95 (50)	~170	3299	3660	-82
5 (30) + 95 (50) + 60 (60)	159	3300	3655	-82
5 (30) + 95 (50) + 300 (60)	166	3303	3657	-82
5 (30) + 95 (50) + 300 (60)	~156	3310	3660	30

[a] ^{19}F (470.592 MHz) and ^{125}Te (157.790 MHz) NMR spectra of the samples were recorded in 5-mm medium-walled glass NMR tubes.

[b] The ^{123}Te satellites are too weak and are not observed. Consequently, $^1J(^{19}F_A - ^{123}Te)$ and $^1J(^{19}F_B - ^{123}Te)$ values are not reported.

[c] Resonance is too broad and is not reported.

Table 6.7 ^{19}F and ^{125}Te NMR Parameters for the $F_5Te–O–TeF_5$ Impurity Resulting from the Decomposition of $N(CH_2CH_3)_4^+As(OTeF_5)_4^-$ in SO_2ClF.[a]

Warming Time (Temp.) for Decomposition of $N(CH_2CH_3)_4^+As(OTeF_5)_4^-$ [min. (°C)][b]	Chemical Shifts (ppm)			Coupling Constants (Hz)			T (°C) at which Spectrum was Acquired
	$\delta(^{19}F)_A$	$\delta(^{19}F)_B$	$\delta(^{125}Te)$	$^2J(^{19}F_A - ^{19}F_B)$	$^1J(^{19}F_A - ^{125}Te)$	$^1J(^{19}F_B - ^{125}Te)$	
5 (30) + 35 (50)	-48.9	c	c	183	c	c	-82
5 (30) + 95 (50)	-48.7	-38.9	570.3	182	3277	3671	-82
5 (30) + 95 (50) + 60 (60)	-48.8	-38.9	573.3	183	3254	c	-82
5 (30) + 95 (50) + 300 (60)	-49.0	-39.1	571.4	180	c	c	-82
5 (30) + 95 (50) + 300 (60)	-49.6	-39.3	572.0	182	c	3704	30

[a] ^{19}F (470.592 MHz) and ^{125}Te (157.790 MHz) NMR spectra of the samples were recorded in 5-mm medium-walled glass NMR tubes.

[b] The $F_5TeOTeF_5$ impurity was not present after warming the sample of $N(CH_2CH_3)_4^+As(OTeF_5)_4^-$ in SO_2ClF for 5 min at 30 °C and for 5 min at 30 °C + 5 min at 50 °C.

[c] Resonances are too weak and are not reported.

$$As(OTeF_5)_4^- \longrightarrow O{=}AsOTeF_5 + OTeF_5^- + F_5TeOTeF_5 \qquad (6.3)$$

present in the sample, $F_5TeOTeF_5$, was determined from the relative intensities of the $^{19}F_A$ and ^{125}Te signals, as well as from a simulation of the ^{19}F and ^{125}Te NMR spectra at -82 °C following decomposition of the sample for 5 min at 30 °C + 95 min at 50 °C + 5 h at 60 °C (Figures 6.17 and 6.18). The calculated percentages given in Table 6.8 indicate that after almost 7 h of warming, the relative intensity of the $F_5TeOTeF_5$ impurity was *ca.* 45% that of the $As(OTeF_5)_4^-$ anion.

Exchange Dynamics of $N(CH_3)_4^+Sb(OTeF_5)_4^-$ in CH_3CH_2CN

Although the barrier to intramolecular exchange for the $Sb(OTeF_5)_4^-$ anion in CH_3CN appeared to be sufficiently high, based on the ^{19}F and ^{125}Te NMR spectra at -40 °C (*vide supra*), the exchange process could not be investigated below the freezing point of CH_3CN (-43.8 °C). Instead, variable-temperature ^{19}F and ^{125}Te NMR spectra of $N(CH_3)_4^+Sb(OTeF_5)_4^-$ were recorded in another polar solvent, CH_3CH_2CN, having a much lower freezing point (-92.8 °C; Figures 6.19 and 6.20). The qualitative changes in the multiplet patterns on cooling the temperature are analogous to those reported for $Te(OTeF_5)_4$.[115] The ^{19}F and ^{125}Te NMR spectra of $Sb(OTeF_5)_4^-$ in CH_3CH_2CN at -97.5 °C show two distinct $OTeF_5$ environments, as well as some overlapping unidentified resonances. Since the axial bonds in a trigonal bipyramid are generally somewhat longer than the equatorial bonds,[151] the Te–F bonds and magnitude of $^1J(^{19}F\text{-}^{125}Te)$ for the axial $OTeF_5$ groups should be smaller than for the equatorial $OTeF_5$ groups. An absolute assignment of the two different $OTeF_5$ environments could not be made,

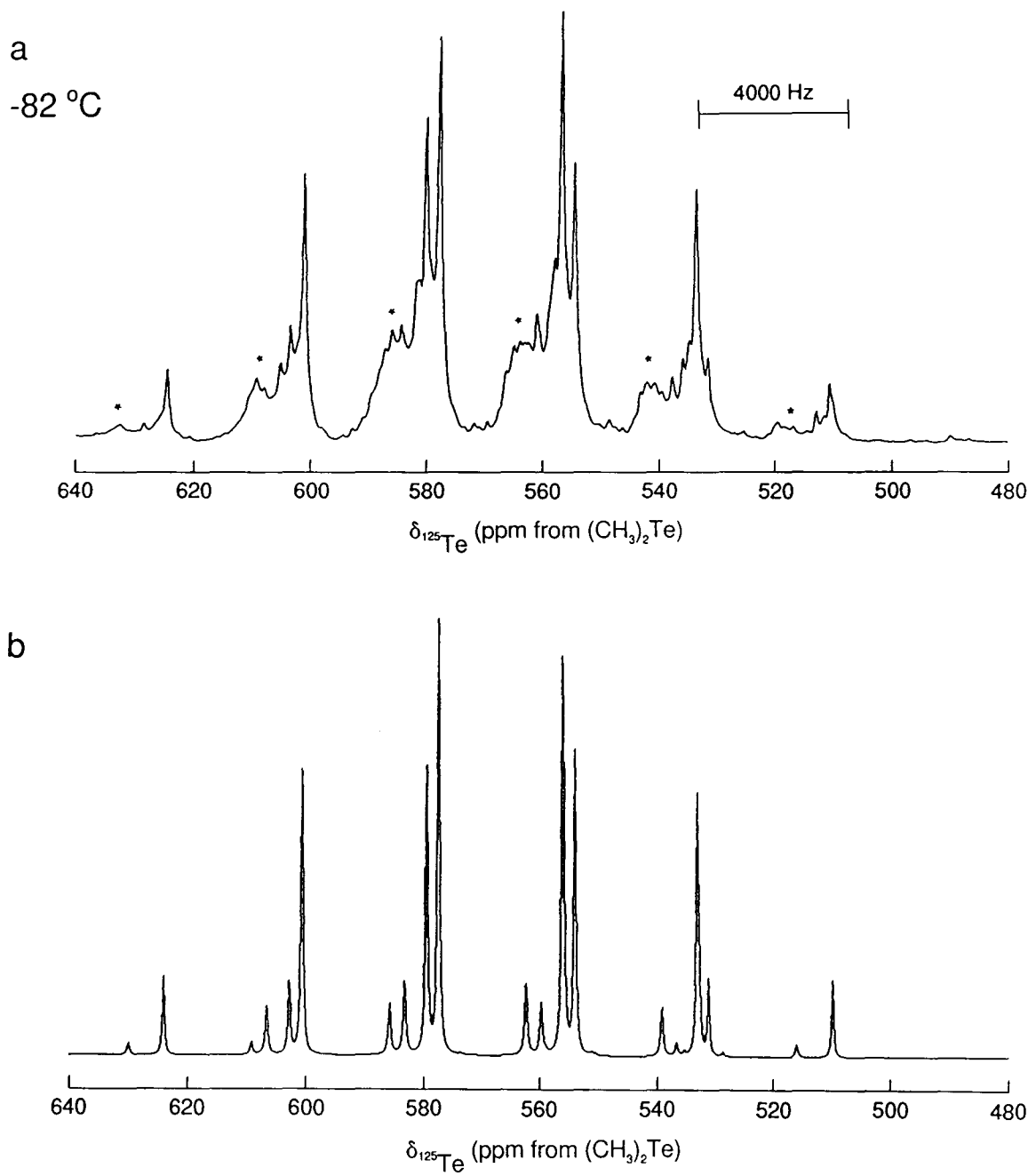

Figure 6.17 ^{125}Te NMR spectra (157.790 MHz) of $N(CH_2CH_3)_4^+As(OTeF_5)_4^-$ in SO_2ClF recorded at -82 °C following decomposition of the sample for 5 min at 30°C + 95 min at 50 °C + 300 min at 60 °C: (a) observed; (b) calculated. Percentage of $F_5TeOTeF_5$ impurity, denoted by *, is ~30 %.

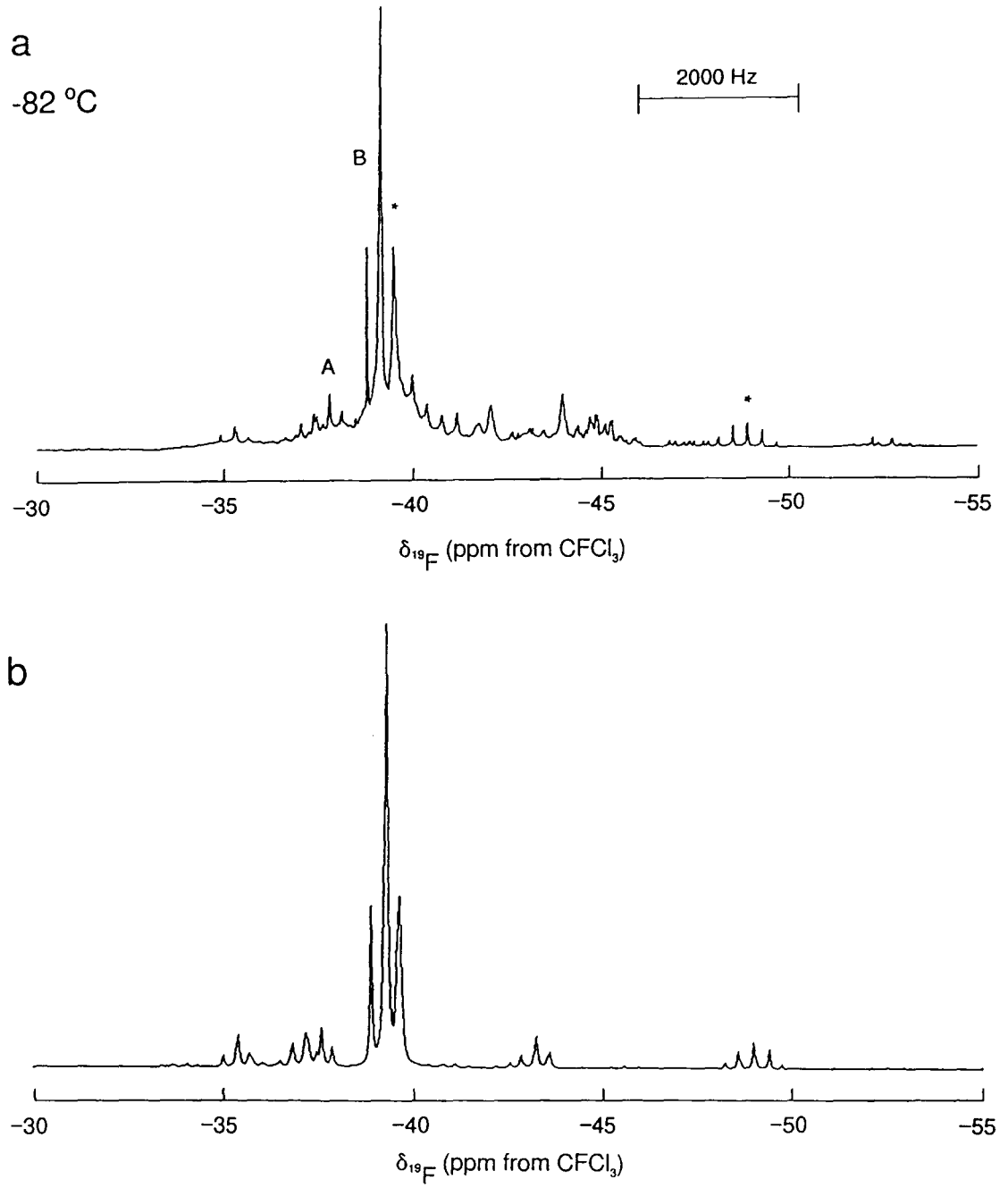

Figure 6.18 ^{19}F NMR spectrum (470.592 MHz) of $N(CH_2CH_3)_4^+As(OTeF_5)_4^-$ in SO_2ClF recorded at -82 °C following decomposition of the sample for 5 min at 30°C + 95 min at 50 °C + 300 min at 60 °C: (a) observed; (b) calculated. Percentage of $F_5TeOTeF_5$ impurity, denoted by *, is ~40 %.

Table 6.8 Percentage of $F_5TeOTeF_5$ Impurity Resulting from the Decomposition of $N(CH_2CH_3)_4^+As(OTeF_5)_4^-$ in SO_2ClF.

Time (Temp.) for Decomposition of $N(CH_2CH_3)_4^+As(OTeF_5)_4^-$ in SO_2ClF [min. (°C)]	T (°C) at which Spectrum was Acquired	Percentage of $F_5Te–O–TeF_5$ Impurity (%)[a]
5 (30) + 35 (50)	-82	3.4
5 (30) + 95 (50)	-82	21.5
5 (30) + 95 (50) + 60 (60)	-82	43.9 (46.8)[b]
5 (30) + 95 (50) + 300 (60)	-82	41.9 (41.2)[b] (30, 40)[c]
5 (30) + 95 (50) + 300 (60)	30	45.5

[a] Unless otherwise specified, the percentage of $F_5TeOTeF_5$ (X) in the sample of $As(OTeF_5)_4^-$ (Y) =

$$\frac{[\text{Relative Intensity at } \delta(^{19}F_A)_X/2]}{[(\text{Relative Intensity at } \delta(^{19}F_A)_X/2) + (\text{Relative Intensity at } \delta(^{19}F_A)_Y/4)]} \times 100\%$$

[b] Percentage of $F_5TeOTeF_5$ in the sample of $As(OTeF_5)_4^-$ was calculated as in a (above) but using relative intensities at $\delta(^{125}Te)$.

[c] Determined from (^{125}Te, ^{19}F) simulated NMR spectra.

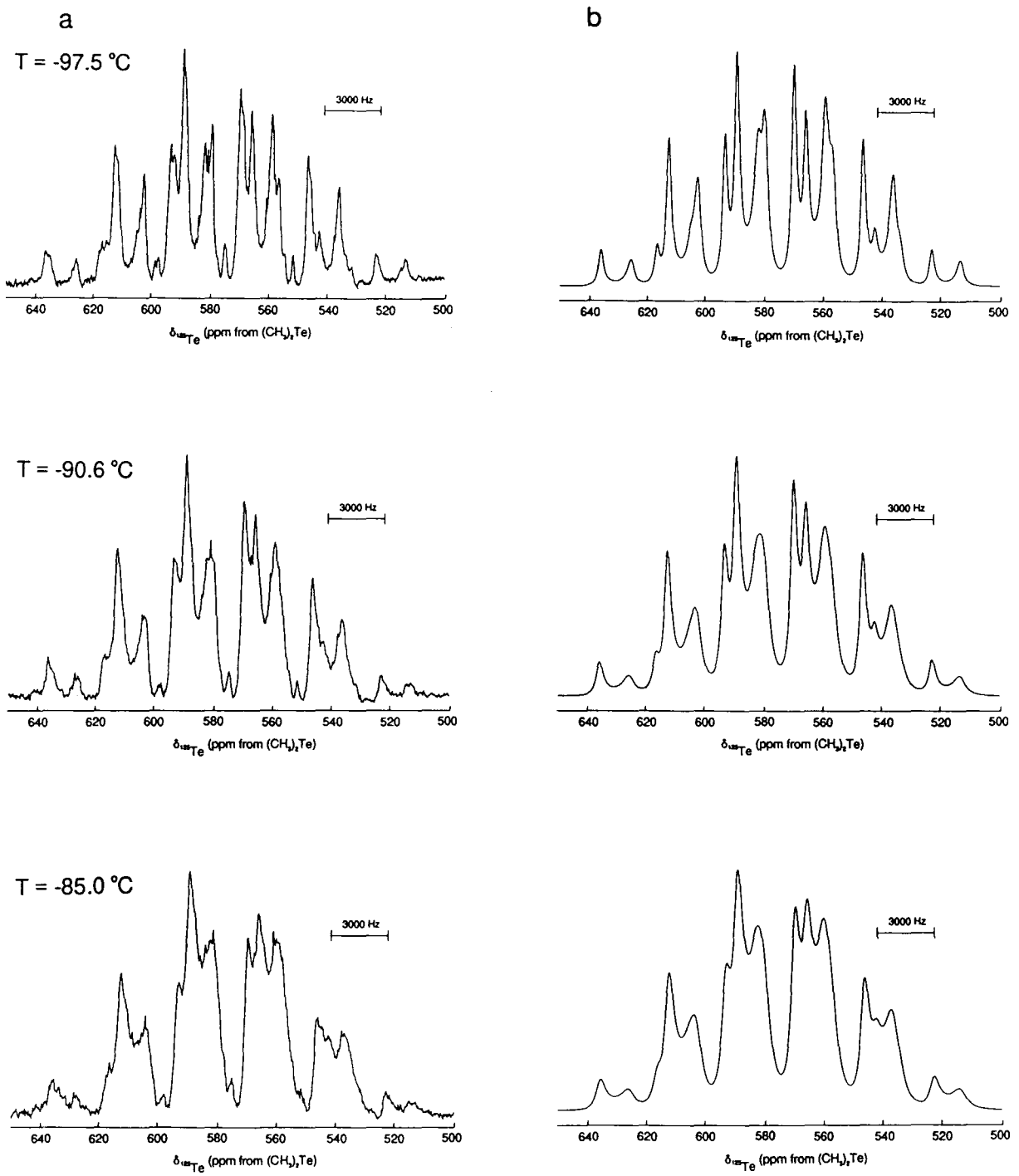

Figure 6.19 Variable-temperature ^{125}Te NMR spectra (157.790 MHz) of $N(CH_3)_4^+Sb(OTeF_5)_4^-$ in CH_3CH_2CN: (a) observed spectrum; (b) calculated spectrum.

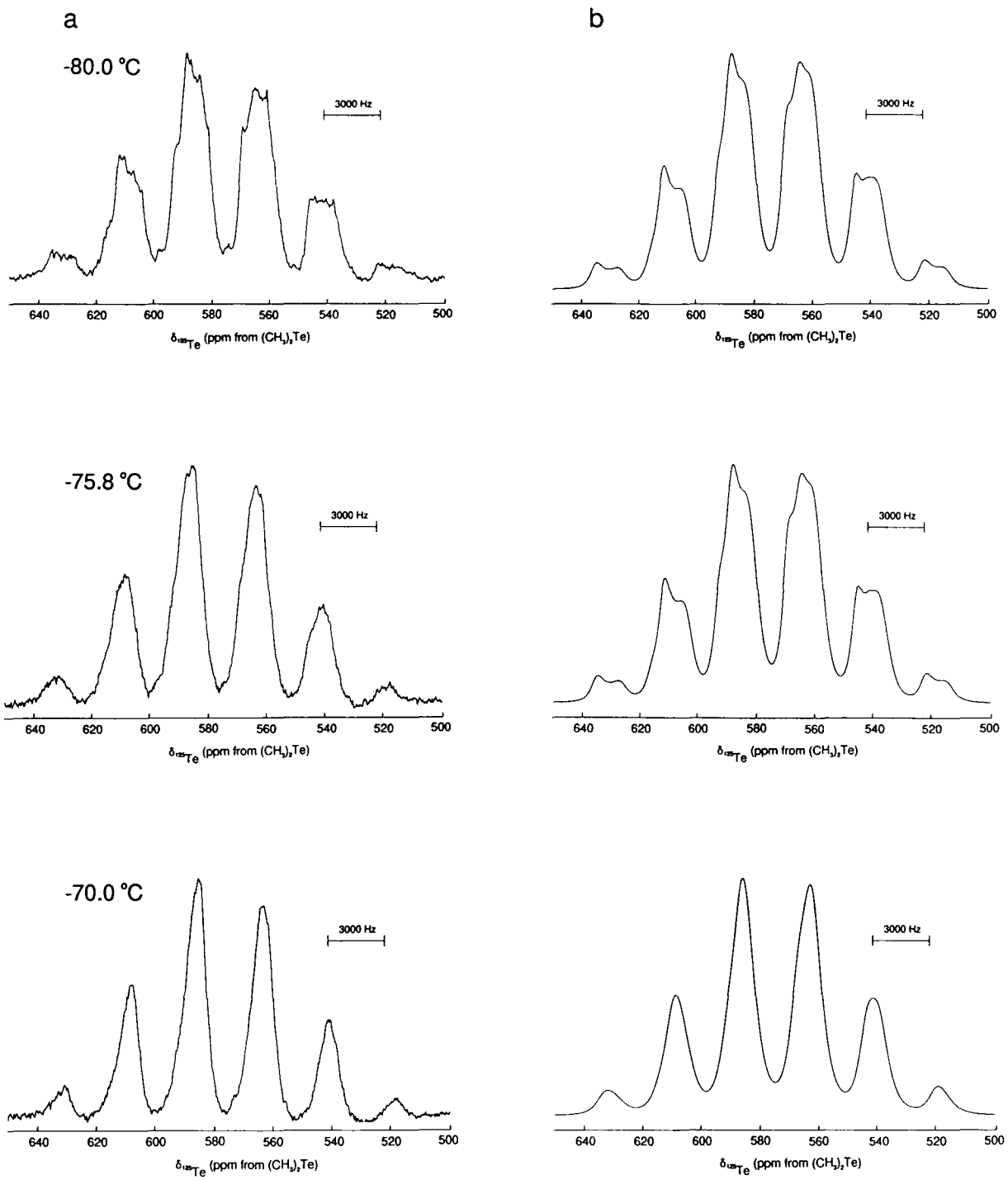

Figure 6.19 (continued)

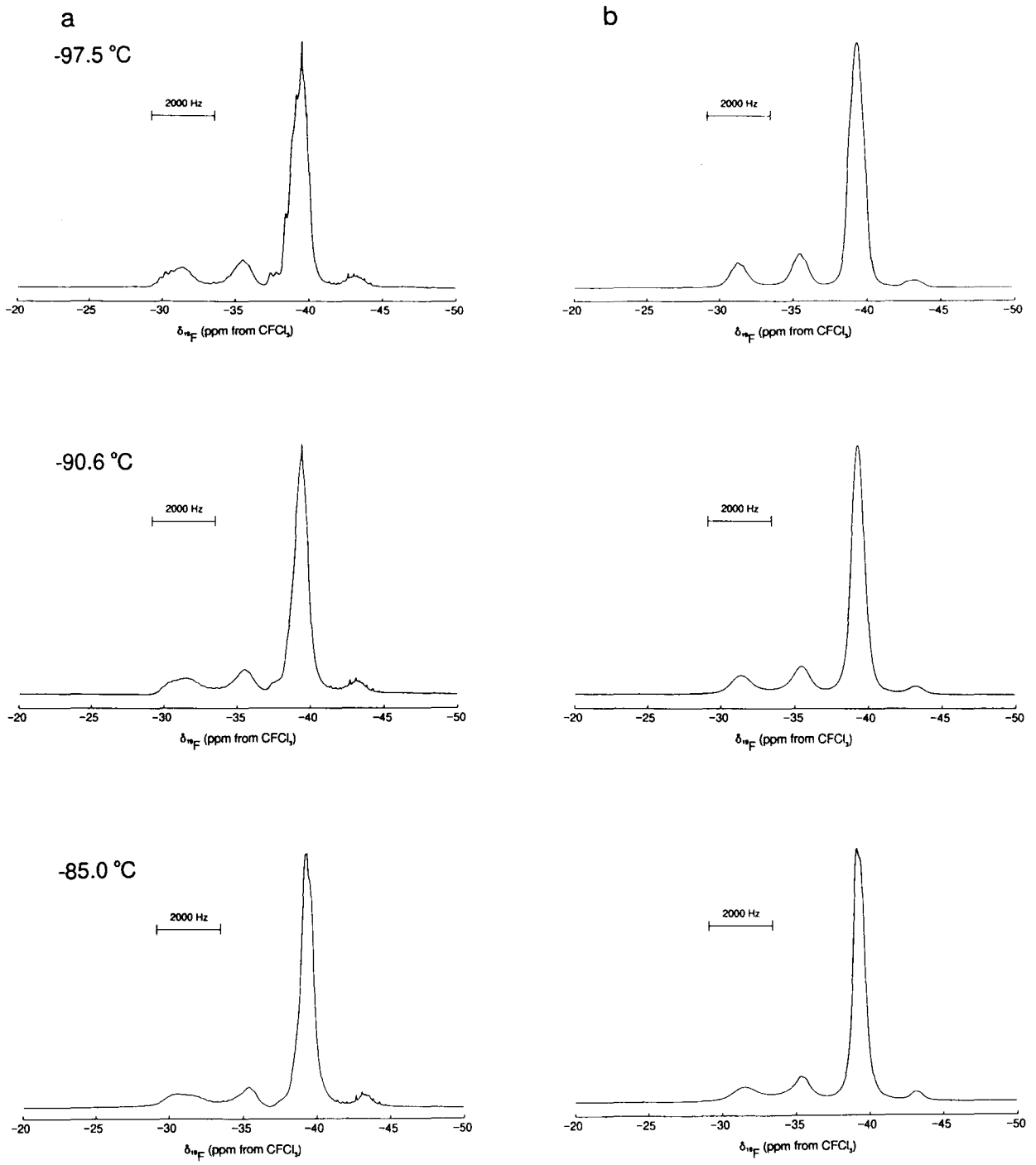

Figure 6.20 Variable-temperature ^{19}F NMR spectra (470.592 MHz) of $N(CH_3)_4^+Sb(OTeF_5)_4^-$ in CH_3CH_2CN: (a) observed spectrum; (b) calculated spectrum.

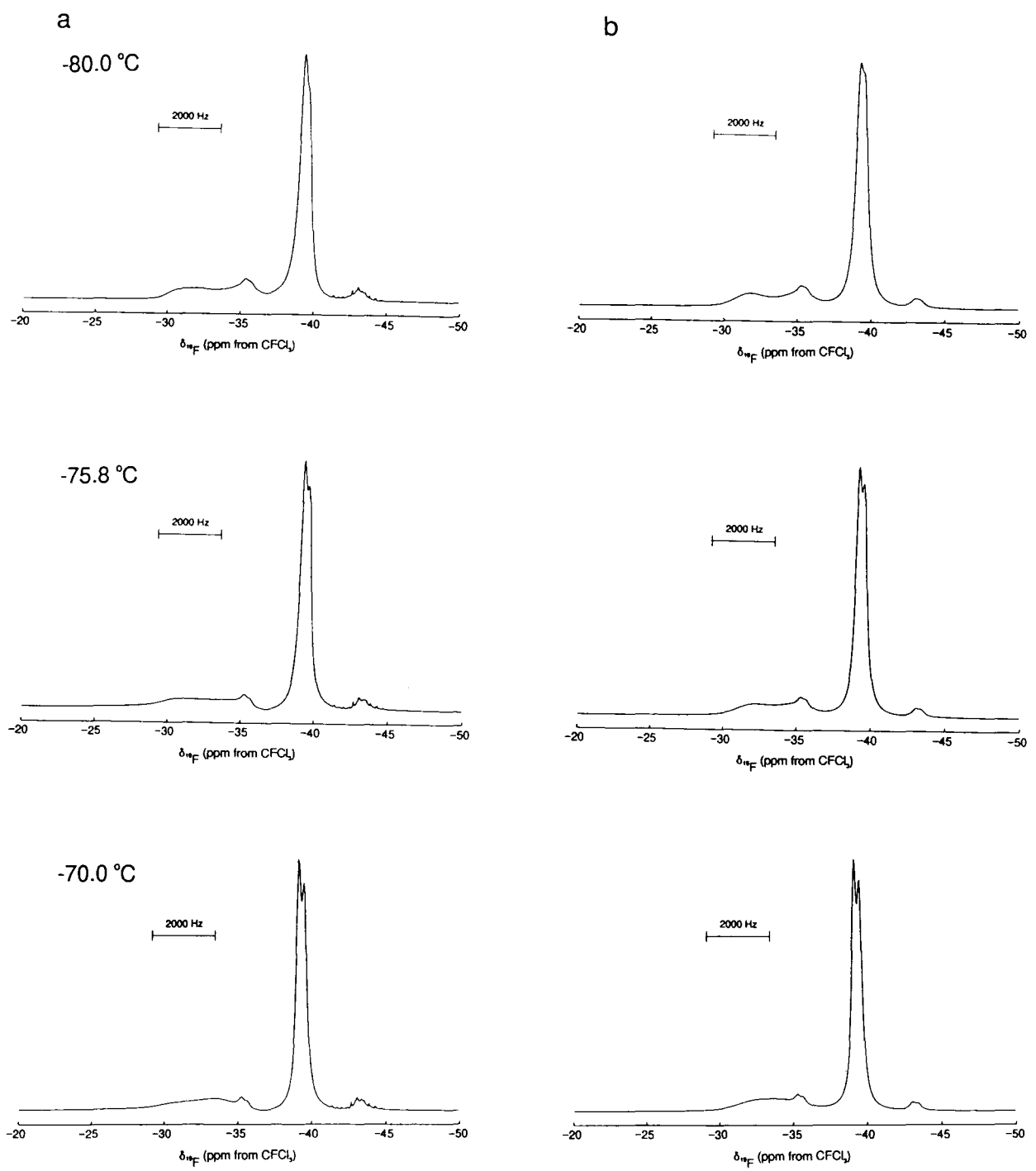

Figure 6.20 (continued).

however one set of $OTeF_5$ resonances was clearly much broader in both the ^{19}F and ^{125}Te NMR spectra. Based on a comparison of the axial and equatorial assignments in the ^{19}F and ^{125}Te NMR spectra of $Te(OTeF_5)_4$, it was postulated that the broader signals observed in the spectra of $Sb(OTeF_5)_4^-$ corresponded to the equatorial $OTeF_5$ groups. Upon warming to -70 °C, the two sets of $OTeF_5$ resonances broadened and eventually coalesced to give a single, averaged AB_4 pattern in the ^{19}F spectrum (Figure 6.20) and a doublet of quintets in the ^{125}Te spectrum (Figure 6.19). Although NMR spectroscopy alone cannot identify the mechanism responsible for the intramolecular exchange process, it is most likely the classical Berry pseudorotation. The ^{19}F NMR spectra of $Sb(OTeF_5)_4^-$ in CH_3CH_2CN were also recorded at -31.1 °C and 30 °C and each displayed one sharp AB_4 pattern as expected (Figure 6.21). However, since the sample became purple in color at 30 °C, the ^{125}Te NMR spectrum was not recorded at this temperature owing to the instability of the sample and the long acquisition time that would have been required.

Rate data at the different temperatures (-97.5 °C – -70 °C) were extracted for an equal-population two-site exchange process from the temperature dependence of the ^{19}F and ^{125}Te NMR chemical shift differences of the axial and equatorial environments by visual matching of the experimental spectra with those generated by the MEXICO[129] program for exchanging systems (Table 6.9). Using previously established equations,[196,197] and Arrhenius and Eyring plots of the ^{19}F and ^{125}Te NMR rate data (Figures 6.22 and 6.23), values for E_a, $\Delta H^{\ddagger}$, $\Delta S^{\ddagger}$, and $\Delta G^{\ddagger}$ were determined (Table 6.10). The averaged values (E_a = 19.910 $kJmol^{-1}$, $\Delta H^{\ddagger}$ = 18.280 kJmol, $\Delta S^{\ddagger}$ = -81.438 $JK^{-1}mol^{-1}$,

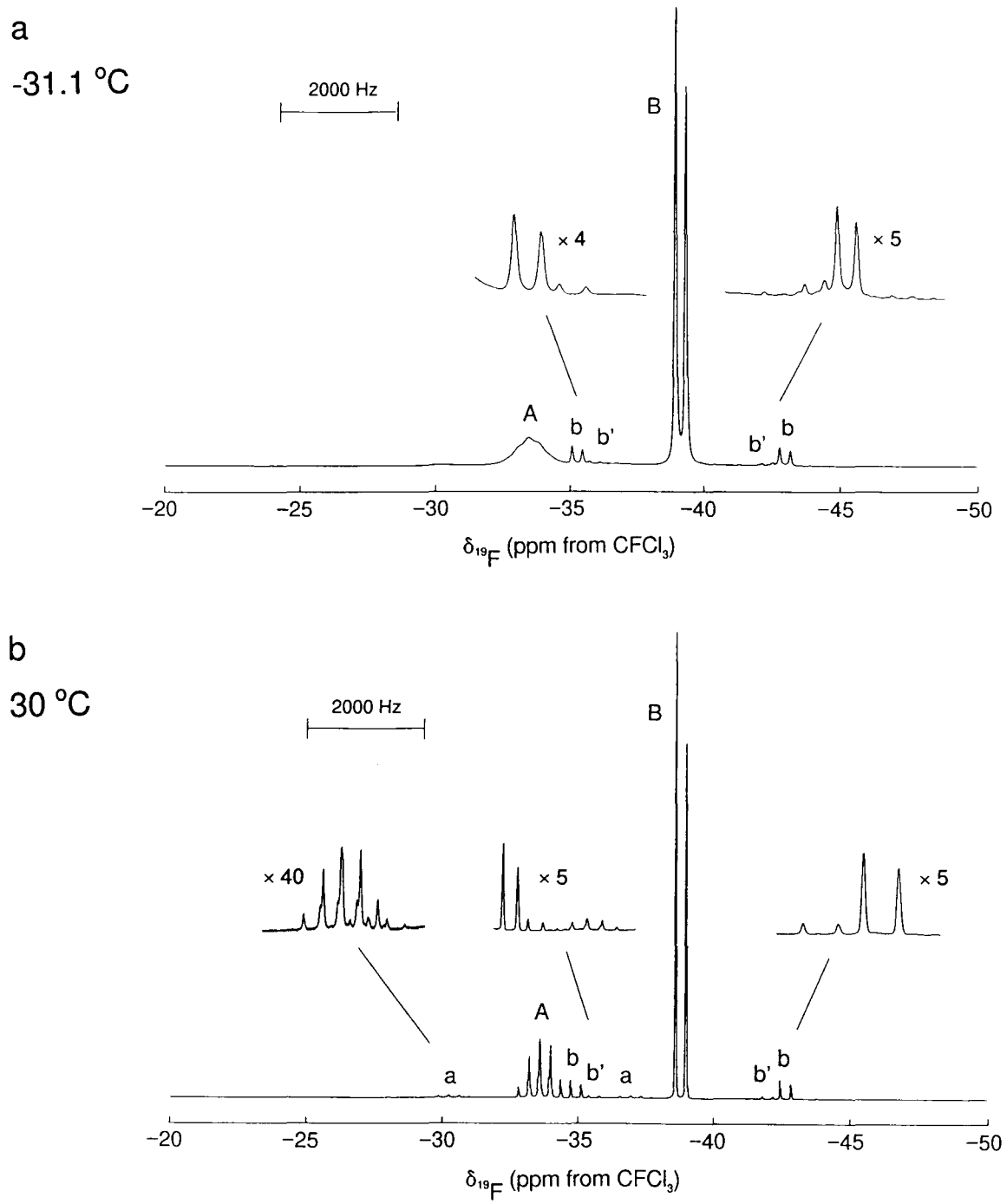

Figure 6.21 ^{19}F NMR spectra (470.592 MHz) of $N(CH_3)_4^+Sb(OTeF_5)_4^-$ in CH_3CH_2CN: (a) recorded at -31.1 °C; (b) recorded at 30 °C. A and B denote the axial and equatorial $OTeF_5$ groups, respectively, a and b indicate satellites resulting from the couplings $^1J(^{19}F_A\text{-}^{125}Te)$ and $^1J(^{19}F_B\text{-}^{125}Te)$, respectively, and primes denote ^{123}Te satellites where they can be observed.

Table 6.9 Exchange Rate Data Extracted from the Variable-Temperature ^{125}Te and ^{19}F NMR Spectra of $N(CH_3)_4^+Sb(OTeF_5)_4^-$ in CH_3CH_2CN.

^{125}Te

T (°C)	T(K)	$1/T \times 10^{-3}$ (K^{-1})	k (s^{-1})	ln k	ln (k/T)
-97.5	175.65	5.693	800	6.685	1.516
-90.6	182.55	5.478	1200	7.090	1.883
-85.0	188.15	5.315	1800	7.496	2.258
-80.0	193.15	5.177	2700	7.901	2.638
-75.8	197.35	5.067	3500	8.161	2.876
-70.0	203.15	4.922	4400	8.389	3.075

^{19}F

T (°C)	T(K)	$1/T \times 10^{-3}$ (K^{-1})	k (s^{-1})	ln k	ln (k/T)
-97.5	175.65	5.693	700	6.551	1.383
-90.6	182.55	5.478	1200	7.090	1.883
-85.0	188.15	5.315	1900	7.550	2.312
-80.0	193.15	5.177	2700	7.901	2.638
-75.8	197.35	5.067	3500	8.161	2.876
-70.0	203.15	4.922	4500	8.412	3.098

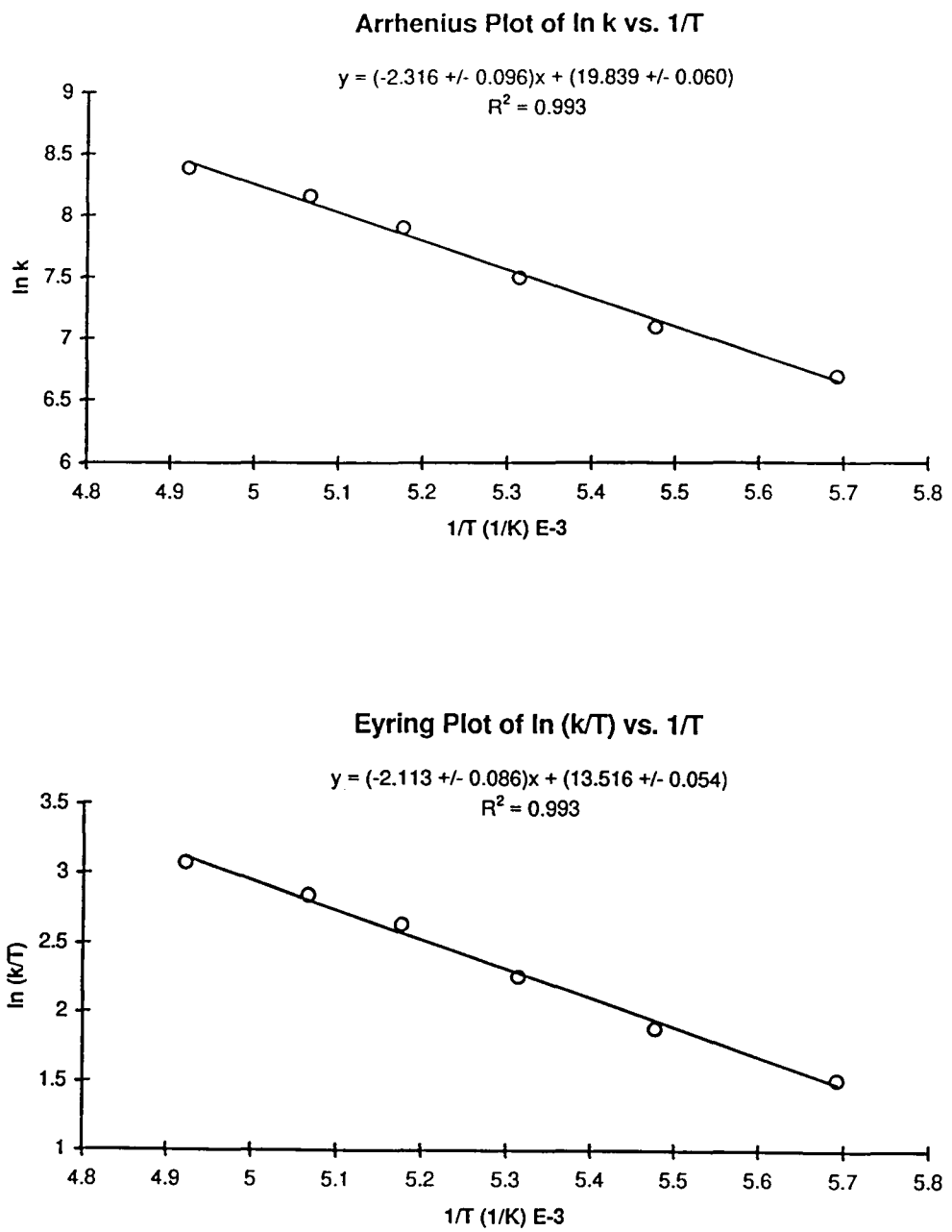

Figure 6.22 Arrhenius and Eyring plots of the exchange rate data extracted from the variable-temperature ^{125}Te NMR spectra (157.790 MHz) of $N(CH_3)_4^+Sb(OTeF_5)_4^-$ in CH_3CH_2CN. The slope of the line is given as y; R^2 is the correlation coefficient.

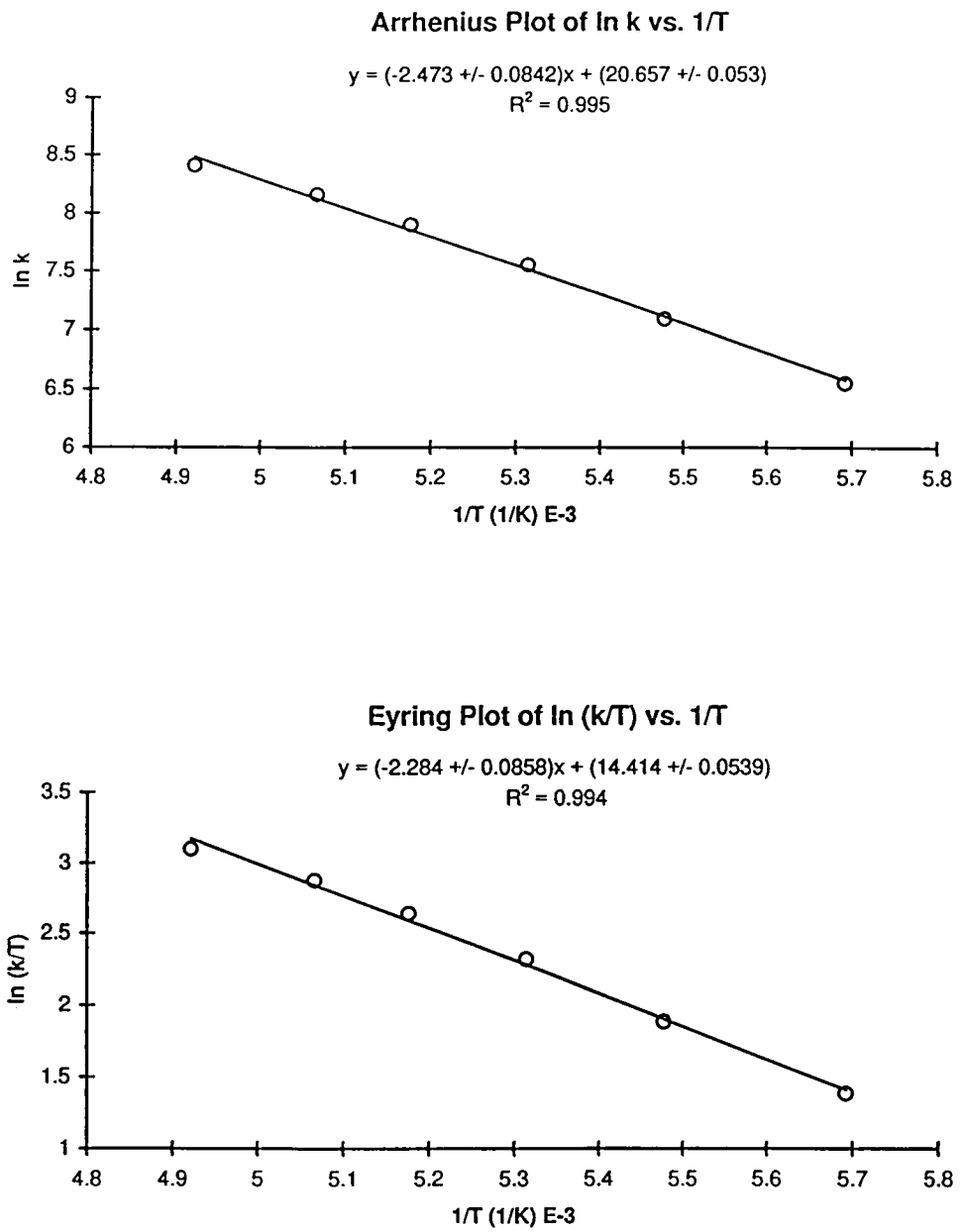

Figure 6.23 Arrhenius and Eyring plots of the exchange rate data extracted from the variable-temperature ^{19}F NMR spectra (470.592 MHz) of $N(CH_3)_4^+Sb(OTeF_5)_4^-$ in CH_3CH_2CN. The slope of the line is given as y; R^2 is the correlation coefficient.

Table 6.10 Kinetic Data Calculated from the Arrhenius and Eyring Plots of the Exchange Rate Data Extracted from the Variable-Temperature ^{125}Te and ^{19}F NMR Spectra of $N(CH_3)_4^+Sb(OTeF_5)_4^-$ in CH_3CH_2CN.

	^{125}Te	^{19}F	Average
E_a ($kJmol^{-1}$)[a]	19.258 ± 0.795	20.562 ± 0.700	19.910 ± 0.530
$\Delta H^{\ddagger}$ (kJmol)[b]	17.569 ± 0.718	18.991 ± 0.713	18.280 ± 0.506
$\Delta S^{\ddagger}$ ($JK^{-1}mol^{-1}$)[c]	-85.171 ± 0.451	-77.705 ± 0.448	-81.438 ± 0.318
$\Delta G^{\ddagger}$ ($kJmol^{-1}$)[d]	42.962 ± 0.795	42.159 ± 0.726	42.561 ± 0.515

[a] Calculated from Arrhenius plots where slope = $-E_aR^{-1}$.
[b] Calculated from Eyring plots where slope = $-\Delta H^{\ddagger}R^{-1}$.
[c] Calculated from Eyring plots where y-intercept = $[\Delta S^{\ddagger}R^{-1} + \log(K_Bh^{-1})]$
[d] Calculated from Eyring plots where $\Delta G^{\ddagger} = \Delta H^{\ddagger} - T\Delta S^{\ddagger}$

and $\Delta G^{\ddagger}$ = 42.561 $kJmol^{-1}$) differ from those obtained using similar techniques with the reported rate data for the intramolecular exchange process in the isovalent $Te(OTeF_5)_4$ (E_a = 31.012 $kJmol^{-1}$, $\Delta H^{\ddagger}$ = 29.690 kJmol, $\Delta S^{\ddagger}$ = 0.406 $JK^{-1}mol^{-1}$, and $\Delta G^{\ddagger}$ = 29.569 $kJmol^{-1}$)[115] and PF_4^- (E_a = 45.621 $kJmol^{-1}$, $\Delta H^{\ddagger}$ = 43.548 kJmol, $\Delta S^{\ddagger}$ = -13.143 $JK^{-1}mol^{-1}$, and $\Delta G^{\ddagger}$ = 47.467 $kJmol^{-1}$)[116] molecules. In contrast to $Te(OTeF_5)_4$ and PF_4^-, the intramolecular exchange process in $Sb(OTeF_5)_4^-$ appeared to be much faster and suggested another exchange mechanism.

In the PF_4^- anion an intermolecular exchange produced by the addition of excess F^- to a sample of PF_4^- in CH_3CN caused the intramolecular exchange in PF_4^- to slow down. Similarly, an excess of $N(CH_2CH_3)_4^+OTeF_5^-$ was added to a sample of $N(CH_3)_4^+Sb(OTeF_5)_4^-$ in CH_3CH_2CN (2 moles of $OTeF_5^-$: 1 mole of $Sb(OTeF_5)_4^-$) in order to slow down the intramolecular exhange in $Sb(OTeF_5)_4^-$. As expected, the ^{125}Te and ^{19}F NMR spectra at -30.5 °C displayed single doublet-of-quintet and AB_4 patterns, respectively (Figures 6.24 and 6.25; Table 6.11). However, at -95.8 °C one set of $OTeF_5$ environments, assumed to be the equatorial $OTeF_5$ groups, almost completely collapsed while another set of unidentified signals increased in intensity. A comparison of the ^{19}F and ^{125}Te NMR spectra of $Sb(OTeF_5)_4^-$ with excess $OTeF_5^-$ at -95.8 °C (Figures 6.24 and 6.25) with those of the synthetic precursors, $Sb(OTeF_5)_3$ (Figure 6.13) and $N(CH_2CH_3)_4^+OTeF_5^-$ (Figure 6.14) in CH_3CH_2CN at -97.6 °C and -94.8 °C, respectively, revealed the presence of a thermodynamic equilibrium according to equation (6.4). That

$$Sb(OTeF_5)_4^- \rightleftarrows Sb(OTeF_5)_3 + OTeF_5^- \qquad (6.4)$$

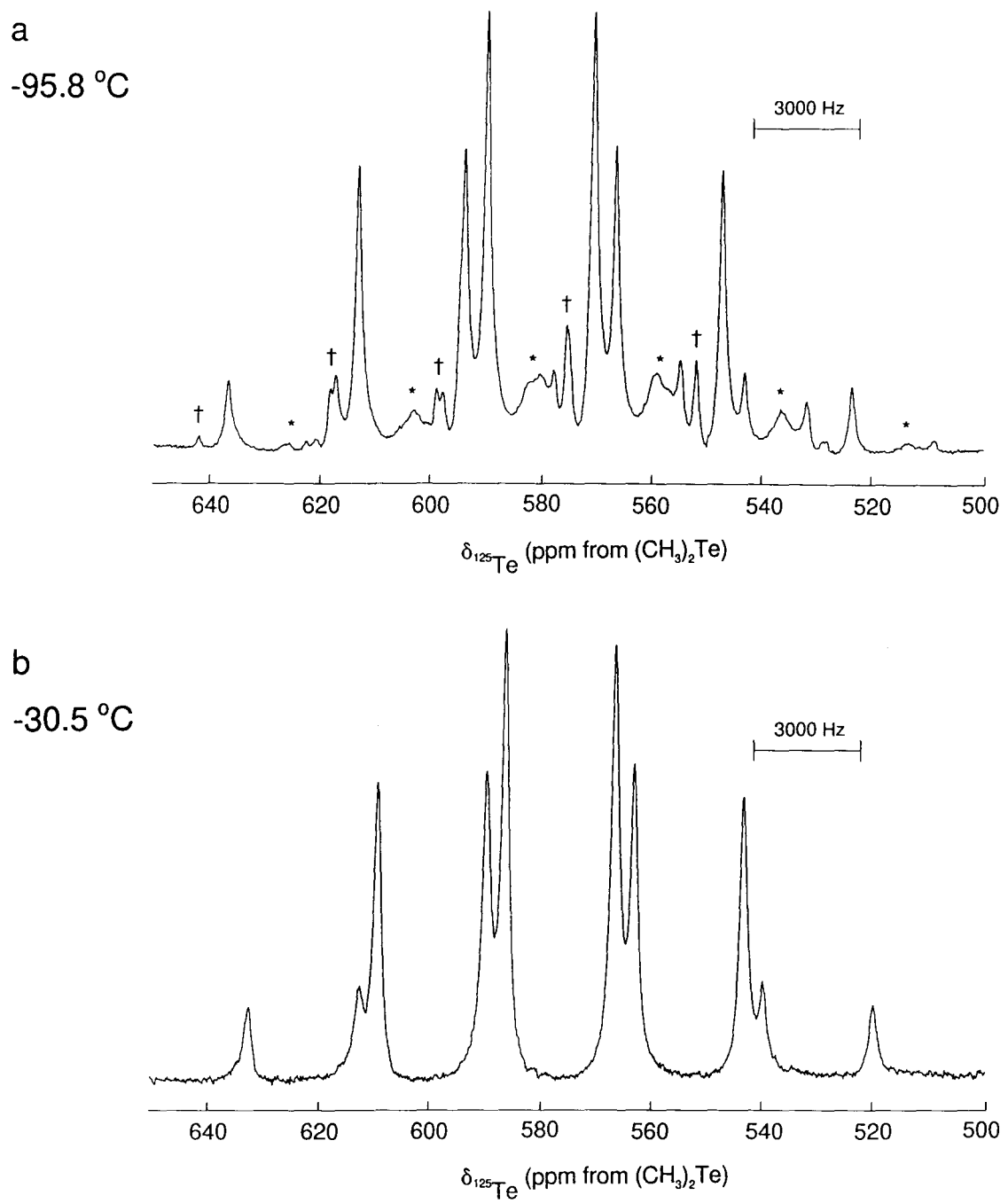

Figure 6.24 ^{125}Te NMR spectra (157.790 MHz) of $N(CH_3)_4^+Sb(OTeF_5)_4^-$ in CH_3CH_2CN containing an excess of $N(CH_2CH_3)_4^+OTeF_5^-$: (a) recorded at -95.8 °C; (b) recorded at -30.5 °C. The symbols, * and †, denote resonances from $Sb(OTeF_5)_3$ and $N(CH_2CH_3)_4^+OTeF_5^-$, respectively.

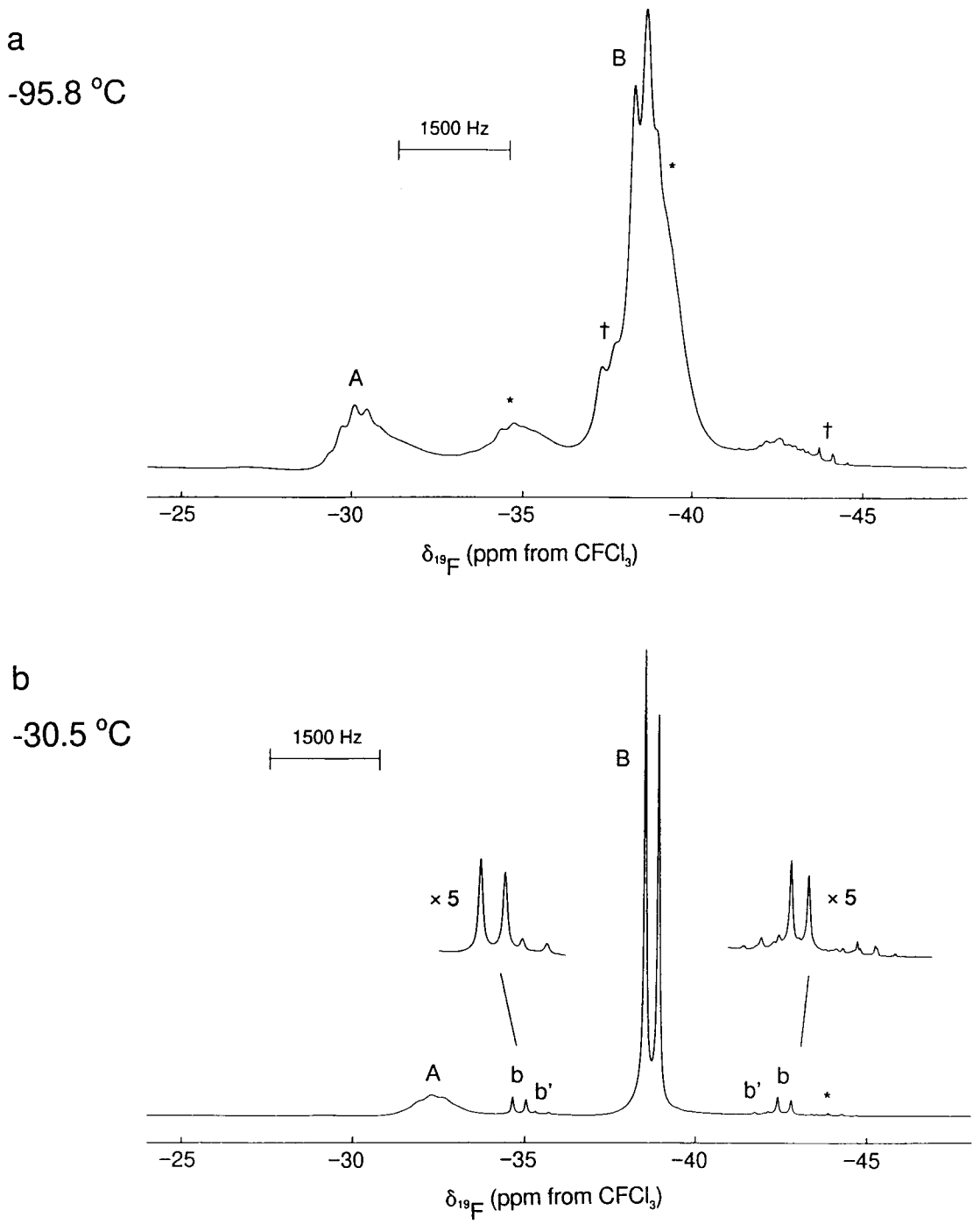

Figure 6.25 ^{19}F NMR spectra (470.592 MHz) of $N(CH_3)_4^+Sb(OTeF_5)_4^-$ in CH_3CH_2CN containing an excess of $N(CH_2CH_3)_4^+OTeF_5^-$: (a) recorded at -95.8 °C; (b) recorded at -30.5 °C. The symbols, * and †, denote resonances from $Sb(OTeF_5)_3$ and $N(CH_2CH_3)_4^+OTeF_5^-$, respectively.

Table 6.11 ^{19}F and ^{125}Te NMR Parameters for $N(CH_3)_4^+Sb(OTeF_5)_4^-$ in CH_3CH_2CN with Excess $N(CH_2CH_3)_4^+OTeF_5^-$.[a]

T (°C)	Species	Chemical Shifts (ppm)			Coupling Constants (Hz)				
		$\delta(^{19}F)_A$	$\delta(^{19}F)_B$	$\delta(^{125}Te)$	$^2J(^{19}F_A-^{19}F_B)$	$^1J(^{19}F_A-^{125}Te)$	$^1J(^{19}F_B-^{125}Te)$	$^1J(^{19}F_A-^{123}Te)$	$^1J(^{19}F_B-^{123}Te)$
-95.8	$Sb(OTeF_5)_4^-$	-30.1	-34.8	580.0	165	3334	3611	c	c
	$Sb(OTeF_5)_3$	-38.5	-39.1	570.0	165	3065	3687	c	c
	$OTeF_5^-$	c	-37.5	~607.0	193	c	~3624	c	c
-30.5	b	-32.3	-38.7	576.0	182	3117	3652	c	3030

[a] ^{19}F (470.592 MHz) and ^{125}Te (157.790 MHz) NMR spectra of the samples were recorded in 5-mm medium-walled glass NMR tubes.
[b] The $Sb(OTeF_5)_4^-$, $Sb(OTeF_5)_3$, and $OTeF_5^-$ species are exchanging.
[c] Resonances are too weak, broad, or overlapping with other resonances and are not reported.

is, below *ca.* -75.8 °C the resonances previously ascribed to the axial and equatorial $OTeF_5$ groups in $Sb(OTeF_5)_4^-$ actually corresponded to $Sb(OTeF_5)_4^-$ and $Sb(OTeF_5)_3$, respectively, and the previously unidentified resonances represented $OTeF_5^-$ (Table 6.12). Above *ca.* -75.8 °C, $Sb(OTeF_5)_4^-$, $Sb(OTeF_5)_3$, and $OTeF_5^-$ displayed an averaged signal in the ^{19}F and ^{125}Te NMR spectra. As the concentration of $OTeF_5^-$ anions was increased, the equilibrium shifted to the left [see eq (6.4)] resulting in a decrease in the intensity of the $Sb(OTeF_5)_3$ signals and an increase in those attributed to $Sb(OTeF_5)_4^-$. An equilibrium constant for equation (6.4) could not be determined from the relative intensities of the $Sb(OTeF_5)_4^-$, $Sb(OTeF_5)_3$, and $OTeF_5^-$ resonances in the ^{19}F and ^{125}Te NMR spectra due to broadening and overlap of the signals. However, the ^{19}F and ^{125}Te NMR spectra for the combined $Sb(OTeF_5)_4^-$ and $Sb(OTeF_5)_3$ molecules in CH_3CH_2CN at -97.5 °C were simulated by an isotopomer NMR program (Figures 6.26 and 6.27). The spectra confirmed the thermodynamic equilibrium observed between the molecules. The $Sb(OTeF_5)_4^-$ anion is still undergoing intramolecular exchange, however, at -97.5 °C the exchange has not yet been slowed down enough to observe separate axial and equatorial $OTeF_5$ environments.

X-Ray Crystal Structure of $[N(CH_3)_4^+]_2[Sb(OTeF_5)_5^{2-}]$

Details of the data collection parameters and other crystallographic information are given in Table 6.13. Atomic coordinates, isotropic thermal parameters, bond lengths, and angles are not listed for the preliminary structure of $[N(CH_3)_4^+]_2[Sb(OTeF_5)_5^{2-}]$ since they are largely affected by the disorder.

Table 6.12 ^{19}F and ^{125}Te NMR Parameters for $N(CH_3)_4^+Sb(OTeF_5)_4^-$ and its Impurities in CH_3CH_2CN.[a]

T (°C)	Species	Chemical Shifts (ppm)			Coupling Constants (Hz)				
		$\delta(^{19}F)_A$	$\delta(^{19}F)_B$	$\delta(^{125}Te)$	$^2J(^{19}F_A - ^{19}F_B)$	$^1J(^{19}F_A - ^{125}Te)$	$^1J(^{19}F_B - ^{125}Te)$	$^1J(^{19}F_A - ^{123}Te)$	$^1J(^{19}F_B - ^{123}Te)$
-97.5	$Sb(OTeF_5)_4^-$	-30.2	-38.7	580.0	~183	3224	3615	c	c
	$Sb(OTeF_5)_3$	-35.5	-39.6	569.5	~180	3052	3688	c	c
	$OTeF_5^-$	c	-37.6	~606.5	186	c	c	c	c
-90.6	$Sb(OTeF_5)_4^-$	-31.4	~-39.4	579.7	c	c	c	c	c
	$Sb(OTeF_5)_3$	-35.5	~-39.4	570.3	c	c	c	c	c
	$OTeF_5^-$	c	~-37.5	~606.2	c	c	c	c	c
-85.0	$Sb(OTeF_5)_4^-$	-30.6	~-39.3	579.4	c	c	c	c	c
	$Sb(OTeF_5)_3$	-35.4	~-39.3	571.1	c	c	c	c	c
	$OTeF_5^-$	c	c	~609.0	c	c	c	c	c
-80.0	$Sb(OTeF_5)_4^-$	-31.3	~-39.2	579.2	c	c	c	c	c
	$Sb(OTeF_5)_3$	-35.4	~-39.2	572.9	c	c	c	c	c
	$OTeF_5^-$	c	c	~607.0	c	c	c	c	c
-75.8	b	c	-39.3	~575.9	146	c	3661	c	c
-70.0	b	-33.4	-39.3	~576.5	162	c	3654	c	c
-31.1	b	-33.4	-39.1	d	181	~3030	3646	c	3023
30.0	b	-33.6	-38.8	d	182	3147	3634	2616	3013

[a] ^{19}F (470.592 MHz) and ^{125}Te (157.790 MHz) NMR spectra of the samples were recorded in 5-mm medium-walled glass NMR tubes.
[b] The $Sb(OTeF_5)_4^-$, $Sb(OTeF_5)_3$, and $OTeF_5^-$ species are exchanging.
[c] Resonances are too weak, broad, or overlapping with other resonances and are not reported.
[d] ^{125}Te NMR spectrum was not acquired because the sample undergoes slow decomposition at room temperature.

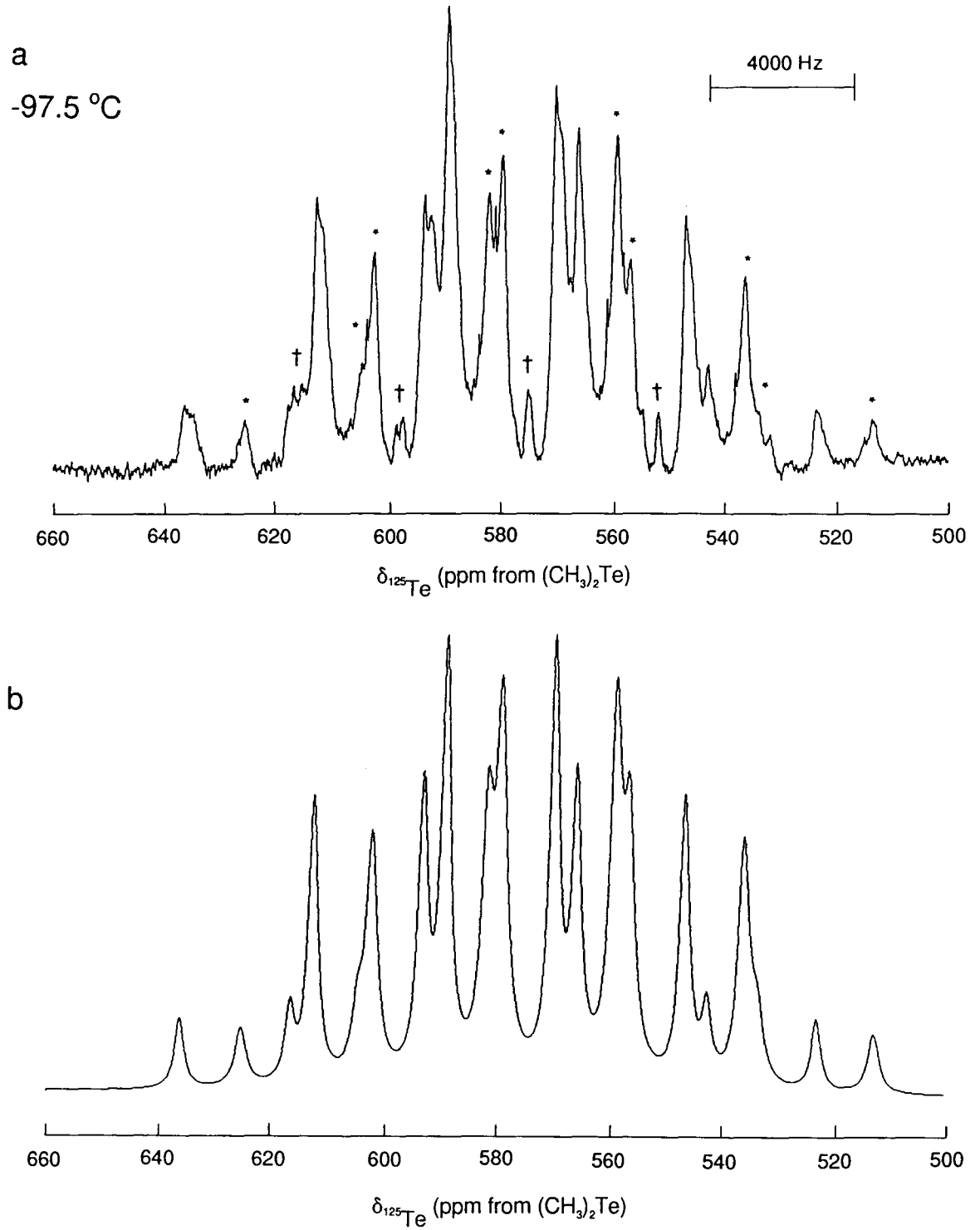

Figure 6.26 ^{125}Te NMR spectrum (157.790 MHz) for the thermodynamic equilibrium of $Sb(OTeF_5)_4^-$, $Sb(OTeF_5)_3$, and $OTeF_5^-$ in CH_3CH_2CN recorded at -97.5 °C: (a) observed; (b) calculated for $Sb(OTeF_5)_4^-$ and $Sb(OTeF_5)_3$. The symbols, * and †, denote resonances from $Sb(OTeF_5)_3$ and $OTeF_5^-$, respectively. Unmarked resonances represent those from $Sb(OTeF_5)_4^-$.

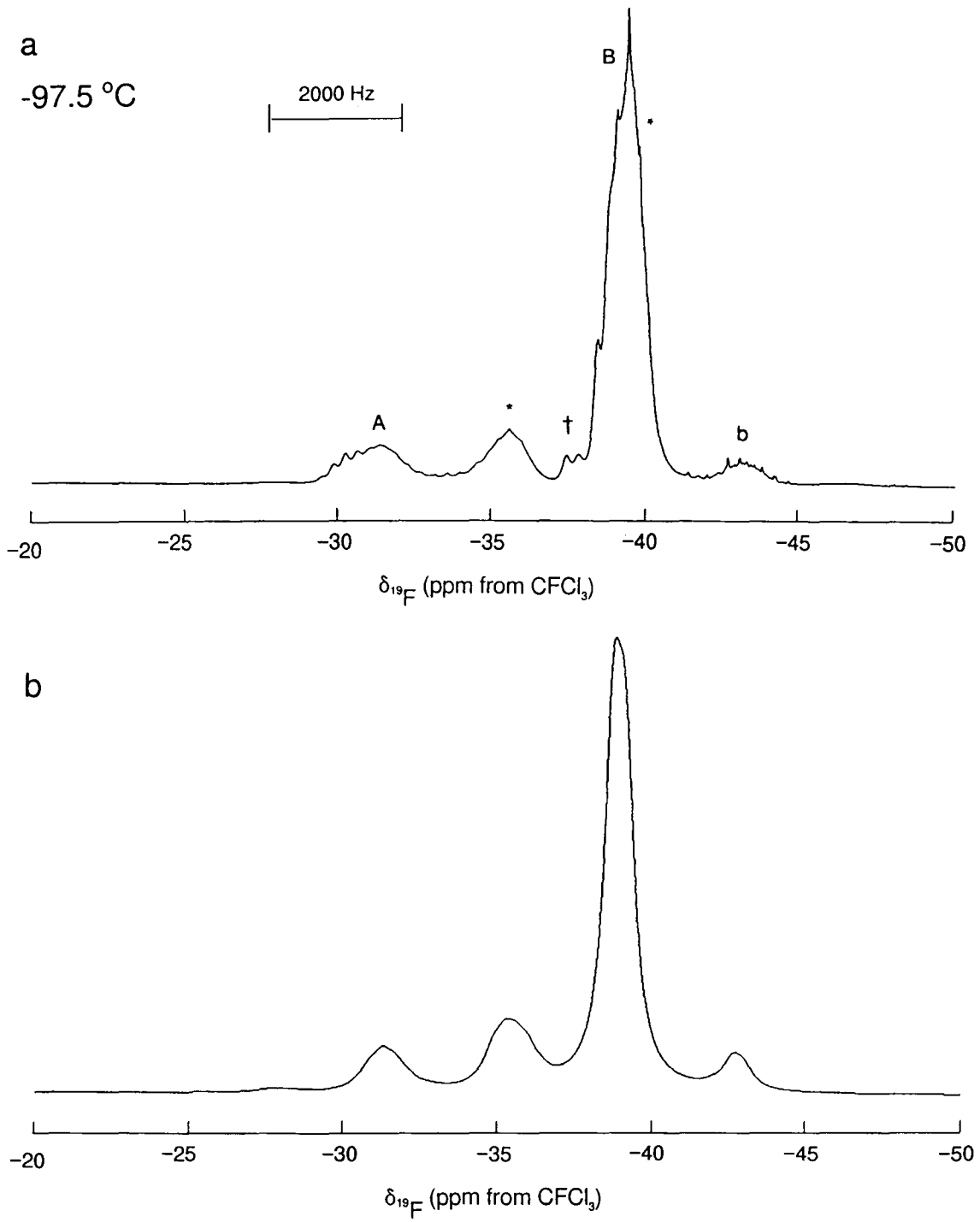

Figure 6.27 ^{19}F NMR spectrum (470.592 MHz) for the thermodynamic equilibrium of $Sb(OTeF_5)_4^-$, $Sb(OTeF_5)_3$, and $OTeF_5^-$ in CH_3CH_2CN recorded at -97.5 °C: (a) observed; (b) calculated for $Sb(OTeF_5)_4^-$ and $Sb(OTeF_5)_3$. The symbols, * and †, denote resonances from $Sb(OTeF_5)_3$ and $OTeF_5^-$, respectively. Unmarked resonances represent those from $Sb(OTeF_5)_4^-$.

Table 6.13 Summary of Crystal Data and Refinement Results for $[N(CH_3)_4^+]_2[Sb(OTeF_5)_5^{2-}]$.

	$[N(CH_3)_4^+]_2[Sb(OTeF_5)_5^{2-}]$
empirical formula	$C_4H_{12}NSbO_4F_20Te_4$
space group (No.)	I4
a (Å)	11.5351(2)
b (Å)	11.5351(2)
c (Å)	14.5907(4)
α (deg.)	90
β (deg.)	90
γ (deg.)	90
V (Å^3)	1941.42(7)
molecules/unit cell	2
mol. wt. (g mol^{-1})	1463.04
calcd. density (g cm^{-3})	2.503
T (°C)	-60
μ (mm^{-1})	4.534
λ (Å) used for data collection	0.71073
final agreement factors[a]	$R_1 = 0.0891$
	$wR_2 = 0.2436$

[a] R_1 is defined as $\Sigma||F_o| - |F_c||/\Sigma|F_o|$ for $I > 2\sigma(I)$.
wR_2 is defined as $[\Sigma[w(F_o^2 - F_c^2)^2]/\Sigma w(F_o^2)^2]^{1/2}$ for $I > 2\sigma(I)$.

The $Sb(OTeF_5)_5^{2-}$ anion is isostructural with $Te(OTeF_5)_5^-$.[112] The central Sb(III) atom in $Sb(OTeF_5)_5^{2-}$ is coordinated to four crystallographically equivalent equatorial $OTeF_5$ groups and one crystallographically non-equivalent axial $OTeF_5$ group (Figure 6.28a) Even though the anion is highly disordered (Figure 6.28b), it is clear that, as expected for a molecule possessing an AX_5E geometry, the O_{ax}–Sb–O_{eq} angles are smaller than 90° and the central antimony atom is found to be displaced below the average plane defined by the four equatorial oxygen atoms which were found to be coplanar.

The extended structure of the $[N(CH_3)_4^+]_2[Sb(OTeF_5)_5^{2-}]$ salt is dominated by the larger $Sb(OTeF_5)_5^{2-}$ anions with the cations occupying all available interstitial cavities (Figure 6.29). The crystal packing along the a-axis consists of infinite layers of anions surrounding a layer of cations each occupying the apical position of an anion (Figure 6.29a). The carbon atoms of these cations are positionally disordered with the axial tellurium atoms of the anions and have been omitted in the diagrams for clarity.

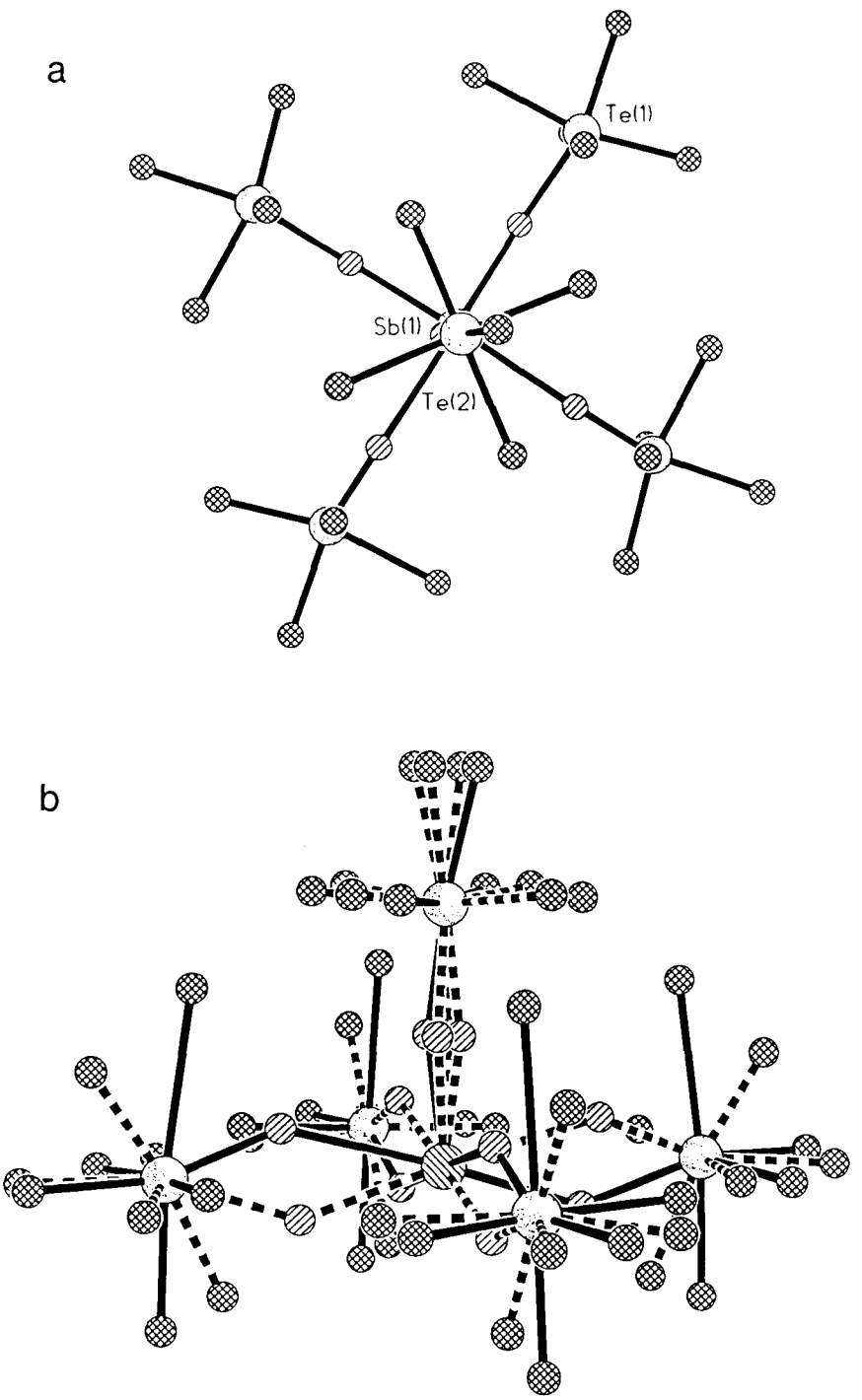

Figure 6.28 Structure of $[N(CH_3)_4^+]_2[Sb(OTeF_5)_5^{2-}]$. (a) Geometry of the $Sb(OTeF_5)_5^{2-}$ anion along the axial $OTeF_5$ group; (b) disordered geometry of the $Sb(OTeF_5)_5^{2-}$ anion along two equatorial $OTeF_5$ groups.

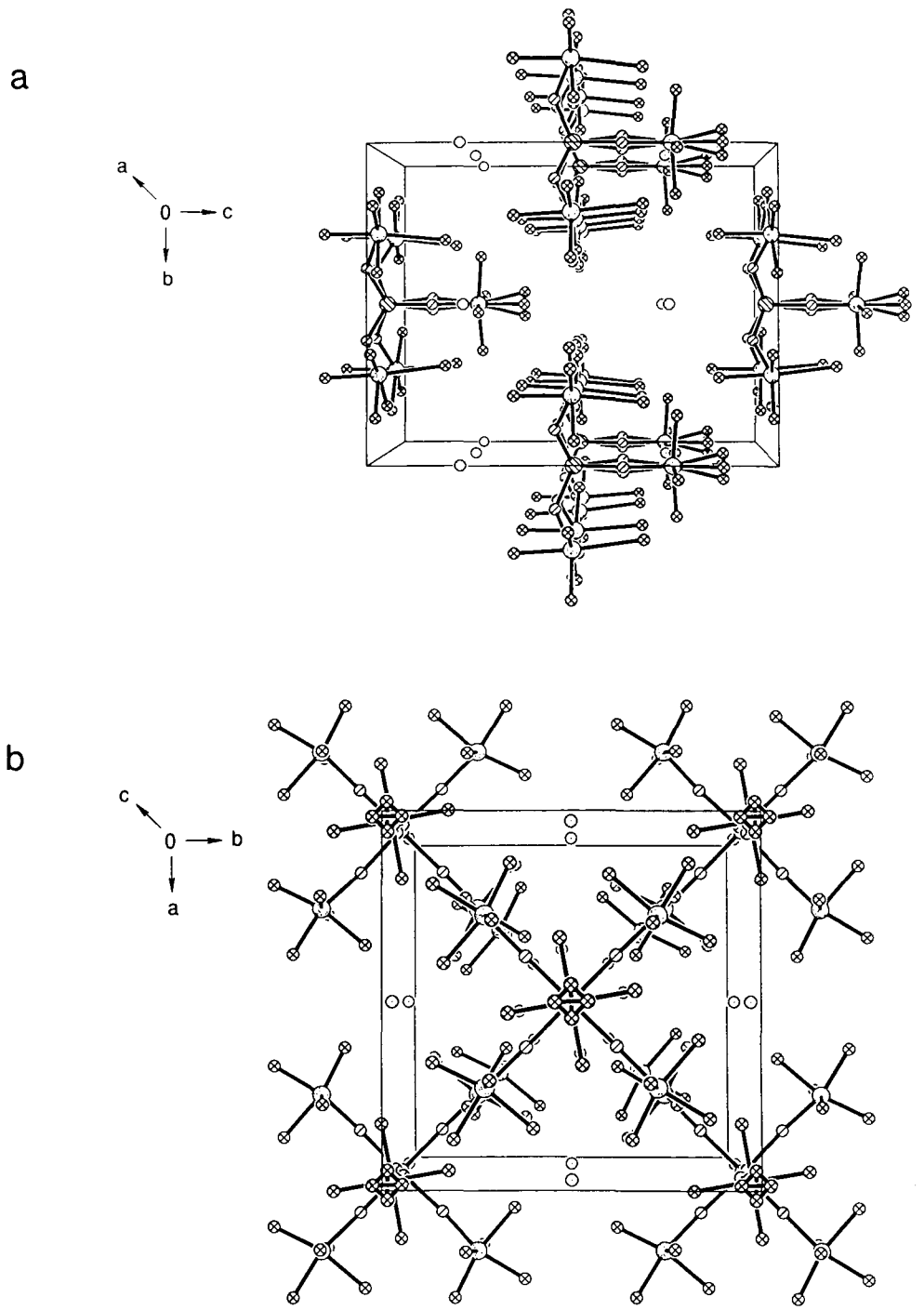

Figure 6.29 View of the $[N(CH_3)_4^+]_2[Sb(OTeF_5)_5^{2-}]$ unit cell: (a) along the a-axis; (b) along the c-axis. For clarity, the methyl groups of the $N(CH_3)_4^+$ cations have been omitted.

CHAPTER 7

SUMMARY, CONCLUSIONS, AND DIRECTIONS FOR FUTURE RESEARCH

SUMMARY

The present work represents a significant extension of noble-gas chemistry, and in particular, the structural characterizations by X-ray crystallography of xenon(II) compounds containing xenon-nitrogen and xenon-oxygen bonds, and the syntheses and characterization by Raman and multi-NMR spectroscopy of two new $OTeF_5$ derivatives of As(III) and Sb(III).

Xe(II)–N Bonded Compounds

A significant portion of this Thesis has been devoted to the structural characterizations and bonding of the Lewis acid cation, XeF^+, with a variety of oxidatively resistant nitrogen base centers, namely, HCN, $CH_3C{\equiv}N$, $(CH_3)_3CC{\equiv}N$, *s*-$C_3F_3N_3$, C_5F_5N, and F_5TeNH_2. The syntheses and characterizations in the solid-state by low-temperature Raman spectroscopy and in HF and/or BrF_5 solutions by ^{129}Xe, $^{14/15}N$, ^{13}C, ^1H NMR spectroscopy of the Xe–N bonded adduct cations studied in the present work have previously been described.[68-70,72,85] Accordingly, these syntheses were repeated with the view to obtain the low-temperature X-ray crystal structures of representative examples.

The reaction of $XeF^+AsF_6^-$ with the appropriate nitrogen base in anhydrous HF led to the formation of $R–C{\equiv}N–XeF^+AsF_6^-$ (R = H, CH_3, $(CH_3)_3C$) [eq (7.1)] and

$$R–C{\equiv}N + XeF^+AsF_6^- \xrightarrow{HF} R–C{\equiv}N–XeF^+AsF_6^- \quad (7.1)$$

$F_5TeN(H)Xe^+AsF_6^-$ [eqs (7.2), (7.3), (7.4)]. The reaction of $XeF^+AsF_6^-$ with neat $C_3F_3N_3$

$$XeF^+AsF_6^- + HF \rightleftharpoons XeF_2 + H_2F^+AsF_6^- \quad (7.2)$$

$$F_5TeNH_2 + H_2F^+AsF_6^- \rightleftharpoons F_5TeNH_3^+AsF_6^- + HF \quad (7.3)$$

$$F_5TeNH_3^+AsF_6^- + XeF_2 \rightleftharpoons F_5TeN(H)Xe^+AsF_6^- + 2HF \quad (7.4)$$

at room temperature gave $C_3F_3N_2N–XeF^+AsF_6^-$ [eq (7.5)]. The reaction of the

$$C_3F_3N_3 + XeF^+AsF_6^- \longrightarrow C_3F_3N_2N–XeF^+AsF_6^- \quad (7.5)$$

protonated C_5F_5N, formed according to equation (7.6), with XeF_2 in BrF_5 solvent gave $C_5F_5N–XeF^+AsF_6^-$ [eq (7.7)].

$$C_5F_5N + AsF_5 \xrightarrow{HF} C_5F_5NH^+AsF_6^- \quad (7.6)$$

$$C_5F_5NH^+AsF_6^- + XeF_2 \xrightarrow{BrF_5} C_5F_5N–XeF^+AsF_6^- + HF \quad (7.7)$$

Detailed structural characterizations of the adducts by low-temperature single-crystal X-ray diffraction was facilitated by recent developments in this laboratory that have led to a reliable and routine method for the low-temperature growing, mounting, and data collection of thermally unstable crystals (see **Experimental Section**). The $R–C{\equiv}N–XeF^+AsF_6^-$ (R = H, CH_3, $(CH_3)_3C$) series of compounds represent the first detailed structures containing formally sp-hybridized nitrogen centers that are bonded to xenon. The $MeCN{\cdots}Xe–C_6F_5^+$ cation[66] has been reported previously, but the Xe···N interaction is considerably weaker than those in the present structures. The X-ray crystal

structures of *s*-$C_3F_3N_2N$–$XeF^+AsF_6^-$·2.5BrF_5 and C_5F_5N–$XeF^+AsF_6^-$·2.5BrF_5 represent unique examples in which XeF^+ functions as an aromatic substituent and the nitrogen atom bonded to xenon has formal sp^2-hybridization. The previously reported X-ray crystal structure of 2,6-$C_5H_3F_2N$···Xe–$C_6F_5^+$ also contains xenon coordinated to an aromatic ring through the lone pair of electrons on nitrogen, but the Xe···N bond distance is much longer than those in the present structures. Furthermore, the $F_5TeN(H)Xe^+AsF_6^-$ salt represents the only crystallographically characterized example where xenon is bonded to a formally sp^3-hybridized nitrogen and the only example of a Xe–N bonded compound that was prepared from an inorganic ammonium base. The effect on the bonding of the F_5TeN group following protonation of F_5TeNH_2 and coordination to xenon were also investigated by determining the X-ray crystal structures of F_5TeNH_2 and $F_5TeNH_3^+AsF_6^-$. Density functional theory (LDFT/DZVP) calculations which were done for $F_5TeN(H)Xe^+AsF_6^-$, $F_5TeNH_3^+AsF_6^-$, and F_5TeNH_2 accurately reproduce the structures and have been used to assign their vibrational spectra, but are not included in this Thesis.

Since HCN was oxidatively among the most resistant ligands investigated in this Thesis, the low-temperature X-ray crystal structure of $HC{\equiv}NH^+AsF_6^-$ was determined in order to better understand the nature of the bonding in $HC{\equiv}N$–$XeF^+AsF_6^-$, as well as to complement recent theoretical investigations of the $HC{\equiv}N$–NgF^+ (Ng = Xe, Kr) cations at the SCF level.[88-95]

Xe(II)–O Bonded Compounds

The $F_5TeN(H)Xe^+$ cation is isolobal with the F_5ChOXe^+ cations (Ch = Se, Te) which have also been characterized in the present work by single-crystal X-ray diffraction. Both crystal structures are novel and show a significant bonding interaction between the anion and the cation. The X-ray crystal structures of $Xe(OChF_5)_2$ (Ch = Te, Se) were also obtained in this work. Their structures were repeated in order to obtain more complete and precise geometrical data for comparison with the structures of the $F_5ChOXe^+AsF_6^-$ salts. Although the structure of $Xe(OSeF_5)_2$ is similar to the previous report, the structure of $Xe(OTeF_5)_2$ contradicts the earlier study. The $F_5ChOXe^+AsF_6^-$ salts and the $Xe(OChF_5)_2$ compounds have been previously prepared and characterized by Raman and multi-NMR spectroscopy. The neutral $Xe(OChF_5)_2$ compounds were prepared by $OTeF_5$ substitution reactions involving XeF_2 and $B(OTeF_5)_3$ or SeO_2F_2 [eqs (7.8) and (7.9)], and the $F_5ChOXe^+AsF_6^-$ salts were prepared by the reaction of

$$3XeF_2 + 2B(OTeF_5)_3 \longrightarrow 3Xe(OTeF_5)_2 + 2BF_3 \quad (7.8)$$

$$2SeO_2F_2 + 3XeF_2 \longrightarrow Xe(OSeF_5)_2 + 2Xe + O_2 \quad (7.9)$$

$Xe(OChF_5)_2$ with XeF_2 to form $FXeOChF_5$, followed by fluoride abstraction from $FXeOChF_5$ using the strong Lewis fluoroacid, AsF_5 [eqs (7.10) and (7.11)].

$$Xe(OChF_5)_2 + XeF_2 \longrightarrow 2FXeOChF_5 \quad (7.10)$$

$$FXeOChF_5 + AsF_5 \longrightarrow XeOChF_5^+AsF_6^- \quad (7.11)$$

Characterizations of the $XeOChF_5^+AsF_6^-$ salts by solid-state low-temperature Raman spectroscopy were repeated to accurately assign all vibrational modes which were previously tentative owing, in part, to uncertainties regarding the degree of site symmetry

lowering and vibrational coupling within the unit cells (factor-group splitting), as well as uncertainties relating to the assignments of Ch–O stretches. Assignments were aided by the crystal structures (*i.e.*, knowledge of crystal symmetries in dealing with the factor-group problem) and by calculations performed at the density functional theory (LDFT/DZVP) level. Calculations at this level were previously shown to accurately predict the geometries and vibrational spectra for transition metal compounds,[199] osmium and technetium oxide fluorides,[200,201] as well as main-group species such as $TeOF_6^{2-}$,[202] $TeOF_5^-$,[171] IOF_6^-,[203] and XeF_5^-.[204] However, in the present work, several discrepancies between the calculated and observed geometries were found. As a result, it has not been possible to accurately assign the vibrational spectra. The calculations are currently being repeated at the Hartree-Fock level.

$OTeF_5$ Derivatives of As(III) and Sb(III)

The known chemistry of the $OTeF_5$ derivatives of As and Sb has also been extended by the syntheses and detailed characterizations by ^{19}F and ^{125}Te NMR spectroscopy and by Raman spectroscopy of the pnicogen anions, $Pn(OTeF_5)_4^-$ (Pn = Sb, As), as their $N(CH_3)_4^+$ and $N(CH_2CH_3)_4^+$ salts. The salts were prepared by the reaction of $Pn(OTeF_5)_3$ (Pn = Sb or As) with $NR_4^+OTeF_5^-$ (R = CH_3, CH_2CH_3) in SO_2ClF solvent [eq (7.12)]. The Raman and ^{19}F and ^{125}Te NMR spectra of the $Pn(OTeF_5)_4^-$ anions at various temperatures are consistent with their predicted geometries; *i.e.*, trigonal bipyramidal arrangement of four bond pairs and an electron lone pair with two axial and

$$Pn(OTeF_5)_3 + NR_4^+OTeF_5^- \xrightarrow{SO_2ClF,\ 25\ ^\circ C} NR_4^+Pn(OTeF_5)_4^- \qquad (7.12)$$

two equatorial $OTeF_5$ groups. The anions undergo intramolecular exchange by means of the classical Berry pseudorotation mechanism in which the axial and equatorial $OTeF_5$ groups simultaneously interchange. However, due to freezing of the solvents, the exchanges could not be slowed down sufficiently on the NMR time scale to observe separate $OTeF_5$ environments. Besides intramolecular exchange, a thermodynamic equilibrium was also observed to occur among $Sb(OTeF_5)_4^-$, $Sb(OTeF_5)_3$, and $OTeF_5^-$ in CH_3CH_2CN solutions of $Sb(OTeF_5)_4^-$ [eq (7.13)].

$$Sb(OTeF_5)_4^- \rightleftharpoons Sb(OTeF_5)_3 + OTeF_5^- \qquad (7.13)$$

The $As(OTeF_5)_4^-$ anion was found to be thermally less stable in CH_3CN and SO_2ClF solvents when compared to its antimony analogue. The stepwise decomposition of $N(CH_2CH_3)_4^+As(OTeF_5)_4^-$ in SO_2ClF was studied by ^{19}F and ^{125}Te NMR. Thermolysis of the sample gave several decomposition products, the most intense of which was identified as $F_5TeOTeF_5$.

All attempts to crystallize $Sb(OTeF_5)_4^-$ were unsuccessful and produced the less soluble $Sb(OTeF_5)_5^{2-}$ anion instead, whose preliminary disordered X-ray crystal structure is reported in this thesis. Like its isoelectronic Te(IV) analogue, $Te(OTeF_5)_5^-$,[112] the SbO_5 arrangement of $Sb(OTeF_5)_5^{2-}$ is also square pyramidal in shape.

The $Pn(OTeF_5)_4^-$ anions represent new examples demonstrating the high effective group electronegativity of the $OTeF_5$ group. Their formal (-1) charges are dispersed over 20 fluorines, making them weakly coordinating, but less so than that of the recently characterized $Pn(OTeF_5)_6^-$ anions (Pn = As, Sb, Bi).[107] Because the $Pn(OTeF_5)_4^-$ anions

are expected to be less strongly oxidizing than their $Pn(OTeF_5)_6^-$ counterparts, they may have a role in stabilizing low oxidation state species.

Structural Characterization by X-ray Crystallography of Other Compounds

Although unintended, the low-temperature X-ray crystal structure of $Xe_2F_3^+AsF_6^-$ was obtained in this work by the reaction of excess $XeF^+AsF_6^-$ with $(CH_3)_3CC{\equiv}N$ in anhydrous HF solvent. The structure is in agreement with the room temperature structure previously reported by Bartlett *et al.* in 1974,[21] however the final R-factor and precision of the geometrical parameters obtained in the present work are significantly smaller partially due to the refinement of a two-fold orientationally disordered AsF_6^- anion that was missed in the previous determination.

CONCLUSION

Table 7.1 summarizes the Xe–F and Xe–L bond lengths determined from X-ray crystallography for the Xe(II) derivatives described in this Thesis. In the Xe–N bonded compounds, the order of increasing ionic character of the Xe–F bonds parallels the increase in the covalent nature of the Xe–N bonds as follows: *s*-$C_3F_3N_2N{-}XeF^+AsF_6^-{\cdot}2.5BrF_5$ < $C_5F_5N{-}XeF^+AsF_6^-{\cdot}2.5BrF_5$ < $HC{\equiv}N{-}XeF^+AsF_6^-$ < $(CH_3)_3CC{\equiv}N{-}XeF^+AsF_6^-$ < $CH_3C{\equiv}N{-}XeF^+AsF_6^-{\cdot}HF$ < $F_5TeN(H)Xe^+AsF_6^-$, indicating that *s*-$C_3F_3N_2N{-}XeF^+AsF_6^-{\cdot}2.5BrF_5$ contains the weakest Xe–N bond known in this series.

Table 7.1 Summary of the Xe–F and Xe–L (L = N, O) Bond Lengths Determined by X-ray Crystallography for the Xe(II) Compounds Described in this Thesis

Compound	Xe–F (Å)[a]	Xe–L (Å)
$F_5TeN(H)Xe^+AsF_6^-$	2.580(3)	2.044(4)
$CH_3C{\equiv}N{-}XeF^+AsF_6^-\cdot HF$	1.957(5)	2.179(7)
$(CH_3)_3CC{\equiv}N{-}XeF^+AsF_6^-$	1.952(3)	2.212(4)
$HC{\equiv}N{-}XeF^+AsF_6^-$	1.936(2)	2.235(3)
$C_5F_5N{-}XeF^+AsF_6^-\cdot 2.5BrF_5$	1.932(6)	2.287(7)
$s\text{-}C_3F_3N_2N{-}XeF^+AsF_6^-\cdot 2.5BrF_5$	1.931(5)	2.316(6)
$XeOTeF_5^+AsF_6^-$	2.24(3)	1.96(4)
$XeOSeF_5^+AsF_6^-$	2.31(4)	2.04(4)
$Xe(OTeF_5)_2$		2.119(11), 2.112(12)
$Xe(OSeF_5)_2$		2.16(3)

[a] Represents the bridging bond length between xenon and a fluorine atom of AsF_6^- in the $F_5TeN(H)Xe^+AsF_6^-$ and $XeOChF_5^+AsF_6^-$ (Ch = Te, Se) salts.

Prior to these X-ray crystal structure determinations, Raman and multi-NMR spectroscopic parameters served as probes in assessing the bonding in these species. It was observed for the R–C≡N–$XeF^+AsF_6^-$ (R = H, CH_3, $(CH_3)_3C$), *s*-$C_3F_3N_2N$–$XeF^+AsF_6^-$, and C_5F_5N–$XeF^+AsF_6^-$ adducts that as the covalent nature of the Xe–N bond increases, the base strength of the nitrogen ligand group increases, the effective electronegativity of the nitrogen atom decreases, and the ^{129}Xe nucleus becomes more shielded in the ^{129}Xe NMR spectrum (see Table 3.3). Additionally, the Xe–F and Xe–N bond length trends correlate with ν(Xe–L) (L = F, N) provided from Raman spectroscopy, which signify increased covalency of the Xe–L bonds with shifts to higher frequency, and *vice versa*. Therefore, among these adducts which have formal sp- or sp^2-hybridization at the nitrogen center, the effective group electronegativities of the nitrile bases are lower and the Xe–N bonds are the most covalent.

The highly shielded ^{129}Xe NMR resonance for the $F_5TeN(H)Xe^+$ cation compared to those of other Xe–N bonded compounds is consistent with it having the most covalent Xe–N bond. As a consequence, the Xe–F bond is completely ionized in solution and only a weak fluorine bridge interaction is observed between the anion and the cation in the solid-state. The X-ray structural data and ^{129}Xe NMR resonances for the isoelectronic $F_5TeN(H)Xe^+$ and F_5TeOXe^+ cations, as well as for XeF^+, also reflect the higher electronegativities of the $OTeF_5$ and F ligands compared to the $F_5TeN(H)$ group (see Table 5.3). Generally the xenon nucleus becomes more shielded with increasing ionic character of the Xe···F bridge bond in the order: $XeF^+AsF_6^-$ < $XeOChF_5^+AsF_6^-$ <

$F_5TeN(H)Xe^+AsF_6^-$. In the cases where $OChF_5$ groups replace both fluorine atoms in XeF_2, the ^{129}Xe shieldings also increase. The differences between ionic characters of the Xe···F bridging bonds in the $OChF_5$, F, and $F_5TeN(H)$ analogues correlate with the relative electronegativities of these groups, and subsequent Lewis acidities of the cations, $F_5TeN(H)Xe^+$, $XeChOTeF_5^+$, and XeF^+. Based on the trends, the relative group electronegativities increase in the order: $F_5TeN(H) > OSeF_5 > OTeF_5 > F$.

DIRECTIONS FOR FUTURE RESEARCH

The successful preparations and low-temperature structural characterizations of the xenon(II)-nitrogen bonded species in the present work were achieved by utilizing the hard Lewis acid, XeF^+, to form adducts with a variety of oxidatively resistant Lewis nitrogen bases having first adiabatic ionization potentials higher than the estimated electron affinity of XeF^+ (10.9 eV). Several organic nitrogen bases were studied (*i.e.*, nitriles, perfluoropyridine, trifluorotriazine) and a single inorganic ammonium salt. Several other Xe–N bonded adduct cations not investigated in the present work which should also be characterized by X-ray crystallography include the perfluoroalkanenitriles, $R_FC{\equiv}N{-}XeF^+AsF_6^-$ (R_F = CF_3, C_2F_5, *n*-C_3F_7). These adducts have previously been synthesized and characterized by Raman and multi-NMR spectroscopy[14,58] and based on the trends observed in these methods for the compounds studied in the present work, the Xe–N bonds in these adducts should be slightly more ionic than that found in $(CH_3)_3CC{\equiv}N{-}XeF^+$, but more covalent than that in $HC{\equiv}N{-}XeF^+$. The $HC{\equiv}N{-}KrF^+$ cation would be of great interest to characterize, however, its AsF_6^- salt is explosive in

the solid-state. Although, $CF_3C{\equiv}N{-}KrF^+$, $C_2F_5C{\equiv}N{-}KrF^+$, and $n\text{-}C_3F_7C{\equiv}N{-}KrF^+$ have been characterized by NMR spectroscopy,[72] nothing is known about their solid-state stabilities. It may prove possible to obtain crystalline material suitable for an X-ray structure determination of one or more of these cations with AsF_6^- as the counterion.

The series $F_3S{\equiv}N{-}XeF^+$, $F_4S{=}N{-}Xe^+$, and $F_5SN(H)Xe^+$ have previously been synthesized and characterized by Raman and multi-NMR spectroscopy.[14] Definitive X-ray crystal structures of this series of cations would provide a better understanding of the bonding and effects of group electronegativity anticipated when the nitrogen lone pair hybridization changes from sp to sp^2 to sp^3. Additionally, the crystal structure of $F_5SN(H)Xe^+$ would be the second definitive example where an inorganic base is utilized as a precursor to a compound where xenon is bonded to formally sp^3-hybridized nitrogen. The geometrical parameters obtained for this compound could be compared with those of the analogous $F_5TeN(H)Xe^+$ cation described in this Thesis.

The successful preparations of the $F_5TeN(H)Xe^+$ and $F_5SN(H)Xe^+$ cations suggest that $F_3CN(H)Xe^+$ may also be prepared by the reaction of the inorganic base, CF_3NH_2, with XeF^+ in anhydrous HF solvent [eq (7.14)]. Characterization of this cation by low-

$$CF_3NH_3^+AsF_6^- + XeF^+AsF_6^- \xrightarrow{HF} F_3CN(H)Xe^+AsF_6^- + HF \qquad (7.14)$$

temperature X-ray crystallography would give the third definitive example where xenon is bonded to a formally sp^3-hybridized nitrogen.

The successful structural characterizations of the $XeOChF_5^+AsF_6^-$ salts (Ch = Te, Se) by X-ray crystallography suggests that it should also be possible to structurally characterize $Sb_2F_{11}^-$ salts of $XeOChF_5^+$. The $XeOTeF_5^+Sb_2F_{11}^-$ salt has previously been

prepared by the solvolysis of $XeOTeF_5^+AsF_6^-$ in SbF_5 at room temperature resulting in displacement of AsF_5 by the stronger fluoride acceptor SbF_5 [eq (7.15)].[56] The structures

$$XeOTeF_5^+AsF_6^- + 2SbF_5 \longrightarrow XeOTeF_5^+Sb_2F_{11}^- + AsF_5 \qquad (7.15)$$

of the weakly basic $Sb_2F_{11}^-$ salts would represent the closest approximations to free $XeOChF_5^+$ cations, similar to that observed for $XeF^+Sb_2F_{11}^-$ which has a very weak fluorine bridge interaction between the xenon atom and the $Sb_2F_{11}^-$ anion.[11,20]

By analogy with the Lewis acid character of XeF^+ and the syntheses and structural characterizations of several Xe–N bonded adduct cations, the weaker Lewis acid behaviors of $XeOChF_5^+$ (Ch = Te, Se) have recently been utilized for the isolation and characterization by NMR spectroscopy of $CH_3C{\equiv}N{-}XeOTeF_5^+$,[17] $C_5F_5N{-}XeOTeF_5^+$,[17] *s*-$C_3F_3N_2N{-}XeOTeF_5^+$,[17,130] and $F_3S{\equiv}N{-}XeOSeF_5^+$.[17] Characterization of these cations and others such as $HC{\equiv}N{-}XeOChF_5^+$ and $(CH_3)_3CC{\equiv}N{-}XeOChF_5^+$ by low-temperature X-ray crystallography would represent the first structurally detailed examples of xenon compounds containing novel N–Xe–O linkages.

Characterization by low-temperature X-ray crystallography of the first fully substituted $OTeF_5$ salt prepared to date, namely $XeOTeF_5^+Sb(OTeF_5)_6^-$, should also be attempted [eqs (7.16), (7.17)], along with the syntheses and structural characterizations

$$Sb(OTeF_5)_3 + Xe(OTeF_5)_2 \xrightarrow{SO_2ClF} Sb(OTeF_5)_5 + Xe \qquad (7.16)$$

$$Sb(OTeF_5)_5 + Xe(OTeF_5)_2 \longrightarrow XeOTeF_5^+Sb(OTeF_5)_6^- \qquad (7.17)$$

of Xe–N bonded adducts of this compound with several Lewis nitrogen base ligands (D) [eq (7.18)].

$$D + XeOTeF_5^+Sb(OTeF_5)_6^- \longrightarrow D\text{–}XeOTeF_5^+Sb(OTeF_5)_6^- \quad (7.18)$$

Lastly, the isolation and characterization of the $P(OTeF_5)_4^-$ anion would provide a comparison with the weakly coordinating $Pn(OTeF_5)_4^-$ anions (Pn = Sb, As) described in this Thesis. The $P(OTeF_5)_4^-$ anion is the $OTeF_5$ analog of PF_4^-, which has only recently been synthesized and fully characterized.[116] The synthetic route for the preparation of the $P(OTeF_5)_4^-$ anion should be analogous to that used for $Pn(OTeF_5)_4^-$ [eq (7.19)].

$$P(OTeF_5)_3 + NR_4^+OTeF_5^- \xrightarrow{SO_2ClF} NR_4^+P(OTeF_5)_4^- \ (R = CH_3, CH_2CH_3) \quad (7.19)$$

Although the precursor, $P(OTeF_5)_3$, has not yet been synthesized, there are several possible synthetic approaches to this compound as given by equations (7.20) – (7.22).

$$PCl_3 + 3HOTeF_5 \longrightarrow P(OTeF_5)_3 + 3HCl \quad (7.20)$$

$$PF_3 + B(OTeF_5)_3 \longrightarrow P(OTeF_5)_3 + BF_3 \quad (7.21)$$

$$PCl_3 + 3ClOTeF_5 \longrightarrow P(OTeF_5)_3 + 3Cl_2 \quad (7.22)$$

The $P(OTeF_5)_4^-$ anion should exhibit intramolecular exchange analogous to the $Pn(OTeF_5)_4^-$ anions. However, the activation energy barrier for the exchange is expected to be smaller than that obtained for the PF_4^- anion due to the larger $OTeF_5$ ligands. Consequently, unlike the $Pn(OTeF_5)_4^-$ anions, it should be possible to slow down the exchange in $P(OTeF_5)_4^-$ sufficiently on the NMR time scale to observe separate $OTeF_5$ environments.

APPENDIX

Table A Crystal Data and Structure Refinements.

Structures from Chapter 3

	$HC{\equiv}N{-}XeF^+AsF_6^-$	$HC{\equiv}NH^+AsF_6^-$	$CH_3C{\equiv}N{-}XeF^+AsF_6^-{\cdot}HF$	$(CH_3)_3CC{\equiv}N{-}XeF^+AsF_6^-$
Empirical formula	$AsCF_7HNXe$	$AsCF_6H_2N$	$AsC_4F_7H_9NXe$	$AsC_5F_7H_9NXe$
Formula weight (g mol^{-1})	366.25	216.96	400.28	422.35
Temperature (°C)	-122	-122	-125	-127
Wavelength (Å)	0.71073	0.71073	0.71073	0.71073
Crystal system	Orthorhombic	Triclinic	Triclinic	Orthorhombic
Space group (No.)	*Pbca* (61)	$P\bar{1}$ (2)	$P\bar{1}$ (2)	$Pca2_1$ (29)
Unit cell dimensions	a = 9.8025(8) Å	a = 5.051(2) Å	a = 7.8397(8) Å	a = 17.9177(8) Å
	b = 10.5354(8) Å	b = 5.088(2) Å	b = 7.9901(8) Å	b = 6.0500(2) Å
	c = 14.5381(11) Å	c = 5.359(2) Å	c = 8.5539(9) Å	c = 10.9365(4) Å
	$\alpha = 90^\circ$	$\alpha = 98.983(6)^\circ$	$\alpha = 94.873(2)^\circ$	$\alpha = 90^\circ$
	$\beta = 90^\circ$	$\beta = 98.96(2)^\circ$	$\beta = 114.9090(10)^\circ$	$\beta = 90^\circ$
	$\gamma = 90^\circ$	$\gamma = 95.146(4)^\circ$	$\gamma = 94.045(3)^\circ$	$\gamma = 90^\circ$
Volume ($Å^3$)	1501.4(2)	133.48(10)	480.85(9)	1185.54
Z	8	1	2	4
Density (calculated) (g cm^{-3})	3.241	2.699	2.765	2.366
Absorption coefficient (mm^{-1})	9.033	6.414	7.078	5.737
F(000)	1312	102	364	784
Crystal size (mm^3)	0.34 × 0.20 × 0.05	0.12 × 0.10 × 0.06	0.12 × 0.10 × 0.04	0.22 × 0.05 × 0.04
θ range for data collection	2.80 to 27.41°	3.91 to 30.48°	2.65 to 27.49°	2.27 to 27.35°
Index ranges	$-12 \le h \le 12$	$-7 \le h \le 7$	$-10 \le h \le 10$	$-23 \le h \le 23$
	$-13 \le k \le 13$	$-7 \le k \le 7$	$-7 \le k \le 10$	$-7 \le k \le 7$
	$-17 \le l \le 18$	$-7 \le l \le 7$	$-11 \le l \le 11$	$-14 \le l \le 14$

Table A (continued)

Reflections collected	11913	3881	3300	10673
Independent reflections	1710 [R_{int} = 0.0301]	817 [R_{int} = 0.0191]	1676 [R_{int} = 0.0181]	2664 [R_{int} = 0.0398]
Refinement method	Full-matrix least-squares on F^2	Full-matrix least-squares on F^2	Full-matrix least-squares on F^2	Full-matrix least-squares on F^2
Data/restraints/parameters	1710 / 0 / 105	817 / 0 /48	1672 / 0 / 122	2661 / 1 / 173
Goodness-of-fit on F^2	1.058	1.273	1.076	0.976
Final R indices [$I > 2\sigma(I)$]	R_1 = 0.0210 wR_2 = 0.0560	R_1 = 0.0431 wR_2 = 0.1191	R_1 = 0.0530 wR_2 = 0.1357	R_1 = 0.0257 wR_2 = 0.0443
R indices (all data)	R_1 = 0.0241 wR_2 = 0.0574	R_1 = 0.0456 wR_2 = 0.1216	R_1 = 0.0623 wR_2 = 0.1448	R_1 = 0.0377 wR_2 = 0.0468
Extinction coefficient	0.0082(3)	0.17(2)	0.003(2)	0.0016(2)
Absol. structure parameter				0.053(12)
Largest difference peak and hole (e $Å^{-3}$)	0.784 and -0.836	1.204 and -0.932	1.858 and –1.964	0.490 and -0.366

Table A (continued)

	***s*-$C_3F_3N_2N$–$XeF^+AsF_6^-$·2.5BrF_5**	**C_5F_5N–$XeF^+AsF_6^-$ · 2.5BrF_5**	**$Xe_2F_3^+AsF_6^-$**
Empirical formula	$AsC_3F_{22.5}N_3XeBr_{2.5}$	$AsC_5F_{24.5}NXeBr_{2.5}$	AsF_9Xe_2
Formula weight (g mol^{-1})	911.55	945.55	508.52
Temperature (°C)	-122	-122	-127
Wavelength (Å)	0.71073	0.71073	0.71073
Crystal system	Triclinic	Triclinic	Monoclinic
Space group (No.)	$P\bar{1}$ (2)	$P\bar{1}$ (2)	C_2/c (15)
Unit cell dimensions	a = 7.831(3) Å	a = 7.871(3) Å	a = 25.756(3) Å
	b = 10.353(4) Å	b = 10.353(4) Å	b = 8.5556(11) Å
	c = 13.282(5) Å	c = 13.282(5) Å	c = 15.356(2) Å
	α = 75.179(9)°	α = 75.179(9)°	α = 90°
	β = 75.797(6)°	β = 75.797(6)°	β = 126.592(5)°
	γ = 73.135(7)°	γ = 73.135(7)°	γ = 90°
Volume ($Å^3$)	979.0(6)	1033.0(7)	2716.9(6)
Z	2	2	12
Density (calculated) (g cm^{-3})	3.092	3.040	3.730
Absorption coefficient (mm^{-1})	8.746	8.306	11.203
F(000)	832	864	2664
Crystal size (mm^3)	0.21 × 0.07 × 0.03	0.2 × 0.06 × 0.06	0.2 × 0.2 × 0.2
θ range for data collection	1.61 to 27.61°	2.10 to 27.52°	1.97 to 27.76°
Index ranges	$-10 \le h \le 10$	$-10 \le h \le 10$	$-33 \le h \le 33$
	$-13 \le k \le 13$	$-13 \le k \le 13$	$-11 \le k \le 11$
	$-16 \le l \le 16$	$-18 \le l \le 18$	$-19 \le l \le 19$

Table A (continued)

Reflections collected	9403	10349	12899
Independent reflections	3682 [R_{int} = 0.0294]	3930 [R_{int} = 0.0560]	2984 [R_{int} = 0.0618]
Refinement method	Full-matrix least-squares on F^2	Full-matrix least-squares on F^2	Full-matrix least-squares on F^2
Data/restraints/parameters	3679 / 0 /308	3923 / 0 / 339	2980 / 0 / 175
Goodness-of-fit on F^2	1.052	0.989	1.034
Final R indices [$I > 2\sigma(I)$]	R_1 = 0.0473	R_1 = 0.0580	R_1 = 0.0456
	wR_2 = 0.1188	wR_2 = 0.1447	wR_2 = 0.0823
R indices (all data)	R_1 = 0.0608	R_1 = 0.0892	R_1 = 0.0779
	wR_2 = 0.1280	wR_2 = 0.1621	wR_2 = 0.0924
Extinction coefficient	0.0017(5)	0.0030(6)	0.00021(3)
Largest difference peak and hole (e $Å^{-3}$)	2.203 and -1.410	1.874 and -1.686	1.643 and -1.122

Table A (continued)

Structures from Chapter 4

	$F_5TeNH_3^+AsF_6^-$	$F_5TeN(H)Xe^+AsF_6^-$	F_5TeNH_2	F_5TeNH_2
Empirical formula	$H_3AsF_{11}NTe$	$HAsF_{11}NXe$	H_2F_5NTe	H_2F_5NTe
Formula weight	428.55 g mol^{-1}	557.84 g mol^{-1}	238.63 g mol^{-1}	238.63 g mol^{-1}
Temperature	-109 °C	-109 °C	-5 °C	-113 °C
Wavelength	0.71073 Å	0.71073 Å	0.71073 Å	0.71073 Å
Crystal system	Monoclinic	Triclinic	Cubic	Monoclinic
Space group (No.)	$P2_1/m$ (11)	$P\bar{1}$ (2)	$I\bar{4}3m$ (217)	$P2_1$ (4)
Unit cell dimensions	a = 6.6397(2) Å	a = 5.3898(3) Å	a = 6.404(5) Å	a = 5.163(2) Å
	b = 17.00680(10) Å	b = 7.0580(3) Å	b = 6.404(5) Å	b = 9.083(4) Å
	c = 11.1684(3) Å	c = 12.5326(4) Å	c = 6.404(5) Å	c = 5.262(2) Å
	$\alpha = 90°$	$\alpha = 86.736(3)°$	$\alpha = 90°$	$\alpha = 90°$
	$\beta = 105.636(2)°$	$\beta = 84.064(3)°$	$\beta = 90°$	$\beta = 112.223(8)°$
	$\gamma = 90°$	$\gamma = 85.531(3)°$	$\gamma = 90°$	$\gamma = 90°$
Volume	1214.47(5) $Å^3$	472.18(4) $Å^3$	262.6(4) $Å^3$	228.4(2) $Å^3$
Z	6	2	2	2
Density (calculated)	3.516 g cm^{-3}	3.924 g cm^{-3}	3.018 g cm^{-3}	3.469 g cm^{-3}
Absorption coefficient	7.889 mm^{-1}	10.295 mm^{-1}	5.665 mm^{-1}	6.512 mm^{-1}
F(000)	1164	492	212	212
Crystal size (mm^3)	0.4 × 0.15 × 0.1	0.8 × 0.16 × 0.15	0.35 × 0.26 × 0.12	0.15 × 0.08 × 0.02
		0.22 × 0.08 × 0.07		
θ range for data collection	1.89 to 27.51°	1.64 to 28.75°	4.50 to 27.23 °	4.49 to 27.89°
Index ranges	$-8 \le h \le 8$	$-7 \le h \le 7$	$-7 \le h \le 8$	$-6 \le h \le 6$
	$-21 \le k \le 22$	$-9 \le k \le 9$	$-8 \le k \le 8$	$-11 \le k \le 11$
	$-14 \le l \le 14$	$0 \le l \le 16$	$-8 \le l \le 8$	$-6 \le l \le 6$
Reflections collected	11924	2202	1202	2333
Independent reflections	2705 [R_{int} = 0.0296]	2202 [R_{int} = 0.0000]	72 [R_{int} = 0.0348]	942 [R_{int} = 0.0194]

Table A (continued)

Refinement method	Full-matrix least-squares on F^2	Full-matrix least-squares on F^2	Full-matrix least-squares on F^2	Full-matrix least-squares on F^2
Data / restraints / parameters	2705 / 0 /208	2199 / 0 / 141	72 / 0 / 7	938 / 1 / 65
Goodness-of-fit on F^2	1.066	1.080	0.912	1.078
Final R indices [$I > 2\sigma(I)$]	$R_1 = 0.0271$ $wR_2 = 0.0735$	$R_1 = 0.0373$ $wR_2 = 0.0946$	$R_1 = 0.0324$ $wR_2 = 0.1001$	$R_1 = 0.0415$ $wR_2 = 0.1132$
R indices (all data)	$R_1 = 0.0335$ $wR_2 = 0.0764$	$R_1 = 0.0441$ $wR_2 = 0.0972$	$R_1 = 0.0325$ $wR_2 = 0.1001$	$R_1 = 0.0467$ $wR_2 = 0.1180$
Extinction coefficient	0.0042(2)	0.0176(14)	0.001(10)	0.051(8)
Largest diff. peak and hole (e $Å^{-3}$)	1.077 and -0.893	1.427 and -1.910	0.395 and -0.332	1.675 and -2.611

Table A (continued)

Structures from Chapter 5

	$XeOTeF_5^+AsF_6^-$	$XeOSeF_5^+AsF_6^-$	$Xe(OTeF_5)_2$	$Xe(OSeF_5)_2$
Empirical formula	$AsF_{11}OTeXe$	$AsF_{11}OSeXe$	$F_{10}O_2Te_2Xe$	$F_{10}O_2Se_2Xe$
Formula weight	558.82	510.18	608.50	511.22
Temperature	-60	-113	-127	-45
Wavelength	0.71073 Å	0.71073 Å	0.71073 Å	0.71073 Å
Crystal system	Tetragonal	Tetragonal	Monoclinic	Rhombohedral
Space group (No.)	*P4/n* (85)	*P4/n* (85)	$P2_1/c$ (14)	$R\bar{3}$ (148)
Unit cell dimensions	a = 6.13560(10) Å	a = 6.1195(7) Å	a = 10.289(2) Å	a = 8.3859(6) Å
	b = 6.13560(10) Å	b = 6.1195(7) Å	b = 9.605(2) Å	b = 8.3859(6) Å
	c = 13.8232(2) Å	c = 13.0315(2) Å	c = 10.478(2) Å	c = 12.0355(13) Å
	$\alpha = 90^\circ$	$\alpha = 90^\circ$	$\alpha = 90^\circ$	$\alpha = 90^\circ$
	$\beta = 90^\circ$	$\beta = 90^\circ$	$\beta = 106.599(4)^\circ$	$\beta = 90^\circ$
	$\gamma = 90^\circ$	$\gamma = 90^\circ$	$\gamma = 90^\circ$	$\gamma = 120^\circ$
Volume	520.383(14) $Å^3$	488.01(8) $Å^3$	992.3(3) $Å^3$	732.98(11) $Å^3$
Z	2	2	4	3
Density (calculated)	3.566 g cm^{-3}	3.472 g cm^{-3}	4.073 g cm^{-3}	3.474 g cm^{-3}
Absorption coefficient	9.347 mm^{-1}	10.766 mm^{-1}	9.368 mm^{-1}	11.108 mm^{-1}
F(000)	492	456	1056	684
Crystal size (mm^3)	0.6 × 0.3 × 0.02	0.15 × 0.08 × 0.02	0.25 × 0.20 × 0.06	0.3 × 0.25 × 0.2
θ range for data collection	1.47 to 27.35°	1.56 to 27.51°	2.07 to 27.53 °	3.28 to 27.40°
Index ranges	$-7 \le h \le 7$	$-7 \le h \le 7$	$-13 \le h \le 13$	$-10 \le h \le 10$
	$-7 \le k \le 7$	$-5 \le k \le 7$	$-12 \le k \le 12$	$-10 \le k \le 10$
	$-17 \le l \le 17$	$-16 \le l \le 16$	$-13 \le l \le 13$	$-15 \le l \le 15$
Reflections collected	4623	2891	9271	2134

Table A (continued)

Independent reflections	591 [R_{int} = 0.0780]	539 [R_{int} = 0.0367]	2135 [R_{int} = 0.1208]	376 [R_{int} = 0.0350]
Refinement method	Full-matrix least-squares on F^2	Full-matrix least-squares on F^2	Full-matrix least-squares on F^2	Full-matrix least-squares on F^2
Data / restraints / parameters	590 / 46 / 91	539 / 12 / 71	2133 / 0 / 140	376 / 0 / 44
Goodness-of-fit on F^2	0.923	1.141	0.946	1.363
Final R indices [$I > 2\sigma(I)$]	R_1 = 0.0453 wR_2 = 0.1345	R_1 = 0.0730 wR_2 = 0.1664	R_1 = 0.0680 wR_2 = 0.1589	R_1 = 0.0534 wR_2 = 0.1676
R indices (all data)	R_1 = 0.0506 wR_2 = 0.1395	R_1 = 0.0856 wR_2 = 0.1769	R_1 = 0.1299 wR_2 = 0.1900	R_1 = 0.0720 wR_2 = 0.1907
Extinction coefficient	0.008(3)	0.001(2)	0.0020(4)	0.002(2)
Largest diff. peak and hole (e $Å^{-3}$)	1.113 and -0.673	4.453 and -1.696	2.715 and -3.795	1.271 and -0.904

Table B Atomic Coordinates ($\times 10^4$) and Equivalent Isotropic Displacement Coefficients ($Å^2 \times 10^3$).

Structures from Chapter 3

	x	y	z	U(eq)[a]
		HC≡N–$XeF^+AsF_6^-$		
Xe(1)	1878(1)	9936(1)	934(1)	21(1)
As(1)	1253(1)	8006(1)	3603(1)	20(1)
F(1)	189(2)	9044(2)	693(1)	30(1)
F(2)	650(2)	6502(2)	3379(1)	35(1)
F(3)	2643(2)	7704(2)	2895(2)	34(1)
F(4)	-139(2)	8284(2)	4304(1)	36(1)
F(5)	1857(2)	9507(2)	3832(2)	39(1)
F(6)	373(2)	8593(2)	2669(1)	31(1)
F(7)	2185(2)	7433(2)	4527(1)	34(1)
N(1)	3827(3)	10965(3)	1216(2)	27(1)
C(1)	4823(3)	11442(3)	1353(2)	26(1)
H(1)	5576(51)	11921(46)	1434(33)	57(14)
		HC≡$NH^+AsF_6^-$		
As(1)	5000	5000	5000	18(1)
F(1)	2214(7)	3066(7)	5591(7)	30(1)
F(2)	3066(7)	5730(8)	2329(7)	33(1)
F(3)	4153(8)	7753(7)	6830(7)	34(1)
N(1)	432(11)	528(11)	9307(11)	26(1)
C(1)	432(11)	528(11)	9307(11)	26(1)

Table B (continued)

		$CH_3C{\equiv}N{-}XeF^+AsF_6^-{\cdot}HF$		
Xe(1)	7476(1)	8008(1)	3966(1)	23(1)
As(1)	5515(1)	7461(1)	7681(1)	22(1)
F(1)	10033(7)	8499(8)	5816(7)	37(2)
F(2)	7199(8)	9035(8)	7810(8)	38(2)
F(3)	6614(9)	6001(8)	6927(8)	41(2)
F(4)	6875(9)	7119(11)	9772(8)	50(2)
F(5)	4393(8)	8918(8)	8362(7)	34(1)
F(6)	3787(9)	5909(8)	7481(9)	42(2)
F(7)	4150(8)	7808(9)	5549(7)	36(2)
F(8)	10786(9)	6622(11)	3168(10)	61(2)
N(1)	4588(11)	7462(11)	1939(10)	26(2)
C(1)	3103(13)	7303(13)	892(12)	26(2)
C(2)	1189(14)	7125(18)	-479(14)	40(3)

		$(CH_3)_3CC{\equiv}N{-}XeF^+AsF_6^-$		
F(1)	8538(2)	12815(5)	-5865(3)	47(1)
Xe(1)	7679(1)	11629(1)	-4987(1)	26(1)
N(1)	6703(2)	10192(6)	-4035(4)	36(1)
C(1)	6233(3)	9093(7)	-3668(5)	28(1)
C(2)	5589(3)	7795(8)	-3187(5)	28(1)
C(3)	5580(5)	8077(12)	-1795(5)	52(2)
C(4)	4880(3)	8749(10)	-3784(6)	44(2)
C(5)	5707(4)	5349(9)	-3544(6)	43(1)
As(1)	8314(1)	6461(1)	-2182(1)	29(1)
F(2)	7895(2)	6532(4)	-751(2)	41(1)
F(3)	9125(2)	7476(8)	-1590(4)	70(1)
F(4)	8713(2)	6393(5)	-3608(3)	60(1)

Table B (continued)

F(5)	8010(2)	9093(5)	-2448(3)	63(1)
F(6)	8618(2)	3831(5)	-1880(4)	82(2)
F(7)	7499(3)	5427(7)	-2769(4)	82(1)
H(1)	6001(39)	7703(125)	-1382(69)	72(25)
H(2)	5489(41)	9685(111)	-1530(72)	80(23)
H(3)	5149(30)	7447(83)	-1463(46)	33(15)
H(4)	4778(36)	10135(104)	-3346(68)	74(24)
H(5)	4479(28)	7961(74)	-3316(45)	32(14)
H(6)	4879(29)	8722(68)	-4829(60)	54(16)
H(7)	5773(29)	5378(94)	-4429(51)	57(18)
H(8)	5333(29)	4611(86)	-3199(49)	45(17)
H(9)	6153(28)	4994(71)	-3027(44)	28(13)

s-$C_3F_3N_2N$–$XeF^+AsF_6^- \cdot 2.5BrF_5$

F(1)	4466(8)	6468(5)	9929(4)	51(1)
Xe(1)	4074(1)	8181(1)	8911(1)	27(1)
N(1)	3572(7)	10264(6)	7723(4)	24(1)
C(1)	2643(9)	11440(8)	8036(6)	25(2)
F(2)	2085(6)	11328(4)	9055(3)	33(1)
N(3)	2258(8)	12655(7)	7420(5)	29(1)
C(3)	2875(9)	12629(8)	6415(6)	26(2)
F(4)	2493(6)	13795(5)	5751(4)	40(1)
N(5)	3857(8)	11564(7)	5967(5)	28(1)
C(5)	4174(9)	10425(8)	6653(6)	25(2)
F(6)	5190(6)	9314(5)	6340(3)	34(1)
As(1)	1884(1)	19342(1)	1967(1)	22(1)
F(7)	380(6)	20461(5)	1214(4)	38(1)

Table B (continued)

F(8)	3401(6)	18190(5)	2730(4)	34(1)
F(9)	1716(6)	17973(5)	1511(4)	37(1)
F(10)	3695(5)	19570(5)	953(3)	35(1)
F(11)	112(6)	19107(5)	3008(3)	36(1)
F(12)	2121(5)	20676(4)	2453(3)	33(1)
Br(1)	795(1)	8041(1)	6053(1)	27(1)
F(13)	2541(7)	6812(5)	5590(4)	52(1)
F(14)	-393(7)	7715(6)	5211(4)	51(1)
F(15)	1814(6)	9175(5)	4968(4)	45(1)
F(16)	2308(7)	8116(5)	6827(4)	48(1)
F(17)	156(8)	6681(6)	7028(4)	53(1)
Br(2)	3500(1)	15315(1)	2813(1)	29(1)
F(18)	3754(7)	13649(5)	3448(4)	47(1)
F(19)	4497(7)	15455(5)	3824(4)	46(1)
F(20)	1387(6)	15568(6)	3657(4)	52(1)
F(21)	2599(8)	14784(6)	1928(4)	54(1)
F(22)	5703(7)	14710(6)	2096(4)	60(2)
Br(3)	82(3)	4869(2)	376(2)	45(1)
F(23)	249(25)	4695(20)	-923(12)	95(5)
F(24)	-983(26)	3493(20)	648(22)	99(5)
F(25)	-2021(27)	6044(19)	200(21)	99(5)
F(26)	1373(26)	6085(20)	-230(22)	99(5)
F(27)	1951(27)	3492(19)	288(21)	99(5)

C_5F_5N–$XeF^+AsF_6^- \cdot 2.5BrF_5$

F(1)	5559(9)	8522(7)	-143(5)	53(2)
Xe(1)	5971(1)	6832(1)	902(1)	31(1)

Table B (continued)

N(1)	6460(10)	4806(8)	2115(6)	26(2)
C(1)	5838(13)	4768(11)	3114(8)	29(2)
F(2)	4869(7)	5931(6)	3321(4)	33(1)
F(3)	5571(8)	3585(6)	4831(4)	36(1)
F(4)	7522(8)	1220(6)	4279(4)	37(1)
F(5)	8751(8)	1251(6)	2264(4)	39(2)
F(6)	7987(8)	3708(6)	872(4)	37(1)
C(2)	6179(12)	3580(10)	3860(6)	24(2)
C(3)	7176(12)	2377(10)	3576(7)	28(2)
C(4)	7786(12)	2411(10)	2556(7)	28(2)
C(5)	7420(12)	3618(11)	1857(7)	27(2)
As(1)	8168(1)	5592(1)	-1977(1)	26(1)
F(7)	7864(8)	4293(6)	-2393(5)	38(1)
F(8)	8436(8)	6925(6)	-1595(5)	41(2)
F(9)	6432(8)	5360(7)	-968(4)	45(2)
F(10)	9864(8)	5834(7)	-2997(4)	42(2)
F(11)	6605(8)	6772(6)	-2679(5)	40(2)
F(12)	9711(8)	4469(7)	-1269(5)	43(2)
Br(1)	10628(1)	3056(1)	-3944(1)	39(1)
F(13)	12256(10)	1732(8)	-4332(6)	67(2)
F(14)	11723(9)	4110(9)	-5033(6)	71(2)
F(15)	9902(10)	1749(7)	-2947(6)	62(2)
F(16)	9342(10)	2805(9)	-4718(6)	72(2)
F(17)	12216(9)	3057(8)	-3238(6)	65(2)
Br(2)	6391(1)	9642(1)	-2806(1)	42(1)
F(18)	6056(10)	11304(7)	-3450(5)	59(2)
F(19)	5460(12)	9481(8)	-3783(7)	79(3)

Table B (continued)

F(20)	7249(10)	10176(7)	-1971(5)	57(2)
F(21)	4196(10)	10168(11)	-2139(7)	110(4)
F(22)	8508(9)	9461(8)	-3602(5)	56(2)
Br(3)	9876(3)	9992(3)	408(3)	40(1)
F(24)	8605(32)	8827(29)	666(24)	100(11)
F(26)	7997(28)	11276(23)	241(13)	61(5)
F(25)	11802(32)	8526(26)	387(17)	82(7)
F(27)	11105(37)	11262(29)	-9(20)	87(8)
F(23)	9986(47)	10073(38)	-760(21)	133(14)

$Xe_2F_3^+AsF_6^-$

F(2)	1087(3)	2455(8)	5705(5)	47(2)
Xe(1)	572(1)	2974(1)	4183(1)	25(1)
F(1)	0	3657(11)	2500	53(3)
F(3)	589(4)	-620(10)	7494(6)	74(3)
Xe(2)	1090(1)	1184(1)	7712(1)	32(1)
F(4)	1623(4)	3273(8)	7969(7)	66(2)
Xe(3)	2221(1)	4604(1)	7698(1)	26(1)
F(5)	2736(3)	5860(7)	7454(6)	43(2)
As(1)	-854(1)	2388(1)	4846(1)	27(1)
F(6)	-1024(5)	753(9)	5270(7)	78(3)
F(7)	-1481(4)	3351(11)	4688(7)	81(3)
F(8)	-696(4)	4047(8)	4405(6)	58(2)
F(9)	-222(4)	1485(10)	4986(7)	74(3)
F(10)	-1356(4)	1763(10)	3527(6)	69(2)
F(11)	-368(4)	3042(10)	6159(6)	70(2)
As(2)	2500	2500	5000	24(1)

Table B (continued)

F(12)	2325(8)	535(18)	4857(12)	51(3)
F(12A)	1968(8)	1064(18)	4815(12)	51(3)
F(13)	2808(8)	2294(20)	4249(13)	45(3)
F(13A)	2432(8)	1918(20)	3884(13)	45(3)
F(14)	1736(10)	2840(22)	3807(19)	62(5)
F(14A)	1858(10)	3722(22)	4168(19)	62(5)

[a] Equivalent isotropic U is defined as one-third of the trace of the orthogonalized U_{ij} tensor.

Structures from Chapter 4

	x	y	z	U(eq)[a]
		$F_5TeNH_3^+AsF_6^-$		
Te(1)	1677(1)	7500	3399(1)	19(1)
F(1)	2696(4)	7500	5074(2)	30(1)
F(2)	3515(3)	6742(1)	3247(2)	30(1)
F(3)	-206(3)	6740(1)	3474(2)	31(1)
N(1)	512(5)	7500	1503(3)	23(1)
Te(2)	3323(1)	5006(1)	-3344(1)	15(1)
F(4)	3673(3)	4279(1)	-2114(2)	25(1)
F(5)	2976(3)	5766(1)	-4528(2)	27(1)
F(6)	524(3)	5022(1)	-3504(2)	26(1)
F(7)	6121(3)	5014(1)	-3167(2)	26(1)
F(8)	2970(3)	4250(1)	-4518(2)	27(1)
N(2)	3735(4)	5874(1)	-2036(2)	21(1)
As(1)	0	5000	0	15(1)

Table B (continued)

F(9)	-138(3)	5653(1)	-1181(2)	29(1)
F(10)	2685(3)	4950(1)	239(2)	29(1)
F(11)	324(2)	5764(1)	1049(2)	23(1)
As(2)	1623(1)	2500	3083(1)	16(1)
F(12)	637(3)	2500	1496(2)	25(1)
F(13)	-163(2)	3222(1)	3189(2)	25(1)
F(14)	3403(3)	3220(1)	2971(2)	27(1)
F(15)	2586(4)	2500	4665(2)	28(1)
As(3)	5010(1)	7500	116(1)	17(1)
F(16)	6130(4)	7500	1697(2)	28(1)
F(17)	3269(2)	6782(1)	272(2)	25(1)
F(18)	6731(2)	6776(1)	-42(2)	24(1)
F(19)	3927(3)	7500	-1474(2)	23(1)

$F_5TeN(H)Xe^+AsF_6^-$

Te(1)	7238(1)	7452(1)	6027(1)	18(1)
F(1)	9002(8)	8228(5)	4812(3)	32(1)
F(2)	10142(7)	6840(6)	6607(3)	30(1)
F(3)	7326(8)	5080(5)	5522(3)	30(1)
F(4)	7111(8)	9810(5)	6556(3)	27(1)
F(5)	4429(7)	8098(5)	5389(3)	28(1)
N(1)	5127(10)	6557(8)	7318(4)	24(1)
Xe(1)	6087(1)	7396(1)	8745(1)	21(1)
As(1)	8885(1)	7585(1)	11485(1)	19(1)
F(6)	6577(8)	7256(6)	12491(3)	35(1)
F(7)	9059(8)	9851(5)	11852(3)	34(1)

Table B (continued)

F(8)	11075(9)	7870(6)	10437(4)	44(1)
F(9)	11104(8)	6710(6)	12269(4)	39(1)
F(10)	8539(8)	5354(5)	11078(3)	33(1)
F(11)	6617(8)	8425(6)	10647(3)	33(1)
H(1)	5255(122)	5241(92)	7357(51)	15(16)
		F_5TeNH_2 (-5 °C)		
Te(1)	0	0	0	99(1)
F/N	0	2846(26)	0	280(18)
N/F	0	2846(26)	0	280(18)
		F_5TeNH_2 (-113 °C)		
Te(1)	4764(1)	8557(13)	7466(1)	19(1)
F(1)	7138(36)	9934(9)	9679(41)	31(4)
F(2)	6996(12)	8668(21)	5418(13)	29(2)
F(3)	7148(46)	7184(11)	9787(38)	42(5)
F(4)	2548(49)	10067(10)	5433(41)	38(5)
F(5)	2816(12)	8569(24)	9791(13)	46(2)
N(1)	2566(54)	6976(14)	5176(56)	21(4)

[a] Equivalent isotropic U is defined as one-third of the trace of the orthogonalized U_{ij} tensor.

Table B (continued)

Structures from Chapter 5

	x	y	z	U(eq)[a]
		$XeOTeF_5^+AsF_6^-$		
As(1)	2500	2500	8632(1)	56(1)
F(6)	3337(118)	1953(205)	7469(14)	101(15)
F(7)	435(45)	-205(29)	8848(16)	56(6)
F(8)	4965(28)	2424(43)	9252(15)	66(5)
F(9)	2383(78)	5243(37)	8394(40)	67(12)
F(10)	-89(43)	2659(117)	8168(42)	103(17)
F(11)	1537(88)	3296(87)	9818(17)	96(10)
Xe(1)	2500	2500	11336(1)	59(1)
Te(1)	2500	2500	13809(1)	83(1)
O(1)	3620(79)	1715(83)	12619(23)	103(11)
F(1)	1605(120)	3126(143)	15015(19)	145(19)
F(2)	-186(44)	3046(66)	13322(25)	132(10)
F(3)	5283(48)	2703(99)	14263(40)	176(18)
F(4)	1652(74)	-298(45)	14090(41)	154(15)
F(5)	2040(98)	5328(48)	13572(33)	164(16)
		$XeOSeF_5^+AsF_6^-$		
As(1)	2500	2500	8551(2)	40(1)
F(6)	1593(87)	1724(86)	7349(26)	90(11)
F(7)	2595(39)	-166(38)	8881(30)	38(6)
F(8)	35(46)	2577(46)	9242(25)	48(7)
F(9)	2539(36)	5263(35)	8362(25)	33(5)
F(10)	5097(45)	2567(44)	8003(27)	52(9)

Table B (continued)

F(11)	3547(87)	3459(86)	9763(31)	88(12)
Xe(1)	2500	2500	11406(1)	43(1)
O(1)	1250(125)	1619(118)	12795(29)	97(18)
Se(1)	2500	2500	13917(2)	56(1)
F(1)	3768(74)	2936(95)	15079(30)	100(14)
F(2)	2119(75)	5115(661)	13664(29)	73(12)
F(3)	2708(48)	-53(42)	14426(23)	54(6)
F(4)	-226(73)	3066(88)	14104(41)	105(15)
F(5)	5041(56)	2257(69)	13397(30)	70(10)
		$Xe(OTeF_5)_2$		
Xe(2)	5000	10000	0	22(1)
O(2)	6781(12)	8804(12)	727(12)	30(3)
Te(2)	6761(1)	7147(1)	1606(1)	24(1)
F(6)	6780(12)	5472(12)	2493(12)	51(3)
F(7)	5248(10)	6532(11)	341(10)	35(3)
F(8)	8281(11)	7637(12)	2962(10)	41(3)
F(9)	7870(11)	6347(12)	731(11)	46(3)
F(10)	5665(11)	7833(11)	2568(10)	39(3)
Xe(1)	10000	5000	5000	21(1)
O(1)	9517(12)	3449(13)	3499(11)	34(3)
Te(1)	8303(1)	2037(1)	3494(1)	22(1)
F(1)	7067(10)	626(10)	3414(10)	35(3)
F(2)	9208(10)	1383(11)	5156(10)	35(3)
F(3)	7244(12)	2559(13)	1820(10)	41(3)
F(4)	9243(11)	843(12)	2735(11)	43(3)
F(5)	7291(9)	3169(10)	4274(9)	27(2)

Table B (continued)

		$Xe(OSeF_5)_2$ [b]		
Xe(1)	0	0	5000	75(1)
Se(1)	0	0	2276(1)	65(1)
O(1)	-563(44)	-1159(32)	3350(21)	94(9)
F(3)	2196(18)	1087(36)	2857(12)	172(9)
F(2)	-1706(75)	-887(61)	1500(33)	125(18)
F(1)	1009(54)	1965(40)	1533(38)	206(18)

[a] Equivalent isotropic U is defined as one-third of the trace of the orthogonalized U_{ij} tensor.

[b] Site occupancy factors (sof) for $Xe(OSeF_5)_2$ are: Xe(1) = 0.16667, Se(1) = 0.33333, O(1) = 0.33333, F(1) = 0.66667, F(2) = 0.33333, and F(3) = 0.66667.

Table C Anisotropic Displacement Parameters ($Å^2 \times 10^3$).[a]

Structures from Chapter 3

	U_{11}	U_{22}	U_{33}	U_{23}	U_{13}	U_{12}
			$HC{\equiv}N{-}XeF^+AsF_6^-$			
Xe(1)	20(1)	22(1)	20(1)	1(1)	1(1)	-1(1)
As(1)	17(1)	23(1)	20(1)	2(1)	-1(1)	0(1)
F(1)	25(1)	32(1)	33(1)	2(1)	-4(1)	-8(1)
F(2)	36(1)	27(1)	42(1)	-1(1)	4(1)	-8(1)
F(3)	22(1)	45(1)	35(1)	5(1)	7(1)	1(1)
F(4)	31(1)	49(1)	28(1)	3(1)	7(1)	15(1)
F(5)	39(1)	24(1)	55(1)	-3(1)	-16(1)	-3(1)
F(6)	24(1)	43(1)	25(1)	9(1)	-7(1)	0(1)
F(7)	32(1)	42(1)	29(1)	9(1)	-6(1)	9(1)
N(1)	29(1)	27(1)	24(1)	-2(1)	1(1)	1(1)
C(1)	23(2)	25(2)	29(2)	-1(1)	1(1)	1(1)
			$HC{\equiv}NH^+AsF_6^-$			
As(1)	18(1)	20(1)	20(1)	6(1)	7(1)	5(1)
F(1)	24(2)	32(2)	36(2)	11(1)	10(1)	0(1)
F(2)	31(2)	41(2)	29(2)	14(2)	2(1)	9(2)
F(3)	36(2)	30(2)	35(2)	-3(1)	12(2)	11(1)
N(1)	25(2)	28(2)	27(2)	5(2)	4(2)	6(2)
C(1)	25(2)	28(2)	27(2)	5(2)	4(2)	6(2)
			$CH_3C{\equiv}N{-}XeF^+AsF_6^-{\cdot}HF$			
Xe(1)	23(1)	26(1)	19(1)	5(1)	8(1)	3(1)
As(1)	24(1)	24(1)	20(1)	5(1)	11(1)	5(1)
F(1)	24(3)	44(4)	33(3)	8(3)	3(2)	-1(3)
F(2)	37(3)	33(4)	48(4)	1(3)	25(3)	-6(3)
F(3)	57(4)	39(4)	47(4)	10(3)	38(3)	20(3)
F(4)	44(3)	86(6)	27(3)	22(3)	17(3)	24(4)
F(5)	38(3)	32(4)	36(3)	2(3)	21(3)	7(3)
F(6)	45(3)	27(3)	64(4)	3(3)	35(3)	-1(3)
F(7)	31(3)	57(4)	21(3)	11(3)	10(2)	12(3)
F(8)	39(4)	93(7)	47(4)	-13(4)	17(3)	12(4)
N(1)	28(4)	29(5)	25(4)	8(4)	13(3)	4(4)

Table C (continued)

C(1)	27(4)	25(5)	26(4)	9(4)	12(4)	0(4)
C(2)	32(5)	62(8)	29(5)	13(5)	13(4)	11(5)

$(CH_3)_3CC{\equiv}N{-}XeF^+AsF_6^-$

F(1)	40(2)	50(2)	50(2)	9(2)	17(2)	-8(2)
Xe(1)	28(1)	23(1)	26(1)	1(1)	0(1)	-1(1)
N(1)	33(3)	30(2)	44(3)	-1(2)	5(2)	0(2)
C(1)	25(3)	25(2)	32(3)	-7(2)	2(2)	5(2)
C(2)	22(3)	24(2)	39(3)	-2(2)	1(2)	-5(2)
C(3)	67(5)	60(5)	29(3)	-5(3)	10(3)	-21(4)
C(4)	30(3)	45(4)	58(4)	14(3)	-2(3)	7(3)
C(5)	47(4)	34(3)	47(4)	1(3)	4(3)	-11(3)
As(1)	28(1)	29(1)	31(1)	-4(1)	2(1)	-3(1)
F(2)	59(2)	31(1)	35(2)	-1(1)	13(2)	-5(1)
F(3)	45(3)	111(3)	55(2)	15(2)	-12(2)	-38(2)
F(4)	60(2)	80(2)	39(2)	-10(2)	20(2)	-7(2)
F(5)	102(3)	46(2)	42(2)	7(2)	2(2)	27(2)
F(6)	96(3)	43(2)	107(4)	19(2)	62(3)	27(2)
F(7)	42(2)	131(3)	74(3)	-57(3)	6(2)	-33(3)

***s*-$C_3F_3N_2N{-}XeF^+AsF_6^-{\cdot}2.5BrF_5$**

F(1)	75(4)	30(3)	39(3)	5(2)	-10(3)	-7(3)
Xe(1)	31(1)	24(1)	25(1)	-4(1)	-3(1)	-8(1)
N(1)	20(3)	32(4)	22(3)	-5(3)	-3(2)	-11(3)
C(1)	15(3)	35(4)	26(4)	-6(3)	-7(3)	-5(3)
F(2)	37(2)	33(3)	22(2)	-1(2)	1(2)	-6(2)
N(3)	24(3)	27(4)	35(4)	-2(3)	-10(3)	-3(3)
C(3)	23(3)	26(4)	30(4)	4(3)	-7(3)	-13(3)
F(4)	36(2)	39(3)	38(3)	9(2)	-12(2)	-11(2)
N(5)	26(3)	40(4)	21(3)	-4(3)	-6(2)	-13(3)
C(5)	21(3)	33(4)	27(4)	-8(3)	-6(3)	-12(3)
F(6)	36(2)	38(3)	30(2)	-15(2)	2(2)	-10(2)
As(1)	17(1)	28(1)	22(1)	-4(1)	-2(1)	-7(1)
F(7)	32(2)	41(3)	37(3)	2(2)	-17(2)	-6(2)
F(8)	29(2)	35(3)	39(3)	2(2)	-16(2)	-7(2)
F(9)	35(2)	37(3)	47(3)	-18(2)	-8(2)	-12(2)
F(10)	24(2)	56(3)	28(2)	-14(2)	7(2)	-19(2)
F(11)	28(2)	50(3)	30(2)	-5(2)	4(2)	-20(2)
F(12)	30(2)	33(3)	39(3)	-17(2)	1(2)	-10(2)

Table C (continued)

Br(1)	23(1)	26(1)	28(1)	-6(1)	-2(1)	-6(1)
F(13)	45(3)	35(3)	69(4)	-25(3)	-1(3)	4(2)
F(14)	57(3)	62(4)	50(3)	-16(3)	-18(3)	-25(3)
F(15)	37(3)	46(3)	43(3)	2(2)	5(2)	-13(2)
F(16)	43(3)	51(3)	57(3)	-8(2)	-28(2)	-11(2)
F(17)	64(3)	46(3)	44(3)	6(2)	-3(3)	-25(3)
Br(2)	29(1)	25(1)	31(1)	-4(1)	-6(1)	-6(1)
F(18)	63(3)	25(3)	44(3)	2(2)	-7(2)	-5(2)
F(19)	49(3)	47(3)	46(3)	-4(2)	-26(2)	-12(2)
F(20)	27(3)	67(4)	51(3)	-13(3)	-2(2)	0(2)
F(21)	75(4)	55(3)	42(3)	-5(2)	-12(3)	-35(3)
F(22)	34(3)	71(4)	56(4)	-7(3)	9(2)	-5(3)
Br(3)	56(1)	41(1)	44(1)	-6(1)	-20(1)	-15(1)
F(23)	137(14)	125(13)	48(9)	-42(9)	-39(9)	-30(11)
F(24)	65(4)	50(9)	180(17)	-16(8)	-17(6)	-22(5)
F(25)	65(4)	50(9)	180(17)	-16(8)	-17(6)	-22(5)
F(26)	65(4)	50(9)	180(17)	-16(8)	-17(6)	-22(5)
F(27)	65(4)	50(9)	180(17)	-16(8)	-17(6)	-22(5)

C_5F_5N–$XeF^+AsF_6^- \cdot 2.5BrF_5$

F(1)	51(4)	34(4)	54(4)	16(3)	-9(3)	-6(3)
Xe(1)	29(1)	27(1)	33(1)	1(1)	-6(1)	-9(1)
N(1)	24(4)	31(5)	28(4)	-7(4)	-11(4)	-8(3)
C(1)	26(5)	35(6)	32(5)	-14(5)	-9(4)	-7(4)
F(2)	37(3)	23(3)	37(3)	-12(3)	-11(3)	1(2)
F(3)	39(3)	42(4)	23(3)	-9(3)	1(3)	-11(3)
F(4)	39(3)	35(3)	33(3)	-2(3)	-11(3)	-7(3)
F(5)	44(4)	28(3)	44(3)	-18(3)	-7(3)	2(3)
F(6)	44(4)	36(4)	24(3)	-6(3)	-3(3)	-2(3)
C(2)	22(5)	31(6)	17(4)	0(4)	-3(4)	-9(4)
C(3)	26(5)	27(5)	27(5)	9(5)	-9(4)	-11(4)
C(4)	25(5)	27(5)	32(5)	-3(5)	-7(4)	-9(4)
C(5)	21(5)	31(6)	28(5)	-11(5)	2(4)	-7(4)
As(1)	23(1)	28(1)	28(1)	-5(1)	-5(1)	-9(1)
F(7)	35(3)	35(4)	47(3)	-17(3)	-3(3)	-7(3)
F(8)	34(3)	41(4)	56(4)	-23(3)	-9(3)	-11(3)
F(9)	29(3)	71(5)	37(3)	-11(3)	5(3)	-25(3)
F(10)	32(3)	60(4)	36(3)	-12(3)	3(3)	-22(3)
F(11)	33(3)	34(3)	55(4)	-4(3)	-23(3)	-7(3)
F(12)	35(3)	40(4)	48(4)	1(3)	-17(3)	-3(3)

Table C (continued)

Br(1)	27(1)	30(1)	58(1)	-10(1)	-8(1)	-6(1)
F(13)	48(4)	59(5)	88(6)	-38(5)	-5(4)	9(4)
F(14)	30(4)	78(6)	86(6)	4(5)	-3(4)	-15(4)
F(15)	63(5)	33(4)	81(5)	-3(4)	-5(4)	-14(3)
F(16)	59(5)	92(7)	81(6)	-23(5)	-26(4)	-28(4)
F(17)	48(4)	51(5)	107(6)	-22(4)	-41(4)	-3(3)
Br(2)	33(1)	29(1)	57(1)	8(1)	-15(1)	-10(1)
F(18)	73(5)	33(4)	53(4)	9(3)	-4(4)	-12(3)
F(19)	89(6)	59(5)	105(6)	11(5)	-70(5)	-29(4)
F(20)	73(5)	51(5)	48(4)	-6(4)	-8(4)	-24(4)
F(21)	31(4)	149(10)	83(6)	37(6)	6(4)	-1(5)
F(22)	33(4)	76(6)	56(4)	-24(4)	-8(3)	0(3)
Br(3)	37(1)	43(1)	45(1)	-20(2)	-4(2)	-13(1)
F(24)	40(10)	76(15)	207(33)	-78(22)	12(18)	-30(9)
F(25)	61(13)	72(14)	99(15)	8(16)	-40(15)	-5(10)
F(26)	47(9)	59(12)	64(11)	10(12)	-7(11)	-18(8)
F(27)	72(16)	73(16)	129(22)	-24(16)	-2(15)	-47(13)

$Xe_2F_3^+AsF_6^-$

F(2)	46(4)	57(5)	22(3)	5(3)	12(3)	-6(3)
Xe(1)	27(1)	27(1)	22(1)	-3(1)	15(1)	-3(1)
F(1)	84(8)	41(6)	23(5)	0	26(5)	0
F(3)	68(5)	97(7)	49(5)	-6(4)	31(4)	-58(5)
Xe(2)	26(1)	45(1)	28(1)	8(1)	16(1)	-5(1)
F(4)	115(7)	43(5)	91(6)	-30(4)	89(6)	-37(4)
Xe(3)	32(1)	22(1)	26(1)	-3(1)	17(1)	-4(1)
F(5)	39(4)	34(4)	62(5)	3(3)	34(4)	-3(3)
As(1)	27(1)	26(1)	30(1)	0(1)	18(1)	2(1)
F(6)	142(8)	45(5)	99(7)	4(5)	100(7)	-12(5)
F(7)	63(5)	112(8)	86(6)	7(6)	55(5)	27(5)
F(8)	89(6)	37(4)	56(5)	-5(3)	48(5)	-10(4)
F(9)	70(5)	84(6)	99(7)	33(5)	68(6)	40(5)
F(10)	75(5)	80(6)	43(5)	-28(4)	29(4)	-41(5)
F(11)	71(5)	74(6)	33(4)	-5(4)	14(4)	-3(4)
As(2)	23(1)	31(1)	21(1)	-1(1)	15(1)	-3(1)
F(12)	72(10)	44(8)	53(6)	-2(5)	47(7)	-20(7)
F(12A)	72(10)	44(8)	53(6)	-2(5)	47(7)	-20(7)
F(13)	64(10)	55(8)	38(9)	-7(6)	42(9)	-8(7)
F(13A)	64(10)	55(8)	38(9)	-7(6)	42(9)	-8(7)
F(14)	41(8)	76(15)	72(14)	46(11)	35(10)	25(11)

Table C (continued)

F(14A)	41(8)	76(15)	72(14)	46(11)	35(10)	25(11)

[a] The anisotropic displacement factor exponent takes the form: $-2\pi^2[h^2 a^{*2} U_{11} + ... + 2hka^*b^*U_{12}]$

Structures from Chapter 4

	U_{11}	U_{22}	U_{33}	U_{23}	U_{13}	U_{12}
			$F_5TeNH_3^+AsF_6^-$			
Te(1)	20(1)	15(1)	22(1)0	7(1)	0	
F(1)	36(1)	32(2)	20(1)	0	3(1)	0
F(2)	29(1)	24(1)	37(1)	0(1)	9(1)	11(1)
F(3)	33(1)	25(1)	38(1)	4(1)	12(1)	-10(1)
N(1)	21(2)	24(2)	22(2)	0	3(1)	0
Te(2)	17(1)	14(1)	14(1)	-1(1)	4(1)	0(1)
F(4)	34(1)	17(1)	22(1)	5(1)	4(1)	-2(1)
F(5)	36(1)	24(1)	20(1)	7(1)	5(1)	0(1)
F(6)	16(1)	28(1)	31(1)	-4(1)	3(1)	-1(1)
F(7)	18(1)	29(1)	33(1)	-2(1)	7(1)	1(1)
F(8)	34(1)	24(1)	22(1)	-9(1)	5(1)	1(1)
N(2)	24(1)	18(1)	20(1)	-1(1)	4(1)	0(1)
As(1)	16(1)	15(1)	14(1)	0(1)	4(1)	-1(1)
F(9)	42(1)	23(1)	20(1)	5(1)	5(1)	-4(1)
F(10)	16(1)	30(1)	39(1)	-7(1)	5(1)	-1(1)
F(11)	27(1)	20(1)	23(1)	-7(1)	6(1)	-1(1)
As(2)	15(1)	14(1)	19(1)	0	5(1)	0
F(12)	27(1)	29(2)	18(1)	0	4(1)	0
F(13)	23(1)	20(1)	34(1)	-2(1)	10(1)	5(1)
F(14)	24(1)	21(1)	37(1)	1(1)	9(1)	-6(1)
F(15)	30(1)	30(2)	22(1)	0	4(1)	0
As(3)	18(1)	15(1)	17(1)	0	3(1)	0
F(16)	34(1)	30(2)	16(1)	0	0(1)	0
F(17)	24(1)	18(1)	34(1)	2(1)	9(1)	-5(1)
F(18)	23(1)	17(1)	32(1)	-1(1)	7(1)	5(1)
F(19)	27(1)	21(1)	18(1)	0	2(1)	0

Table C (continued)

$F_5TeN(H)Xe^+AsF_6^-$

Te(1)	17(1)	20(1)	19(1)	0(1)	-2(1)	-4(1)
F(1)	32(2)	39(2)	23(2)	1(2)	7(2)	-11(2)
F(2)	15(2)	37(2)	37(2)	5(2)	-6(2)	-3(2)
F(3)	36(2)	22(2)	31(2)	-7(2)	-2(2)	-3(2)
F(4)	36(2)	19(2)	28(2)	-4(1)	-4(2)	-7(2)
F(5)	22(2)	36(2)	28(2)	6(2)	-11(2)	-3(2)
N(1)	21(3)	30(3)	23(2)	-2(2)	-7(2)	-7(2)
Xe(1)	20(1)	24(1)	20(1)	-1(1)	-2(1)	-1(1)
As(1)	17(1)	19(1)	22(1)	0(1)	-2(1)	-2(1)
F(6)	34(3)	42(2)	29(2)	-4(2)	10(2)	-9(2)
F(7)	44(3)	20(2)	43(2)	-6(2)	-15(2)	-5(2)
F(8)	37(3)	44(2)	45(2)	2(2)	21(2)	-7(2)
F(9)	36(3)	35(2)	50(2)	6(2)	-24(2)	3(2)
F(10)	38(2)	21(2)	40(2)	-10(2)	1(2)	-3(2)
F(11)	34(2)	37(2)	29(2)	-4(2)	-16(2)	6(2)

F_5TeNH_2 (-113 °C)

Te(1)	17(1)	24(1)	16(1)	0(1)	6(1)	1(2)
F(1)	17(8)	37(7)	42(9)	-22(6)	12(7)	-9(7)
F(2)	24(2)	36(4)	32(3)	3(5)	16(2)	1(5)
F(3)	45(13)	47(9)	24(8)	9(7)	2(8)	8(9)
F(4)	43(10)	34(6)	37(8)	10(5)	15(7)	3(6)
F(5)	31(3)	86(6)	27(3)	-27(8)	17(3)	-1(11)
N(1)	17(9)	17(5)	30(9)	-10(5)	10(7)	-9(6)

F_5TeNH_2 (-5 °C)

Te(1)	99(1)	99(1)	99(1)	0	0	0
F/N	372(28)	96(8)	372(28)	0	66(283)	0
N/F	372(28)	96(8)	372(28)	0	66(283)	0

[a] The anisotropic displacement factor exponent takes the form: $-2\pi^2[h^2 a^{*2} U_{11} + \ldots + 2hka^*b^*U_{12}]$

Table C (continued)

Structures from Chapter 5

	U_{11}	U_{22}	U_{33}	U_{23}	U_{13}	U_{12}
			$XeOTeF_5^+AsF_6^-$			
Xe(1)	49(1)	49(1)	79(1)	0	0	0
Te(1)	85(1)	85(1)	79(1)	0	0	0
As(1)	42(1)	42(1)	84(1)	0	0	0
F(6)	77(29)	117(56)	109(18)	-30(34)	19(19)	9(16)
F(7)	70(12)	42(10)	56(14)	-1(10)	16(16)	0(7)
F(8)	43(8)	88(12)	67(11)	-4(12)	7(8)	-5(7)
F(9)	64(19)	50(13)	88(28)	-13(14)	-19(26)	16(10)
F(10)	62(15)	131(25)	117(33)	36(19)	-20(18)	-5(15)
F(11)	116(34)	92(22)	79(10)	-21(18)	25(20)	44(13)
			$XeOSeF_5^+AsF_6^-$			
As(1)	26(1)	26(1)	67(1)	0	0	0
F(11)	76(27)	79(27)	108(21)	-17(22)	8(22)	-41(18)
Xe(1)	31(1)	31(1)	67(1)	0	0	0
O(1)	127(50)	97(33)	66(21)	-15(24)	-10(26)	-52(28)
Se(1)	51(1)	51(1)	67(2)	0	0	0
			$Xe(OTeF_5)_2$			
Xe(1)	28(1)	18(1)	21(1)	-1(1)	13(1)	-1(1)
O(1)	46(8)	38(8)	29(7)	-18(6)	27(6)	-21(7)
Te(1)	28(1)	19(1)	23(1)	-5(1)	14(1)	-1(1)
F(1)	40(6)	29(6)	40(6)	-13(5)	19(5)	-14(5)
F(2)	41(7)	26(6)	41(6)	2(5)	14(5)	-1(5)
F(3)	60(8)	48(7)	20(5)	-3(5)	17(5)	-9(6)
F(4)	48(7)	44(7)	51(7)	-16(6)	33(6)	4(6)
F(5)	27(6)	30(6)	27(5)	-6(4)	14(4)	-3(5)
Xe(2)	26(1)	18(1)	25(1)	3(1)	11(1)	-1(1)
O(2)	36(7)	19(7)	42(8)	1(6)	25(6)	-1(6)
Te(2)	31(1)	20(1)	24(1)	4(1)	11(1)	4(1)
F(6)	70(9)	30(7)	58(8)	28(6)	28(7)	9(6)
F(7)	43(7)	31(7)	32(6)	-3(5)	9(5)	-7(5)

Table C (continued)

F(8)	41(7)	47(7)	27(6)	7(5)	0(5)	9(6)
F(9)	51(7)	42(8)	48(7)	-6(6)	18(6)	9(6)
F(10)	46(7)	43(8)	38(6)	9(5)	29(5)	7(5)
			$Xe(OSeF_5)_2$			
Xe(1)	79(1)	79(1)	69(1)	0	0	39(1)
Se(1)	66(1)	66(1)	65(1)	0	0	33(1)
O(1)	153(25)	46(11)	51(8)	-6(9)	-3(12)	27(14)
F(3)	48(6)	285(24)	107(9)	-6(10)	-13(6)	26(10)
F(2)	132(39)	119(28)	129(24)	-55(22)	-101(25)	66(27)
F(1)	187(31)	61(10)	321(40)	85(16)	39(30)	25(12)

[a] The anisotropic displacement factor exponent takes the form: $-2\pi^2[h^2 a^{*2} U_{11} + ... + 2hka^*b^*U_{12}]$

Table D Hydrogen Coordinates ($\times 10^4$) and Isotropic Displacement Parameters ($Å^2 \times 10^3$).[a]

	x	y	z	U(eq)[a]
		$CH_3C{\equiv}N{-}XeF^+AsF_6^-{\cdot}HF$		
H(1A)	1114(30)	7925(68)	-1307(54)	49
H(1B)	304(19)	7361(95)	26(17)	49
H(1C)	857(41)	5968(32)	-1083(64)	49
H(2)	10785(9)	6039(11)	4037(10)	73
		$F_5TeNH_3^+AsF_6^-$		
H(1A)	1474(25)	7500	1172(9)	34
H(1B)	-209(19)	7892(10)	1278(7)	34
H(2A)	4999(22)	5986(3)	-1786(5)	32
H(2B)	3062(12)	6271(7)	-2349(6)	32
H(2C)	3310(8)	5719(3)	-1440(11)	32
		F_5TeNH_2 (-113 °C)		
H(1A)	2730(54)	6167(14)	6213(56)	31
H(1B)	752(54)	7236(14)	4399(56)	31
H(1C)	3228(54)	6784(14)	3856(56)	31

[a] Equivalent isotropic U is defined as one-third of the trace of the orthogonalized U_{ij} tensor.

Table E Closest Atomic Contacts (in Å).

$HC{\equiv}N{-}XeF^{+}AsF_6^{-}$

Xe(1)···F(1A)	3.293	N(1)···F(4A)	3.094
Xe(1)···F(2A)	3.140	N(1)···F(7A)	3.141
Xe(1)···F(4A)	3.420		
Xe(1)···F(5A)	3.350		
Xe(1)···F(6)	3.247		
Xe(1)···F(7A)	3.565		
Xe(1)···F(7B)	3.241		

$CH_3C{\equiv}N{-}XeF^{+}AsF_6^{-}{\cdot}HF$

Xe(1)···F(1A)	3.236	H(2)···F(1)	2.635
Xe(1)···F(2)	3.421	H(2)···F(7A)	2.630
Xe(1)···F(3)	3.380		
Xe(1)···F(4A)	3.419	N(1)···F(4A)	3.083
Xe(1)···F(5A)	3.320	N(1)···F(5A)	3.007
Xe(1)···F(6A)	3.190	N(1)···F(6A)	3.050
Xe(1)···F(7)	3.407		
Xe(1)···F(8)	3.193		

$(CH_3)_3CC{\equiv}N{-}XeF^{+}AsF_6^{-}$

Xe(1)···F(2A)	3.356	N(1)···F(2A)	2.990
Xe(1)···F(2B)	3.249	N(1)···F(5)	2.989
Xe(1)···F(5)	3.227		
Xe(1)···F(5A)	3.335		
Xe(1)···F(6A)	3.385		
Xe(1)···F(7A)	3.356		

***s*-$C_3F_3N_2N{-}XeF^{+}AsF_6^{-}\cdot 2.5BrF_5$**

Xe(1)···F(2)	3.210	Xe(1)···F(12A)	3.444
Xe(1)···F(6)	3.298	Xe(1)···F(16)	3.406
Xe(1)···F(7A)	3.389	Xe(1)···F(22A)	3.523
Xe(1)···F(9A)	3.479	Xe(1)···F(24A)	3.228
Xe(1)···F(10A)	3.296	Xe(1)···F(26A)	3.271
Xe(1)···F(10B)	3.352	Xe(1)···F(27A)	3.373

Table E (continued)

C_5F_5N–$XeF^+AsF_6^- \cdot 2.5BrF_5$

Xe(1)···F(2)	3.192	Xe(1)···F(9A)	3.349
Xe(1)···F(6)	3.193	Xe(1)···F(12A)	3.371
Xe(1)···F(7A)	3.525	Xe(1)···F(24)	3.257
Xe(1)···F(8)	3.535	Xe(1)···F(25B)	3.374
Xe(1)···F(9)	3.296	Xe(1)···F(27A)	3.270

$Xe_2F_3^+AsF_6^-$

Xe(1)···F(3A)	3.232	Xe(3)···F(2)	3.261
Xe(1)···F(3B)	3.305	Xe(3)···F(5A)	3.218
Xe(1)···F(6)	3.325	Xe(3)···F(7A)	3.433
Xe(1)···F(8)	3.236	Xe(3)···F(8A)	3.474
Xe(1)···F(9)	3.214	Xe(3)···F(10A)	3.295
Xe(1)···F(11A)	3.440	Xe(3)···F(12F)	3.293
Xe(1)···F(12A)	3.518	Xe(3)···F(12G)	3.318
Xe(1)···F(13B)	3.357	Xe(3)···F(13B)	3.370
Xe(1)···F(14)	3.383	Xe(3)···F(13C)	3.308
Xe(1)···F(14A)	3.384	Xe(3)···F(13D)	3.275
		Xe(3)···F(13E)	3.357
Xe(2)···F(2)	3.265	Xe(3)···F(14D)	3.254
Xe(2)···F(5A)	3.195	Xe(3)···F(14E)	3.422
Xe(2)···F(6A)	3.222		
Xe(2)···F(9)	3.486	F(1)···F(3A)	3.010
Xe(2)···F(10B)	3.464	F(1)···F(3B)	3.010
Xe(2)···F(11)	3.411	F(4)···F(5A)	2.948
Xe(2)···F(11B)	3.581	F(4)···F(14D)	3.011
Xe(2)···F(12D)	3.245		
Xe(2)···F(12E)	3.262		

F_5TeNH_2 (-113 °C)

N(1)···F(3)	2.828	N(1)···F(7)	2.663
N(1)···F(4)	2.833	N(1)···F(3A)	3.073
N(1)···F(6)	2.703	N(1)···F(6A)	3.020

Table E (continued)

$F_5TeNH_3^+AsF_6^-$

N(1)···F(2)	2.709	N(2)···F(6)	2.730
N(1)···F(3)	2.703	N(2)···F(7)	2.707
N(1)···F(17)	2.844	N(2)···F(13)	2.828
N(1)···F(18)	2.909	N(2)···F(14)	2.855
N(2)···F(4)	2.713	N(2)···F(19)	2.831
N(2)···F(5)	2.698		

$F_5TeN(H)Xe^+AsF_6^-$

Xe(1)···F(2)	3.300	N(1)···F(2)	2.776
Xe(1)···F(4)	3.169	N(1)···F(2A)	2.905
Xe(1)···F(7A)	3.385	N(1)···F(3)	2.661
Xe(1)···F(7B)	3.377	N(1)···F(4)	2.693
Xe(1)···F(8A)	3.265	N(1)···F(5)	2.645
Xe(1)···F(9A)	3.412	N(1)···F(6B)	2.899
Xe(1)···F(10)	3.520	N(1)···F(9A)	3.011
Xe(1)···F(10A)	3.260	N(1)···F(10A)	3.008
Xe(1)···F(10B)	3.378		
Xe(1)···F(11A)	3.281		
H(1)···F(3)	2.455		
H(1)···F(6A)	2.076		
H(1)···F(9A)	2.380		
H(1)···F(10A)	2.723		

---

r_{vdW}: Xe, 2.20 Å; N, 1.50 – 1.60 Å; NH_4^+, 1.51 Å; F, 1.35 – 1.50 Å; H, 1.20 – 1.45 Å.[192-194]

REFERENCES

1. Schrobilgen, G.J. *Synthetic Fluorine Chemistry.* Olah, G.A.; Prakash, G.K.S; Chambers, R.D. John Wiley & Sons, Inc., New York, **1992**, Chapt. 1, pp. 1-30.

2. Schrobilgen, G.J. *The Encyclopedia of Nuclear Magnetic Resonance.* Grant, D.M.; Harris, R.K. John Wiley & Sons, Inc., New York, **1996**, pp. 3251.

3. Selig, H.; Holloway, J.H. *Topics in Current Chemistry*, **1984**, *124*, 33.

4. Holloway, J.H. *Noble Gas Chemistry.* Methuen & Co., Bungay, Suffolk, **1968**.

5. Laszlo, P.; Schrobilgen, G.J. *Angew. Chem.* **1988**, *100*, 495; *Angew. Chem., Int. Ed. Engl.* **1988**, *27*, 479.

6. Claassen, H.H. *The Noble Gases.* D.C. Heath & Co., Boston, **1966**.

7. *Noble-Gas Compounds.* H.H. Hyman, Ed., The University of Chicago Press, Chicago, **1963**.

8. G.J. Schrobilgen. *NMR and the Periodic Table.* Mann, R.K., Academic Press, London, **1974**, Chapt. 14, pp. 439-454.

9. Gillespie, R.J.; Landa, B.; Schrobilgen, G.J. *J. Inorg. Nucl. Chem.* **1976**, 179.

10. Selig, H.; Holloway, J.H. *Topics in Current Chemistry.* F.L. Boschke, Ed.; Springer-Verlag: New York, **1984**, pp. 33 – 90.

11. Bartlett, N. *Endeavour* **1972**, *31*, 107.

12. Gerken, M.; Schrobilgen, G.J. *Coord. Chem. Rev.*, in press.

13. Bartlett, N.; Sladky, F.O. *Comprehensive Inorganic Chemistry.* Bailar, J.C.; Emeleus, H.J.; Nyholm, R.; Trotman-Dickenson, A.F. Pergamon Press: New York, **1973**, Vol. 1., Chapt. 6.

14. Schrobilgen, G.J. Final Technical Report No. PL-TR-91-3108, Feb. 1992, Contract F49620-87-C-0049, Phillips Laboratory, Propulsion Directorate, USAF Systems Command, Edwards Air Force Base, Ca., vol. 2, part V, pp. 22-103.

15. Hoppe, R.; Dahne, W.; Mattauch, H.; Rodder, K.M. *Angew. Chem., Int. Ed. Engl.* **1962**, 1, 599.

16. Berry, R.S.; Reimann, C.W. *J. Chem. Phys.* **1963**, *38*, 1540.

17. Sladky, F.O.; Bulliner, P.A.; Bartlett, N. *J. Chem. Soc., Chem. Commun.* **1968**, 1048.

18. Seppelt, K.; Lentz, D. *Inorg. Chem.* **1982**, *29*, 167.

19. Zalkin, A.; Ward, D.L.; Biagioni, R.N.; Templeton, D.H.; Bartlett, N. *Inorg. Chem.* **1978**, *17*, 1318.

20. Faggiani, R.; Kennepohl, D.K.; Lock, C.J.L.; Schrobilgen, G.J. *Inorg. Chem.* **1986**, *25*, 563.

21. Bartlett, N.; DeBoer, B.G.; Hollander, F.J.; Sladky, F.O.; Templeton, D.H.; Zalkin, A. *Inorg. Chem.* **1974**, *13*, 780.

22. Bartlett, N.; Gennis, M.; Gibler, D.; Morrell, B.K.; Zalkin, A. *Inorg. Chem.* **1973**, *12*, 1717.

23. MeRae, V.M.; Peacock, R.D.; Russell, D.R. *J. Chem. Soc., Chem. Commun.* **1969**, 62.

24. Coulson, C.A. *J. Chem. Soc.* **1964**, 1442.

25. Pimentel, G.C. *J. Chem. Phys.* **1951**, *19*, 466.

26. Whalen, J.M. Ph.D. Thesis, McMaster University, Hamilton, Ontario, Canada, **1994**.

27. Sladky, F.O.; Bulliner, P.A.; Bartlett, N. *J. Chem. Soc. (A)*, **1969**, 2179.

28. Holloway, J.H.; Knowles, J.G. *J. Chem. Soc. (A)*, **1969**, 756.

29. McRae, V.M.; Peacock, R.D.; Russell, D.R. *Chem. Commun.* **1969**, 62; Burgess, J.; Fraser, C.J.W.; McRae, V.M.; Peacock, R.D.; Russell, D.R. *J. Inorg. Nucl. Chem. Suppl.*, **1976**, 183.

30. Tucker, P.A.; Taylor, P.A.; Holloway, J.H.; Russell, D.R. *Acta. Crystallogr. B 31*, **1975**, 906.

31. Levy, H.A.; Argon, P.A. *J. Am. Chem. Soc.* **1963**, *85*, 241.

32. Frlec, G.; Holloway, J.H. *J. Chem. Soc., Dalton Trans.* **1975**, 535.

33. Gillespie, R.J.; Netzer, A.; Schrobilgen, G.J. *Inorg. Chem.* **1974**, *13*, 1455.

34. Gillespie, R.J.; Landa, B. *Inorg. Chem.* **1973**, *12*, 1383.

35. Bartlett, H.; Gennis, M.; Gibler, D.D.; Morrell, B.K.; Zalkin, A. *Inorg. Chem.* **1973**, *12*, 1717.

36. Huheey, J.E. *Inorg. Chem.* **1978**.

37. Huheey, J.E.; Keiter, E.A.; Keiter, R.L. *Principles of Structure and Reactivity, 4th Edition.* Harper Collins College Publishers, **1993**, Chapt. 4, pp. 113-119; Chapt. 8, pp. 290-296.

38. Bondi, A. *J. Phys. Chem.* **1964**, *68*, 441.

39. Bartlett, N.; Sladky, F.O. *Chem. Commun.* **1968**, 1046.

40. Wechsberg, M.; Bulliner, P.A.; Sladky, F.O.; Mews, R.; Bartlett, N. *Inorg. Chem.* **1972**, *11*, 30063.

41. Seppelt, K. *Angew. Chem. Int. Ed. Engl.* **1982**, *21*, 877.

42. Syvret, R.G.; Schrobilgen, G.J. *Inorg. Chem.* **1989**, *28*, 1564.

43. Gillespie, R.J.; Schrobilgen, G.J.; Slim, D.R. *J. Chem. Soc., Dalton Trans.* **1977**, 1003.

44. Emara, A.A.A. Ph.D. Thesis, McMaster University, Hamilton, Ontario, Canada, **1991**.

45. Birchall, T.; Myers, R.D.; Waard, H.; Schrobilgen, G.J. *Inorg. Chem.* **1982**, *21*, 1068.

46. Engelbrecht, A.; Sladky, F. *Int. Rev. Sci. Inorg. Chem. Ser.* **1975**, 170.

47. Sladky, F.; Kropshofer, H. *Inorg. Nucl. Chem. Lett.* **1972**, *8*, 195.

48. Christe, K.O.; Dixon, D.A.; Sanders, J.C.P.; Schrobilgen, G.J.; Wilson, W.W. *Inorg. Chem.* **1993**, *32*, 4089.

49. Seppelt, K.; Nöthe, D. *Inorg. Chem.* **1973**, *12*, 2727.

50. Templeton, L.K.; Templeton, D.H.; Seppelt, K.; Bartlett, N. *Inorg. Chem.* **1976**, *15*, 2718.

51. Sladky, F. *Monatsh. Chem.* **1970**, *101*, 1559.

52. Sladky, F. *Monatsh. Chem.* **1970**, *101*, 1571.

53. Sladky, F. *Monatsh. Chem.* **1970**, *101*, 1578.

54. Sladky, F. *Angew. Chem.* **1969**, *81*, 536; *Angew. Chem. Int. Edit.* **1969**, *8*, 523.

55. Sladky, F. *Angew. Chem.* **1970**, *82*, 357; *Angew. Chem. Int. Ed. Engl.* **1970**, *9*, 375.

56. Keller, N.; Schrobilgen, G.J. *Inorg. Chem.* **1981**, *20*, 2118.

57. Syvret, R.G.; Mitchell, K.M.; Sanders, J.C.P.; Schrobilgen, G.J. *Inorg. Chem.* **1992**, *31*, 3381.

58. Jameson, C.J. *Multinuclear NMR* J. Mason Ed., Plenum Press, New York, **1987**, Chapt. 18, pp. 463-475.

59. Schrobilgen, G.J.; Holloway, J.H.; Granger, P.; Brevard, C. *Inorg. Chem.* **1978**, *17*, 980.

60. Seppelt, K.; Rupp, H.H. *Z. Anorg. Allg. Chem.* **1974**, *409*, 338.

61. Holloway, J.H.; Schrobilgen, G.J. *Inorg. Chem.* **1980**, *19*, 2632.

62. Sawyer, J.F.; Schrobilgen, G.J.; Sutherland, S.J. *Inorg. Chem.* **1982**, 21, 4064.

63. DesMarteau, D.D.; LeBlond, R.D.; Hossain, S.F.; Nothe, D. *J. Am. Chem. Soc.* **1981**, *103*, 7734.

64. Schumacher, G.A.; Schrobilgen, G.J. *Inorg. Chem.* **1983**, *22*, 2178.

65. Floropoulos, J.; DesMarteau, D.D. *J. Am. Chem. Soc.* **1982**, *104*, 4260.

66. Frohn, H.J.; Jakobs, S.; Henkel, G. *Angew. Chem. Int. Ed. Engl.* **1989**, *28*, 11.

67. Frohn, H.J.; Schroer, T.; Henkel, G. *Z. Natur. Section B*, **1995**, *50*, 1799.

68. Emara, A.A.A.; Schrobilgen, G.J. *Inorg. Chem.* **1992**, *31*, 1323.

69. Emara, A.A.A.; Schrobilgen, G.J. *J. Chem. Soc., Chem. Commun.*, **1987**, 1644.

70. Emara, A.A.A.; Schrobilgen, G.J. *J. Chem. Soc., Chem. Commun.* **1988**, 257.

71. Schumacher, G.A.; Schrobilgen, G.J. *Inorg. Chem.* **1983**, *22*, 2178.

72. Schrobilgen, G.J. *J. Chem. Soc., Chem. Commun.* **1988**, 1506.

73. Bock, H.; Dammel, R.; Lentz, D. *Inorg. Chem.* **1984**, *23*, 153.

74. Dibeler, V.H.; Liston, S.K. *J. Chem. Phys.* **1968**, *48*, 4765.

75. Van der Kelen, G.P.; DeBièvre, P.J. *Bull. Soc. Chim. Belg.* **1960**, *69*, 379.

76. Beach, D.B.; Jolly, W.L.; Mews, R.; Waterfeld, A. *Inorg. Chem.* **1984**, *23*, 4080.

77. Rider, D.M.; Ray, G.W.; Darland, E.J.; Leroi, G.E. *J. Chem. Phys.* **1981**, *74*, 1652.

78. Field, F.H.; Franklin, J.L. *Electron Impact Phenomena and the Properties of Gaseous Ions*. Academic: New York, **1957**, Chapt. 4, pp. 113.

79. Brundle, C.R.; Robin, M.B.; Kuebler, N.A. *J. Am. Chem. Soc.* **1972**, *94*, 1466.

80. Levitt, B.W.; Widing, H.F.; Levitt, L.S. *Chem. Ind.* **1973**, 793.

81. Suffolk, R.J. *J. Elec. Spec.* **1974**, *3*, 53.

82. Collin, J. *Can. J. Chem.* **1959**, *37*, 1053.

83. Omura, I.; Baba, H.; Higasi, K.; Kanoaka, *Y. Bull. Chem. Soc. Jpn.* **1957**, *30*, 633.

84. Eickes, C. B.Sc. Thesis, McMaster University, Hamilton, Ontario, Canada, **1995**.

85. Schrobilgen, G.J. *J. Chem. Soc., Chem. Commun.* **1988**, 863.

86. Gillespie, R.J.; Schrobilgen, G.J. *Inorg. Chem.* **1976**, *15*, 22.

87. Coulson, C.A. *J. Am. Chem. Soc.* **1964**, *5*, 1442.

88. MacDougall, P.J.; Schrobilgen, G.J.; Bader, F.W. *Inorg. Chem.* **1989**, *28*, 763.

89. Liebman, J.F.; Allen, L.C. *J. Am. Chem. Soc.* **1970**, *92*, 3539.

90. Liebman, J.F.; Allen, L.C. *J. Am. Chem. Soc., Chem. Commun.* **1969**, 1355.

91. Liu, B.; Schaefer, J.F. *J. Chem. Phys.* **1971**, *55*, 2369.

92. Frenking, G.; Koch, W.; Deakyne, A.; Liebman, J.F.; Bartlett, N., in press.

93. Hottoka, M.; Roos, B.; Delos, J.B.; Srivastoava, R.; Sharma, R.B.; Koski, W.S. *Phys. Rev. A,* **1987**, *45*, 4515.

94. Basch, H.; Moskowitz, J.W.; Hollister, C.; Hankin, D. *J. Chem. Phys.* **1971**, *55*, 1922.

95. Bagus, P.S.; Liu, B.; Schaefer, H.F. *J. Am. Chem. Soc.* **1972**, *94*, 6635.

96. Seppelt, K. *Z. Anorg. Allg. Chem.* **1973**, *399*, 65.

97. Miller, P.K.; Abney, K.D.; Rappé, A.K.; Anderson, O.P.; Strauss, S.H. *Inorg. Chem.* **1988**, *27*, 2255.

98. Seppelt, K. *Acc. Chem. Research* **1979**, *12*, 211.

99. Damerius, R.; Huppmann, P.; Lentz, D.; Seppelt, K. *J. Chem. Soc., Dalton Trans.* **1984**, 2821.

100. Engelbrecht, A.; Sladky, F. *MTP Int. Rev. Sci.: Inorg. Chem., Ser. One* **1972**, *2*, Chapt. 5.

101. Porcham, W.; Engelbrecht, A. *Monatsh. Chem.* **1971**, *102*, 333.

102. Seppelt, K. *Z. Anorg. Allg. Chem.* **1974**, *406*, 287.

103. Kropshofer, H.; Leitzke, O.; Peringer, P.; Sladky, F. *Chem. Ber.* **1981**, *114*, 2644.

104. Engelbrecht, A.; Sladky, F. *Angew. Chem.* **1964**, *76*, 379.

105. Jacob, E.; Lentz, D.; Seppelt, K.; Simon, A. *Z. Anorg. Allg. Chem.* **1981**, *472*, 7.

106. Sladky, F.; Kropshofer, H. *J. Chem. Soc., Chem. Commun.* **1973**, 600.

107. Mercier, H.P.A.; Sanders, J.C.P.; Schrobilgen, G.J. *J. Am. Chem. Soc.* **1993**, *115*, 11279.

108. Meakin, P.; Muetterties, E.L.; Jesson, J.P. *J. Am. Chem. Soc.* **1972**, *94*, 5271.

109. Seppelt, K. *Z. Anorg. Allg. Chem.* **1973**, *399*, 65.

110. Casteel, J.W.; MacLeod, D.M.; Mercier, H.P.A.; Schrobilgen, G.J. *Inorg. Chem.* **1996**, *35*, 7279.

111. Colsman, M.R.; Newbound, T.D.; Marshall, L.J.; Noirot, M.D.; Miller, M.M.; Wulfsberg, G.P.; Frye, J.S.; Anderson, O.P.; Strauss, S.J. *J. Am. Chem. Soc.* **1990**, *112*, 2349.

112. Mercier, H.P.A.; Sanders, J.C.P.; Schrobilgen, G.J. *Inorg. Chem.* **1995**, *34*, 5261.

113. Seppelt, K. *Z. Anorg. Allg. Chem.* **1977**, *428*, 35.

114. Casteel, W.J.; Kolb, P.; LeBlond, N.; Mercier, H.P.A.; Schrobilgen, G.J. *Inorg. Chem.* **1996**, *35*, 929.

115. Collins, M.J.; Schrobilgen, G.J. *Inorg. Chem.* **1985**, *24*, 2608.

116. Christe, K.O.; Wilson, W.W. *J. Fluorine Chem.* **1990**, *47*, 117.

117. Christe, K.O.; Dixon, D.A.; Mercier, H.P.A.; Sanders, J.C.P.; Schrobilgen, G.J.; Wilson, W.W. *J. Am. Chem. Soc.* **1994**, *116*, 2850.

118. Seel, F.; Gombler, W.J. *J. Fluorine Chem.* **1974**, *4*, 327.

119. Gibson, J.A.; Ibbott, D.G.; Janzen, A.F. *F. Can. J. Chem.* **1973**, *51*, 3203.

120. Janzen, A.F. *Coord. Chem. Rev.* **1994**, *130*, 355.

121. Kropshofer, H.; Leitzke, O.; Peringer, P.; Sladky, F. *Chem. Ber.* **1981**, *114*, 2644.

122. Mercier, H.P.A.; Sanders, J.C.P.; Schrobilgen, G.J.; Tsai, S.S. *Inorg. Chem.* **1993**, *32*, 386.

123. Hartl, H.; Huppmann, P.; Lentz, D.; Seppelt, K. *Inorg. Chem.* **1983**, *22*, 2183.

124. Seppelt, K. *Inorg. Chem.* **1973**, *12*, 2837.

125. Hoffman, C.J. *Inorg. Synth.* **1953**, *4*, 150.

126. Seppelt, K. *Chem. Ber.* **1977**, *110*, 1470.

127. Lentz, D.; Seppelt, K. *Z. Anorg. Allg. Chem.* **1983**, *502*, 83.

128. Schrobilgen, G.J., work in progress.

129. Bain, A.D. MEX/MEXICO: The McMaster Program for Exchange Lineshape Calculations. March 1997; Bain, A.D.; Duns, G.J. *Can. J. Chem.* **1996**, *74*, 819; Bain, A.D.; Duns, G.J. *Methods for Stucture Elucidation by High-Resolution NMR*, Elsevier Science B.V., **1997**, Chapt. 12, pp. 227-263.

130. Paprica, A. B.Sc. Thesis, McMaster University, Hamilton, Ontario, Canada, **1989**.

131. Minkwitz, R.; Nowicki, J. *Z. Anorg. Allg. Chem.* **1991**, *596*, 93.

132. Peach, M.E.; Waddington, J.C. *J. Chem. Soc.* **1962**, 600.

133. Deno, N.C.; Gaugler, R.W.; Wisotsky, M.J. *J. Org. Chem.* **1966**, *31*, 1967.

134. Olah, G.A.; Kiovsky, T.E. *J. Am. Chem. Soc.* **1968**, *90*, 4666.

135. Constant, G.; Daran, J.; Jeannin, Y.; Morancho, R. *J. Coord. Chem.* **1973**, *2*, 303.

136. Winnewisser, G. *J. Mol. Spectrosc.* **1971**, *39*, 149.

137. Brackemeyer, T.; Erker, G.; Fröhlich, R.; Prigge, J.; Peuchert, U. *Chem. Ber.* **1997**, *130*, 899.

138. Blachnik, R.; Stumpf, K.; Reuter, H.; Pawlak, R. *Z. Kristallogr.* **1998**, *213*, 152.

139. Constant, G.; Daran, J.C.; Jeannin, Y. *J. Solid State Chem.* **1970**, *2*, 421.

140. Chavant, C.; Constant, G.; Jeannin, Y.; Morancho, R. *Acta. Cryst.* **1975**, *B31*, 1823.

141. Jones, P.G.; Roesky, H.W.; Schimkowiak, J. *J. Chem. Soc., Chem. Commun.* **1988**, 730.

142. Duffin, B. *Acta. Cryst.* **1968**, *B24*, 396.

143. Jacobsen, H.; Berke, H.; Döring, S.; Kehr, G.; Erker, G.; Fröhlich, R.; Meyer, O. *Organometallics* **1999**, *18*, 1724.

144. Choplin, F.; Kaufmann, G. *Theoret. Chim. Acta. (Berl.)* **1972**, *25*, 54.

145. Lu, J.; Harrison, W.T.A.; Jacobson, A.J. *Angew. Chem.* **1995**, *107*, 2759; *Angew. Chem. Int. Ed. Engl.* **1995**, *34*, 2557.

146. Connelly, N.G.; Hicks, O.M.; Lewis, G.R.; Moreno, M.T.; Orpen, A.G. *J. Chem. Soc., Dalton Trans.* **1998**, 1913.

147. Werner, B.; Kräuter, T.; Neumüller, B. *Z. Anorg. Allg. Chem.* **1995**, *621*, 346.

148. Apperley, D.C.; Brimah, A.K.; Soliman, T.M.; Fisher, R.D. *Organometallics* **1992**, *11*, 1718.

149. Burbank, R.D.; Bensey, F.N. *J. Chem. Phys.* **1957**, *27*, 981.

150. Robiette, A.G.; Bradley, R.H.; Brier, P.N. *J. Chem. Soc., Chem. Commun.* **1971**, 1567.

151. Gillespie, R.J; Hargittai, I. *The VSEPR Model of Molecular Geometry*. Allyn and Bacon, Barton, **1991**, pp. 59.

152. Gillespie, R.J. *J. Chem. Educ.* **1963**, *40*, 295.

153. Bats, J.W.; Coppens, P.; Koetzle, T.F. *Acta. Crystallogr., Sect. B, 1977, B33*, 37.

154. Jeffrey, G.J.; Stadler, J. *J. Chem. Soc.* **1951**, 1467.

155. Cox, G.W.; Sabine, T.M.; Padmanabhan, V.M.; Ban, N.T.; Chung, M.K.; Surjadi, A.S. *Acta Crystallogr.* **1967**, *23*, 578.

156. Hodgson, P.G.; Moore, F.H.; Kennard, C.H.L. *J. Chem. Soc., Dalton Trans.* **1976**, 1443.

157. Jeffrey, G.J.; Jones, D.W. *Acta Crystallogr.* **1956**, *9*, 283.

158. Tillack, J.V.; Kennard, C.H.L. *J. Chem. Soc. A.* **1970**, 1637.

159. Chen, S.J.; Behrens, U.; Olbrich, F.; Mews, R. *Z. Anorg. Allg. Chem.* **1993**, *619*, 1725.

160. Holtcamp, M.W.; Henling, L.M.; Day, M.W.; Labinger, J.A.; Bercaw, J.E. *Inorg. Chim. Acta.* **1998**, 467.

161. *International Tables for X-Ray Crystallography.* Vol. I, Kynoch Press, Birmingham, England, **1952**.

162. Naumann, D.; Butler, H.; Gnann, R.; Tyrra, W. *Inorg. Chem.* **1993**, *32*, 861.

163. Raddy, G.S.; Goldstein, J.H. *J. Chem. Phys.* **1963**, *39*, 3509.

164. LeBlond, R.D.; DesMarteau, D.D. *J. Chem. Soc., Chem. Commun.* **1974**, 555.

165. Seppelt, K. *Inorg. Chem.* **1973**, *12*, 2837.

166. Turowsky, L.; Seppelt, K. *Inorg. Chem.* **1990**, *29*, 3226.

167. Seppelt, K.; Oberhammer, H. *Inorg. Chem.* **1985**, *24*, 1227.

168. Naumann, D.; Tyrra, W. *J. Chem. Soc., Chem. Commun.* **1989**, *47*.

169. Frohn, H.J.; Jakobs, S. *J. Chem. Soc., Chem. Commun.* **1989**, 625.

170. Butler, H.; Naumann, D.; Tyrra, W. *Eur. J. Solid State Inorg. Chem.* **1992**, *29*, 739.

171. Emsley, J.W.; Feeney, J.; Sutcliffe, L.H. *High-Resolution Nuclear Magnetic Resonance Spectroscopy.* Pergamon Press, New York, **1966**; Vol. 1, Chapt. 9, pp. 184-190.

172. Brunvoll, J.; Kolonits, M.; Bliefert, C.; Seppelt, K.; Hargittai, I. *J. Mol. Struc.* **1982**, *78*, 307.

173. Bürger, H. *Z. Anorg. Allg. Chem.* **1968**, *360*, 97.

174. Burbank, R.D.; Falconer, W.E.; Sunder, W.A. *Science* **1972**, *178*, 1285.

175. Christe, K.O.; Dixon, D.A.; Sanders, J.C.P.; Schrobilgen, G.J.; Wilson, W.W. *Inorg. Chem.* **1993**, *32*, 4089.

176. Strauss, S.H.; Abney, K.D.; Anderson, O.P. *Inorg. Chem.* **1986**, *25*, 2506.

177. Seppelt, K. *Chem. Ber.* **1972**, *105*, 243.

178. Reed, A.E.; Schleyer, P.R. *J. Am. Chem. Soc.* **1990**, *112*, 1434.

179. Binsch, G.; Lambert, J.B.; Roberts, B.W.; Roberts, J.D. *J. Am. Chem. Soc.* **1964**, *86*, 5564.

180. Gilespie, R.J.; Robinson, E.A. *Advances in Molecular Research.* JAI Press Inc., 1998, Vol. 4, pp. 1-41.

181. Schumacher, G.A.; Schrobilgen, G.J. *Inorg. Chem.* **1984**, *23*, 2923.

182. Engelbrecht, A.; Sladky, F. *Angew. Chem.* **1964**, *76*, 389; *Angew. Chem. Int. Ed. Engl.* **1964**, *3*, 383.

183. Seppelt, K. *Angew. Chem.* **1972**, *84*, 212; *Angew. Chem. Int. Ed. Engl.* **1972**, *11*, 630.

184. Zylka, P.; Oberhammer, H.; Seppelt, K. *J. Mol. Struc.* **1991**, *243*, 411.

185. Turowsky, L.; Seppelt, K. *Z. Anorg. Allg. Chem.* **1992**, *609*, 153.

186. Schrobilgen, G.J.; Holloway, J.H.; Granger, P.; Brevard, C. *Inorg. Chem.* **1978**, *17*, 980.

187. Mercier, H.P.A.; Sanders, J.C.P.; Schrobilgen, G.J. *Inorg. Chem.* **1994**, *116*, 2921.

188. Sawyer, J.F.; Schrobilgen, G.J. *Acta. Cryst.* **1982**, *B38*, 1561.

189. Oberhammer, H.; Seppelt, K. *Inorg. Chem.* **1978**, *17*, 1435.

190. Seppelt, K. *Chem. Electroneg. Elem.* **1979**, *12*, 211.

191. Schack, C.J.; Wilson, W.W.; Christe, K.O. *Inorg. Chem.* **1983**, *22*, 18.

192. Seggen, D.M.V.; Hurlburt, P.K.; Anderson, O.P.; Strauss, S.H. *Inorg. Chem.* **1995**, *34*, 3453.

193. Kabish, G. *J. Raman Spectrosc.* **1980**, *9*, 279.

194. Günthard, H.H.; Kováts, E. *Helv. Chim. Acta.* **1952**, 1190.

195. Yamadera, R.; Krimm, S. *Spectrochim. Acta.* **1968**, *24A*, 1677.

196. Spring, C.A.; True, N.S. *J. Am. Chem. Soc.* **1983**, *105*, 7231.

197. Günther, H. *NMR Spectroscopy: An Introduction*. J. Wiley and Sons: New York, **1973**, Ch. 8, pp. 240-287.

198. Siegel, S.; Gebert, E. *J. Am. Chem. Soc., Chem. Com.* **1962**, *85*, 240.

199. Mahler, W.; Meutterties, E.L. *Inorg. Chem.* **1965**, *4*, 1520.

200. Turowsky, L.; Seppelt, K. *Z. Anorg. Allg. Chem.* **1991**, *602*, 79.

201. Sosa, C.; Andzelm, J.; Elkin, B.C.; Wimmer, E.; Dobbs, K.D.; Dixon, D.A. *J. Phys. Chem.* **1992**, *96*, 6630.

202. Christe, K.O.; Curtis, E.C.; Dixon, D.A.; Mercier, H.P.A.; Sanders, J.C.P.; Schrobilgen, G.J.; Wilson, W.W. ACS Symposium Series 555; American Chemical Society: Washington, DC, **1994**; pp. 67.

203. Christe, K.O.; Dixon, D.A.; Mahjoub, A.R.; Mercier, H.P.A.; Sanders, J.C.P.; Seppelt, K.; Schrobilgen, G.J.; Wilson, W.W. *J. Am. Chem. Soc.* **1993**, *115*, 2696.

204. Christe, K.O.; Curtis, E.C.; Dixon, D.A.; Mercier, H.P.A.; Sanders, J.C.P.; Schrobilgen, G.J. *J. Am. Chem. Soc.* **1991**, *113*, 3351.